APPENDIX F

FLUID ENERGY CLOSURE

This section describes the closure relationships for the energy equations given in Section 2.1.1. The quantities required are the phase-change rate, Γ, phasic interfacial heat flows, q_{ig} and $q_{i\ell}$, sensible heat flow between liquid and gas, q_{gl}, and phasic wall heat flows, $q_{w\ell}$ and q_{wg}. Section F.1. below will discuss the interfacial heat transfer between phases, and Section F.2. will discuss wall-to-fluid heat transfer. Before the reader begins this section, a review of the following sections is recommended: Section 2.1., and Appendices D and E. The following nomenclature applies to the models discussed in this section.

NOMENCLATURE

a_i: interfacial-area concentration

$a_1 - a_4$: empirical constants [see Eq. (F-97)]

A: area

$\bar{A}$: average area

A_f: cell-edge flow area

A_{fr}: interfacial surface area for bubbles traveling in the liquid core

B: volume

$\bar{B}$: average volume

B_{cell}: cell volume

c_p: specific heat at constant pressure ($J \cdot kg^{-1} \cdot K^{-1}$)

C^*: dummy constant [see Eq. (F-21)]

C_1, C_2: relaxation constants

C_c: correction factor for droplet internal circulation

C_{eva}: coefficient of evaporation

C_i: steam concentration at the interface

C_r: correction factor for liquid-film interfacial area

C_{u1}, C_{u2}: empirical constants in Eq. (F-118).

Ca: capillary number

D: diameter (m)

D^*: dummy diameter [see Eq. (F-20)]

D_o: diffusion coefficient (m/s)

D_b: bubble Sauter mean diameter

$D_{b,A}$: bubble area-equivalent diameter

$D_{b,V}$: bubble volume-equivalent diameter

D_c: cap-bubble base diameter

D_d: droplet Sauter mean diameter

D_H: hydraulic diameter (m)

D_{vm}: droplet volume median diameter

E: entrainment fraction

f: new-time fraction in Eq. (F-160) or friction factor in Section F.2.2.4.

f_{cp}: two-phase friction factor

f_ℓ: liquid fraction contacting wall

F: correction factor to Dittus-Boelter equation

F_s: sink function

F_u: cold-wall fraction

g: gravitational constant

G: mass flux (kg/m^2-s)

h: heat-transfer coefficient (W$\cdot$ m$^{-2}\cdot$K^{-1})

h': separate phasic heat-transfer coefficient (W$\cdot$ m$^{-2}\cdot$K^{-1})

h^*: phasic enthalpy

h_{fg}: latent heat of vaporization

h_{fls}: liquid-side HTC due to flashing

h_{gl}: gas-to-liquid sensible heat-transfer coefficient

h_{gsav}: single-phase wall-to-vapor heat-transfer coefficient

$h'_{\ell g}$: modified latent heat to account for the superheated vapor (J$\cdot$ kg^{-1})

h_M: mass-transfer coefficient

h_r: radiation heat-transfer coefficient (W$\cdot$ m$^{-2}\cdot$K^{-1})

h_Γ: subcooled-boiling heat-transfer coefficient (W$\cdot$ m$^{-2}\cdot$K^{-1})

H_{ALV}: liquid-side heat-transfer factor during flashing

H_{ALVE}: liquid-side heat-transfer factor during condensation and evaporation

H_{CHTA}: gas-to-liquid sensible heat-transfer factor

H_{CHTI}: vapor-side heat-transfer factor

H_o: empirical constant [see Eqs. (F-30), (F-32)]

J: superficial velocity (m$\cdot$ s^{-1}) or volumetric flux

k: thermal conductivity (W$\cdot$ m$^{-2}\cdot$K^{-1})

$l_{\min}$: thickness related to minimum film thickness

L: length (m)

L_b: length over which saturated boiling takes place (m)

L_c: characteristic length

L_ℓ: stratified liquid level

L_o: Laplace coefficient

M: molecular weight ($kg \cdot mol^{-1}$)

M_{plug}: multiplication factor for plug flow interfacial area

$\dot{m}_e$: evaporative mass flux

$\dot{m}_v$: film vapor mass flux

N: number of bubbles in Section F.1. or number of fields in Section F.2.

P: total pressure (Pa)

q: phasic sensible energy rate of change (heat-transfer rate)

q': heat flux ($W \cdot m^{-2}$)

$q_{g\ell}$: sensible heat flow between liquid and gas

q_{total}: total wall heat-transfer rate

q_{wi}: wall-to-water interface heat-transfer rate

r: radius of radial ring

R: gas constant

s: slip ratio

S: suppression factor in Chen correlation

t: time (s)

t_d: droplet thermal boundary layer lifetime

T: temperature (K)

T^*: dimensionless droplet mixing-cup temperature

T_{NH}: homogenous nucleation temperature

T_{sv}: saturation temperature corresponding to steam partial pressure (K)

V: velocity ($m \cdot s^{-1}$)

V_{bubble}: bubble terminal velocity

V_c: Helmholtz velocity

V^*_{max}: dimensionless droplet maximum circulation velocity

WF, W: weighting factor

W_f: annular-mist-flow weighting factor

W_{fd}: cold-wall liquid-film-flow weighting factor

W_t: transition-flow weighting factor

x: mass quality

x_e: equilibrium quality

x_f: flow quality

X: dummy variable

X_{TT}: Martinelli parameter

z: axial elevation

z_b: bottom elevation of the hydro cell

z_c: entry length for equilibrium entrainment fraction

z_t: top elevation of the hydro cell

Z: transition elevation between flow regimes

α: void fraction

α_d: droplet fraction in gas core

α_{dd}: droplet fraction in channel cross section

α_f: cold-wall liquid-film fraction

α_{fr}: void fraction for bubbles traveling in the liquid-core region

α_{gs}: average void fraction within the liquid slug

α_{hom}: homogeneous void fraction

β: coefficient of thermal expansion (K^{-1})

δ_f: film thickness

Δq: change in heat flux

ΔT_e: effective superheat

Δt: time-step size or time increment (s)

ΔT_{min}: wall superheat at minimum film boiling point (K)

ΔT_{HN}: wall superheat at homogenous nucleation temperature (K)

ΔT_{sat}: wall superheat

ΔT_{sub}: liquid subcooling (°C)

Δr: radial ring increment for 3D component

Δx: cell length for 1D component (m)

Δz: axial level increment for 3D component

$\Delta\theta$: azimuthal segment increment for 3D component

ε: emissivity or surface roughness

Γ: phase change rate per unit volume ($kg/m^3\text{-}s^1$)

λ: square root of phasic density-viscosity product ratio or Taylor instability wavelength defined by Eq. (F-250)

κ: phasic viscosity ratio

μ: dynamic viscosity (Pa·s)

θ: angle of inclination from horizontal (rad)

ρ: density ($kg \cdot m^{-3}$)

σ: surface tension ($N \cdot m^{-1}$)

σ_r: Stefan-Boltzmann constant ($W \cdot m^{-2} \cdot K^{-4}$)

ϕ: cap-bubble wake angle

Ψ: sphericity

χ: dummy integration variable

τ: time (s)

ξ: transition-boiling weighting factor in Section F.2.1.3.1. or coefficient dependent upon the velocity profile in the vapor film in Section F.2.2.4.1.

Subscripts

a: noncondensable gas or air [in Eq. (F-150)]

AG: agitated IAF regime

Brom: related to the Bromley correlation

bub: bubbly flow

CHF: critical heat flux

cond: condensation

core: liquid core

crit, *cr*: critical

D: drag

d: droplet

Den: related to the Denham correlation

dr: related to Dougall-Rohsenow correlation

drop: droplet

DP, *ds*: dispersed (or post-agitated) flow

f: film properties

fBB: related to Bromley correlation

forc: forced convection

film: film boiling

g: gas-vapor mixture

grid: grid spacer

i: interfacial or radial ring counter for 3D component

inv: inverted annular flow

j: azimuthal segment or cell counter for 3D or 1D component

k: axial level counter for 3D component

ℓ: liquid

lam: laminar flow

m: two-phase mixture properties

map: quantities calculated using the basic flow-regime map

max: maximum

min: minimum film boiling or minimum
mist: annular-mist flow
Mod: modified
mod-CSO: modified Chen-Sundaram-Ozkaynak
n: arbitrary index of a single bubble
NC: natural convection
nc: in the presence of noncondensables
nucb: nucleate boiling
plug: plug flow
post-ag: post-agitated flow
RW, *rw*: rough-wavy inverted annular flow
s: steam
sat: saturation
sb: bubbly and transition flow
SM, *sm*: smooth inverted annular flow
st: stratified flow
sub: subcooled boiling
teo: theoretical
TR,trans: transition boiling
TP: two phase
turb: turbulent flow
v: vapor
vf: vapor at film temperature
w: wall
wℓ: wall-to-liquid
wg: wall-to-gas
∞: infinity

Dimensionless Numbers

Eo: Eötvös number
Gr: Grashof number
Ja: Jakob number
Mo: Morton number
Nu: Nusselt number
N_μ: viscosity number
Pe: Peclet number

Pr: Prandtl number

Re: Reynolds number

Sc: Schmidt number

Sh: Sherwood number

St: Stanton number

We_b: bubble Weber number

We_e: effective Weber number

We_m: modified Weber number

F.1. Interfacial Heat Transfer

As discussed before, TRAC solves nonequilibrium, two-phase-flow equations where the liquid and the gas phases are not in thermodynamic equilibrium. As a result, the different phasic temperatures lead to a heat and mass exchange between the phases through the interface. The interfacial transport is calculated in subroutines TF1DS and TF3DS for 1D and 3D components, respectively.

The gas phase is assumed to be a homogeneous mixture of vapor and noncondensable gas in thermodynamic equilibrium. Further, the mixture obeys Dalton's law. The rate of change of the gas-phase sensible energy is given by

$$q_g = \underbrace{\frac{P_s}{P} H_{\mathrm{CHTI}}(T_g - T_{sv})}_{\text{gas to interface}} + \underbrace{\frac{P_a}{P} H_{\mathrm{CHTA}}(T_g - T_\ell)}_{\text{gas to liquid}} , \tag{F-1}$$

where H is the heat-transfer factor, defined as the product of the convective heat-transfer coefficient and the interfacial area. The first term in Eq. (F-1) corresponds to heat transfer to or from the interface (q_{ig}) and is converted to or released as latent heat through phase change. The second term is the direct sensible heat exchange between the liquid and the gas.

Similarly, the rate of change of the liquid-phase sensible energy is given by

$$q_\ell = \underbrace{\{H_{\mathrm{ALVE}}(T_\ell - T_{sv}) + H_{\mathrm{ALV}}\langle T_\ell - T_{\mathrm{sat}}\rangle'\}}_{\text{liquid to interface}} \underbrace{+\frac{P_a}{P} H_{\mathrm{CHTA}}(T_\ell - T_g)}_{\text{liquid to gas}} . \tag{F-2}$$

Likewise, the first term ($q_{i\ell}$) accounts for the sensible heat transferred to or from the interface where it is converted to or released as latent heat, and the second term is the direct sensible heat exchange between the liquid and the gas. In TRAC, evaporation and flashing are accounted for separately. Consequently, we have two liquid-side interfacial heat-transfer factors, H_{ALV} and H_{ALVE}. For condensation and evaporation, H_{ALVE} is used. As shown in Fig. F-1., evaporation occurs if $T_{sv} < T_\ell < T_{\mathrm{sat}}$ and flashing occurs if $T_\ell > T_{\mathrm{sat}}$.

H_{ALV} is used during flashing. Note that the flashing term is incorporated into Eq. (F-2) through a singularity function, which is defined as follows:

$$\langle T_\ell - T_{sat} \rangle' = \begin{cases} 0 & \text{if } T_\ell \le T_{sat} \\ T_\ell - T_{sat} & \text{if } T_\ell > T_{sat} \end{cases} .$$

When Eqs. (F-1) and (F-2) are added, the direct sensible heat-transfer terms cancel out, and we can calculate the mass-transfer rate per unit volume as a result of interfacial heat transfer between the phases as

$$\Gamma_i = \frac{q_{ig} + q_{i\ell}}{B_{cell}(h_v^* - h_\ell^*)} , \tag{F-3}$$

where

$$q_{i\ell} = \underbrace{H_{ALVE}(T_\ell - T_{sv})}_{\text{evaporation or condensation}} + \underbrace{H_{ALV}\langle T_\ell - T_{sat}\rangle'}_{\text{flashing}} \tag{F-4}$$

and

$$q_{ig} = \frac{P_s}{P} H_{CHTI}(T_g - T_{sv}) . \tag{F-5}$$

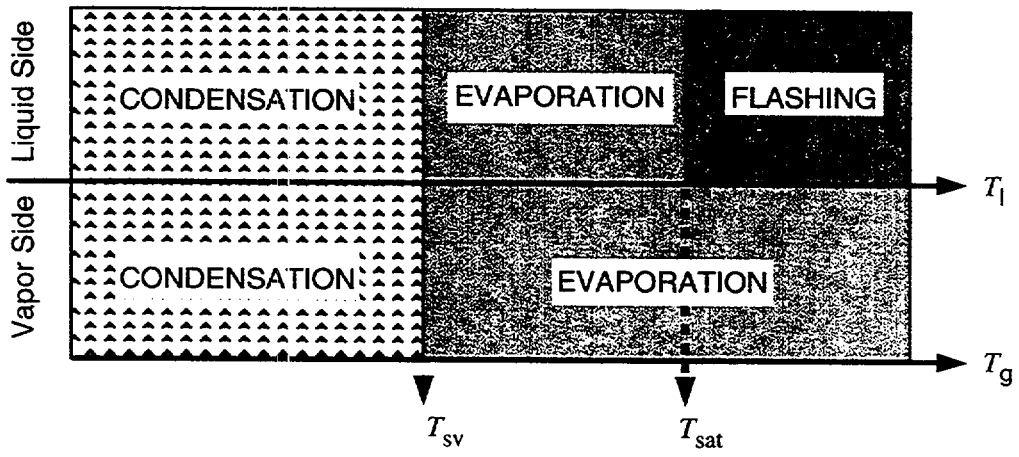

Fig. F-1. Illustration of the selection logic for condensation, evaporation, and flashing.

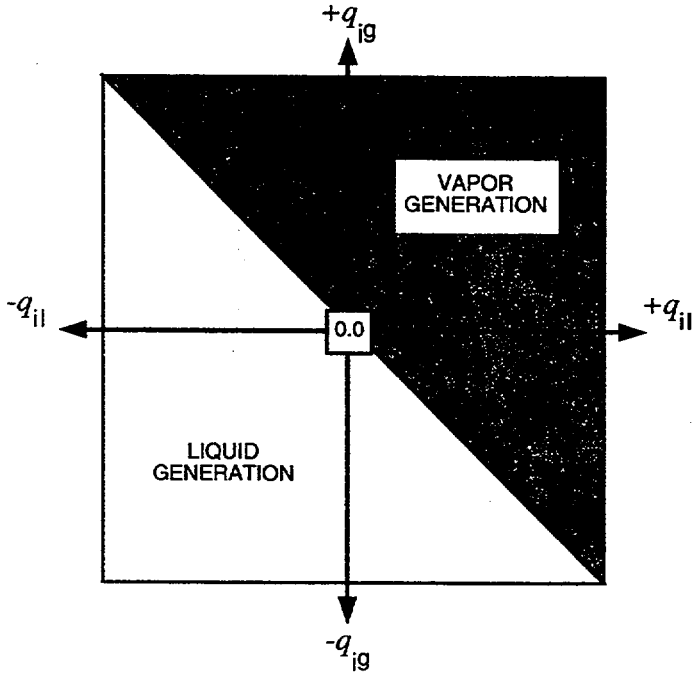

Fig. F-2. Interfacial mass-transfer map.

A positive Γ_i indicates vapor generation and a negative Γ_i indicates liquid generation. Notice that while q_{ig} is negative, $q_{i\ell}$ may be positive, and vice versa. The net vapor or liquid generation is determined by the relative magnitude of these quantities and is illustrated in Fig. F-2. The total rate of phase change also includes the effect of subcooled boiling and is given by

$$\Gamma = \Gamma_i + \Gamma_{sub} \ , \tag{F-6}$$

where Γ_{sub} is determined through wall heat transfer and is treated in Section G.1.

To calculate q_g, q_ℓ, and Γ_i, we need closure relationships for the interfacial area and liquid- and vapor-side heat-transfer coefficients, which provide H_{ALVE}, H_{ALV}, H_{CHTI}, and H_{CHTA}. These closure relationships are provided in subroutine HTIF for 1D and 3D components and are described in the following sections for various flow regimes. In general, the interfacial area and convective heat-transfer coefficients depend on the flow pattern and are calculated in conjunction with a flow-regime map. The flow-regime map of TRAC is discussed in Appendix E and the details are not repeated here. For the sake of completeness, the basic flow-regime map is redrawn in Fig. F-3.

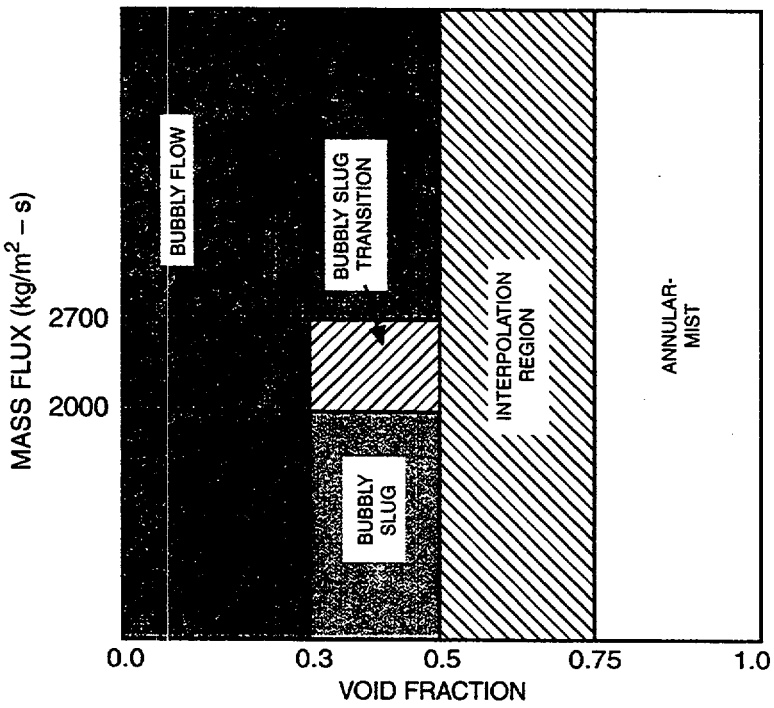

Fig. F-3. TRAC basic flow-regime map.

F.1.1. Models and Correlations in Bubbly Slug Flow

In this section and its subsections, we collectively refer to the three regions in Fig. F-3. labeled "bubbly flow," "bubbly slug transition," and "bubbly slug" as bubbly slug flow. The logic used in determining pure bubbly and transition flows is explained below in Section F.1.1.1. Older versions of TRAC documentation called the "bubbly slug" region in Fig. F-3. simply "slug" flow. Physically, the current names in Fig. F-3. are more accurate (although strictly, "bubbly slug transition" should be called bubbly/bubbly slug transition), but it is more convenient to combine the three names in the figure under the single term "bubbly slug" when describing the interfacial area logic.

For void fractions less than 30%, slugs do not form, irrespective of the mass flux. For void fractions between 30% and 50%, slugs and bubbles coexist for $G < 2000$ kg/m^2-s and slug formation is prohibited for $G > 2700$ kg/m^2-s. The intermediate mass-flux range is treated as a transition region. The models for interfacial area and convective heat-transfer coefficients in bubbly slug flow are described in the following section. The convective-heat-transfer coefficients during condensation and flashing are described in this section. Evaporation is included in Section F.1.7. because it can occur only in the presence of noncondensables. The direct sensible heat transfer between gas and liquid also is possible only in the presence of noncondensables. However, these models are flow-regime dependent and very similar to vapor-to-interface heat-transfer models.

Consequently, the calculation of H_{CHTA} is included in this section, even though it is meaningless unless noncondensables are present.

F.1.1.1. Description of Interfacial-Area Model. An idealized flow pattern for bubbly slug flow (in the sense of Fig. F-3.) is shown in Fig. F-4. Starting from the geometrically idealized shapes in this figure, Ishii and Mishima obtained (Ref. F-1., p. 32, Eq. 54)

$$a_{i,\,\text{bubbly slug}} = \frac{1}{D_{\text{slug}}}\frac{\alpha-\alpha_{gs}}{1-\alpha_{gs}}\frac{4+\dfrac{D_{\text{slug}}}{L_{\text{slug}}}}{1-\dfrac{D_{\text{slug}}}{6L_{\text{slug}}}} + \frac{6\alpha_{gs}}{D_b}\frac{1-\alpha}{1-\alpha_{gs}}, \tag{F-7}$$

where a_i is the interfacial-area concentration, α_{gs} is the average void fraction within the liquid slug, and D_b is the Sauter mean diameter of a spherical bubble population. Assuming that $D_{\text{slug}}/L_{\text{slug}} << 4$ and $D_{\text{slug}} \approx 0.88 D_H$, Ishii and Mishima obtained (Ref. F-1., p. 32, Eq. 55)

$$a_{i,\,\text{bubbly slug}} = \frac{4.5}{D_H}\frac{\alpha-\alpha_{gs}}{1-\alpha_{gs}} + \frac{6\alpha_{gs}}{D_b}\frac{1-\alpha}{1-\alpha_{gs}}. \tag{F-8}$$

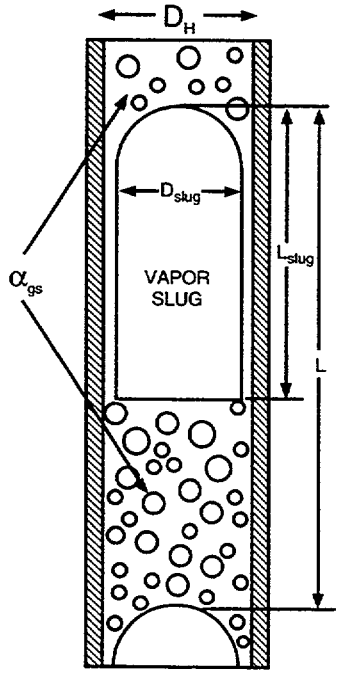

Fig. F-4. Schematic of flow pattern in bubbly slug flow.

In the code this equation appears as

$$a_{i,\text{ bubbly slug}} = \frac{C^*\alpha - \alpha_{gs}}{D^* 1-\alpha_{gs}} + \frac{6\alpha_{gs}}{D_b}\frac{1-\alpha}{1-\alpha_{gs}} \tag{F-9}$$

to include the cap-bubble regime for channels with large hydraulic diameters. The parameters C^* and D^* depend upon whether we have vapor slugs or cap bubbles and are a function of the channel hydraulic diameter. They will be described in Section F.1.1.1.2. Once the interfacial-area concentration is calculated using Eq. (F-9), it is converted to total interfacial area within a given cell through

$$A_{i,\text{ bubbly slug}} = a_{i,\text{ bubbly slug}} B_{\text{cell}} , \tag{F-10}$$

where B_{cell} is the cell volume.

In the code, we calculate the average void fraction in the liquid slug, α_{gs}, as follows:

$$\alpha_{gs} = \begin{cases} 0.3 & \text{if } G < 2000 \text{ kg/m}^2\text{-s} \\ 0.3 + 0.2\left(\frac{G-2000}{700}\right) & \text{if } 2000 \le G < 2700 \text{ kg/m}^2\text{-s} \\ 0.5 & \text{if } G \ge 2700 \text{ kg/m}^2\text{-s} \end{cases} . \tag{F-11}$$

Fernandes (cited in Ref. F-2.) measured α_{gs} in a 5-cm-diameter vertical pipe. In bubbly slug flow, the average α_{gs} is reported as ~27.5%. Barnea and Shemer (Ref. F-2.) also measured α_{gs} in a 5-cm-diameter vertical pipe. They obtained an average value of ~25%. This void fraction also corresponds to the transition from bubbly to bubbly slug flow (in the sense of Fig. F-3.) in their experiment where $G \approx 10$ kg/m^2-s. They concluded that, in the liquid slug between the vapor slugs, the flow behaves as bubbly flow. Based upon this observation, we set $\alpha_{gs} = 0.3$ at mass fluxes less than 2000 kg/m^2-s. This void fraction also corresponds to the case where the probability of collision between spherical bubbles becomes very high, as discussed by Ishii and Mishima (Ref. F-1., p. 37). For $G \approx 2700$ kg/m^2-s, we set $\alpha_{gs} = 0.5$ to be consistent with our flow-regime map. In the intermediate mass flux range, α_{gs} is obtained through linear interpolation as given by Eq. (F-11).

If the actual void fraction, α, is less than α_{gs}, then α_{gs} is set equal to α, i.e., the flow is pure bubbly. The first term in Eq. (F-9) becomes zero and only bubbles contribute to the interfacial-area concentration.

F.1.1.1.1. Bubbly Flow Interfacial Area. In order to compute the bubbly flow interfacial area, we need the Sauter mean diameter of the bubble population. Depending upon the flow conditions and bubble-generation techniques, a wide range of bubble diameters are observed in the literature. We used a simple expression suggested by Ishii (Ref. F-3.), as follows:

$$D_b = 2L_o \ , \tag{F-12}$$

where L_o is the Laplace coefficient defined as

$$L_o = \sqrt{\frac{\sigma}{g(\rho_\ell - \rho_g)}} \ . \tag{F-13}$$

Ishii suggested this expression as an approximate arithmetic average of minimum and maximum bubble diameters observed experimentally. Figure F-5. shows the bubble diameter given by Eq. (F-12) in saturated water as a function of pressure. As shown, bubble diameter is a weak function of pressure and decreases with increasing pressure. As the pressure increases from atmospheric to 10 MPa, the bubble diameter decreases from 5 to 2.8 mm. In the code, the upper and lower limits for bubble diameter are as follows:

$$0.1 \text{ mm} \leq D_b \leq 0.9D_H \ .$$

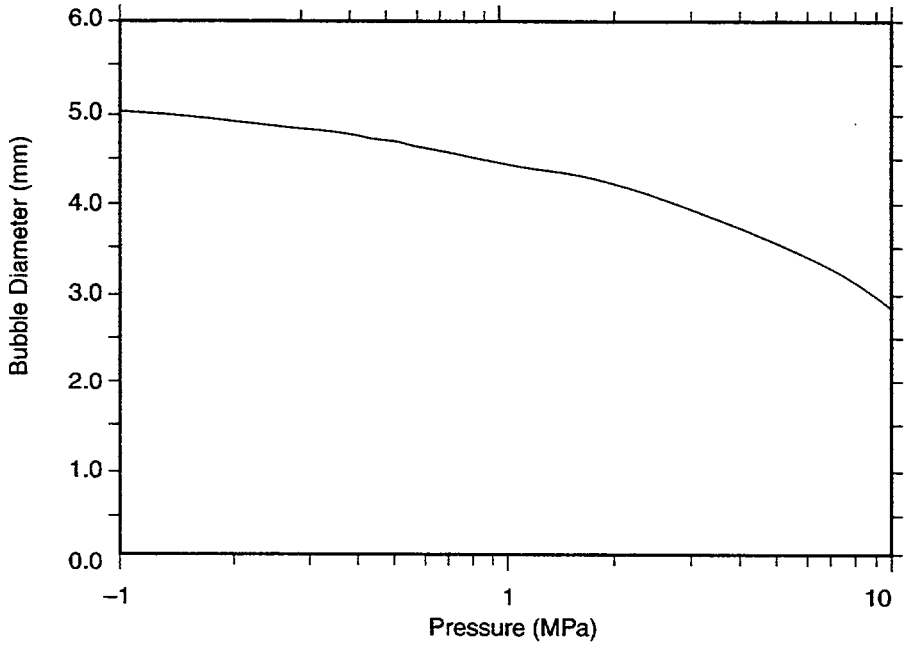

Fig. F-5. Calculated bubble diameters for saturated water as a function of pressure.

F.1.1.1.2. Bubbly Slug Flow Interfacial Area. If $\alpha > \alpha_{gs}$, then slugs or cap bubbles form, depending upon the diameter of the flow channel, and the first term in Eq. (F-9) contributes to the interfacial-area concentration. If the hydraulic diameter is less than a critical diameter, slugs can form and we use $C^*=4.5$ and $D^*=D_H$ as given by Eq. (F-8). Otherwise, cap bubbles can form and appropriate magnitudes for C^* and D^* must be used.

Kataoka and Ishii (Ref. F-4., p. 1933) state that the slug bubbles cannot be sustained in channels with a diameter much larger than $40L_o$. Because of interfacial instability, the slug bubbles disintegrate into cap bubbles. This argument is also consistent with the data of Grace et al. (Ref. F-5.) and the analysis of Kitscha and Kocamustafaogullari (Ref. F-6.). The analysis shows that the maximum stable bubble diameter in an infinite liquid is given by (Ref. F-6., Eq. 44)

$$D_{b,V} = 27.07(1+N_\mu)^{0.83} L_o \ , \tag{F-14}$$

where $D_{b,V}$ is the volume-equivalent bubble diameter and N_μ is the viscosity number defined as

$$N_\mu = \frac{\mu_\ell}{\sqrt{\rho_\ell \sigma L_o}} \ . \tag{F-15}$$

Equation (F-14) agrees well with the data of Grace et al. (Ref. F-5., Fig. 8). For water, $N_\mu << 1$, thus

$$D_{b,V} = 27.07 L_o \ . \tag{F-16}$$

To compare this expression with the criterion of Kataoka and Ishii and the critical channel diameter, we need to convert the volume-equivalent diameter to cap-base diameter.

An idealized cap bubble is shown in Fig. F-6. Ishii and Mishima (Ref. F-1., p. 31) state that the observed wake angle ϕ ranges from 46° to 65°. From pure geometry and using $\phi \approx 55°$, it can be shown that

$$D_{b,V} = 0.6 D_c \ , \tag{F-17}$$

where D_c is the cap-base diameter. Thus, Eq. (F-16) becomes

$$D_c = 45 L_o \ , \tag{F-18}$$

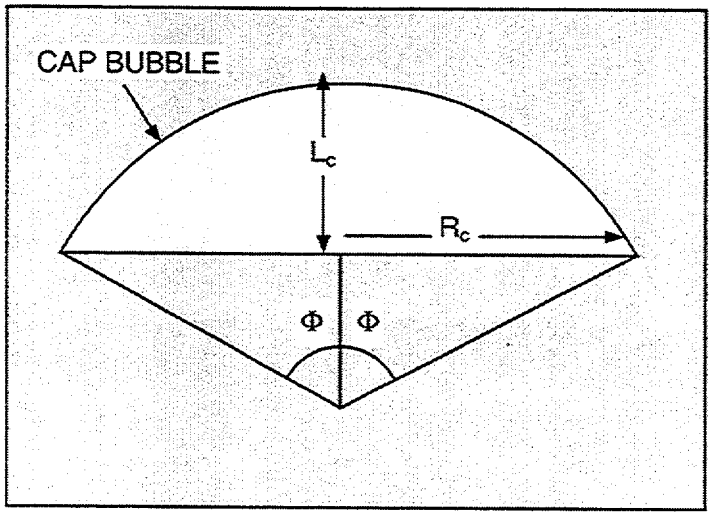

Fig. F-6. Schematic of idealized cap bubble.

which agrees with the criterion cited by Kataoka and Ishii. In the code we assumed that $D_c = 0.9D_{H,crit}$, which yields

$$D_{H,crit} = 50L_0 \quad . \tag{F-19}$$

For saturated water, the critical hydraulic diameter is plotted as a function of pressure in Fig. F-7. As shown, the transition from vapor slugs to cap bubbles occurs at smaller hydraulic diameters with increasing pressure. Using Fig. F-6., it can also be shown that $C^*=16$ for cap bubbles. Consequently, Eq. (F-9) is coded as follows:

$$D^* = \begin{cases} D_H & \text{if } D_H < D_{H,crit} \\ D_{H,crit} & \text{if } D_H \geq D_{H,crit} \end{cases} \tag{F-20}$$

and

$$C^* = \begin{cases} 4.5 & \text{if } D_H < D_{H,crit} \\ 16 & \text{if } D_H \geq D_{H,crit} \end{cases} \quad . \tag{F-21}$$

Figure F-8. illustrates the interfacial-area concentration calculated by TRAC as a function of void fraction and mass flux in the bubbly slug flow regime.

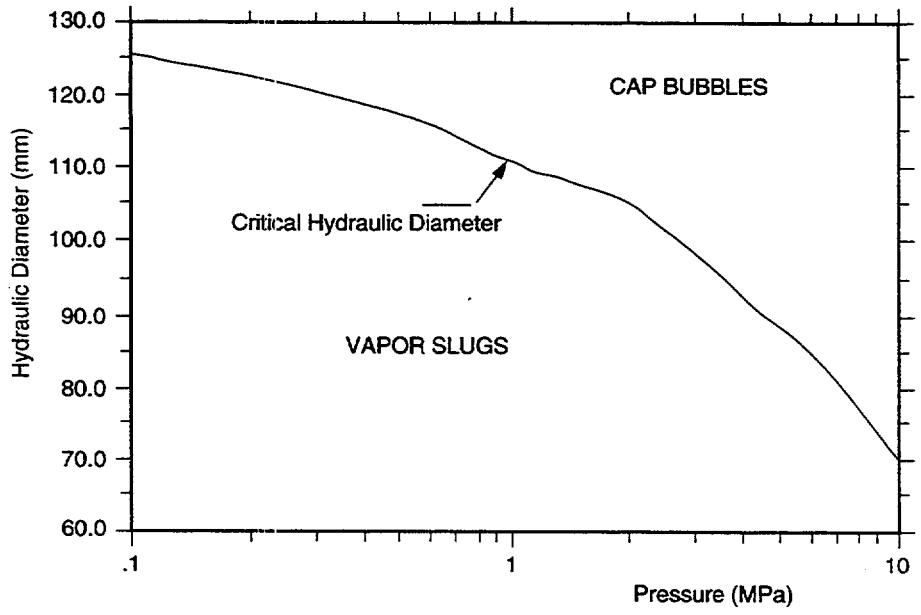

Fig. F-7. Vapor-slug-to-cap-bubbles transition map for saturated water.

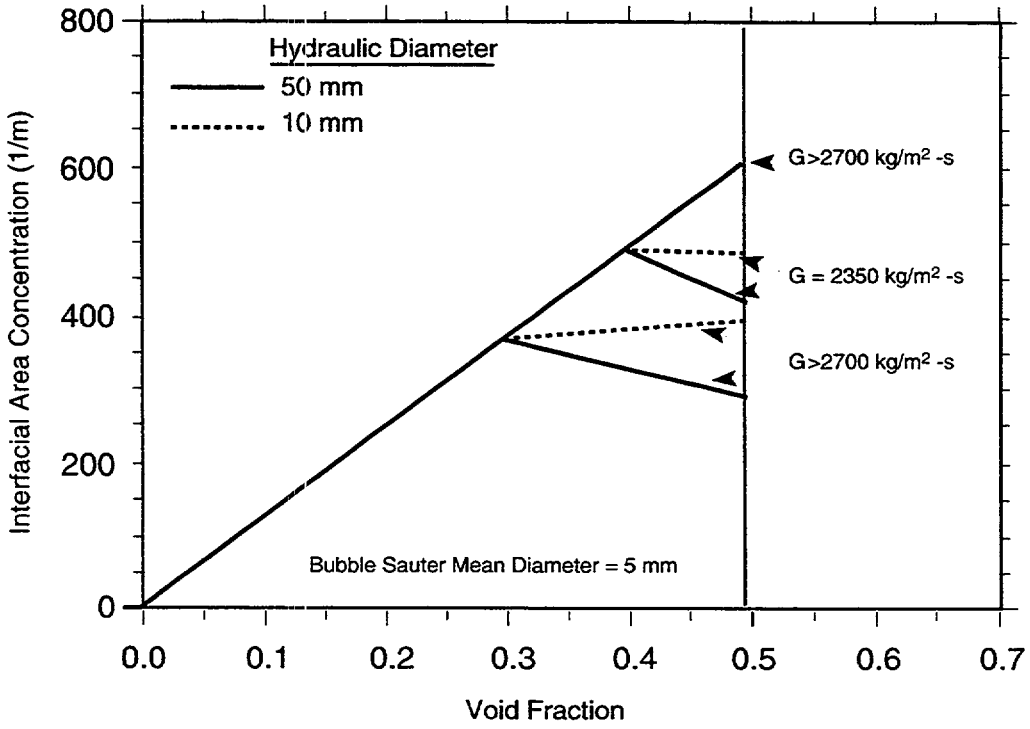

Fig. F-8. Interfacial-area concentration calculated by TRAC in bubbly slug flow.

F.1.1.2. Description of Heat-Transfer Coefficients Models. If the liquid temperature is smaller than the saturation temperature, the liquid side is in condensation mode. To calculate the heat-transfer coefficient during condensation, the correlation developed by Chen and Mayinger is used (Ref. F-7., p. 151, Eq. 24). The correlation is given by

$$Nu = 0.185\, Re^{0.7} \sqrt{Pr_\ell} \quad , \tag{F-22}$$

where

$$Nu = \frac{h_{i\ell} D_b}{k_\ell}$$

and

$$Re = \frac{\rho_\ell D_b (V_g - V_\ell)}{\mu_\ell} \quad .$$

In these experiments, bubbles were produced by blowing saturated vapor into subcooled liquid slowly moving downward. Heat-transfer data are obtained at the interface of condensing bubbles using holographic interferometry and high-speed photography. Ethanol, propanol, refrigerant-113, and water were used as working fluids. These fluids provided Prandtl numbers ranging from 1.96 to 14.4. The experimental Reynolds number ranged from ~350 to ~7000. However, the Reynolds number for only water data had a shorter range from ~4000 to ~7000. In deriving the correlation given by Eq. (F-22), Chen and Mayinger used the experimentally observed bubble detachment diameter in defining *Re* and *Nu*. In the code, we used the Sauter mean diameter given by Eq. (F-12). Chen and Mayinger recommend the use of their correlation for $Re < 10^4$ and $Ja < 80$. The Jakob number, *Ja*, is a measure of liquid subcooling and is defined as

$$Ja = \frac{\rho_\ell c_{p,\ell} \Delta T_{sub}}{\rho_g h_{fg}} \quad .$$

For $Ja < 80$, the condensation is controlled by heat transfer at the phase interface. If $Ja > 100$, the collapse of the vapor bubble is controlled by the inertia of the liquid mass when entering into the space set free by the condensing bubble. The Chen and Mayinger correlation is valid for heat-transfer-controlled condensation. However, in the code, it is also used in the inertia-controlled regime, independently of the Jakob number.

At high Reynolds numbers, we assumed that the Nusselt number is independent of the Reynolds number. This upper limit is calculated through the Chen and Mayinger correlation by setting $Re = 10^4$, which yields

$$Nu_{max} = 116.7 \sqrt{Pr_\ell} \quad . \tag{F-23}$$

For water, $Re=10^4$ corresponds to 0.5–0.6 m/s bubble-relative velocities, which are higher than observed terminal bubble-rise velocities. Thus, for quasi-steady conditions, the Reynolds numbers are usually smaller than 10^4. At low Reynolds numbers, the Chen and Mayinger correlation yields Nusselt numbers smaller than solid-sphere correlations, which is not realistic. Thus, we used the solid-sphere heat-transfer correlation of Whittaker (Ref. F-8.) as the lower limit of the Nusselt number. The original correlation is given by

$$Nu = 2 + (0.4\sqrt{Re} + 0.06Re^{2/3})Pr_\ell^{0.4}\left(\frac{\mu_w}{\mu_\infty}\right) , \tag{F-24}$$

where the Reynolds and Nusselt numbers are defined based upon the sphere diameter, and μ_w and μ_∞ are the fluid viscosities at the sphere wall and far field, respectively. In the code, we neglected the viscosity correction and used the bubble diameter instead of sphere diameter to obtain

$$Nu = 2 + (0.4\sqrt{Re} + 0.06Re^{2/3})Pr_\ell^{0.4} . \tag{F-25}$$

Figure F-9. shows the code-calculated Nu as a function of Re for two values of Pr that are representative of high and low limits for water. Once the liquid-side heat-transfer coefficient is obtained, the heat-transfer factor for condensation is calculated as

$$H_{\text{ALVE, bubbly slug}} = h_{i\ell}A_{i,\text{ bubbly slug}} . \tag{F-26}$$

where $A_{i,\text{bubbly slug}}$ is the total interfacial area given by Eq. (F-10).

During flashing, where $T_\ell > T_{\text{sat}}$, the liquid-side heat-transfer factor is calculated using the following approximate model:

$$10^6 \le \frac{H_{\text{ALV, bubbly slug}}}{B_{\text{cell}}} = [20\times 10^7(T_\ell - T_{\text{sat}})] \le 20\times 10^7 . \tag{F-27}$$

The basis for this model is its high magnitude, which quickly decreases the liquid temperature to saturation temperature. This model is flow-regime independent and is used for all flow patterns. It will be used in the other flow regimes as well.

For both condensation and flashing, the vapor-to-interface and gas-to-liquid heat-transfer coefficients are given by

$$h_{g\ell} = h_{ig} = 1000\text{W/m}^2\text{ K} . \tag{F-28}$$

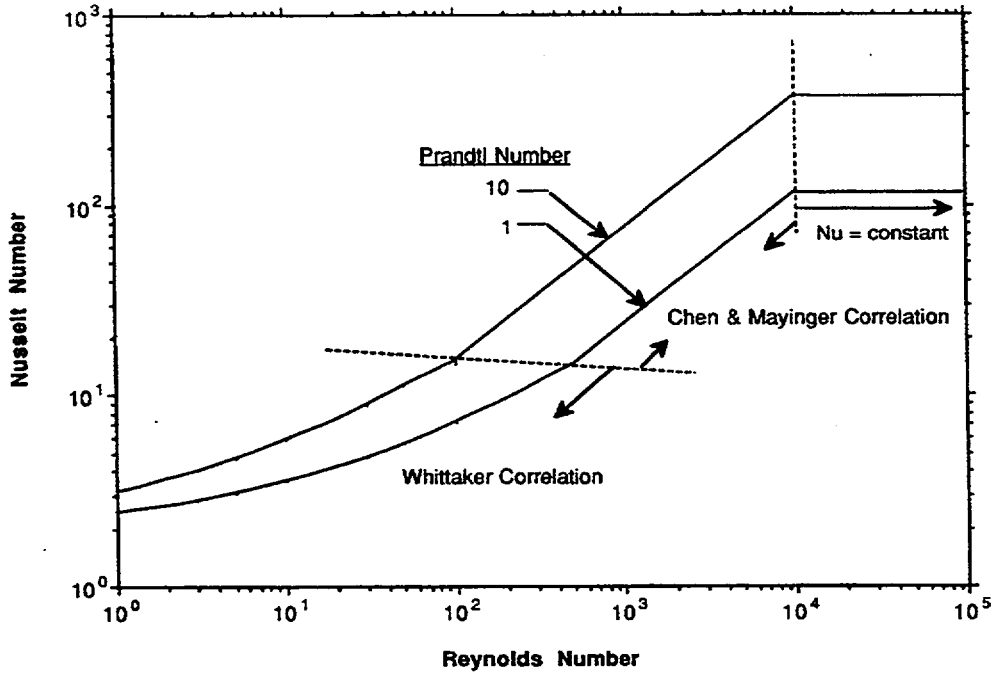

Fig. F-9. TRAC liquid-side heat-transfer-coefficient model during condensation in bubbly slug flow.

Thus,

$$H_{\text{CHTA, bubbly slug}} = H_{\text{CHTI, bubbly slug}} = 1000 A_{i,\text{ bubbly slug}} \,. \tag{F-29}$$

This is also an engineering approximation. This model is motivated by the fact that during quasi-steady conditions, the vapor-side heat-transfer coefficient is commonly about an order of magnitude smaller than the liquid-side heat-transfer coefficients.

F.1.1.3. Effect of Subcooled Boiling. The subcooled-boiling model is documented in Section G.1. and is not repeated here. In subcooled boiling, vapor is generated near the heater wall even though the bulk liquid is subcooled. However, part of this vapor condenses when in contact with the subcooled bulk liquid. Thus, during subcooled boiling, a mechanistic model is required to account for this interfacial condensation. We used the model suggested by Lahey and Moody (Ref. F-9., Eq. 5.174), which is given by

$$q_{\text{cond}} = H_o \frac{D_H}{4} h_{fg} \frac{\rho_\ell \rho_g}{\rho_\ell - \rho_g} \alpha (T_{sv} - T_\ell) \,, \tag{F-30}$$

where H_o is an empirical constant and q_{cond} is the interfacial condensation heat flux. Setting

$$\pi D_H q_{cond} \Delta x = H_{ALVE,sub}(T_{sv} - T_\ell) \ , \tag{F-31}$$

we obtain

$$H_{ALVE,sub} = H_o B_{cell} h_{fg} \frac{\rho_\ell \rho_g}{\rho_\ell - \rho_g} \alpha \ . \tag{F-32}$$

Lahey and Moody (Ref. F-9., p. 221) suggest $H_o = 0.075$ (s-K)$^{-1}$ and we used this value in the code.

We assumed that subcooled boiling can occur only in bubbly flow. Thus, the subcooled-boiling heat-transfer factor is superimposed on the bubbly flow liquid-side heat-transfer factor through a weighting factor as

$$H_{ALVE,bubbly/sub} = W_{sub} H_{ALVE,sub} + (1 - W_{sub}) H_{ALVE,bubbly} \ , \tag{F-33}$$

where the weighting factor is given by

$$0 \le W_{sub} = 10(0.2 - \alpha) \le 1 \ . \tag{F-34}$$

As shown by this equation, if the void fraction is greater than 0.2, the weighting factor becomes zero. Thus, for the subcooled-boiling effect to be present in the interfacial heat transfer, the following conditions must be satisfied:

7. The liquid temperature must be less than saturation temperature.
8. Subcooled boiling must be occurring ($h_\Gamma > 0$).
9. The void fraction must be less than 20%.

F.1.1.4. Assessment. As cited by Ishii and Mishima (Ref. F-1.), there are a number of studies where interfacial areas are measured by chemical-absorption techniques. In these studies, the measured interfacial-area concentrations are reported as a function of liquid and vapor volumetric fluxes. To compare the data with the TRAC prediction, we need the interfacial-area concentration as a function of void fraction. A limited number of studies report void-fraction measurements along with interfacial-area concentration data. The majority of the data correspond to high void fractions. These studies are discussed in Section F.1.10.

Figure 10 in Ref. F-7. shows the comparison of the Chen and Mayinger correlation with their own data. As shown, ±25% discrepancy is typical between the water data and the correlation. The discrepancy increases with an increasing Prandtl number (see the refrigerant-113 data). To assess the Chen-Mayinger bubble-condensation correlation, first we compared it with some of the solid-sphere correlations. The correlations used for this comparison are the ones given by McAdams (Ref. F-10.) as

$$Nu = 0.37Re^{0.6} \quad , \tag{F-35}$$

by Vliet and Leppert (Ref. F-11.) as

$$Nu \times Pr^{0.3}\left(\frac{\mu_w}{\mu_\infty}\right) = 1.2 + Re^{0.54} \quad , \tag{F-36}$$

and by Whittaker (Ref. F-8.) in Eq. (F-25). Figure F-10. shows these correlations for a Prandtl number of unity. In plotting Eq. (F-36), the viscosity correction is neglected. As shown, within its range of applicability, the Chen and Mayinger correlation overpredicts all the solid-sphere data, as expected. At lower Reynolds numbers, all the solid-sphere correlations predict a higher Nusselt number than the Chen-Mayinger correlation. As a result, the Whittaker correlation is used in the code as the lower limit for the Chen-Mayinger correlation. Similar trends are observed at higher Prandtl numbers.

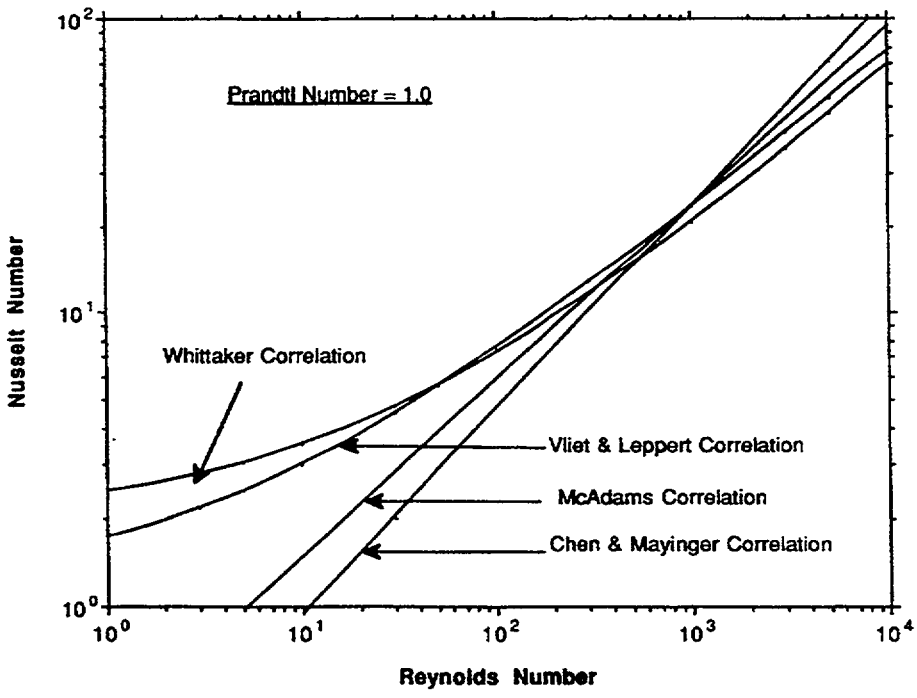

Fig. F-10. Comparison of the Chen and Mayinger with solid sphere heat-transfer correlations.

Brucker and Sparrow (Ref. F-12.) obtained data similar to the data of Chen and Mayinger by introducing steam bubbles into a quiescent subcooled water pool. The pressure in these experiments ranged from 10 to 62 bars. The subcooling of the water ranged from 15°C to 100°C and the initial bubble diameter was approximately 3 mm.

Data were obtained by high-speed motion-picture and frame-by-frame analysis. The bubble-rise velocity ranged from 15 to 25 cm/s, which roughly yields Reynolds numbers ranging from 3000 to 5000. Brucker and Sparrow reported an average heat-transfer coefficient of $h_{i\ell}$~10000 W/m^2-s. They further reported that all data fell within ±50% of this value as well as of the value predicted by the McAdams solid-sphere correlation given by Eq. (F-35). This range is in good agreement with the correlation of Chen and Mayinger, which suggests that their correlation can be extrapolated to higher pressures.

F.1.1.5. Conclusions and Final Remarks. In bubbly flow, vapor and noncondensable-gas mixture is the discontinuous phase and is distributed within the continuous liquid phase as discrete bubbles of different sizes and shapes. To compute the interfacial area within a given volume, the interfacial areas of the individual bubbles must be known, such that

$$A_{i,\text{bubbly}} = \overline{A}_{i,\text{bubble}} = N\left\{\frac{1}{N}\sum_{n=1}^{N} A_{i,n}\right\}, \tag{F-37}$$

where $A_{i,\text{bubbly}}$ is the total interfacial area within a fixed volume of bubbly flow, N is the number of bubbles in that volume, and $A_{i,n}$ is the surface area of an individual bubble, and $\overline{A}_{i,\text{bubble}}$ is the average surface area of the bubble population. If the probability density function, pdf, for bubble surface area is known for a given set of thermal-hydraulic conditions, then the average bubble surface area becomes

$$\overline{A}_{i,\text{bubble}} = \int_0^\infty A_i(\chi_a)\text{pdf}(\chi_a)d\chi_a, \tag{F-38}$$

where χ_a is the size parameter and represents an equivalent radius (or diameter). The total volume of the vapor phase within a fixed material volume is equal to B_{cell} and is related to the volume of individual bubbles through

$$\alpha B_{\text{cell}} = N\overline{B}_{\text{bubble}} = N\left\{\frac{1}{N}\sum_{n=1}^{N} B_n\right\}, \tag{F-39}$$

where B_n is the volume of an individual bubble. An equation similar to Eq. (F-38) can be written if a continuous pdf is known as a function of an equivalent diameter χ_b as follows:

$$\bar{B}_{\text{bubble}} = \int_0^\infty B(\chi_b)\text{pdf}(\chi_b)d\chi_b \ . \tag{F-40}$$

Equivalent bubble diameters can be defined in a number of ways depending upon the applications. For Eq. (F-38) the appropriate equivalent diameter would be the surface-area-based diameter, where the surface areas of the actual bubble and an equivalent spherical bubble are set equal, to yield

$$D_{b,A} = \sqrt{\frac{\bar{A}_{i,\text{bubble}}}{\pi}} \ . \tag{F-41}$$

Similarly, a volume-based equivalent diameter can be defined for use in Eq. (F-40) as follows:

$$D_{b,V} = \left(\frac{6\bar{B}_{\text{bubble}}}{\pi}\right)^{1/3} \ . \tag{F-42}$$

For a sphere, Eqs. (F-41) and (F-42) yield identical diameters. However, for a nonspherical particle, the two diameters are not equal and the definition of the equivalent diameter must be given in reporting the data. Using the proper equivalent diameter also becomes important in averaging the diameter over a certain population of particles, even if they are spherical, in case the population has a nonuniform pdf. In general, the equivalent diameter for a nonuniform distribution can be defined as

$$D_{b,\text{pq}}^{\text{p-q}} = \frac{\int_0^\infty D_{b,\text{p}}^{\text{p}}\text{pdf}(\text{D}_{b,\text{p}})d\text{D}_{b,\text{p}}}{\int_0^\infty D_{b,\text{q}}^{\text{q}}\text{pdf}(\text{D}_{b,\text{q}})d\text{D}_{b,\text{q}}} = \frac{\bar{D}_{b,\text{p}}^{\text{p}}}{\bar{D}_{b,\text{q}}^{\text{q}}} \ , \tag{F-43}$$

where (p=3, q=0) is the volume-based average diameter of the bubble population, (p=2, q=0) is the area-based average diameter of the bubble population, etc. The Sauter mean diameter, which is another important equivalent diameter, corresponds to the case where (p=3, q=2). For p=3 and q=2, for instance, $D_{b,\text{p}}$ and $D_{b,\text{q}}$ are defined by Eqs. (F-41) and (F-42), respectively, for individual bubbles. If the bubbles can be assumed to be spherical in shape, the definition in Eq. (F-43) simplifies because $D_{b,\text{p}}$ becomes equal to $D_{b,\text{q}}$. For nonspherical particles, however, they are not equal, and a larger amount of statistical data is required for the proper definition of equivalent diameters. For instance, let us look at the Sauter mean diameter for a nonspherical bubble population. For a nonspherical object, the sphericity is defined as follows (Ref. F-13.):

$$\Psi = \frac{\text{surface area of volume} - \text{equivalent sphere}}{\text{surface area of particle}} \ .$$

Note that if the particle is a perfect sphere, Ψ becomes 1. Thus, by substituting all the diameters on the right-hand side of Eq. (F-43) with the equivalent diameter defined by Eq. (F-42), the Sauter mean diameter becomes

$$D_b = \frac{\int_0^\infty D_{b,V}^3 \mathrm{pdf}(D_{b,V}) dD_{b,V}}{\int_0^\infty \left(D_{b,V}^2 / \Psi\right) \mathrm{pdf}\left(D_{b,V}\right) dD_{b,V}} \quad , \tag{F-44}$$

which assumes that sphericity is a deterministic function of the bubble equivalent diameter. Now, to define the Sauter mean diameter, deterministic data for Ψ as a function of $D_{b,V}$ are needed, in addition to the pdf for $D_{b,V}$. If the sphericity becomes a statistical function, the definition becomes even more complicated. The Sauter mean diameter is important for our particular application because, when the interfacial area in bubbly flow is calculated from a given void fraction, we obtain

$$A_{i,\mathrm{bubbly}} = \frac{6\alpha B_{\mathrm{cell}} \int_0^\infty (D_{b,V}^2 / \Psi) \mathrm{pdf}(D_{b,V}) dD_{b,V}}{\int_0^\infty D_{b,V}^3 \mathrm{pdf}(D_{b,V}) dD_{b,V}} = \frac{6\alpha B_{\mathrm{cell}}}{D_b} \quad . \tag{F-45}$$

Because we are not aware of extensive statistical data that would enable an accurate quantification of Eq. (F-45), we are forced to assume that the bubbles are nearly spherical. This practice is rather common in many other applications of two-phase flow. On the other hand, there are studies indicating that under commonly encountered situations, bubbles are nonspherical. For instance, Fig. F-11. obtained from Ref. F-13., Fig. 2.5, illustrates a typical map for bubble shapes. The map is plotted as a function of Reynolds, Eötvös, and Morton numbers that are defined as follows:

$$Re = \frac{\rho_\ell D_{b,V} V_{\mathrm{bubble}}}{\mu_\ell} \quad ,$$

$$Eo = \frac{g(\rho_\ell - \rho_g) D_{b,V}^2}{\sigma} \quad ,$$

and

$$Mo = \frac{g\mu_\ell^4 (\rho_\ell - \rho_g)}{\rho_\ell^2 \sigma^3} \quad .$$

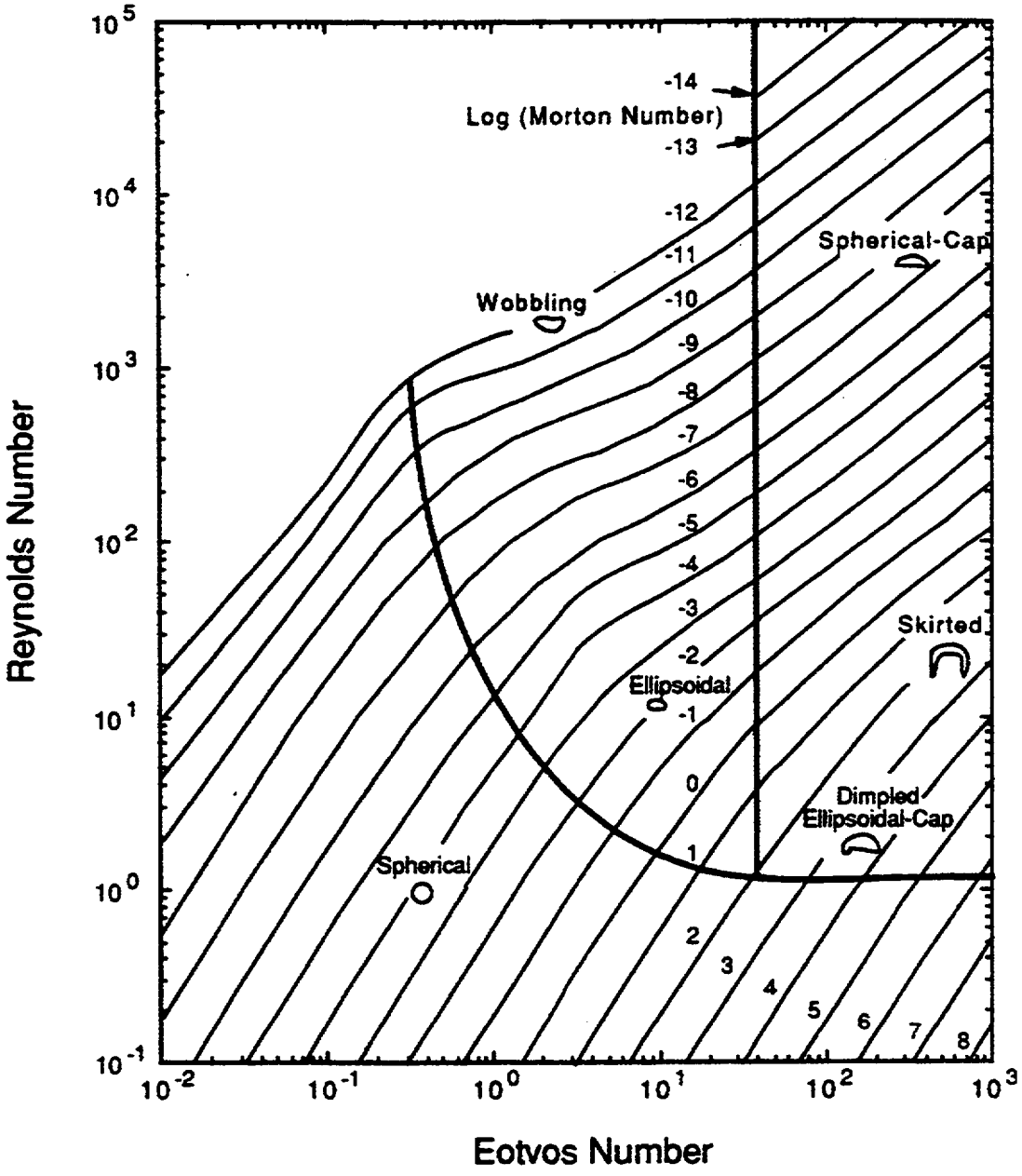

Fig. F-11. A typical map for bubble shapes (Ref. F-13., p. 27, Fig. 2.5).

Note that the Morton number is directly related to the viscosity number defined earlier. Here it is referred to as the Morton number merely for consistency with the original reference (Ref. F-13.). This map is given for bubbles freely rising in liquids. Thus, the Reynolds number is based upon bubble terminal velocity. A similar map, however, can be used as a first estimate of bubble shapes in two-phase-flow situations by replacing the bubble terminal velocity with bubble relative velocity (Ref. F-1.). The Morton number for saturated water at various pressures is on the order of 10^{-12}. Thus, the bubble shape is

spherical if the Eötvös number is less than 0.3. For an Eötvös number between 0.3 and 40, the bubble shape is shown to be wobbling and, for an Eötvös number greater than 40, the bubbles will have a spherical cap shape.

In TRAC, the bubble diameter is calculated using Eq. (F-12), which corresponds to a constant-Eötvös-number criterion given by $Eo=4$, where the constant 4 is suggested as an average value by Ishii (Ref. F-3.). Ishii reported that the bubble diameter range is given by

$$4\sqrt{2}Mo^{1/12} < \sqrt{Eo} < 4 \quad ,$$

where the Morton number is on the order of 10^{-12}. Thus,

$$0.57 < \sqrt{Eo} < 4 \quad .$$

Ishii recommends $Eo=4$ as a rough estimate for practical use. This simply reflects an approximate arithmetic average between maximum and minimum bubble diameters and does not take into account the bubble size and shape probability distributions. Consequently, it is difficult to determine whether it corresponds to the volume mean, to the area mean, or to the Sauter mean diameter. Ishii recommends its use as drag diameter, which is defined as

$$D_{b,D} = \frac{3 \times \text{Bubble Volume}}{\text{Projected Bubble Area}} \quad .$$

For a population of spherical bubbles, the drag diameter is equivalent to the Sauter mean diameter. For nonspherical bubbles, however, the two quantities are different. Note that the map provided by Clift et al. in Fig. F-11. suggests wobbling bubbles for $Eo=4$. Presently, not enough data exist to quantify how well the $Eo=4$ criterion approximates the Sauter mean diameter needed to estimate the interfacial area. Furthermore, this formulation is independent of local-instantaneous phasic velocities (inertia forces) that are known to influence the bubble diameter in steady-state situations. However, the quasi-steady assumption inherent in the code makes it difficult to incorporate such dependence through Weber-number correlations, for instance, during transient analysis. Because the quasi-steady assumption allows an instantaneous change in bubble size due to a sudden change in velocity, a constant-Weber-number criterion results in sudden and unrealistic changes in the bubble sizes, which occasionally may lead to numerical oscillations.

Our final remarks about the heat-transfer correlations used in bubbly slug flow are that some of our simple models could have been replaced by better-founded correlations. For instance, the flashing model could have been replaced by either the Chen-Mayinger correlation, or by a solid-sphere heat-transfer correlation along with bubble-growth equations, such as the one by Mikic et al. (Ref. F-14.). Further discussion of why these

approximate models are used and what their implications are can be found in Section F.1.10.

F.1.2. Models and Correlations in Annular-Mist Flow

As shown in Fig. F-3., annular-mist flow occurs if the void fraction is greater than or equal to 75%, independent of mass flux. A schematic of flow pattern in annular-mist flow is shown in Fig. F-12. As shown, the liquid flows as droplets in the gas core and also forms a liquid film on a solid wall. Therefore, a more rigorous treatment requires at least two fields for the liquid phase. In TRAC, the liquid phase is represented as a single field. Thus, the characteristics of liquid droplets and film must be properly superimposed within a single field. The following generic equation shows the way the various closure parameters are calculated in annular-mist flow:

$$X = (1-W_f)(X_{\text{drop}} + X_{\text{film}}) + W_f X_{\text{drop,max}} \ , \tag{F-46}$$

where X represents either A_i, H_{ALVE}, or H_{CHTI}. The weighting factor, W_f, is introduced to account for the fact that beyond a certain limit in phasic velocities, all the liquid will be entrained in the form of droplets, thus no liquid film will exist. The phasic velocities are compared to a critical velocity defined based upon Helmholtz disturbance wave and given by

$$V_c = \left[\frac{g\sigma(\rho_\ell - \rho_g)}{\rho_g^2}\right]^{1/4} . \tag{F-47}$$

Then the weighting factor is coded as follows:

$$W_f = \begin{cases} 0 & \text{if } \max(V_\ell, V_g) < 10V_c \\ 0.5\dfrac{\max(V_\ell, V_g)}{V_c} - 5 & \text{if } 10V_c \le \max(V_\ell, V_g) \le 12V_c \\ 1 & \text{if } \max(V_\ell, V_g) > 12V_c \end{cases} . \tag{F-48}$$

Figure F-13. illustrates the transition from annular-mist to mist flow as a function of pressure for saturated water. As shown in this figure, the critical velocity is a strong function of pressure and decreases rapidly with increasing pressure.

F.1.2.1. Description of Interfacial-Area Models. The interfacial area (A_i) Eq. (F-46) becomes

$$A_{i,\text{annular-mist}} = (1-W_f)(A_{i,\text{drop}} + A_{i,\text{film}}) + W_f A_{i,\text{drop,max}} \ . \tag{F-49}$$

The individual contributions of the droplet and film flow on the interfacial area are described in the following sections.

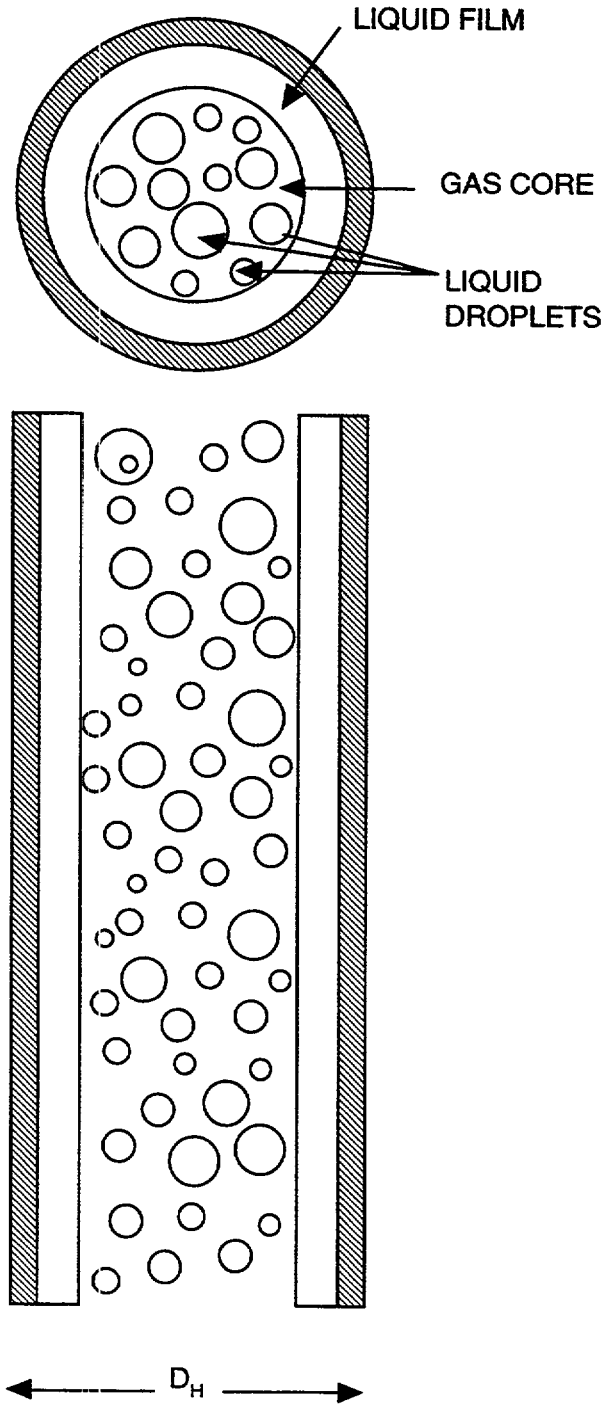

Fig. F-12. Schematic of flow pattern in annular-mist flow.

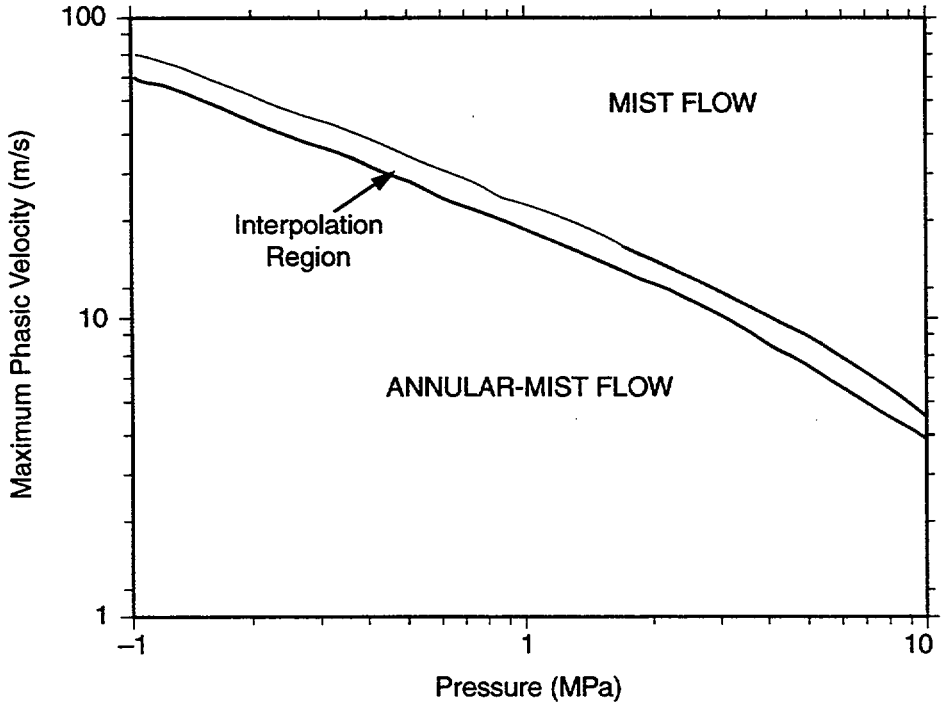

Fig. F-13. Transition from annular-mist to mist flow as a function of pressure for saturated water.

F.1.2.1.1. Mist-Flow Interfacial Area. The interfacial-area concentration in the mist-flow portion is given by (Ref. F-15., p. 55, Eq. 89) as

$$a_{i,\,\mathrm{drop}} = \frac{\alpha}{1-\alpha_d}\left(\frac{6\alpha_d}{D_d}\right), \tag{F-50}$$

where D_d is the Sauter mean diameter of the droplet population and α_d is the droplet fraction in the gas core. If all the liquid is entrained as liquid droplets, then $\alpha_d = 1-\alpha$ and

$$a_{i,\mathrm{drop,max}} = B_{\mathrm{cell}}\,\frac{6(1-\alpha)}{D_d}\quad . \tag{F-51}$$

The droplet Sauter mean diameter is calculated using the correlations of Kataoka et al. (Ref. F-16.) and Kitscha and Kocamustafaogullari (Ref. F-6.). Kataoka et al. proposed a droplet diameter model that assumes that the majority of droplets are generated at the time of entrainment and that the size distribution is a direct reflection of the entrainment mechanism. The final correlation is obtained by combining with a large amount of data as follows (Ref. F-16., Eq. 28):

$$D_{vm} = 0.028 \frac{\sigma}{\rho_g (\alpha V_g)^2} Re_\ell^{-1/6} Re_g^{-2/3} \left(\frac{\rho_g}{\rho_\ell}\right)^{-1/3} \left(\frac{\mu_g}{\mu_\ell}\right)^{2/3} , \qquad \text{(F-52)}$$

where D_{vm} is the droplet volume median diameter,

$$Re_\ell = \frac{\rho_\ell D_H (1-\alpha) V_\ell}{\mu_\ell} ,$$

and

$$Re_g = \frac{\rho_g D_H \alpha V_g}{\mu_g} .$$

The database of this correlation is summarized in Table F-1. (obtained from Ref. F-16., Table 1). Data were obtained using an air-water mixture. Kataoka et al. argued that, within the range investigated, the droplet diameter shows little sensitivity to liquid Reynolds number as

$$0.24 \leq Re_\ell^{-1/6} \leq 0.46 .$$

Using an average value of $Re_\ell^{-1/6} \approx 0.35$, they obtained (Ref. F-16., Eq. 42)

$$D_{vm} = 0.01 \frac{\sigma}{\rho_g (\alpha V_g)^2} Re_g^{2/3} \left(\frac{\rho_g}{\rho_\ell}\right)^{-1/3} \left(\frac{\mu_g}{\mu_\ell}\right)^{2/3} . \qquad \text{(F-53)}$$

TABLE F-1.
Database of Droplet Diameter Correlation
Kataoka et al. (Ref. F-15., Table 1)

Reference	Geometry	Flow Direction	Measurement	Operational Conditions
Wicks & Dukler (1966) Wicks (1967)	1.9 × 15-cm channel	Vertical down	Electrical conductance	P = 1 atm R_{ef} = 930 – 9700 $R_{eg} = 6.6 - 17 \times 10^4$
Cousins & Hewitt (1968)	0.95-cm tube	Vertical up	Photography	P = 2 atm R_{ef} = 640 – 4200 $R_{eg} = .6 - 6.2 \times 10^4$
Lindsted et al. (1978)	3.2-cm tube	Vertical up	Photography	P = 1 atm R_{ef} = 100 – 3500 $R_{eg} = 2.5 - 4.4 \times 10^4$

To calculate the interfacial-area concentration, we need the Sauter mean diameter. Kataoka et al. report that (Ref. F-16., Table 2)

$$\frac{D_d}{D_{vm}} = 0.796 \quad .$$

Therefore, the droplet Sauter mean diameter is calculated using

$$D_d = 7.96 \times 10^{-3} \frac{\sigma}{\rho_g (\alpha V_g)^2} \; Re_g^{2/3} \left(\frac{\rho_g}{\rho_\ell}\right)^{-1/3} \left(\frac{\mu_g}{\mu_\ell}\right)^{2/3} \quad . \tag{F-54}$$

This correlation, however, shows that $D_d \sim (D_H)^{2/3}$ which can result in unrealistically large droplet diameters in flow channels with large hydraulic diameter. We believe that this feature results from the limited database of the correlation. As shown in Table F-1., the maximum hydraulic diameter in the database is 3.37 cm (corresponding to the channel used by Wicks). It is expected that beyond a certain limiting value, the effect of hydraulic diameter on droplet size will vanish. Kitscha and Kocamustafaogullari (Ref. F-6.) formulated this problem and proposed a correlation for maximum droplet diameter in a high-velocity gas-field free of wall effects. The correlation is given by (Ref. F-6., Eq. 38)

$$\left(\frac{D_{\max}}{L_o}\right)^2 + 0.26 We_m \left(\frac{D_{\max}}{L_o}\right) - 16 = 0 \quad , \tag{F-55}$$

where the modified Weber number is defined as

$$We_m = \frac{\rho_g (\alpha V_g)^2 L_o}{\sigma} \quad .$$

Kitscha and Kocamustafaogullari compared Eq. (F-55) with the maximum droplet diameter correlation of Kataoka et al. (Ref. F-16., Eq. 43) and showed that Eq. (F-55) is over-predicted by Kataoka et al. for hydraulic diameters larger than ~5 cm. The value of this critical diameter changes with gas velocity and pressure. In the code, we used the correlation of Kitscha and Kocamustafaogullari as the upper limit of the correlation of Kataoka et al. given by Eq. (F-54). However, we modified Eq. (F-55) to yield the Sauter mean diameter rather than the maximum diameter. The conversion between these two quantities is also obtained from the relation reported by Kataoka et al. (Ref. F-16., Table 2) as follows:

$$\frac{D_d}{D_{\max}} = 0.254 \quad .$$

Consequently, Eq. (F-55) yields

$$D_d = 0.254 L_o \left[-0.13 We_m + \sqrt{16 + (0.13 We_m)^2} \right] \quad . \tag{F-56}$$

Note that for small values of modified Weber number, the droplet diameter is given by

$$D_d \approx L_o \quad ,$$

which is a criterion that is commonly used to determine the size of the dispersed phase [see the bubble diameter correlation given by Eq. (F-11)]. In the code, the droplet diameter is given by the minimum of either Eq. (F-54) or Eq. (F-56). We further imposed the following limits on the droplet diameter:

$$84\ \mu\text{m} \le D_d \le 4\ \text{mm} .$$

Figure F-14. shows the droplet diameters predicted by the TRAC model for air-water mixture at atmospheric pressure and 20°C. The hydraulic diameter is also varied in this figure. As shown, the correlation of Kataoka et al. is effective for small hydraulic diameters. As the hydraulic diameters increase, the effective range of the correlation by Kitscha and Kocamustafaogullari also increases. Beyond a certain hydraulic diameter (~55 mm for this case), the correlation of Kitscha and Kocamustafaogullari always dominates. Note that this limiting hydraulic diameter decreases with increasing temperature. For saturated water at or above atmospheric pressure, the correlation of Kitscha and Kocamustafaogullari dominates beyond ~20-mm hydraulic diameter. In Fig. F-15., the effect of pressure on the droplet diameter is illustrated using saturated water properties at 1 and 20 atm for a hydraulic diameter of 10 mm. This figure shows that the droplet diameter is not strongly affected by the pressure at low gas-flow rates, whereas it decreases rapidly with increasing pressure at higher gas-flow rates.

The knowledge of the void fraction and the droplet Sauter mean diameter is sufficient to obtain the interfacial-area concentration in mist flow ($a_{i,\text{drop,max}}$). However, in annular-mist flow we further need to know the fraction of liquid in the form of entrained droplets (α_d). This quantity is based upon the entrainment fraction, E, defined by Ishii and Mishima (Ref. F-17.) as

$$E = \frac{J_d}{J_\ell} \quad , \tag{F-57}$$

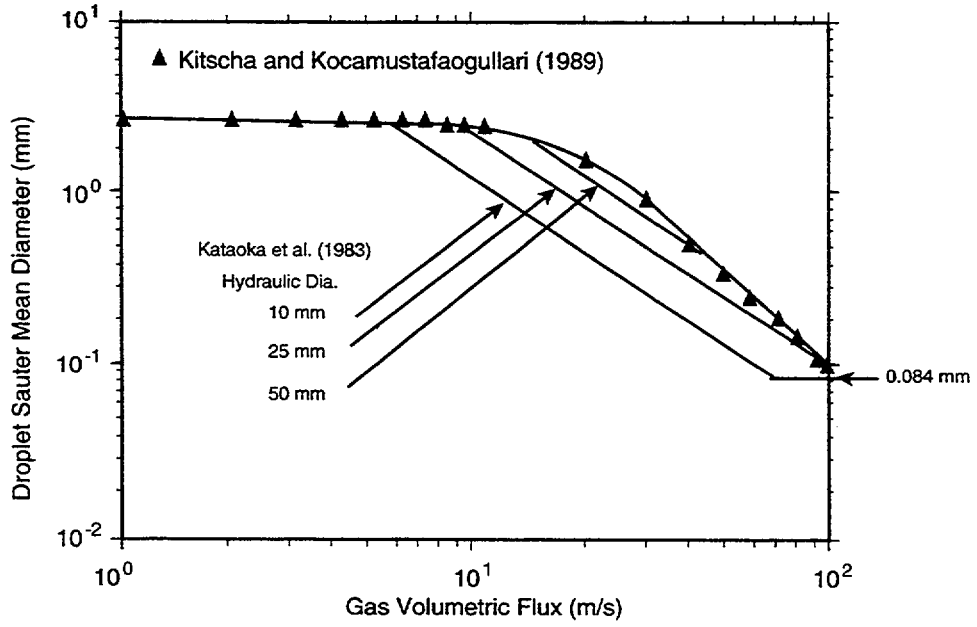

Fig. F-14. Droplet diameter calculated by TRAC for air-water mixture at atmospheric pressure and 20°C temperature in tubes with various hydraulic diameters.

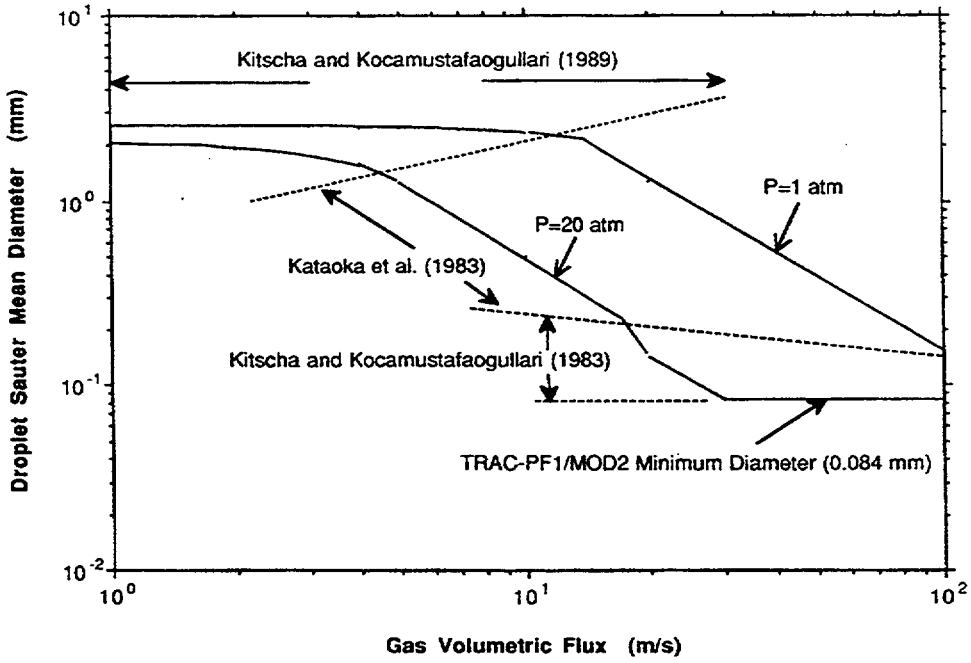

Fig. F-15. Droplet diameter calculated by TRAC for saturated water at 1 and 20 atm and for a 10-mm hydraulic diameter.

where J_d is the droplet volumetric flux and J_ℓ is the total liquid volumetric flux (or superficial velocity). The entrainment fraction is calculated using the correlation developed by Ishii and Mishima, which is given as (Ref. F-17., p. 10, Eq. 23, and Ref. F-18., Eq. 28)

$$E = \tanh\left(7.25\times10^{-7} We_e^{1.25} Re_\ell^{0.25}\right) \quad , \tag{F-58}$$

where the effective Weber number is defined as

$$We_e = \frac{\rho_g(\alpha V_g)^2 D_H}{\sigma}\left(\frac{\rho_\ell - \rho_g}{\rho_g}\right)^{1/3} \quad ,$$

and

$$Re_\ell = \frac{\rho_\ell(1-\alpha)V_\ell D_H}{\mu_\ell} \quad .$$

Figure F-16. shows the calculated entrainment fraction for saturated water at atmospheric pressure as a function of gas volumetric flux and the parameter $s\alpha/(1-\alpha)$, where s is the slip ratio. As shown, the entrainment fraction is a strong function of the former, whereas it is weakly affected by the latter. Figure F-17. illustrates the effect of pressure using saturated water properties. As shown, the entrainment fraction increases with increasing pressure. As discussed before, the entrainment fraction correlation is limited by the transition to fully mist flow described by Eqs. (F-46), (F-47), and (F-48). These limits are also superimposed on Figs. F-16. and F-17. Ishii and Mishima compared Eq. (F-58) to various data within the following parametric range:

$$\begin{aligned} 1 &\le P \le 4\ \text{atm}, \\ 0.95 &\le D_H \le 3.2\ \text{cm}, \\ 370 &\le Re_\ell \le 6400, \text{ and} \\ & J_g < 100\ \text{m/s}. \end{aligned}$$

Equation (F-58) is proposed as a fully developed entrainment correlation for adiabatic flow. It is valid beyond a certain distance, z_c, away from the entrance. This entry length is correlated by Mishima and Ishii as (Ref. F-17., p. 13, Eq. 35, and Ref. F-18., Eq. 36)

$$z_c \approx 600 D_H \frac{1}{\sqrt{Re_\ell}}\sqrt{\alpha V_g}\left[\frac{\sigma g(\rho_\ell - \rho_g)}{\sigma_g^2}\left(\frac{\rho_g}{\rho_\ell - \rho_g}\right)^{2/3}\right]^{-1/8} \quad . \tag{F-59}$$

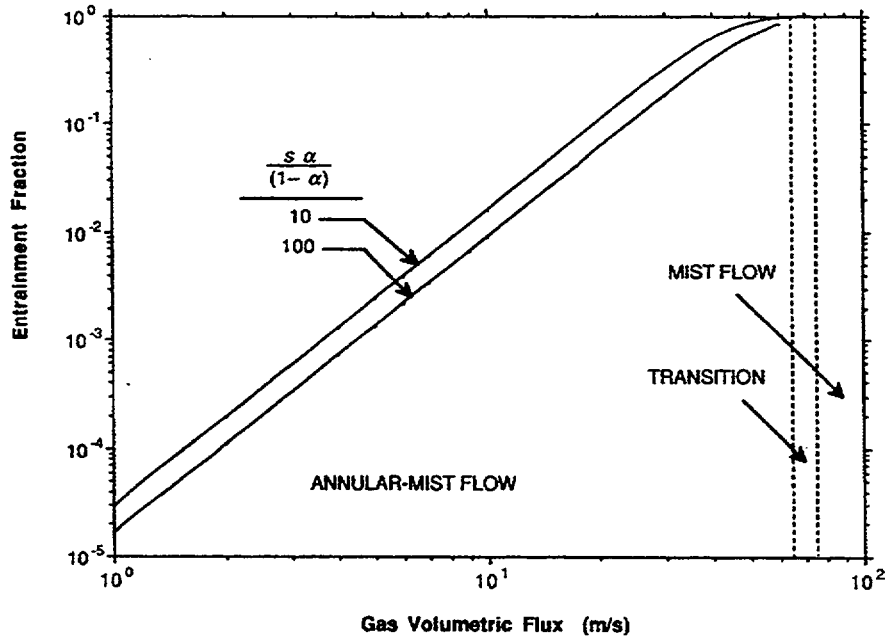

Fig. F-16. TRAC-calculated entrainment fraction for saturated water at atmospheric pressure.

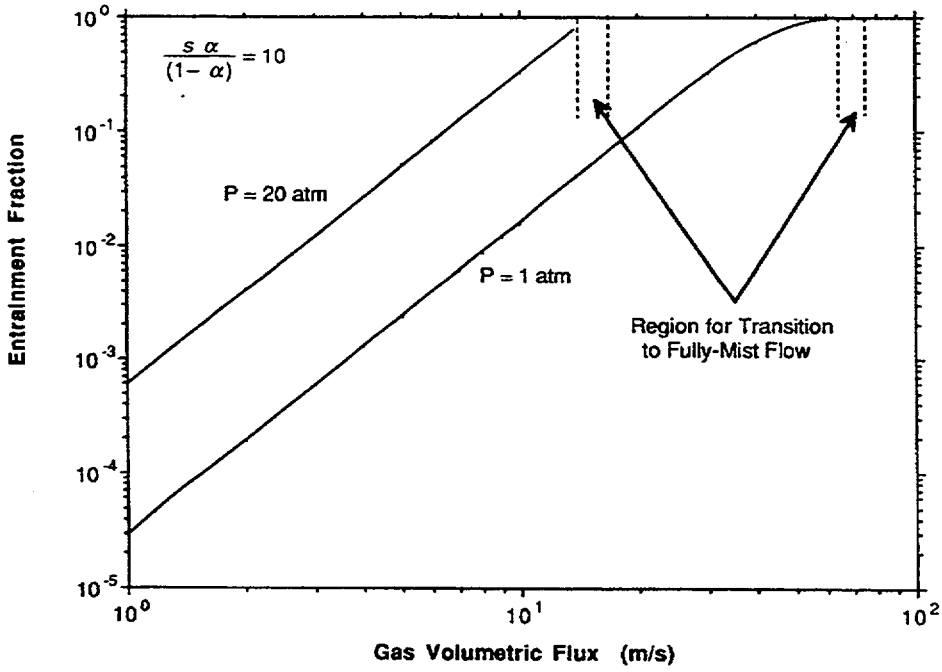

Fig. F-17. Effect of pressure on the entrainment fraction for saturated water.

Within the entry length, the entrainment rate is formulated as an exponential relaxation that approaches Eq. (F-58) as the distance approaches z_c. In the code, we neglected the entry length and used Eq. (F-58) within a given cell, assuming local-instantaneous equilibrium.

Assuming that the velocity of the droplets is approximately equal to the gas velocity and using the definition of the entrainment fraction given by Eq. (F-57), the following relationship between E and α_d can be obtained:

$$\frac{\alpha_d \alpha V_g}{1-\alpha_d} = E(1-\alpha)V_\ell \quad . \tag{F-60}$$

Setting $1-\alpha_d \approx 1$, Eq. (F-60) yields

$$\alpha_d \approx E\frac{(1-\alpha)V_\ell}{\alpha V_g} \quad , \tag{F-61}$$

which can be replaced into Eq. (F-50) to obtain the mist portion of the interfacial-area concentration in annular-mist flow. Then, the interfacial area in a given cell is calculated as

$$A_{i,\text{drop}} = B_{\text{cell}} a_{i,\text{drop}} \quad . \tag{F-62}$$

F.1.2.1.2. Annular-Mist-Flow Interfacial Area. From purely geometric considerations, the interfacial-area concentration for the liquid film can be calculated as (Ref. F-15., p. 55, Eq. 89)

$$A_{i,\text{film}} = \frac{4C_r}{D_H}\sqrt{\frac{\alpha}{1-\alpha_d}} \quad , \tag{F-63}$$

where α_d is given by Eq. (F-61) and C_r is a correlation factor that accounts for interfacial waviness. In the code, the surface waves are ignored for thick films. However, if the film becomes very thin, rivulet formation is acknowledged and its effect is incorporated into C_r. This effect is calculated using the following simple model:

$$C_r = \frac{D_H(1-\alpha)}{l_{\min}} \le 1 \quad , \tag{F-64}$$

where $l_{\min}$ is set to 0.1 mm. Physically, this model neglects α_d and assumes that a liquid film thinner than 25 μm cannot be stable and breaks into rivulets. Having obtained α_d and C_r, the film flow contribution to the total interfacial area can be calculated as

$$A_{i,\text{film}} = B_{\text{cell}} a_{i,\text{film}} \quad . \tag{F-65}$$

F.1.2.2. Description of Heat-Transfer Coefficient Models. During condensation and flashing, the heat-transfer factors are calculated as

$$H_{\mathrm{ALVE}} = (1-W_f)(H_{\mathrm{ALVE,drop}} + H_{\mathrm{ALVE,film}}) + W_f H_{\mathrm{ALVE,drop,max}} \,, \tag{F-66}$$

$$H_{\mathrm{ALV}} = (1-W_f)(H_{\mathrm{ALV,drop}} + H_{\mathrm{ALV,film}}) + W_f H_{\mathrm{ALV,drop,max}} \,, \tag{F-67}$$

$$H_{\mathrm{CHTI}} = (1-W_f)(H_{\mathrm{CHTI,drop}} + H_{\mathrm{CHTI,film}}) + W_f H_{\mathrm{CHTI,drop,max}} \,, \tag{F-68}$$

and

$$H_{\mathrm{CHTA}} = (1-W_f)(H_{\mathrm{CHTA,drop}} + H_{\mathrm{CHTA,film}}) + W_f H_{\mathrm{CHTA,drop,max}} \,. \tag{F-69}$$

During flashing, the maximum H_{ALV} predicted by either Eq. (F-67) or Eq. (F-27) is used. Liquid- and vapor-side heat-transfer coefficients for the droplets and liquid film are described in the following sections.

F.1.2.2.1. Mist-Flow Heat-Transfer Coefficients. The liquid-side interfacial heat-transfer coefficient, $h_{i\ell}$, is calculated using the transient conduction solution in liquid droplets. The conduction solution is approximated as follows (Ref. F-19., Eqs. 4 and 6):

$$Nu = \frac{\pi}{3} C_c \frac{1+T^*}{T^*} \,, \tag{F-70}$$

where

$$Nu = \frac{h_{i\ell} D_d}{k_\ell}$$

and T^* is the dimensionless instantaneous mixing cup temperature given by

$$T^* \approx \left[1 - \exp\left(-4\pi^2 C_c \frac{k_\ell t}{\rho_\ell c_{p,\ell} D_d^2} \right) \right]^{1/2} \,. \tag{F-71}$$

The conduction solution was used in the code because Ford and Lekic (Ref. F-20.) were able to correlate their single-component (steam/water) droplet-condensation data with reasonable accuracy. Also, Iciek et al. (Ref. F-21., p. 175) suggest that for small droplets with low relative velocity and for fluids with a high ratio of liquid viscosity to vapor viscosity, the condensation solution is satisfactory.

In Eqs. (F-70) and (F-71), C_c is a correction factor to account for circulation effects within the droplet. In the code, we assumed that such effects are negligible and C_c is set equal to 1. To use this transient solution in a quasi-steady, single-liquid-field code, we need to estimate a mean free path for the droplet population. Knowing the mean free path and the droplet velocity, we can estimate the droplet thermal-boundary-layer lifetime, defined as the time elapsed between the initiation of thermal-boundary-layer growth and destruction. We can assume that the thermal boundary layer is destroyed through droplet coalescence, breakup, deposition, and entrainment. In the code, it is arbitrarily assumed that the mean free path is equal to channel hydraulic diameter. The droplet velocity is calculated as

$$V_d = V_g - V_r \ ,$$

where the relative velocity, V_r, is obtained from a force balance between gravity and drag using an interfacial-drag coefficient of 0.44, which yields (Ref. F-22., p. 14, Eq. 18)

$$V_r = 2.462\sqrt{g\frac{\rho_\ell - \rho_g}{\rho_g}\frac{D_d}{2}} \ . \tag{F-72}$$

At each cell, we assumed that the average droplet is in the middle of its thermal lifetime, t_d. Thus, t in Eq. (F-71) is replaced by $t_d/2$ where

$$t_d \approx \frac{D_H}{V_r} \ . \tag{F-73}$$

Therefore, knowing the liquid-side heat-transfer coefficient, the heat-transfer factors become

$$H_{\text{ALVE,drop}} = h_{i\ell} A_{i,\text{drop}} \text{ and} \tag{F-74}$$

$$H_{\text{ALVE,drop,max}} = h_{i\ell} A_{i,\text{drop,max}} \tag{F-75}$$

during condensation, and

$$H_{\text{ALV,drop}} = h_{i\ell} A_{i,\text{drop}} \text{ and} \tag{F-76}$$

$$H_{\text{ALV,drop,max}} = h_{i\ell} A_{i,\text{drop,max}} \tag{F-77}$$

during flashing. Note that further correction is made on the combined H_{ALV} for annular-mist flow, as described in Section F.1.2.2.

During both condensation and evaporation, the vapor-side heat-transfer coefficient is calculated using the correlation developed by Ryskin, given by (Ref. F-23., Eq. 3)

$$Nu = 2 + \sqrt{V^*_{\max} Pe} \ . \tag{F-78}$$

In Eq. (F-78), the Nusselt and Peclet numbers are defined as

$$Nu = \frac{h_{ig} D_d}{k_g}$$

and

$$Pe = \frac{\rho_g c_{p,g} D_d V_r}{k_g} \ ,$$

respectively, where V_r is obtained from Eq. (F-72). The maximum dimensionless circulation velocity at the surface of the drop is defined as

$$V^*_{\max} = \frac{1.5}{1 + \dfrac{2.8(1+2\lambda)(2+3\kappa)}{(2+3\lambda)\sqrt{Re_g}}} \ ,$$

where

$$Re_g = \frac{\rho_g D_d V_r}{\mu_g} \ ,$$

$$\lambda = \sqrt{\frac{\rho_\ell \mu_\ell}{\rho_g \mu_g}} \ ,$$

and

$$\kappa = \frac{\mu_\ell}{\mu_g} \ .$$

Thus, the vapor-side heat-transfer factors can be calculated as

$$H_{\text{CHTI,drop}} = h_{i,g} A_{i,\text{drop}} \tag{F-79}$$

and

$$H_{\text{CHTI,drop,max}} = h_{i,g} A_{i,\text{drop,max}} \cdot \tag{F-80}$$

The same model given by Eq. (F-78) is used to calculate the direct sensible heat factor, H_{CHTA}, between the gas and liquid phases. In order to calculate H_{CHTA}, the mixture properties are replaced by noncondensable-gas properties in the model.

F.1.2.2.2. Annular-Mist-Flow Heat-Transfer Coefficients. For the liquid film, both the liquid- and vapor-side heat-transfer coefficients are calculated using a Stanton-number correlation given by

$$St = 0.0045 \left(\frac{\rho_g V_g \mu_\ell}{\rho_\ell V_\ell \mu_g} \right)^{1/3} . \tag{F-81}$$

This correlation was originally developed by Bankoff (Ref. F-24., Eq. 21) for the liquid-side heat-transfer coefficient during stratified cocurrent steam-water flow. The advantage of this correlation is its independence from the position vector, which makes its use convenient in an Eulerian quasi-steady code, such as TRAC. For saturated water, the effect of slip ratio and pressure on the calculated Stanton number is illustrated in Fig. F-18. For the original correlation, the Stanton number is defined based upon the liquid properties and liquid velocity. In the code, the Stanton number is defined as

$$St \equiv \frac{h_{i,\ell}}{\rho_\ell c_{p,\ell} V_\ell} ,$$

$$St \equiv \frac{h_{i,g}}{\rho_g c_{p,g} |V_g - V_\ell|} ,$$

or

$$St \equiv \frac{h_{g\ell}}{\rho_a c_{p,a} |V_g - V_\ell|}$$

to calculate the liquid-side, the vapor-to-interface, or the gas-to-liquid heat-transfer coefficient.

Thus, the heat-transfer factors can be obtained as

$$H_{\text{ALVE,film}} = h_{i\ell} A_{i,\text{film}} , \tag{F-82}$$

$$H_{\text{ALV,film}} = h_{i\ell} A_{i,\text{film}} , \tag{F-83}$$

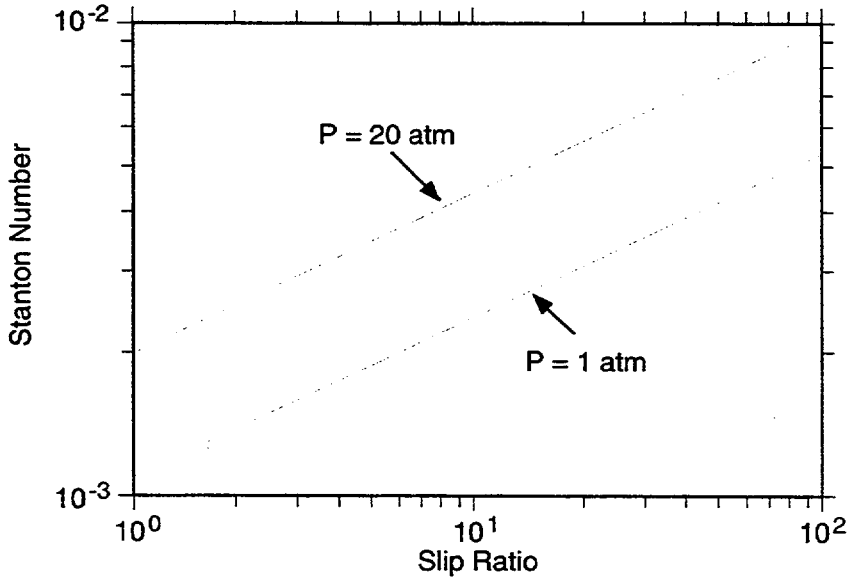

Fig. F-18. Calculated Stanton numbers for liquid-film flow using saturated water properties.

$$H_{\text{CHTI,film}} = h_{i\ell} A_{i,\text{film}} \,, \tag{F-84}$$

and

$$H_{\text{CHTA,film}} = h_{g\ell} A_{i,\text{film}} \,. \tag{F-85}$$

F.1.2.3. Assessment. The droplet diameter model of TRAC is compared with more recent data of Lopes and Dukler (Ref. F-25.). In this study, air-water mixture is used in a 10-m-long vertical pipe with an internal diameter of 50.74 mm. Lopes and Dukler used a novel laser optical technique to measure simultaneously the droplet size and axial and radial velocities. The technique allows these measurements for droplets passing through a fixed point in the flow channel; thus, it provides statistical data on temporal variations. From these data, various mean droplet diameters are computed and reported (Ref. F-25., Table 3.2). In the experiments, the liquid volumetric flux ranged between 3.4 and 12.1 cm/s and the gas volumetric flux ranged between 14 and 25 m/s. As shown in Fig. F-14., within this range of J_g and for $D_H \approx 50$ mm the droplet diameters are predicted by the correlation of Kataoka et al. (Ref. F-16.). Consequently, the data of Lopes and Dukler are compared with this correlation and the results are shown in Fig. F-19. As shown, the correlation agrees well with the data obtained near the wall (15–20 mm from the centerline). The data obtained at the centerline is overpredicted by the code by about 40%. Apparently, the droplet Sauter mean diameter is larger near the wall. We have to note that the correlation of Kataoka et al. represents the area-averaged data. Unfortunately, Lopes and Dukler did not compute their area-averaged data. However,

because the area of radial rings is larger near the wall than around the centerline, the area-averaged data are expected to be much closer to the data near the wall than to the data at the centerline. The database of the Kataoka et al. correlation mostly contains data from photographic observations (see Table F-1.). As discussed by Lopes and Dukler, these data seem to be biased towards larger droplets because very small droplets (less than ~100 μm) cannot be detected, which may be another reason for the slight overprediction by the correlation. Finally, as reported by Kataoka et al. (Ref. F-16., Fig. 3), the accuracy of their correlation is within ±40% when compared to its own database. All data of Lopes and Dukler fall within this range.

For the droplet-field liquid-side heat-transfer coefficient, the transient conduction solution is used based upon the observations of Ford and Lekic (Ref. F-20.) and the suggestion by Iciek et al. (Ref. F-21.). Based on a comparison of Eq. (F-71) to data, a correlation for the correction factor C_c is suggested as

$$C_c = 0.153\left[\left(\frac{\mu_g}{\mu_g + \mu_\ell}\right)\frac{\rho_\ell c_{p,\ell} V_d D_d}{k_\ell}\right]^{0.454}, \tag{F-86}$$

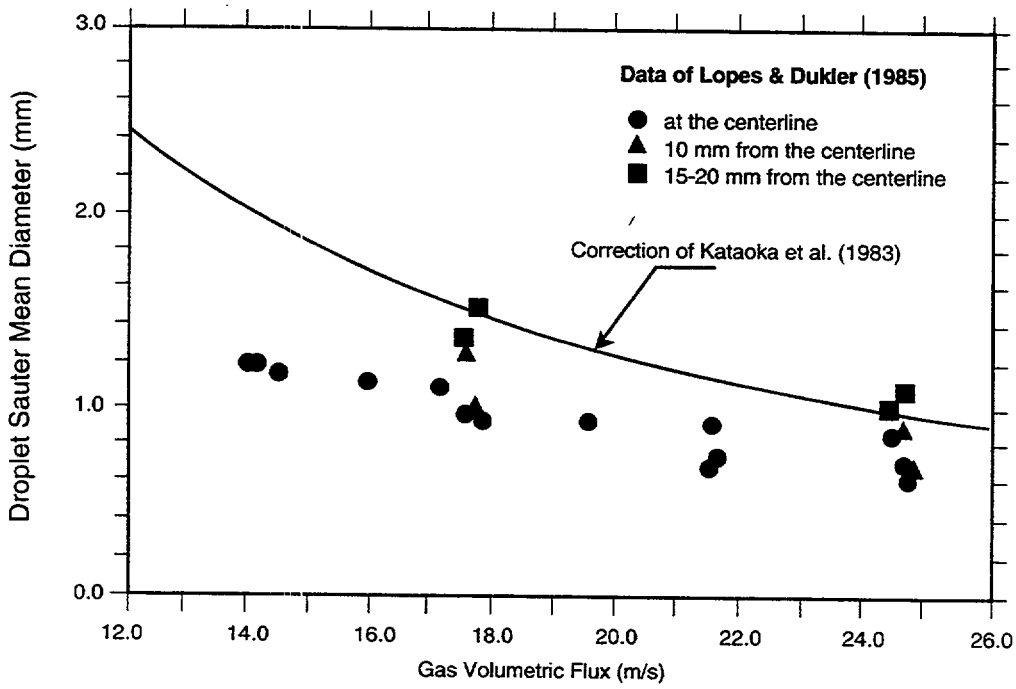

Fig. F-19. Comparison of Kataoka et al. correlation (Ref. F-6.) with the data of Lopes and Dukler (Ref. F-25.).

where V_d is the droplet velocity traveling through a stationary steam volume. In a mist-flow scenario, it must be replaced by the relative velocity. The relative velocity in mist flow is usually very small, however. Thus the correction factor tends towards 1 with decreasing relative velocity. Consequently, it is concluded that the transient conduction solution is a fairly reasonable representation of liquid-side heat transfer within droplets. The major source of error is the time-averaging of this transient process over an assumed droplet lifetime. This will be further discussed in Section F.1.2.4. Furthermore, the correlation for entrainment fractions also has limited accuracy: (*i*) it assumes a local-instantaneous equilibrium for entrainment phenomena and introduces considerable error if these conditions are not satisfied, and (*ii*) its accuracy is limited from ±50% to ±75%, especially for 1% to 10% entrainment fractions (Ref. F-17., Fig. 13, and Ref. F-18., Fig. 13). In the TRAC-M/F77 Developmental Assessment Manual (Refs. F-99. and F-100.), we showed that the new droplet-condensation model agrees fairly well with the data of Aoki et al. (Ref. F-26.) and Akimoto et al. (Ref. F-27.).

The correlation proposed by Ryskin (Ref. F-23.) to calculate the vapor-side heat-transfer coefficient for droplets is a theoretically based correlation and no data comparison was provided. For water, it commonly yields Nusselt numbers on the order of unity, comparable to the conduction solution. Actually, as the relative velocity tends towards zero, as expected in mist flow, the Ryskin correlation yields $Nu = 2$, which is the steady-state conduction limit. This would also be obtained by using Whittaker's solid sphere correlation (Ref. F-8.) given by Eq. (F-24).

The Bankoff correlation used to calculate the liquid- and vapor-side heat-transfer correlations for the liquid film was originally developed for horizontal, stratified, condensing-flow conditions. As shown by Bankoff (Ref. F-24., Fig. 7), the correlation is accurate only within 100% when compared to its own database. The liquid layer thickness is much larger under these conditions as compared to the liquid-film thickness in annular-mist flow. The heat-transfer mechanism may change considerably with this thickness. In stratified condensing flow, the heat-transfer is commonly dominated by highly turbulent mixing. For thin liquid films, conduction or laminar convection may be the dominant mechanisms. Finally, the application of the Bankoff correlation to calculate the vapor-side heat-transfer coefficient is an engineering approximation.

F.1.2.4. Conclusion and Final Remarks. The lengthy discussion of the averaging of the statistical data of the dispersed-phase sizes, provided in Section F.1.1.5., also applies to droplet flow. However, the droplets are smaller in size and tend to be more spherical than bubbles. Consequently, the sphericity considerations are expected to be less important. Furthermore, the data used by Kataoka et al. (Ref. F-16.) and the recent data of Lopes and Dukler (Ref. F-25.) are examined and the effect of statistical variations on the various averages are incorporated. Consequently, droplet diameters are better documented than bubble diameters. However, the parametric range of the data and the resulting correlations are limited. Both the diameter and the entrainment fraction correlations are based upon low-pressure air-water data. In the code, these relations are used at high pressures and use steam-water properties. As illustrated before, pressure and steam properties considerably change the quantitative predictions. The trends

follow our physical expectations. However, the quantitative error committed by extrapolating these correlations beyond their parametric range cannot be quantified. Further data are needed for this purpose.

A discrete phase, such as drops in annular-mist flow, usually exhibits a transient heat-transfer characteristic with a small time constant. For proper averaging of this transient behavior, further model development efforts are needed, for instance for the average droplet lifetime. Such a model for a mean free path can be obtained from carefully obtained data, as in the study of Lopes and Dukler. More similar data are needed, however, where sizes and velocities are measured simultaneously over a wider parametric range to obtain a widely applicable model.

F.1.3. Models and Correlations in Churn (Transition) Flow

Transition flow exists if the void fraction is between 50% and 75%. This regime is commonly called churn flow in two-phase-flow literature. In TRAC, we treat this regime as an interpolation regime between bubbly slug (in the sense of the three regimes up to a void fraction of 0.5) and annular-mist-flow regimes (see Fig. F-3.). The closure parameters are obtained from the following relationship:

$$X_{\text{transition}} = (1 - W_t)X_{\text{bubbly slug}_{(\alpha = 0.5)}} + W_t X_{\text{annular mist}_{(\alpha = 0.75)}} , \tag{F-87}$$

where X corresponds to either A_i, H_{ALVE}, H_{ALV}, H_{CHTI}, or H_{CHTA}. The linear weighting factor, W_t, is defined based upon the void fraction as follows:

$$0 \le W_t = \frac{\alpha - 0.5}{0.25} \le 1 . \tag{F-88}$$

Note that for flashing, the calculated value of H_{ALV} is compared with Eq. (F-27) and the maximum is chosen.

We are not aware of any interfacial-area or heat-transfer models that are specifically developed for churn flow. This may be due to the chaotic nature of the flow pattern, which does not lend itself to a simple geometric idealization. Consequently, we could not make any separate-effect assessments.

F.1.4. Models and Correlations in Stratified Flow

Stratified flow is super-imposed on the general flow-regime map if certain criteria—in terms of phasic velocities and channel orientation—are met to yield phase stratification. The criteria are described in the flow-regime map description (Appendix E). The weighting factor that superimposes stratified flow on the flow-regime map, W_{st}, is different for 1D and 3D components. It is calculated in the interfacial shear packages [subroutine StbVel1D (FEMOM in TRAC-M/F77) for 1D and subroutine CIF3 for 3D] and carried over to interfacial heat-transfer calculations. In interfacial drag routines, the weighting factors are computed as cell-edge quantities. An arithmetic average is calculated in subroutine HTIF to obtain a cell-centered weighting factor. A weighting

factor of unity implies full stratification whereas a weighting factor of zero means the stratification conditions are not met. In the accumulator and during condensation in the pressurizer, W_{st} is set equal to 1 to represent vertically stratified flow.

With the known weighting factor, the various closure parameters are calculated based upon

$$X_{\text{map-stratified}} = (1 - W_{st})X_{\text{map}} + W_{st}X_{\text{stratified}} \ , \tag{F-89}$$

where X corresponds to either A_i, H_{ALVE}, or H_{ALV}. The subscript *map* refers to quantities calculated using the basic flow-regime map as described in Sections F.1.1., F.1.2., and F.1.3. Note that for flashing, the calculated value of H_{ALV} is compared with Eq. (F-27) and the maximum is chosen. For vapor-side heat-transfer factors, no modification is made due to stratified flow; consequently,

$$H_{\text{CHTI,map-stratified}} = H_{\text{CHTI,map}} \tag{F-90}$$

and

$$H_{\text{CHTA,map-stratified}} = H_{\text{CHTA,map}} \ . \tag{F-91}$$

F.1.4.1. Interfacial-Area Model. Figure F-20. shows a schematic of horizontal stratified flow in a circular pipe. From purely geometric considerations and neglecting the surface waves, the interfacial area is calculated as

$$A_i = D_H \times \Delta x \sqrt{1 - \left(1 - \frac{2L_\ell}{D_H}\right)^2} \ . \tag{F-92}$$

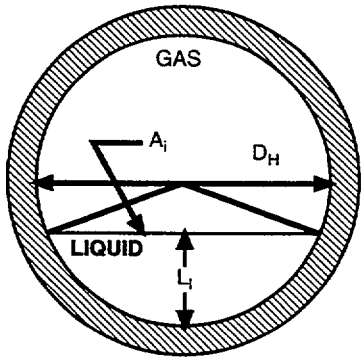

Fig. F-20. Schematic of stratified flow.

For vertically stratified flow, such as in the accumulator and pressurizer, the interfacial area is equal to the average cross-sectional area within the cell given by

$$A_i = \frac{B_{\text{cell}}}{\Delta x} \ . \tag{F-93}$$

F.1.4.2. Interfacial Heat-Transfer Models. For the liquid-side heat-transfer coefficient, a constant-Stanton-number criterion is used. The value of the Stanton number is fixed as suggested by Linehan et al. (Ref. F-28., p. 17) at

$$St \equiv \frac{h_{i,\ell}}{\rho_\ell c_{p,\ell} V_\ell} = 0.0073 \ . \tag{F-94}$$

Linehan et al. obtained the magnitude of the Stanton number using their experimental data where steam condenses on subcooled water. They used a horizontal rectangular channel that was 46-cm long, 15-cm wide, and 1.7-cm high. Steam and subcooled water were injected separately, satisfying stratified-flow conditions. The steam Reynolds number ranged from 14000 to 17500. The liquid Reynolds number corresponding to injection flow rate ranged between 250 to 1800. The inlet liquid subcooling ranged between 7°C and 80°C. The value of the liquid-side interfacial heat-transfer coefficient obtained from Eq. (F-91) is used to compute the stratified-flow heat-transfer factors during condensation and flashing.

As mentioned above, no modification is made to the vapor-side heat-transfer coefficient due to stratification, except in the accumulator where

$$h_{gl} = h_{ig} = 10000 \ \frac{\text{W}}{\text{m}^2\text{-K}} \ . \tag{F-95}$$

F.1.4.3. Assessment. As discussed in Section F.1.2.2.2., the Bankoff correlation (Ref. F-24.), which we are using to estimate the heat-transfer coefficient in liquid films, was originally developed for stratified-condensing-cocurrent flow. Thus, we compared the constant-Stanton-number criterion proposed by Linehan et al. with the Bankoff correlation. The comparison is shown in Fig. F-21. As shown, if the slip ratio is on the order of unity, the two correlations are in order of magnitude agreement.

Increasing the pressure increases the Stanton number predicted by the Bankoff correlation. If we consider that the Bankoff and the Linehan et al. correlations are accurate within ±100%, the agreement in Fig. F-21. must be considered to be satisfactory.

Kim (Ref. F-29.) measured condensation rates in countercurrent stratified steam-water flow. In these experiments, Kim used rectangular channels with different inclination angles from horizontal, θ. Table F-2., obtained from Ref. F-29., Table 2-2, shows the parametric range for various tests. Kim obtained an empirical power-law correlation in the form

$$Nu_\ell = a_1 Re_v^{a_2} Re_\ell^{a_3} Pr_\ell^{a_4} \ . \tag{F-96}$$

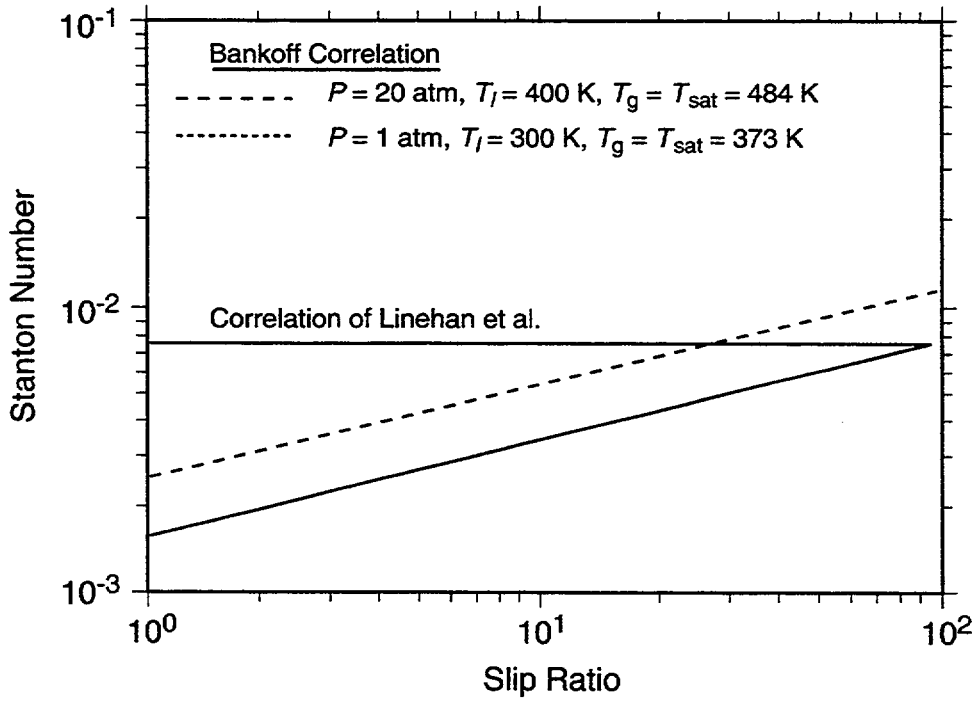

Fig. F-21. Comparison of Bankoff (Ref. F-24.) and Linehan et al. correlations. (Ref. F-28.).

TABLE F-2.
Parametric Range of Kim's Experiments
(Ref. F-29., Table 2-2)

Data Set	Aspect Ratio[a]	q	Re_g	Re_j
A	5	4°	2500 ~ 30000	800 ~ 15000
B	5	30°	5000 ~ 30000	1000 ~ 8000
C	5	87°	3000 ~ 20000	800 ~ 7000
D, E	5	33°	3000 ~ 18000	800 ~ 5000

a. This is width-to-height ratio for rectangular channels.

Equation (F-96) can be written in Stanton-number form as follows:

$$St_\ell = a_1 Re_v^{a_2} Re_\ell^{a_3 - 1} Pr_\ell^{a_4 - 1} \quad . \tag{F-97}$$

Table F-3., obtained from Ref. F-29., Table 3-1, shows the empirical constants a_1 through a_4 for different experiments. Figure F-22. shows the comparison of the Linehan et al. correlation—used in the code—with the Kim correlations. Only tests denoted by A, B, and E are plotted in this figure. As shown in Fig. F-22. and in Table F-3., the inclination angle, the appearance of the interface, the liquid Reynolds number, and the vapor Reynolds number strongly affect the results. Our constant-Stanton-number correlation is the same order of magnitude with the majority of Kim's data.

TABLE F-3.
Empirical Constants of Kim's Correlations
(Ref. F-29., Table 3-1)

Data Set	a_1	a_2	a_3	a_4	
A	6.30×10^{-6}	0.900	0.75	0.81	
B	1.35×10^{-4}	0.350	1.00	0.56	
C	8.45×10^{-10}	1.230	1.47	0.50	
D	1.73×10^{-1}	0.027	0.49	0.42	smooth interface
E	3.43×10^{-10}	2.100	0.56	1.16	rough interface

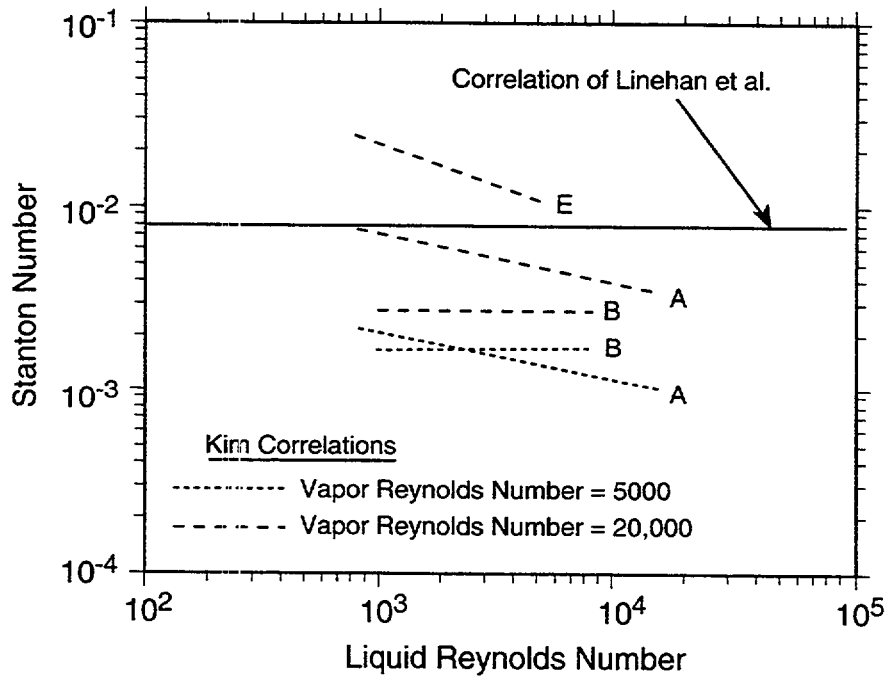

Fig. F-22. Comparison of Kim (Ref. F-29.) and Linehan et al. (Ref. F-28.) correlations.

F.1.4.4. Conclusion and Final Remarks. Stratified flow with phase change is not very easy to analyze using an Eulerian quasi-steady code. The averaging of various models is typically done over the stratified-flow length, which is commonly much greater than a typical cell length. Even for the experiments where the stratified-flow conditions are carefully controlled, the resulting correlations in the literature have a low degree of accuracy. In an integral analysis, the detection of the onset of stratified flow is difficult because it depends on history and upstream effects. Consequently, the total length of the stratified-flow region cannot be accurately predicted for proper averaging. This situation becomes more complicated during a hydrodynamic transient. Within this perspective, a very accurate stratified-flow heat-transfer package is not possible. The current package must be judged on its overall performance in an integral analysis. We must note that, in stratified flow, especially with high gas velocities, one would expect the interface to be wavy. Consequently, our geometric model to estimate the interfacial area is not accurate. However, the constant-Stanton-number criterion developed by Linehan et al. already accounts for this waviness in the correlation. The heat-transfer coefficients are obtained directly from the local rate of change of the liquid flow rate. The measured change in liquid flow rates is converted to an interfacial heat-transfer coefficient assuming the incremental time-averaged interfacial area to be smooth. As a result, any error committed by assuming a smooth interface is already absorbed by the $St = 0.0073$ correlation.

F.1.5. Models and Correlations in Plug Flow

The existence of the liquid plug is superimposed upon bubbly slug/transition/annular-mist/stratified flows if the liquid side is under condensation mode. A schematic of plug flow is shown in Fig. F-23. The weighting factor, W_{plug}, incorporates the effect of plugging on the liquid-side condensation heat-transfer factor as follows:

$$H_{ALVE,map-stratified\text{-}plug} = (1 - W_{plug}) H_{ALVE,map-stratified} + W_{plug} H_{ALVE,plug} \quad . \tag{F-98}$$

The purpose of W_{plug} is to recognize when the void fractions in three contiguous cells are significantly different from each other and at least one cell has a void fraction above 50% but below 75%, warranting the assumption that plugs may exist. The weighting factor W_{plug} is given by

$$0 \le W_{plug} \equiv \frac{(\alpha_{max} - \alpha_{min})(\alpha_{max} - 0.5)(0.75 - \alpha_{min})}{(0.75 - 0.5)^3} \le 1 \ , \tag{F-99}$$

where α_{min} and α_{max} are the minimum and maximum of the void fractions in the group of three contiguous cells. Figure F-24. is a contour plot showing W_{plug} in terms of α_{min} and α_{max}. Notice that when $\alpha_{min} = \alpha_{max}$, $\alpha_{max} \le 0.5$, or $\alpha_{min} \ge 0.75$, W_{plug} is equal to zero, which means that there is no plugging.

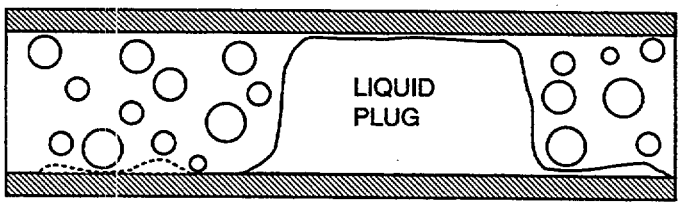

Fig. F-23. Schematic of plug flow.

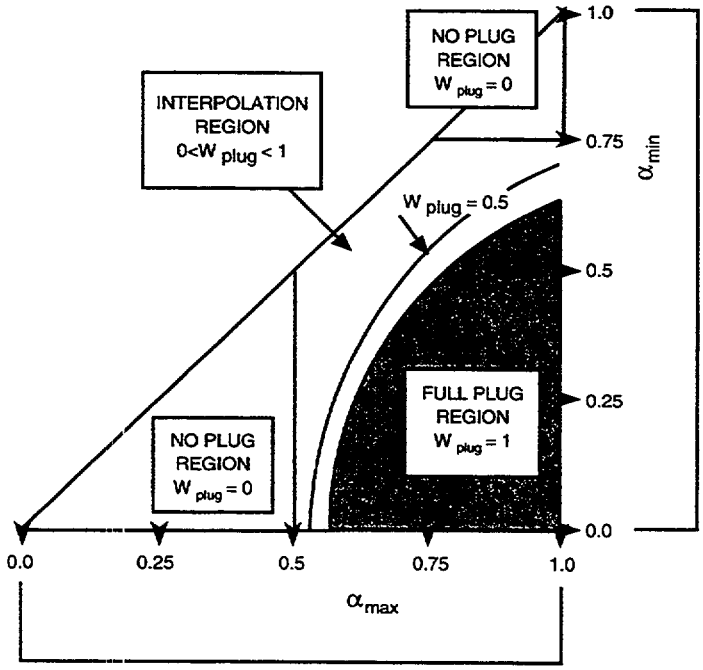

Fig. F-24. Liquid plug formation map.

F.1.5.1. Interfacial-Area Model. The interfacial area of a plug is calculated assuming a cylindrical geometry, which yields

$$A_{i,\text{plug}} = M_{\text{plug}} \times \frac{\pi}{4} D_H^2 \ , \qquad \text{(F-100)}$$

where M_{plug} is either 1 or 2, depending upon whether the plug is confined within one or more cells.

F.1.5.2. Heat-Transfer Coefficient Models. The liquid-side heat-transfer coefficient is calculated through a simple constant-Stanton-number model given by

$$St \equiv \frac{h_{i,\ell}}{\rho_\ell c_{p,\ell} V_\ell} = 0.02 \ . \qquad \text{(F-101)}$$

Vapor-side heat-transfer is not affected by plug formation.

F.1.5.3. Assessment. To the best of our knowledge, no interfacial heat-transfer model specifically has been developed for liquid plugs. Liquid-plug behaviors were experimentally observed by Akimoto et al. (Ref. F-30.). The plug behavior predicted by TRAC is in good agreement with these data. This comparison is further documented in the TRAC-M/F77 Developmental Assessment Manual (Refs. F-99. and F-100.).

F.1.5.4. Conclusions and Final Remarks. Currently, the TRAC model for condensation during plugging is a simple model. Unfortunately, we are not aware of a mechanistic model to replace the $St = 0.02$ criterion. However, the existing model seems to predict well the plug behavior in the experiments of Akimoto et al. (Ref. F-30.).

F.1.6. Reflood Models and Correlations

During reflood of the core region, a special flow-regime map is activated. The flow-regime map during reflood shown in Fig. F-25. is based upon the observations of DeJarlais and Ishii (Ref. F-31.). Figure F-25. illustrates that, along the flow channel, various flow configurations occur beyond the CHF point. Because of considerable differences in flow patterns, these various regimes require different closure relationships. Such relationships are incorporated into the code in accordance with the flow patterns shown in Fig. F-25. Naturally, in order to make transitions from one flow pattern to the next, the various elevations for such transitions must be known. The code calculates these elevations through mechanistic models mostly scaled through capillary number. These models are discussed in Section F.2.2. and are not repeated here.

This document only describes the core reflood model that is in TRAC-M/F90 (Version 3.0), which was bought over from MOD2. References F-101. and F-102. describe the additional reflood model that was developed for TRAC-M/F77.

The reflood model is applicable only for the VESSEL component and is used only in a core region that is specified in the VESSEL's input. The model is activated by the user via the NAMELIST input variable NEWRFD (which cannot be changed in a restart calculation). In addition to setting NEWRFD, the user must also specify a reflood trip and identify that trip via HTSTR input variable IRFTR2. If the reflood model is activated at the start of a LOCA transient, it will be used also during the blowdown and refill phases of the transient.

Note that the work of DeJarlais and Ishii, on which the reflood model is based, is directly applicable to high reflood rates.

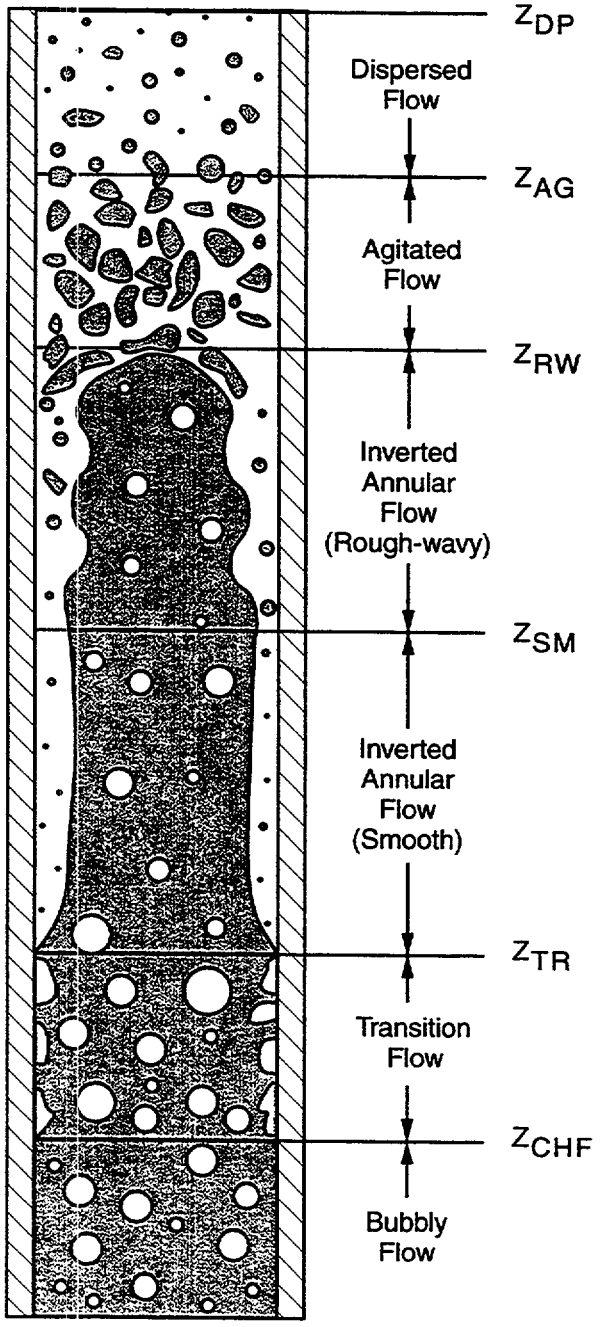

Fig. F-25. Flow-regime map during reflood.

The discussion in this section presumes that the elevations Z_{CHF}, Z_{TR}, Z_{SM}, Z_{RW}, Z_{AG}, and Z_{DP} are known. (Z_{DP} is the transition to highly dispersed flow. See Sections F.1.6.2., F.2.2., and Appendix H, Section H.1.5.) Depending upon the location of a given cell with reference to these elevations, the appropriate closure relationships are computed using weighting factors based upon the cell length. The weighting factors are determined

using the top and bottom cell-edge elevation of a given cell, denoted by z_t and z_b, respectively. Table F-4. reports the way the following weighting factors are calculated:

$$0 \le W_{sb} = \frac{Z_{TR} - z_t}{\Delta x} \le 1 \tag{F-102}$$

$$0 \le W_{sm} = \frac{\min(Z_{SM}, z_t) - \max(Z_{TR}, z_b)}{\Delta x} \le 1 \tag{F-103}$$

$$0 \le W_{rw} = \frac{\min(Z_{AG}, z_t) - \max(Z_{SM}, z_b)}{\Delta x} \le 1 \tag{F-104}$$

$$W_{inv} = W_{rw} + W_{sm} \tag{F-105}$$

$$W_{ds} = 1 - W_{sb} - W_{rw} - W_{sm} \tag{F-106}$$

Once the weighting factors are obtained from Table F-4., they are used to calculate the various closure relationships through

$$X_{\text{reflood}} = W_{sb} \times X_{\text{bubbly}} + W_{ds} \times X_{\text{dispersed}} + W_{inv} \times X_{\text{inverted}} , \tag{F-107}$$

where X represents either A_i, H_{ALVE}, H_{CHTI}, or H_{CHTA}. For flashing, the maximum between H_{ALVE} and the model discussed in the next section is used. If noncondensables are present, H_{ALVE} for evaporation and condensation is modified as described in Section F.1.7. The individual models used for bubbly, dispersed, and inverted annular flows are described in the following subsections.

TABLE F-4.
Weighting Factors of Reflood Interfacial Heat-Transfer Models

z	W_{sb}	W_{sm}	W_{rw}	W_{ds}	W_{inv}
$z_t \le Z_{TR}$	1	0	0	0	0
$Z_{TR} < z_t < Z_{SM}$	Eq. (F-102)	Eq. (F-103)	0	0	Eq. (F-105)
$Z_{SM} < z_t < Z_{AG}$	Eq. (F-102)	Eq. (F-103)	Eq. (F-104)	0	Eq. (F-105)
$Z_{AG} < z_t$	Eq. (F-102)	Eq. (F-103)	Eq. (F-104)	Eq. (F-106)	Eq. (F-105)
$z_b \ge Z_{AG}$	0	0	0	1	0

F.1.6.1. Bubbly Flow Models. In bubbly CHF upstream of the quench front, the void fraction is restricted to the following range: $0.05 \le \alpha \le 0.30$. Slugs are not allowed to form. The interfacial area and heat-transfer coefficients, except for the flashing model, are identical to those described in Sections F.1.1.1.1., F.1.1.2., and F.1.1.3. When the reflood model is used and $T_\ell > T_{sat}$, the liquid-side heat-transfer factor is not calculated by Eq. (F-27). The reflood model uses a simple flashing model to determine the liquid-side heat-transfer factor. This simple model uses the kinetic theory of evaporation from liquid surfaces (see Ref. F-32., p. 56). The theoretical maximum evaporation rate was converted to an equivalent HTC. The coefficient of evaporation of 0.04 (suggested by Hsu and Graham, Ref. F-33.) to predict the evaporation rate in experimental studies was modified for each of the individual flow regimes in nucleate and film boiling. The liquid-side HTC due to flashing is given by the following equation:

$$h_{fls} = C_{eva} h_{fls,teo} = C_{eva} \times 0.01857 \frac{\rho_v h_{fg}^2}{T_{sat}^{1.5}} \quad . \tag{F-108}$$

The coefficient of evaporation, C_{eva}, is defined for bubbly and annular-mist-flow regimes in the nucleate-boiling region. The selection of C_{eva} is considered to be void-fraction dependent in the bubbly flow when the cell void fraction is between 0.3 and 0.5. The evaluation logic of C_{eva} for the bubbly flow is

$$C_{eva} = 0.002 \times \left[C_1 + (C_2 - C_1) \times \left(\frac{\alpha - 0.3}{0.5 - 0.3} \right)^{0.5} \right] \text{if } 0.3 < \alpha < 0.5 , \tag{F-109}$$

$$C_{eva} = 0.002 C_2 \text{ if } \quad \alpha = 0.5 , \text{ and} \tag{F-110}$$

$$C_{eva} = 0.002 C_1 \text{ if } \quad \alpha < 0.3 . \tag{F-111}$$

The current values for C_1 and C_2 are 0.1 so that C_{eva} becomes 0.0002 for all void fractions up to 0.5 in bubbly flow. The interfacial surface area in bubbly flow is identical to that described in Section F.1.1.1.1. The liquid-side heat-transfer factor during the flashing in the bubbly flow is given by

$$H_{ALV,bub} = h_{fls} A_{i,bubble} \quad . \tag{F-112}$$

C_{eva} is selected as 0.0002 in the annular-mist-flow regime. The liquid-side heat-transfer factor during flashing in annular-mist flow is given by

$$H_{ALV,mist} = h_{fls} A_{i,mist} \quad . \tag{F-113}$$

The interfacial surface area, $A_{i,mist}$, is identical to that described in Section F.1.2.

If the flow regime is determined as the transition between bubbly and annular-mist flows ($0.5 < \alpha < 0.75$), an interpolation is used to determine $H_{ALV,trans}$ in the nucleate-boiling region as

$$H_{ALV,trans} = W \times H_{ALV,mist} + (1-W) \times H_{ALV,bubbly} \ , \tag{F-114}$$

where

$$W = \frac{\alpha}{0.75-0.5} - \frac{0.5}{0.75-0.5} = 4\alpha - 2 \ . \tag{F-115}$$

F.1.6.2. Dispersed (Post-Agitated) and Highly Dispersed Inverted Annular Flows. This flow regime is furthest from the quench front, as shown in Eq. (F-25). The region immediately above elevation Z_{AG} is considered to be the post-agitated region of dispersed flow. As shown in Section F.2.2. and in Appendix H (Section H.1.5.), at higher elevations we distinguish a highly dispersed flow regime. The void fraction is restricted to being between 0.3 and 0.9995. If there is a cold wall adjacent to the hydro cell, however, liquid film is allowed to form. Thus, the models are very similar to those used in annular-mist flow.

F.1.6.2.1. Interfacial-Area Models. Using a simple force balance, the thickness of a stable film on a cold wall is calculated as

$$10^{-17} \le \delta_{\ell f} = \frac{0.0025 D_H \rho_\ell V_g^2}{g\rho_\ell D_H - 0.75\rho_g V_g^2} \le 5 \text{ mm} \ , \tag{F-116}$$

where the minimum limit on the denominator is 0.01. With a known film thickness, the liquid fraction corresponding to the film can be computed as

$$\alpha_f = \frac{4F_u \delta_{\ell f}}{D_H} \ , \tag{F-117}$$

where F_u is the cold-wall fraction adjacent to the hydro cell. The liquid-film fraction also is estimated with the following equations:

$$\alpha_f = F_u W_{fd} (1-\alpha) \ , \tag{F-118}$$

where W_{fd} is the cold-wall liquid-fraction weighting factor defined as

$$W_{fd} = 0 \qquad \text{if} \quad \alpha \le \min(\alpha_{AG}, 0.7)$$

$$W_{fd} = 5\left[\frac{0.98 - \alpha^*}{0.98 - \min(\alpha_{AG}, 0.7)}\right]^{0.35} \qquad \text{if} \quad \min(\alpha_{AG}, 0.7) < \alpha < 0.98 \qquad \text{(F-119)}$$

$$W_{fd} = 5 \qquad \text{if} \quad \alpha \ge 0.98 \ ,$$

where α^* is the void fraction that has been constrained to be between 0.3 and 0.9995. (The tests are made with the actual void fraction.) In TRAC-M/F77, the exponent 0.35 in Eq. (F-119) is 0.5 for the reflood model in that code based on MOD2.

The liquid-film fraction, α_f, is selected as the minimum of values obtained from Eqs. (F-117) and (F-118).

The liquid droplet fraction is obtained by

$$\alpha_{dd} = 1 - \alpha_f - \alpha \ . \qquad \text{(F-120)}$$

Then, the interfacial areas corresponding to liquid film and droplets are obtained as

$$A_{i,\text{film}} = \frac{4\alpha_f B_{\text{cell}}}{D_H} \qquad \text{(F-121)}$$

and

$$A_{i,\text{drop}} = B_{\text{cell}} \frac{6\alpha_{dd}}{D_d} \ . \qquad \text{(F-122)}$$

The final interfacial area in the dispersed (or post-agitated) IAF is

$$A_{i,\text{dispersed (or post-agitated)}} = A_{i,\text{film}} + A_{i,\text{drop}} \ . \qquad \text{(F-123)}$$

The droplet Sauter mean diameter in Eq. (F-119) is calculated using the same models as the annular-mist-flow models, given by Eqs. (F-54) and (F-56).

F.1.6.2.2. Vapor-Side Heat-Transfer Models. Before the vapor-to-interface heat-transfer factor is calculated in the dispersed-flow regime, a mass fraction is calculated as

$$x_\ell = \frac{\rho_g V_g (1 - \alpha_{dd})}{\rho_g V_g (1 - \alpha_{dd}) + \rho_\ell V_\ell \alpha_{dd}} \ . \qquad \text{(F-124)}$$

Based upon this mass fraction, we calculate a homogeneous void fraction defined as

$$\alpha_{\text{hom}} = \frac{x_\ell \rho_\ell}{x_\ell \rho_\ell + (1 - x_\ell)\rho_g} \,. \tag{F-125}$$

Then, if $\alpha_{\text{hom}} \geq 1$ and $1 - \alpha_{dd} \leq 0.95$, $H_{\text{CHTI,dispersed}}$ is set to 10^{-6} W/K. Otherwise, the correlation proposed by Unal et al. (Ref. F-32.) is used to calculate H_{CHTI}. The correlation was originally developed for the vapor-generation rate (see Ref. F-33., Eq. 21). In the code, we converted it to a heat-transfer factor as follows:

$$H_{\text{CHTI, }ds} = 0.05 \times 0.315 \exp\left(-C_{u1}\frac{P}{P_{cr}}\right)\left[V_g \rho_g \left(\frac{1-\alpha_{dd}}{\alpha_{\text{hom}}}\right)\right]^{C_{u2}} \tag{F-126}$$

$$\times \frac{k_g Pr_g^{0.33}\left[g(\rho_\ell - \rho_g)\right]^{0.725}}{\mu_g^{0.55}(2\sigma)^{0.725}} B_{\text{cell}} \left[\frac{\sqrt{\rho_g \sigma \sqrt{\frac{\sigma}{g(\rho_\ell - \rho_g)}}}}{\mu_g}\right]^{0.4833} ,$$

where the constants C_{u1} and C_{u2} are given as 10.894 and 0.55 in the original reference. During code assessment, they are modified to be 30 and 0.33, respectively.

If the cell void fraction is less than 0.98, then the flow regime is post-agitated IAF. The H_{CHTI} in post-agitated IAF is calculated also by Eq. (F-126) with a void-fraction weighting applied between smooth and dispersed IAFs, as indicated by

$$H_{\text{CHTI, post-ag}} = H_{\text{CHTI, }ds}\left[\frac{\alpha - \alpha_{\text{SM}}}{\alpha_{\text{DP}} - \alpha_{\text{SM}}}\right] . \tag{F-127}$$

Using an exponent of 0.01 results in $H_{\text{CHTI,post-ag}}$ being equal to $H_{\text{CHTI},ds}$ in post-agitated IAF.

In the presence of noncondensables, the gas-to-liquid sensible heat-transfer factor, H_{CHTA}, is calculated using previously described models. For the droplets, the Ryskin correlation described in and given by Eq. (F-78) is used to calculate $h_{gl,\text{drop}}$ using noncondensable-gas properties. For the liquid film, the Bankoff correlation given by Eq. (F-81) is used, also using noncondensable-gas properties. Then, the final quantity is obtained as

$$H_{\text{CHTI,dispersed}} = W_{fd}(A_{i,\text{drop}} h_{g\ell,\text{drop}} + A_{i,\text{film}} A_{g\ell,\text{film}}) + (1 - W_{fd}) A_{i,\text{drop,max}} h_{g\ell,\text{drop}} \,, \tag{F-128}$$

where W_{fd} is the weighting factor as described before.

F.1.6.2.3. Liquid-Side Heat-Transfer Models. In the reflood model, the liquid-side heat-transfer factor, H_{ALVE}, is not calculated in subroutine HTIF for the inverted-annular-flow regimes when $T_\ell < T_{sat}$. Rather, the sensible heat that goes to the subcooled liquid is calculated in subroutine HTVSSL in the wall-to-liquid HTC. If the liquid is superheated, the coefficient of evaporation for the flashing model, C_{eva}, is set to 0.002. The H_{ALV} for the dispersed (or post-agitated IAF) is calculated as

$$H_{\text{ALV, dispersed (or post-agitated)}} = h_{fls} A_{i,\text{ dispersed (or post-agitated)}} , \tag{F-129}$$

where h_{fls} is calculated by Eq. (F-108).

F.1.6.3. Inverted Annular Flow. In inverted annular flow, the void fraction is limited between 0.05 and 0.95. The following models are used to calculate the interfacial area and heat-transfer factors.

F.1.6.3.1. Interfacial-Area Model. First, we calculated the hydraulic diameter of the liquid core from purely geometric considerations as

$$D_{H,\text{core}} = D_H \sqrt{1-\alpha} \ . \tag{F-130}$$

Then, the interfacial area is computed as

$$A_{i,\text{inverted}} = \pi D_H \Delta x \ . \tag{F-131}$$

In the case of flashing, the interfacial area is recalculated considering possible bubbles in the liquid core. Using an expression suggested by Denham (Ref. F-34.), the vapor film thickness is calculated as

$$\delta_{vf} = \sqrt{\frac{V_\ell \mu_v}{g(\rho_\ell - \rho_v)}} \tag{F-132}$$

The wall void fraction can be calculated by

$$\alpha_w = 4\frac{\delta_{vf}}{D_H}\left(1 - \frac{\delta_{vf}}{D_H}\right) \ . \tag{F-133}$$

The interfacial surface area near the wall then becomes

$$A_w = \pi\left(D_H - 2\delta_{vf}\right)\Delta z \ . \tag{F-134}$$

The void fraction for bubbles traveling in the liquid-core region is

$$\alpha_{fr} = \alpha - \alpha_w \ . \tag{F-135}$$

The bubble diameter is calculated as it was calculated for the bubbly flow in Section F.1.1.1. The interfacial surface area for bubbles traveling in the liquid core is

$$A_{fr} = \frac{6\alpha_{fr} B_{\text{cell}}}{D_b} \ . \tag{F-136}$$

The total interfacial area becomes

$$A_{i,\text{ inverted}} = A_w + A_{fr} \ . \tag{F-137}$$

F.1.6.3.2. Vapor-Side Heat-Transfer Models. For the vapor-side heat-transfer, the following simple models are used

$$H_{\text{CHTI, inverted}} = 3 \times 10^3 \times A_{i,\text{ inverted}} \tag{F-138}$$

and

$$H_{\text{CHTA,inverted}} = 10^3 \times A_{i,\text{ inverted}} \ . \tag{F-139}$$

F.1.6.3.3. Liquid-Side Heat-Transfer Model. In the reflood model, the liquid-side heat-transfer factor, H_{ALVE}, is not calculated in subroutine HTIF for the inverted-annular-flow regimes when $T_\ell < T_{\text{sat}}$. Rather, the sensible heat that goes to the subcooled liquid is calculated in subroutine HTVSSL in the wall-to-liquid HTC. If the liquid is superheated, the coefficient of evaporation for the flashing model, C_{eva}, is set to 0.002. The H_{ALV} for the IAFs (smooth, rough-wavy, and agitated IAFs) is calculated as

$$H_{\text{ALV,inverted}} = h_{\text{fls}} A_{i,\text{inverted}} \ , \tag{F-140}$$

where h_{fls} is calculated by Eq. (F-108).

F.1.6.4. Effect of Grid Spacers. If there is a grid spacer in the hydro cell and the hydro cell is fully above the quench front, then the calculated vapor-to-liquid heat-transfer factor is modified as

$$H_{\text{CHTI, grid}} = H_{\text{CHTI}} + \frac{D_H}{B_{\text{cell}}} \times \frac{10^6}{T_g - T_{sv}} \ . \tag{F-141}$$

No modifications are made to the liquid-side heat-transfer factor.

F.1.6.5. Assessment. Extensive assessment results for the reflood model are provided in Section F.2. and also in the TRAC-M/F77 Developmental Assessment Manual (Refs. F-99. and F-100.). These results are not repeated here.

F.1.7. The Effect of Noncondensables

The noncondensables affect the interfacial heat- and mass-transfer rates by lowering the partial pressure and thus, the saturation temperature of steam. In addition, the existence of noncondensables triggers a new set of models in the code. These models are described below.

F.1.7.1. Effects on Liquid-Side Heat-Transfer. On the liquid side, the presence of noncondensables affects both the evaporation and condensation.

F.1.7.1.1. Evaporation. If noncondensable gases are present, T_{sat} is greater than T_{sv}. Consequently, evaporation mode is possible when $T_{sv} < T_\ell < T_{sat}$. In the code, we assumed that the interfacial mass transfer is diffusion controlled, regardless of the amount of noncondensables. A simple diffusion model, independent of the flow-regime map, is used. The mass-transfer coefficient is obtained from the following equation:

$$Sh = 3.656 \qquad \text{if} \quad Re \le 2300 \text{ and}$$

$$Sh = 0.023 Re^{0.8} Sc^{1/3} \quad \text{if} \quad Re > 2300 , \tag{F-142}$$

where Sh, Sc, and Re are Sherwood, Schmidt, and Reynolds numbers defined as

$$Sh = \frac{h_M D_H}{D_o} ,$$

$$Sc = \frac{\mu_g}{\rho_g D_o} ,$$

and

$$Re = \frac{G_g D_H}{\mu_g} .$$

These equations are reported in Ref. F-35. for mass-transfer coefficient h_M in fully developed pipe flow with constant concentration on the pipe wall. Note that Eq. (F-142) is identical to the analytical solution for laminar flow and the well-known Dittus-Boelter equation for turbulent flow if the Sherwood number is replaced by the Nusselt number and the Schmidt number is replaced by the Prandtl number. The diffusion coefficient is obtained from a curve fit to a theoretical equation for the diffusion of steam in air. The curve fit is given by

$$D_o = \frac{1\times 10^{-3}}{P}(-699.2438 + 4.9249T_g + 0.0171T_g^2) \ , \tag{F-143}$$

where the diffusion coefficient D_o is in m/s, gas temperature T_g is in K, and total pressure P is in Pa. The curve fit is obtained for T_g between 273 and 600 K. Once the mass-transfer coefficient, h_M, is obtained from Eq. (F-142), the evaporative mass flux can be computed as

$$\dot{m}_e = h_M(C_i - C_\infty) \ , \tag{F-144}$$

where C_i and C_∞ are the steam concentration at the interface and away from the interface, respectively. We assumed that at the interface, the steam concentration is equal to the density of pure steam with $T=T_\ell$ and $P=P_{sat}$ when $T_{sat}=T_\ell$. Using an ideal-gas approximation, the density is calculated as

$$C_i = \rho_s = \frac{(P_{sat})_{T_{sat}=T_\ell}}{R_s T_\ell} \ , \tag{F-145}$$

where R_s is the ideal-gas constant for steam and is set equal to 462 J/kg-K. Far from the interface, the concentration is given by

$$C_\infty = \rho_g - \rho_a \ , \tag{F-146}$$

where ρ_g and ρ_a are the mixture and noncondensable-gas densities, respectively. This formulation assumes that the densities are additive in the gas mixture. Using Eqs. (F-3) through (F-5) and (F-144) through (F-146), we obtain

$$\frac{1}{h_{fg}}\left[H_{ALVE}(T_\ell - T_{sv}) + \frac{P_s}{P}H_{CHTI}(T_g - T_{sv})\right] = h_M A_i(\rho_s - \rho_g + \rho_a) \ . \tag{F-147}$$

Solving for H_{ALVE}, Eq. (F-147) yields

$$H_{ALVE} = \frac{1}{(T_\ell - T_{sv})}\left[h_M h_{fg} A_i(\rho_s - \rho_g + \rho_a) - \frac{P_s}{P}H_{CHTI}(T_g - T_{sv})\right] . \tag{F-148}$$

In the code, the vapor-side heat-transfer coefficient is neglected (the second term is set to zero). Thus, H_{ALVE} is coded as

$$H_{ALVE} = h_M h_{fg} A_i(\rho_s - \rho_g + \rho_a)\frac{1}{(T_\ell - T_{sv})} \ , \tag{F-149}$$

where $T_\ell - T_{sv}$ is set to 1.

These models represent an approximate formulation of interfacial evaporation in the presence of noncondensables. The model can be improved through the following considerations.

1. Even in the presence of noncondensables, the evaporation process may be heat-transfer controlled. This depends on how the noncondensable gas is distributed within the gas phase and also on the amount of noncondensable gas.
2. By replacing the Sherwood number by the Nusselt number and the Schmidt number by the Prandtl number, various heat-transfer correlations can be converted to mass-transfer correlations. This way, the package can be made flow-regime-dependent instead of using Eq. (F-142) for all the flow regimes.
3. Equation (F-144) can be used directly to compute the evaporation rate. However, this approach requires a model to partition the supply of sensible heat between the phases. The lack of such a model forced us to assume that all the sensible heat is supplied by the liquid side, thus yielding the approximation in Eq. (F-149).

F.1.7.1.2. Condensation. During condensation in the presence of noncondensables, the liquid-side heat-transfer factor, H_{ALVE}, is reduced. The reduction is based upon the empirical correlation developed by Sklover and Rodivilin (Ref. F-36.). The original correlation is given by (Ref. F-36., Eq. 5) as

$$\frac{h_{\ell,nc}}{h_\ell} = 0.366 \left(\frac{G_a G_\ell}{G_s^2} \right)^{-0.2} , \qquad \text{(F-150)}$$

where $h_{l,nc}$ is the liquid-side heat-transfer coefficient in the presence of noncondensables, and G_a, G_ℓ, and G_s are the air, water, and steam mass fluxes, respectively. This is an empirical correlation obtained by measuring the condensation rates on multiple subcooled-water jets. Steam and air are injected perpendicular to the water jets. In the experiments, the liquid mass flux ranged between 3000 and 15000 kg/m^2-s. The steam mass flux ranged between 100 and 710 kg/m^2-s. The range for air mass flux was not reported.

In TRAC, condensable and noncondensable gases in the mixture flow with the same velocity. Thus, Eq. (F-150) reduces to

$$\frac{h_{\ell,nc}}{h_\ell} = 0.366 \left(\frac{\rho_s}{\rho_a} \right)^{0.2} \left(\frac{G_s}{G_\ell} \right)^{0.2} . \qquad \text{(F-151)}$$

In the code, we further assumed that the densities are additive in the gas mixture. As a result of this assumption, the steam density is calculated as

$$\rho_s = \rho_g - \rho_a \ . \tag{F-152}$$

Thus, the final correction is coded as follows:

$$0.1 \le \frac{H_{\mathrm{ALVE},nc}}{H_{\mathrm{ALVE}}} = \frac{h_{\ell,nc}}{h_\ell} = 0.366\left(\frac{\rho_g - \rho_a}{\rho_a}\right)^{0.2}\left(\frac{G_s}{G_\ell}\right)^{0.2} \le 0.1 \ , \tag{F-153}$$

where H_{ALVE} is the flow-regime-dependent heat-transfer factor as described in the previous sections. For fully stratified flow, $H_{\mathrm{ALVE},nc}/H_{\mathrm{ALVE}}$ is limited to be less than 90%. In the code, we limited the mass fluxes as

$$3000 \le G_\ell \le 18\ 000 \ \mathrm{kg/m^2\text{-}s}$$

and

$$0 \le G_s \le 640 \ \mathrm{kg/m^2\text{-}s}$$

to make the model consistent with the experimental database of Sklover and Rodivilin. A contour map for correction in the presence of noncondensables is shown in Fig. F-26.

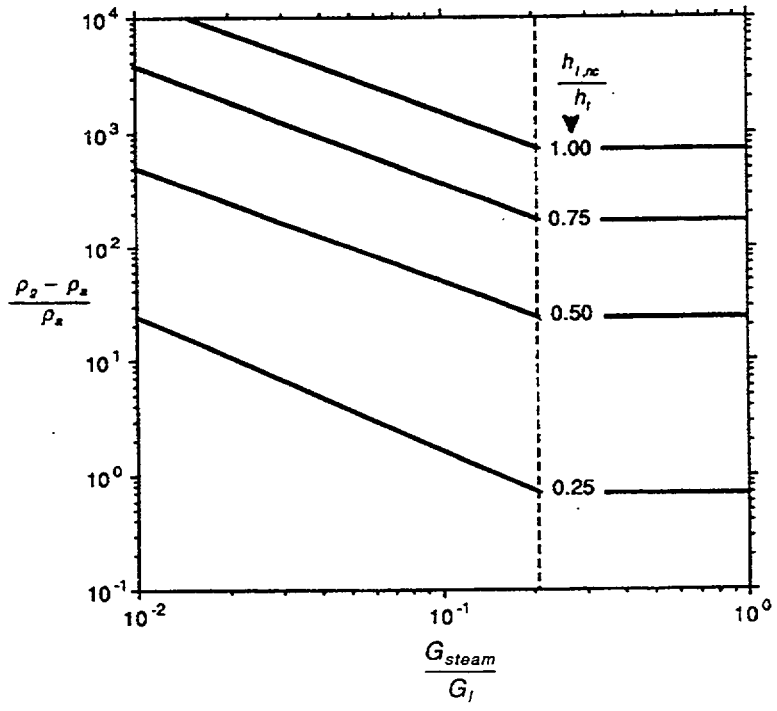

Fig. F-26. Contour map for liquid-side heat-transfer correction in the presence of noncondensables.

A major drawback of this model is that it is flow-regime-independent. Different flow situations and mixing conditions in different flow regimes may yield different models. However, the basic characteristics of the models are expected to be the same. The current model also is highly empirical. Extrapolation beyond its database will lead to questionable results.

F.1.7.2. Vapor-Side Heat Transfer. During evaporation or condensation in the presence of noncondensables, no modifications are made to the gas-to-interface heat-transfer factor, H_{CHTI}. As given by Eq. (F-1), however, the heat-transfer factor is multiplied by the relative partial pressure of steam in the energy equation. Thus, the presence of noncondensables decreases the effective vapor-side heat-transfer factor through the ratio of steam partial pressure and total partial pressure.

The sensible heat transfer between the phases becomes effective only if the partial pressure of noncondensables is non-zero. Thus, the heat-transfer factor, H_{CHTA}, is only effective in the presence of noncondensables. The models for calculating H_{CHTA} are flow-regime dependent and were described in the previous sections.

F.1.8. Magnitude Limits and New-Time/Old-Time Averaging

At the end of subroutine HTIF, the calculated closure quantities are limited due to physical and numerical computations. In the following subsections, the various limiters are described.

F.1.8.1. Limits for Subcooled Vapor. If the vapor temperature is less than the saturation temperature, the vapor-side heat-transfer factor is limited by

$$H_{\text{CHTI, map/stratified/plug/}nc} \le 10^6 \times B_{\text{cell}} \ . \qquad \text{(F-154)}$$

Then, the final value of H_{CHTI} is further modified based upon the degree of subcooling as follows:

$$H_{\text{CHTI, map/stratified/plug/}nc} = H_{\text{CHTI, map/stratified/plug/}nc} \times \exp(T_{sv} - T_g) \ , \qquad \text{(F-155)}$$

where

$$0 \le T_{sv} - T_g \le 7 \ .$$

Note that in the code, this magnitude limit is applied before the effects of liquid plugging and noncondensable gases. In these two cases, no modification is made to H_{CHTI}; thus, the calculated magnitude is final except for old-time weighting.

If the gas temperature is less than the liquid temperature, the magnitude of H_{CHTA} is similarly modified as

$$H_{\text{CHTA, map/stratified/plug/}nc} \le 10^6 \times B_{\text{cell}} \ . \qquad \text{(F-156)}$$

Then, the final value of H_{CHTA} is further modified based upon the temperature difference as follows:

$$H_{\text{CHTA, map/stratified/plug/}nc} = H_{\text{CHTA, map/stratified/plug/}nc} \times \exp(T_\ell - T_g) \ , \qquad \text{(F-157)}$$

where

$$0 \le T_\ell - T_g \le 7 \ .$$

F.1.8.2. Kinetic Theory Limits on Liquid-Side Heat Transfer. In TRAC, we limited the liquid-side heat-transfer coefficient by kinetic theory. We assumed that the condensation or evaporation rate cannot exceed the molecular flux towards the interface. Using the linearized approximation of kinetic theory, the maximum limit of $h_{i\ell}$ is coded as

$$h_{i\ell,\max} = \sqrt{\frac{M_s}{2\pi R_s}} \times \frac{\rho_g h_{fg}^2}{T_g^2} \quad \text{if } T_\ell < T_{sv} \ , \qquad \text{(F-158)}$$

where M_s is the molecular weight of water. The liquid-side heat-transfer factor during condensation or evaporation is limited as

$$0.1 B_{\text{cell}} \le H_{\text{ALVE, map/stratified/plug/}nc\text{/vertical}} \le A_i h_{i\ell,\max} \ . \qquad \text{(F-159)}$$

F.1.8.3. Old-Time/New-Time Averaging. No old-time/new-time averaging is applied if the phasic temperature crosses the saturation line, the cell was single phase at the previous time step, or the magnitudes of H_{ALV}, H_{ALVE}, H_{CHTI}, and H_{CHTA} were less than 10^{-10} at the previous time step. Otherwise different averaging techniques are applied, depending upon whether the code is run in steady-state or in transient mode.

F.1.8.3.1. Steady-State Averagers. During a steady-state run, the following simple old-time/new-time averaging technique is used

$$x^n = f \times X^n + (1-f) \times X^{n-1} \ , \qquad \text{(F-160)}$$

where the superscript n represents the new-time value and $n-1$ is the old-time value. In Eq. (F-160), X corresponds to either H_{ALV}, H_{ALVE}, H_{CHTI}, or H_{CHTA}. In the code, f is currently set equal to 0.1. Thus, the weighting heavily favors the old-time value. This means that many time-step sizes are required before reaching the steady-state value from a given initial condition. The time-wise variation of the quantity X is time-step-size dependent. For this reason, time averaging is more suitable for steady-state calculations where the time-wise variation is not as important as the final equilibrium result. By allowing slower changes of X, this kind of weighting enhances the stability of the numerical scheme.

F.1.8.3.2. Transient Limiters. During a transient run, new-time/old-time averaging given by Eq. (F-160) is not done. Instead, upper and lower bounds for the new-time value are determined based upon an old-time value through a relaxation relationship.

For the vapor-side and liquid-side heat-transfer factors, the following relaxation relationships are used during condensation and evaporation:

$$X^n_{\max} = X^{n-1} \times C_1^{C_2 \times \Delta t} \tag{F-161}$$

and

$$X^n_{\min} = X^{n-1} \times C_1^{-C_2 \times \Delta t} , \tag{F-162}$$

where C_1 and C_2 are relaxation constants. Equations (F-161) and (F-162) are applied to H_{CHTI}, H_{CHTA}, H_{ALVE}, and H_{ALV}. Table F-5. gives the various values of C_1 and C_2 used in subroutine HTIF. Figures F-27. and F-28. illustrate the allowable changes for liquid- and vapor-side heat-transfer factors, respectively.

F.1.9. Notes on the Model Implementation

In this section, some important features of the model implementation are summarized. The interfacial heat-transfer closure relationships are calculated at the cell centers. The fluid properties, pressure, temperature, and void fractions are cell-centered quantities. However, in TRAC, velocities are calculated at the cell edges. In subroutine HTIF, cell-edge velocities are occasionally used. More commonly, cell-centered velocities are used in various correlations. Here, we describe how these cell-centered quantities are obtained.

TABLE F-5.
Relaxation Constants In TRAC

Temperature	X	C_1	C_2
$T_\ell < T_{sv}$	H_{ALVE}	2	8
$T_\ell > T_{sv}$	H_{ALVE}	2	10
$T_\ell > T_{sat}$	H_{ALVE}	2	10
$T_g < T_{sv}$	H_{CHTI}	2	10
$T_g < T_{sv}$	H_{CHTA}	2	10
$T_g \geq T_{sv}$	H_{CHTI}	2	10
$T_g \geq T_{sv}$	H_{CHTA}	2	10

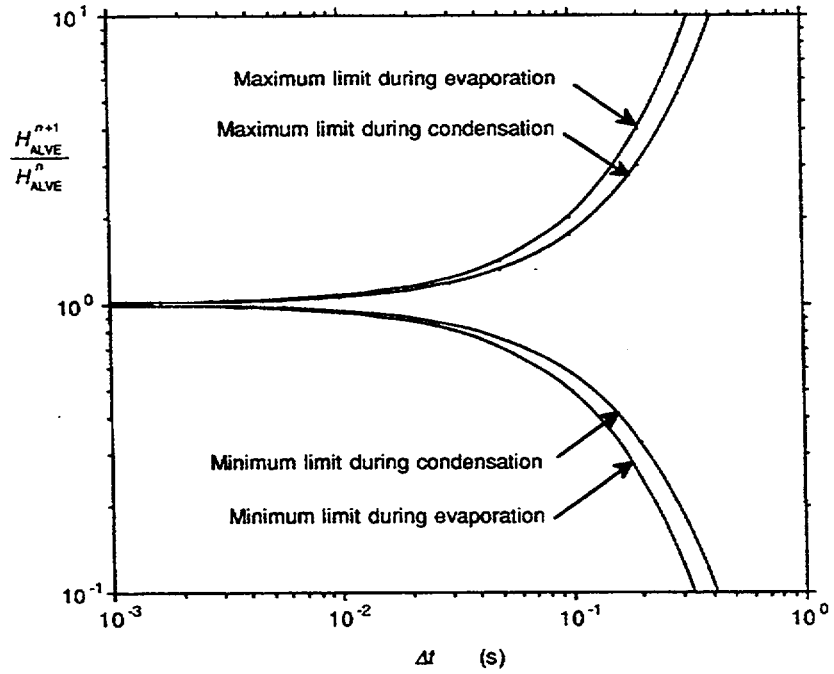

Fig. F-27. Allowable changes on H_{ALVE} within a time step during transient solution.

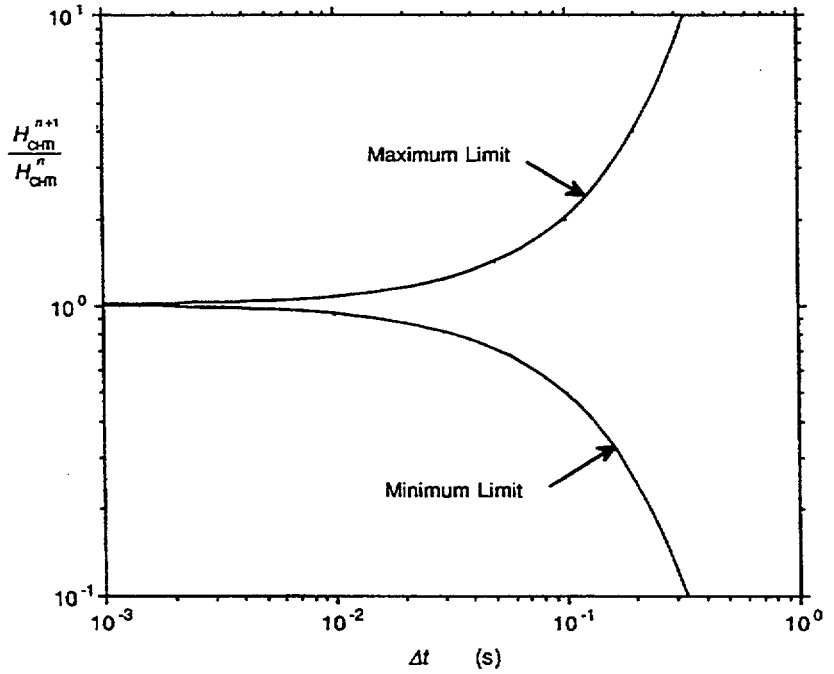

Fig. F-28. Allowable changes on H_{CHTI} within a time step during transient solution.

F.1.9.1. Hydraulic Diameter. For 1D components, the cell-averaged hydraulic diameter is obtained as

$$H_D = 2\sqrt{\frac{B_{\text{cell}}}{\pi \Delta x}} \ . \tag{F-163}$$

For 3D components, the average hydraulic diameter is set equal to the hydraulic diameter in the axial direction. However, if the hydraulic diameter in the axial direction is less than 0.01 mm, then the maximum of the hydraulic diameters in the radial and azimuthal directions is used as the average hydraulic diameter. If the result is still less than 0.01 mm, a volume-averaged diameter is defined as

$$H_D = \frac{2B_{\text{cell}}}{\Delta z(\Delta r + r\Delta\theta)} \ . \tag{F-164}$$

The average hydraulic diameter for a 3D VESSEL cell is computed in subroutine CELLA3. In subroutine HTIF, the average hydraulic diameter in a cell of the 3D VESSEL component is not allowed to be greater than 10 cm.

In all models that require a hydraulic diameter, these average hydraulic diameters are used.

F.1.9.2. Velocities and Mass Fluxes. For 1D components, cell-centered velocities are calculated in subroutine VOLV as

$$(V_\ell)_j = \frac{\left[\rho_\ell(1-\alpha)V_\ell A_f\right]_{j-1/2} + \left[\rho_\ell(1-\alpha)V_\ell A_f\right]_{j+1/2}}{\left[2\rho_\ell(1-\alpha)B_{\text{cell}} / \Delta x\right]_j} \tag{F-165}$$

and

$$(V_g)_j = \frac{\left[\rho_g \alpha V_g A_f\right]_{j-1/2} + \left[\rho_g \alpha V_g A_f\right]_{j+1/2}}{\left[2\rho_g \alpha B_{\text{cell}} / \Delta x\right]_j} \ , \tag{F-166}$$

where the counters $j+1/2$ and $j-1/2$ represent cell-edge quantities, while j represents the cell-centered vector velocity. In subroutine HTIF, the lower limit for the liquid and vapor cell-centered velocities are set to 0.001 and 0.01 m/s, respectively. In the same subroutine, however, the relative velocity is computed as an arithmetic average of the cell-edge relative velocities as

$$(V_r)_j = \frac{1}{2}\left[\ \left|(V_g - V_\ell)_{j-1/2}\right| + \left|(V_g - V_\ell)_{j+1/2}\right|\ \right] \ . \tag{F-167}$$

In subroutine HTIF, this cell-centered relative velocity is not allowed to be less than 0.01 m/s.

The average mass flux for a 1D cell is calculated in subroutine HTIF as

$$G = (1-\alpha)\rho_\ell (V_\ell)_j + \alpha \rho_g (V_g)_j \ . \tag{F-168}$$

For 3D components, the definition of cell-centered velocities is slightly more complicated. They are computed in subroutine CELLA3. For the gas phase, the axial average velocity is calculated as

$$(V_g)_k = \left[\frac{1}{2}\left(\frac{B_{\text{cell},i,j,k}}{\Delta z_{i,j,k}} + \frac{B_{\text{cell},i,j,k+1}}{\Delta z_{i,j,k+1}}\right)\right] V_{g,k+1/2} \ . \tag{F-169}$$

The term in brackets is set to 1 if it is less than 10^{-5}. The azimuthal and radial velocities are computed as

$$\left(V_g\right)_i = \frac{1}{2}\left(V_{g,i+1/2} + V_{g,i-1/2}\right) \tag{F-170}$$

and

$$\left(V_g\right)_j = \frac{1}{2}\left(V_{g,j+1/2} + V_{g,j-1/2}\right) \ . \tag{F-171}$$

Then, the cell-averaged vector velocity is calculated as

$$\left(V_g\right)_{i,j,k} = \sqrt{\left(V_g\right)_i^2 + \left(V_g\right)_j^2 + \left(V_g\right)_k^2} \ . \tag{F-172}$$

In subroutine HTIF, this velocity is limited to be greater than or equal to 0.01 m/s.

For the liquid cell-averaged vector velocity, the same procedure is applied. Subroutine HTIF limits the liquid cell-averaged velocity to be greater than or equal to 0.001 m/s. The cell-centered relative velocity is also calculated in subroutine CELLA3 as

$$(V_r)_{i,j,k} = \sqrt{\left[\left(V_g\right)_i - (V_\ell)_i\right]^2 + \left[\left(V_g\right)_j - (V_\ell)_j\right]^2 + \left[\left(V_g\right)_k - (V_\ell)_k\right]^2} \ , \tag{F-173}$$

and it is limited at the lower end by 0.01 m/s in subroutine HTIF.

Finally, the cell-averaged mass flux is computed in subroutine CELLA3 as

$$G = (1-\alpha)\rho_\ell (V_\ell)_{i,j,k} + \alpha\rho_\ell (V_g)_{i,j,k} \quad . \tag{F-174}$$

In subroutine HTIF, everywhere an average mass flux is needed, the quantities described above are used for 1D and 3D components. The cell-centered velocities are used in most correlations. However, cell-edge velocities are also used occasionally. Cell-edge velocities are used in the entrainment fraction correlation Eq. (F-58)] and in defining the stratified- and plug-flow Stanton numbers [Eqs. (F-94) and (F-101)].

F.1.10. Summary, Conclusions, and Discussion

Section F.1. outlines the constitutive relationships used within TRAC to calculate the interfacial heat-transfer rates. These constitutive relationships are strongly influenced by the flow-regime map and by the phase velocities, and, in turn, predicting these quantities is strongly influenced by the heat-transfer rates. Therefore, success in predicting the interfacial heat-transfer rates is dependent upon how well the flow-regime and the phase velocities are predicted and vice versa. TRAC's interfacial heat-transfer package contains many models. The rest of this section provides a critical general discussion of the interfacial heat-transfer models used in TRAC.

The estimation of the direct-contact condensation rates is an integral part of reactor safety analysis and is a difficult task for the following reasons.

1. In almost all situations, direct-contact condensation in LWR analysis arises during transient accident scenarios. The sources of these transients may differ, but they can be catalogued into the following four basic groups.
    a. In the simplest possible case, the transient remains independent of the condensation process. For instance, during a blowdown-dominated LOCA, direct-contact condensation generally occurs where the pressure, and therefore the saturation temperature, is decreasing as a function of time. This situation arises because the depressurization caused by very localized condensation, if it occurs, is small when compared with the global depressurization.
    b. In certain cases, direct-contact condensation is purely a transient relaxation problem, in which the ambient or global parameters remain constant. These are problems in which one of the phases exists in a limited quantity, such as vapor bubbles in subcooled liquids and subcooled-liquid droplets in saturated vapor. In these types of problems, the steady state is defined by the thermal equilibrium, and heat-transfer and condensation rates converge to zero as the bubble or drop approaches the steady state.

c. Often, the ambient or global parameters are affected by the condensation process itself and a condensation-induced transient may result. Typically, these are the problems in which the condensation causes a rapid change in the specific volume of the vapor. For instance, if the vapor supply is not large enough to replace the condensed vapor, then the condensation is accompanied by a sudden depressurization that decreases the saturation temperature and subsequently causes the condensation to cease. An added level of complexity can occur if the system can resupply the vapor phase and repressurize the region, allowing the cycle to repeat. Such problems are of an oscillatory nature and can be characterized as steam chugging and liquid plugging.
d. Many practical problems require an analysis based on the combination of the above elementary cases.

2. Another difficulty in estimating the direct-contact heat-transfer in reactor safety analysis arises from the fact that condensation or evaporation may occur under a variety of steam/liquid contact configurations. Each configuration may promote different heat-transfer mechanisms: conduction limited, laminar/turbulent-convection limited, mass-transport limited, or combinations of these. Condensation on very thin liquid films or on small droplets, for instance, is likely to be conduction-driven because the liquid motion is too small to enhance convection. On the other hand, condensation on liquid jets and on thick liquid films during cocurrent or countercurrent flow must be modeled using an appropriate convective mechanism. In the early stages of direct-contact condensation, before thermal-boundary-layer development, the heat-diffusion equation yields high condensation rates, which may exceed steam-supply rates. In these cases, the condensation process becomes steam-supply-limited and must be modeled accordingly. Steam-supply-limited condensation becomes particularly important in the presence of noncondensables in the steam environment. These mechanisms result in different condensation rates. Furthermore, each configuration may have different transient response times (relaxation times) and the severity of the induced transients will vary. The steam/liquid contact configurations of principal interest here and the physical situations in which they may occur are as follows:

   a. subcooled-liquid droplets in saturated (or superheated) steam environment (hot- or cold-leg ECC injection, pressurizer spray, upper-head spray);
   b. saturated (or superheated) steam bubble in subcooled liquid (subcooled boiling, CCFL with low vapor-generation rate in core);
   c. saturated (or superheated) steam jet into subcooled-liquid pool (CCFL with high vapor-generation rate in the core);

d. subcooled-liquid jet injected into saturated (or superheated) steam flow (hot- or cold-leg ECC injection);
e. stratified or plugged steam/liquid flows in direct contact (ECC injection), which may include (*i*) slowly moving cocurrent or countercurrent liquid and vapor flow (insufficient drag to cause wave breakup) and (*ii*) cocurrent or countercurrent liquid-vapor flow with sufficient phasic motion to cause interfacial wave instability resulting periodically in extremely high condensation rates; and
f. slowly moving liquid pool in contact with slowly moving steam atmosphere (pressurizer, upper plenum with CCFL).

These configurations are not always independent of each other. In many cases, a few of them coexist and/or one is followed by another. An example is the injection of an ECC liquid into steam flowing in the hot or cold legs. The liquid jet may result in droplets and either countercurrent or cocurrent steam/liquid flow. The prediction of the condensation rates under all these various transients and the various contact configurations requires a wide variety of correlations.

Interfacial heat and mass transfer is an active area of research in two-phase flow and heat transfer. Our understanding of these phenomena continues to grow as we answer more of the above questions. Therefore, it is only natural that the constitutive relationships of TRAC and other similar codes will continue to be improved along with the evolvement of the pertinent literature. Currently, we believe that our interfacial heat-transfer constitutive packages represent a good cross section of the state-of-the-art in this area. Of course, this comment only applies to those studies that can be directly used within a best-estimate code, such as TRAC. We would like to acknowledge that there are various detailed studies of interfacial heat-transfer phenomena that we could not implement into the code. The overwhelming numbers of studies dealing with single droplets or single bubbles are examples of such. Even though these analytical and empirical studies are very useful in understanding the phenomena involved, their results can not be directly implemented into an integral code, such as TRAC. We have to remember that even today's computers are not powerful enough to track down every single bubble or droplet in the flow field. Thus, we need more research in terms of obtaining statistical data that represent an averaged behavior of droplet and bubble fields, etc.

After reading Section F.1., the reader must be aware that we still have a number of simple models in the code. These are commonly constant-Stanton-number or constant-heat-transfer-coefficient models. The following are two reasons for having these in the code: (1) Sometimes it is not possible to find an appropriate model for a specific closure relationship in the open literature. One such example is the heat transfer during the liquid plugging phenomenon. In these cases, we produced our own model based upon our engineering judgment; and (2) Occasionally, we preferred using a simple model instead of a more complicated, literature-based model because we thought that the simpler relation was appropriate for the purpose of a best-estimate code. In doing that, we were motivated by the fact that the computation time is somewhat related to the complexity of the closure relationships, and one purpose of a best-estimate code is to

provide a faster running time. Also, the quasi-steady nature of the solution scheme forces us to make sure that the closure relationship does not show a strong dependence on local instantaneous changes. Because most models available in the literature are steady-state models, they can result in unrealistically rapid changes in the phenomenon when applied to transient analysis. Consequently, this can have a destabilizing effect on the code's numerics. We tried to rectify this problem by using averagers and limiters as discussed in Appendix D. We must note that our current approximate models can easily be replaced by others if the phenomenon under analysis requires more elaborate models. The modular nature of the code makes such replacements easy.

Our models and correlations have shortcomings similar to those of other models and correlations in the literature. Limitations exist on available information in the following areas:

1. Almost all available separate-effects data are obtained from small-scale experiments. Quite often, it is uncertain whether the results of such experiments can be extrapolated to full-plant analysis.
2. Most interfacial heat-transfer data are obtained at or near atmospheric pressure. The extension of the results to the higher pressures that are of interest to PWRs must be done with caution.
3. Almost all the available data in the literature come from steady-state or quasi-steady experiments. We do not have transient models and we lack the necessary information on relaxation time constants. The applicability of such data to transient conditions using a quasi-steady approach is currently an active area of research in the two-phase-flow community.
4. Additional flow regimes and flow-pattern-transition studies directly applicable to nuclear reactor steady-state and transient operating conditions are needed. Further discussion of the limitations of the state of the art in this area is provided in Appendix E, Section E.3.

Despite all these limitations, the interfacial heat-transfer package in TRAC-PF1/MOD2 (and TRAC-M) is considerably improved over that of MOD1. The MOD2 and TRAC-M codes have been able to accurately analyze both the small-scale Akimoto condensation tests and the full-scale UPTF tests. [See the TRAC-M/F77 Developmental Assessment Manual (Refs. F-99. and F-100.).] In addition to adding many new models and correlations, we made conceptual improvements in the following important areas:

1. 1D and 3D constitutive models and correlations are made identical. Differences in these models between 1D and 3D algorithms were an area of criticism in the MOD1 code.
2. Interfacial-shear and heat-transfer packages are made consistent and compatible.

3. In the presence of noncondensables, flashing and evaporation phenomena are recognized as qualitatively and quantitatively different and are implemented separately. Currently we are using simple but separate models for these phenomena. Evaporation is modeled as being mass-transfer controlled through a basic correlation. This is one area where the code will possibly continue to improve as the effect of noncondensables in various flow patterns becomes better understood.

So far we have discussed the heat-transfer aspects of the interfacial heat-transfer phenomenon. Equally important, not only for heat transfer but also for interfacial-shear computation, is the modeling of the interfacial area. We have made improvements in these models as well, but we are again limited by the information available in the open literature.

Predicting interfacial area during reactor safety analysis is a major thrust of research in two-phase flow. As pointed out by Ishii and Mishima (Ref. F-1.), the prediction of this quantity for transients or not fully developed flow situations is beyond the current state of the art. We fully agree with Ishii and Mishima that the most general prediction method for this problem would be to introduce transport equations into the two-fluid formulation for interfacial-area concentration. Currently, we do not have these transport equations in TRAC-M. As a reason for not having this viable mechanistic tool, we would like to cite the following paragraph from Ishii and Mishima (Ref. F-1., p. 5):

> *So far, almost no analyses have been made in this direction. Furthermore, basic experimental data needed to develop this surface-area transport equation are grossly inadequate. In view of fundamental difficulties encountered in modeling entrance and transient flow regimes under reactor-accident conditions, considerable efforts should be made to develop an acceptable data base in this area.*

Currently, in TRAC-PF1/MOD2 and TRAC-M, we have interfacial-area models that are based mostly upon steady-state and fully developed flow data. These models are obviously only valid if the quasi-steady and local equilibrium assumptions are not violated. Even these data are very limited, not only in their parametric range but also in the flow patterns that are studied. Almost all pertinent data are aimed at dispersed-phase flow, such as droplet flow or bubbly flow. Again, almost all the data are obtained from adiabatic air-water experiments, at or near atmospheric pressure, in flow channels long enough to satisfy the fully developed and quasi-steady assumptions.

Studies abound, however, where interfacial-area concentrations are measured for a variety of flow patterns for vertical upflow using chemical-absorption techniques. An extensive list of such studies is provided by Ishii and Mishima (Ref. F-1., Table 2). We tried to analyze these data using TRAC constitutive packages. We could only do independent assessments of the interfacial-area data if the void fraction in the channel was reported along with interfacial-area data. The studies of Shilimkan and Stepanek

(Ref. F-37.), Kasturi and Stepanek (Ref. F-38.), and DeJesus and Kawaji (Ref. F-39.) met this requirement.

In all three studies, the authors used a chemical-absorption technique where carbon dioxide from air was absorbed into sodium-hydroxide solutions with different concentrations. The experiments were very similar as they all dealt with upflow in a long vertical tube. The tube diameters were different in different experiments. DeJesus and Kawaji used a 2.54-cm-i.d. tube whereas Kasturi and Stepanek used a 0.6-cm-i.d. tube. Shilimkan and Stepanek used three different 1-, 1.5-, and 2-cm-i.d. tubes. The interfacial-area concentration and void-fraction data were reported as a function of liquid and gas volumetric fluxes. The ranges of these parameters were similar in all the experiments. DeJesus and Kawaji were able to extend their experiments to higher liquid flow rates and lower void fractions. Unfortunately, a clear trend applicable to all the data could not be observed. We would like to report some examples from this assessment analysis. Figure F-29. shows the results of our assessment with all the data of DeJesus and Kawaji. As shown, there is considerable discrepancy. In Fig. F-30., we report the assessment for a given liquid flow rate and for various void fractions. As shown, the code overpredicts the data at low void fractions (bubbly slug flow), whereas the data are underpredicted at high void fractions (annular-mist flow). This figure also shows the maximum interfacial-area concentration predicted by the code (by assuming all the liquid to be entrained in the annular-mist flow). The data are still overpredicted by this curve. This means that the code is underpredicting the entrainment fraction, provided the droplet diameters are predicted accurately. Our droplet-diameter model and the entrainment fraction model, however, agree fairly well with air-water data, as discussed in Section F.1.2.3.

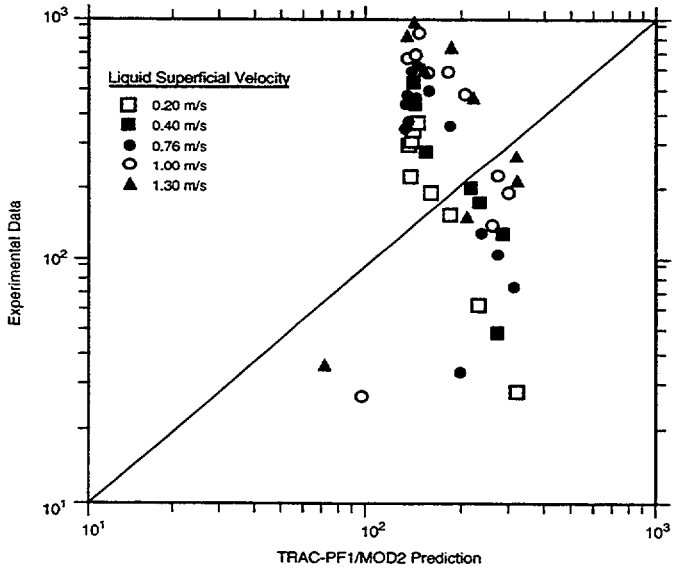

Fig. F-29. TRAC-calculated interfacial-area concentration in comparison with the data of DeJesus and Kawaji (Ref. F-39.).

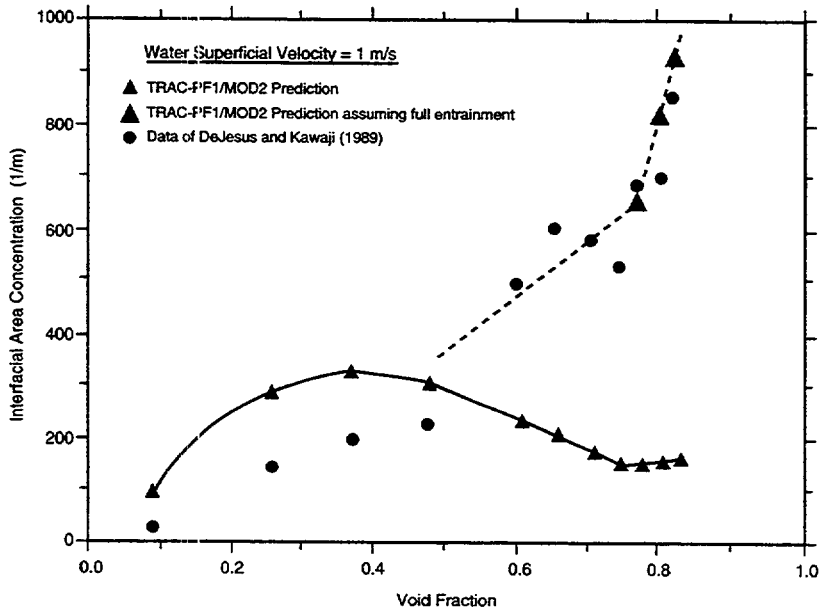

Fig. F-30. Comparison of TRAC results with the data of DeJesus and Kawaji (Ref. F-39.) for $J_l = 1$ m/s.

Similarly, we were surprised that the code overpredicted by so much the bubbly slug interfacial-area data. We decided to back-calculate a Sauter mean diameter from the low-void-fraction data of DeJesus and Kawaji. The calculated results are shown in Fig. F-31. In this figure, the bubbly flow, the slug-flow, or the churn-flow classification is made according to the authors' flow-regime map. All data are for void fractions less than 50% and are treated as bubbly slug flow in the code. As shown, the Sauter mean diameters for their bubbly flow data are quite large and comparable to the pipe size.

This seems to suggest that their experimental setup does not allow a breakup mechanism into dispersed bubbles at these flow rates. The comparison with the data of Kasturi and Stepanek and Shilimkan and Stepanek is not repeated here but exhibited similar patterns during assessment.

Apparently, the available interfacial-area data are not directly applicable for reactor safety analysis, which is the aim of our models. Besides the fact that the chemical-absorption technique has its inherent uncertainties, there may be various reasons why these data exhibit this unexpected behavior.

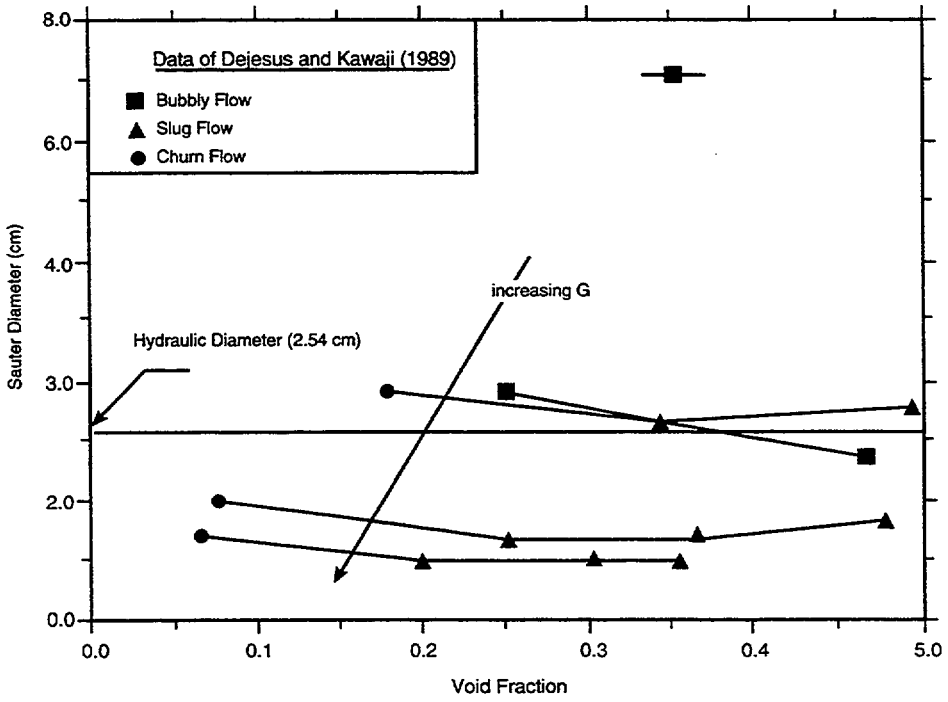

Fig. F-31. Sauter mean diameters for the low-void data of DeJesus and Kawaji (Ref. F-39.).

1. We used air-water properties for this assessment. The properties of CO_2-air and NaOH-water mixtures, however, can be considerably different depending upon concentrations. Thus, there may be a property effect on our existing models. However, if such property effects are indeed this strong, then the experiments do not meet the condition of local equilibrium because the concentration and the properties change along the flow channel as the CO_2 is continuously being absorbed by NaOH.
2. As discussed by Hewitt (Ref. F-40.), the presence of surface-active contaminants can considerably affect the flow patterns. The presence of CO_2 and NaOH may well result in a totally different flow-pattern behavior, such as froth instead of bubbles and slugs, etc.

As a closure, we would like to point out that for developing more accurate models for reactor-safety analysis, interfacial-area data under a variety of conditions are most needed. Currently, the data obtained from chemical-absorption techniques do not seem to fill this gap. Alternatives, such as three-point probe data, must be investigated.

F.2. Wall-to-Fluid Heat Transfer

The wall-to-fluid HTCs are obtained from a heat-transfer-surface model constructed within subroutines HTCOR and HTVSSL. [The terms heat-transfer surface (Ref. F-41.) and boiling surface are used interchangeably in this discussion.] The HTCs in HTCOR are used by all TRAC components under all conditions except for HTSTR components when the core reflood model is active. Subroutine HTVSSL incorporates a model to determine HTCs in the post-CHF region for a HTSTR component that undergoes reflood. (To use HTVSSL, the core reflood model must be activated by the user through an input option.) This section, therefore, is divided into two separate subsections after the introduction. The first section describes HTCs used in subroutine HTCOR, while the second one discusses HTCs used in subroutine HTVSSL.

The boiling surface requires clarification because its use in the past has led to some confusion. The local-conditions hypothesis and the history effect in correlation development are discussed first, independent of the heat-transfer-surface approach. The heat-transfer-surface approach is then reviewed. This approach is independent of the method chosen by the correlation developer.

The Local-Conditions Hypothesis and History Effects in Correlation Development. A principal problem in understanding the boiling surface is that frequently it is confused with the local-conditions hypothesis. In fact, the boiling surface is independent of the local-conditions assumption. The local-conditions assumption implies that the wall heat flux, or HTC, at a given location can be written as a function of the conditions at the same location. This can be expressed in a functional relationship,

$$q_{\text{total}} = f(T_w, D_H, \alpha, P, T_g, T_\ell, V_g, V_\ell) \ , \tag{F-175}$$

which represents any heat-transfer correlation or family of correlations in a two-fluid code, such as TRAC-PF1/MOD1 (Ref. F-42.). This heat flux represents a surface-area-time-averaged quantity resulting from the volume-time-averaged energy equation given in Appendix D by Eq. (D-6). This expression becomes simpler for the case of a homogeneous equilibrium code such as RELAP4 (Ref. F-43.) and is given by

$$q_{\text{total}} = f(T_w, D_H, x_e, P, G) \ . \tag{F-176}$$

Note that the equilibrium quality is defined on an energy basis and, therefore, includes the fluid temperatures for subcooled liquid or superheated vapor. For either of these two cases, the hydraulic parameters, such as α, P, T_g, T_l, V_g, and V_l, for the nonhomogeneous-nonequilibrium case, or x_e, P, and G for the homogeneous-equilibrium case, are values taken at the location at which the heat flux is to be evaluated, i.e., local conditions.

Within the strict definition of the local-conditions assumption, additional fields introduced into the hydraulic model introduce the additional local quantities required to describe the influence of the new fields upon the heat flux. For a code with N fields,

[3×(N−1)+5] independent variables (the same pressure is assumed in all fields) could be used in an expression similar to that given by Eq. (F-175). The above representations have been written as functions of only the local instantaneous hydraulic parameters. However, nothing precludes the inclusion of local rate-of-change terms with respect to either temporal or spatial quantities in the formulation. These terms still fit within the local-conditions hypothesis. For example, the post-CHF dispersed-flow film-boiling regime might include the term dT_g/dz for the nonhomogeneous-nonequilibrium model, so that Eq. (F-175) would be written

$$q_{\text{total}} = f(T_w, D_H, \alpha, P, T_g, dT_g/dz, T_\ell, V_g, V_\ell) \ .$$

The problem with the local-condition hypothesis is that regimes have been found in which its application yields questionable results. The post-CHF and high-void, nonuniform axial-power-profile CHF cases are two such regimes. Thus, history effects sometimes are included to model these regimes more accurately. For the post-CHF regime, the axial position downstream of the CHF point, z_{CHF}, sometimes is included in Eq. (F-175) and produces

$$q_{\text{total}} = f(T_w, D_H, \alpha, P, T_g, T_\ell, V_g, V_\ell, z_{\text{CHF}}) \ . \qquad \text{(F-177)}$$

The high-void nonuniform axial-power-profile CHF case frequently is modeled using a boiling-length correlation. This type of correlation predicts the quality at which CHF occurs, and can be written in functional form as

$$x_{e,\text{CHF}} = f(D_H, P, G, L_b) \ , \qquad \text{(F-178)}$$

where L_b is the length over which saturated boiling takes place.

Computer codes such as TRAC-PF1/MOD1 (Ref. F-42.) historically have avoided the use of the history effect because it requires knowledge of the spatial position at which some event occurs (either the CHF location or the beginning of boiling, respectively, for the two examples mentioned here) to evaluate the heat flux or CHF downstream of the event. The determination and tracking of these locations are difficult and, for PWR applications, frequently poorly defined. One example is the situation in which fluid is flowing into the core through the entrance and the exit simultaneously and, therefore, is producing two different CHF locations in the core. The question becomes, which CHF location is used to calculate the post-CHF heat flux? Similarly, the history-effect correlations for CHF cannot model flow reversals. These correlations assume increasing quality or void fraction along the flow direction. The opposite is seen to be the case in many situations. Although it is possible to address these types of problems in some fashion, the difficulties encountered in addressing them in a general manner have led to an almost exclusive use of local-condition correlations within the codes.

The Heat-Transfer-Surface or Boiling-Surface Approach. To this point nothing has been said about the boiling-surface approach. The discussion has involved only the local-conditions hypothesis, the inclusion of the history effect within the formulation of the heat flux or CHF phenomenon, and comments concerning their potential implementation into the codes.

The term heat-transfer surface or boiling surface arose from some simple observations and in no way influences nor limits any of the previous considerations. To investigate these observations, we will step through a series of thought experiments. Consider first pool boiling for a fixed geometry (a thin horizontal wire within a large pool), pressure, and subcooling where a unique boiling curve exists. Pool-boiling curves for a number of fluid conditions can be collected and can be expressed functionally as

$$q_{\text{total}} = f(T_w, D_H, P, T_\ell) . \tag{F-179}$$

Note that the boiling curve (Ref. F-44.) was first defined as a plot of heat flux versus either wall temperature or wall superheat (wall superheat is obtained by subtracting the saturation temperature from the wall temperature). Typically, the boiling curve is assumed to have single-phase-convection, nucleate-boiling, transition-boiling, and film-boiling regimes. The curves are found either by starting from low power and increasing power to generate the boiling curve or by feedback control of power based upon a desired wall temperature. For the power-controlled experiment, the transition-boiling regime is unstable and historically gave rise to the temperature-control-feedback experiments. The boiling curve is generated by varying only one variable, the power, and assumes the fluid-reservoir size is large enough to maintain a constant fluid temperature during the experiment. Each experimental run varies one of the fluid parameters and yields a single unique boiling curve. Thus, the experiment itself provides proper separation of variables.

Using the family of boiling curves represented by Eq. (F-179), the wall response for any given quasi-steady transient can be analyzed. Considering a pressure-power transient, and plotting heat flux as a function of wall superheat and pressure (a 3D plot), the path across this 3D surface could be traced during the transient. Each constant pressure plane in the 3D surface is the boiling curve obtained experimentally at that pressure.

As an example, consider an experiment with decaying pressure, increasing surface temperature, and fixed fluid temperature for a horizontal wire. The initial conditions for the pressure and wall temperature are 6.9 MPa and the saturation temperature, respectively. This experiment produces an apparent boiling curve across the above 3D plot. This boiling curve is called *apparent* because two of the independent parameters (power and pressure) in Eq. (F-179) are changing as a function of time. This apparent boiling curve has single-phase-convection, nucleate-boiling, transition-boiling, and film-boiling regimes caused by the fact that CHF will be exceeded as the pressure decreases and the power is increased. (Note that CHF becomes a decreasing function of pressure below approximately 6.9 MPa.)

The heat flux in this experiment is affected by two factors that can be represented more clearly by denoting the heat-flux rate of change as obtained from Eq. (F-179) as

$$\frac{dq}{dt} = \frac{\partial q}{\partial T_w}\frac{dT_w}{dt} + \frac{\partial q}{\partial P}\frac{dP}{dt} , \tag{F-180}$$

where the "total" subscript is dropped for convenience. Thus, the change in heat flux at any time t during the transient can be found from

$$\Delta q(\tau) = q(\tau) - q(\tau - \Delta t) = \int_{\tau-\frac{\Delta t}{2}}^{\tau+\frac{\Delta t}{2}} (dq/dt)dt , \tag{F-181}$$

where Δt is some small time period larger than the time constant of the boiling process, but smaller than the time required for the quasi-steady transient to have changed its state. (See the discussion of the time-averaging operator in Appendix D.) Substitution of Eq. (F-180) into Eq. (F-181) yields

$$\Delta q(\tau) = \int_{\tau-\frac{\Delta t}{2}}^{\tau+\frac{\Delta t}{2}} (\partial q/\partial T_w)(dT_w/dt)dt + \int_{\tau-\frac{\Delta t}{2}}^{\tau+\frac{\Delta t}{2}} (\partial q/\partial P)(dP/dt)dt . \tag{F-182}$$

The change in heat flux at any time comprises two parts. One is caused by the wall temperature change over the time period Δt, and the other is caused by the pressure change over the same period. The apparent boiling curve obtained by plotting $q(\tau)$ versus $T_w(\tau)$ for different times τ over the transient includes not only the effect of changing wall temperature but also the effect of changing pressure. Equation (F-182) can be generalized further to include a change in the fluid temperature because of a finite liquid volume (for this consideration, $T_\ell < T_{sat}$ is required) by including the term

$$\int_{\tau-\frac{\Delta t}{2}}^{\tau+\frac{\Delta t}{2}} (\partial q/\partial T_\ell)(dt_\ell/dt)dt .$$

Two rather obvious results are now clear. One is that the boiling curves inherent within Eq. (F-179) are not the same as the apparent boiling curves that arise from a quasi-steady transient. This difference can be amplified further by noting that the slope of the boiling curve, as it has been defined correctly for a simple pool-boiling experiment, is $\partial q/\partial T_w$. The slope of an apparent boiling curve, however, can be obtained from Eq. (F-180) by dividing by dT_w/dt so that

$$\frac{dq}{dT_w} = \frac{\partial q}{\partial T_w} + \frac{\frac{\partial q}{\partial P}\frac{dP}{dt}}{\frac{dT_w}{dt}} . \tag{F-183}$$

The slope of this apparent boiling curve is a combination of the original boiling curve plus an effect introduced by the transient itself.

These observations can be extended in steps to consider forced convection. First, extend the preceding thought-experiment to allow flow across the wire. Again, a unique boiling curve is obtained as the wall temperature is increased while all the other parameters are held constant. In this case, Eq. (F-179) now has the velocity of the subcooled fluid as one of the independent variables, and is given by

$$q_{\text{total}} = f(T_w, D_H, P, T_\ell, V_\ell) \ . \tag{F-184}$$

Arguments similar to those made for the pool-boiling case now can be made for this experiment and for the analysis of any quasi-steady transient. Again, proper separation of the variables is inherent within the experiment.

Next, the flow conditions can be changed to include two-phase flow. Again, boiling curves can be generated by increasing the power or wall temperature. In this case, however, the single-phase-convection portion of the boiling curve will be missing. For this case, Eq. (F-175) would represent the boiling curves obtained and, again, the same arguments may be repeated.

In all the experiments considered so far, the fluid volumes have been large enough so that the fluid properties do not change because of any heat addition. Thus, the fluid variables represent volume-averaged quantities. For example, the liquid temperature, either in Eq. (F-175)for the pool-boiling experiment or in Eq. (F-184) for the single-phase forced-convection experiment, represents the volume-averaged fluid temperature. For the forced-convection experiment, the inlet-flow temperature is equal to the volume-averaged fluid temperature because the fluid volume is large. Each experiment yields a true boiling curve, that is, one with a slope of $\partial q/\partial T_w$.

There are experiments, however, that will not yield true boiling curves and from which the experimentalist and/or correlation developer must extract the functional relationship by proper separation of the variables to obtain such expressions as Eq. (F-175). Consider the case of single-phase subcooled liquid flowing into a heated vertical tube and try to generate a boiling curve for this experiment by varying the power, as was done in the preceding experiments. For this case, the fluid variables in Eq. (F-175) are the local fluid properties at a fixed axial level of the tube (local-conditions hypothesis). Along the tube, the void fraction as well as phasic velocities and temperatures change at each level as the power is increased. No point exists on the tube from which one can plot directly a true boiling curve because the wall temperature and the fluid variables are changing as the power is increased. Therefore the plotting of heat flux versus wall temperature produces an apparent boiling curve that has a slope represented by dq/dT_w, not $\partial q/\partial T_w$.

From these thought experiments, it is obvious that cases exist in which the true boiling curve becomes a mathematical abstraction rather than a curve with physical significance, as in pool boiling, for which the boiling-curve concept was defined originally. The approach used to reach this conclusion has been called the heat-transfer-surface approach or boiling-surface approach because it uses the simple mathematics of functions with N dimensions.

The heat-transfer-surface approach in no way changes work done in the past to develop correlations, as long as the correlation developer used proper techniques to ensure valid separation of variables. It is important to realize that proper separation has not been done in all correlations in the literature. Possibly the most painful example of this problem arises within the definition of the minimum film-boiling temperature, T_{min}. This point is discussed below.

Correlations may be based upon the local-conditions approach or may include the history effect. The heat-transfer-surface approach requires only the addition of as many parameters as the correlation developer feels necessary to represent accurately the history effect. Thus, the trivial point can be made that the true boiling curve obtained from the above experiment with flow up the tube, using z_{CHF} to model the history effect, would be denoted by

$$\left.\frac{\partial q}{\partial T_w}\right|_{D_H,\, \alpha,\, P,\, T_g,\, T_b,\, V_b,\, V_g,\, z_{CHF}\, =\, \text{constant}}$$

The boiling-surface approach does place a strict mathematical definition upon the boiling curve; that is, it is the relationship whose characteristic slope with respect to wall temperature is given by $\partial q/\partial T_w$. For this reason, the adjectives *true* and *apparent* have been used to describe the types of boiling curves possible. The true boiling curve has been differentiated from the apparent boiling curve that is dependent upon the experiment or transient under consideration. This strict definition of the true boiling curve must be applied to ensure a unique mathematical definition of the boiling curve. Failure to satisfy this requirement is the same as saying that proper separation of different effects (variables) is unimportant, and makes application of any correlation developed with this lack of understanding highly questionable for different transients. There is no question but that this point is the most important of all the results from the heat-transfer-surface approach.

One other point is worthy of note. Frequently, 3D plots have been used to represent a boiling surface. Again, it appears that this use has created confusion. As with the boiling curve, there are situations in which the 3D surface has physical meaning and others in which its representation is totally abstract. In the first, simple, pool-boiling experiment, the surface had physical meaning, and movement across the surface could be used to represent what happened in the quasi-steady transient and to obtain the corresponding apparent boiling curve. In the case of forced flow up the tube, the 3D surface would be abstract.

One problem inherent in our 4D world (three spatial coordinates and time) is how to represent something that is dependent upon four or more independent variables. A quantity dependent upon three independent variables can be represented by plotting the quantity itself on the z-axis and using the x-axis, y-axis, and time to represent the three independent variables, that is, make a movie using time to represent one of the independent variables. The appearance, however, of a fourth independent variable creates a problem. One of the variables must remain constant and its effect studied parametrically, or two of the independent variables must vary together in some prescribed manner.

What has been done most frequently in the boiling-surface approach is to designate wall superheat as the y-axis independent variable with heat flux, the dependent quantity, represented on the z-axis. This designation is a natural choice because, historically, everyone thinks in terms of boiling curves. It must be remembered that some of these boiling curves are mathematical, not physical. The variable that frequently has been chosen as the x-axis is either void fraction or quality, depending upon the particular formulation in use, for example Eqs. (F-175) and (F-176). This choice of independent variables yields a right-hand coordinate system that shows the boiling curves progressing from near-single-phase liquid for x-axis $= 0^+$ to near single-phase vapor at x-axis $= 1^-$. [The term *near single phase* is used because once single-phase conditions exist, boiling curves that are defined as having several boiling regimes no longer exist, at least for Eq. (F-175)]. The effects of the remaining independent variables on the surface are then studied parametrically.

Obviously, instead of wall superheat and void fraction, any two independent variables can be chosen if someone desires to study the effects of other variables. The boiling-surface approach is independent of the choice of how to plot the influence of any two of its variables.

Total Wall Heat Flux and Phasic Wall Heat Fluxes. In determining the total wall heat flux for a two-phase mixture in a nonhomogeneous-nonequilibrium code, such as TRAC, the energy from the wall must be partitioned into the components going into the respective phases [see Eqs. (2-1) and (2-2)]. This division is required by the hydraulic model to determine the sensible heat present in each phase. For the solution of the conduction problem associated with each structure present in the fluid, the sum of the energy transferred into the phasic components is required [see Ref. F-98., Eq. (2-93)]. The simple relationship that defines this total wall heat flux with respect to the phasic components is given by

$$q_{\text{total}} = q'_{w\ell} + q'_{wg} \ , \tag{F-185}$$

where

$$q'_{w\ell} = h_{w\ell} \, (T_w - T_\ell) \tag{F-186}$$

and

$$q'_{wg} = h_{wg}(T_w - T_g) \ . \qquad \text{(F-187)}$$

It should be remembered that these phasic HTCs include the fraction of the wall being contacted by the phase according to the definitions used in Section 2.0.

At this point, it is appropriate to consider how we should go about the process of defining the quantities needed in Eqs. (F-185) through (F-187). The basic problem is that the theoretical two-phase two-fluid model requires definition of quantities that the experiments are not yet able to measure. This almost as true today as it was when the development of TRAC began in the early 1970s.

Basically, we have two choices. First, the majority of the closure relations within the literature for the total wall heat flux, q_{total}, are based upon data that cannot be separated into their phasic components. Thus, one choice available to us is to define correlations based upon this ability to calculate the total heat flux removed from the wall by the convective process. Then, we must define one of the phasic components based upon some model that we feel is appropriate. Subtracting this component from the total will then yield the remaining phasic contribution. The advantage to this approach, at least in concept, is that it should preserve the correct total amount of energy removed from the wall. The second choice available to us is the modification of homogeneous thermodynamic-equilibrium models to try to encompass the general characteristics within a particular flow regime. Then we combine various models representing different phenomena to develop the required phasic contributions. The only apparent justification for this choice, at least at this point, is that it provides the desired framework to include improved phasic models easily in the future.

We have chosen to use both methods in TRAC. The factor that influences the selection of the second approach the most is the interdependence of the closure relations. In some regimes, such as fully developed nucleate boiling, for example, departures from mechanical and thermodynamic equilibrium are not as significant, and the first method works reasonably well. For other regimes, such as the post-CHF regime, however, wide departures from equilibrium are encountered. This departure strongly couples the models chosen for the interfacial-drag, the interfacial heat-transfer, and the wall heat-transfer closure relations. Because most of the correlations for the total wall heat transfer are referenced to the saturation temperature of the mixture as the sink temperature, their application to this highly thermodynamic nonequilibrium situation is just as much in question as having chosen the second approach to start. This observation has lead to the choice of the second method for these regimes. In either case, the code developers then use comparison calculations with many experiments, including some of the older experiments that reduced their data using the equilibrium assumption, to ensure that the correct amount of energy is being extracted from the wall. Further definition of how these comparisons can be made and how they are made within this document is contained in Section F.2.2.

Finally, as noted, the phasic HTCs include the fraction of the wall being contacted by the phase according to the definitions used in Section 2.0., given by

$$h_{w\ell} = f_\ell h'_{w\ell}$$

and

$$h_{wg} = (1 - f_\ell) h'_{wg} \ ,$$

where $h'_{w\ell}$ and h'_{wg} are the separate phasic HTCs. The measurements (Refs. F-45. and F-46.) and modeling (Refs. F-47. and F-48.) of the quantity f_ℓ for the most part have been limited to the case of pool boiling on a horizontal surface. Thus, for forced convection, little is known. With this in mind, the effect of the phasic wall contact area is assumed to be encompassed within the phasic models developed under the second method and the weighting factors used to combine the separate correlations.

The Minimum Film-Boiling Temperature and Transition Boiling. The current literature on the minimum film-boiling temperature, T_{min}, and transition boiling for forced convection provides, at best, a very confusing picture. The primary contributing factors in the confusion are believed to be the following:

- that the data-reduction procedure may produce results dependent upon the quenching transient,
- that different types of experiments have been used, and
- the effect of axial conduction upon T_{min}.

The effect of axial conduction has undergone much discussion in the literature, whereas the effect of the other two factors has received little notice.

To understand how the data-reduction procedure and the quenching transient influenced the results obtained for different experiments, two general types of experiments are discussed. Axial conduction is then factored into the discussion conceptually after the effects of these two factors are understood. The first type of experiment considered is forced-convective-quenching experiments with flow inside long tubes and/or outside along bundles of tubes. The second is forced-convective-quenching experiments using short test sections with flow inside tubes having high thermal inertia.

We will first consider the quenching of a point by convection alone. The quenching of this point will be slow enough and generally broad enough that the quasi-steady approach is valid. Thus, the heat flux can be thought of as being represented by Eq. (F-175). To simplify this consideration, the liquid will be assumed to be saturated, $T_\ell = T_{sat}$, so that the wall superheat will be used as a variable instead of the wall

temperature alone. This variable change represents only a rigid body translation of the origin on the temperature axis but is more consistent with standard practices. Also, the velocities will be combined through the mass flux term, G, for the moment, so that either one velocity or the slip ratio remains undefined. Thus, Eq. (F-175) can be rewritten as

$$q_{\text{total}} = q(\Delta T_{\text{sat}}, P, G, \alpha, \ldots) \, . \tag{F-188}$$

Within the data-reduction procedure, the heat flux is assumed to be obtained from a 1D (radial) inverse-conduction calculation using thermocouple measurements at the elevation of interest. If the thermocouple is located on the heated surface, its measurement yields T_w directly, neglecting fin effects; otherwise the inverse calculation must also yield this quantity.

In considering the apparent boiling curve determined from the quenching of the point, the rate of change of heat flux is given by

$$\frac{dq}{dt} = \frac{\partial q}{\partial(\Delta T_{\text{sat}})}\frac{d(\Delta T_{\text{sat}})}{dt} + \frac{\partial q}{\partial P}\frac{dP}{dt} + \frac{\partial q}{\partial G}\frac{dG}{dt} + \ldots \, , \tag{F-189}$$

which is similar to Eq. (F-180). Again, for convenience, the total subscript is dropped. Multiplying both sides of Eq. (F-189) by $dt/d(\Delta T_{\text{sat}})$ then yields

$$\frac{dq}{d(\Delta T_{\text{sat}})} = \frac{\partial q}{\partial(\Delta T_{\text{sat}})} + \frac{\frac{\partial q}{\partial P}\frac{dP}{dt} + \frac{\partial q}{\partial G}\frac{dG}{dt} + \frac{\partial q}{\partial \alpha}\frac{d\alpha}{dt} + \ldots}{\frac{d(\Delta T_{\text{sat}})}{dt}} \, , \tag{F-190}$$

so that the slope of the apparent boiling curve is given by the total derivative of heat flux with respect to wall superheat, $dq/(d\Delta T_{\text{sat}})$. Equation (F-190) indicates how different factors will affect the apparent boiling curve when q is plotted against ΔT_{sat} for given times in the quenching transient. Thus, the apparent boiling curve for quenching experiments with tubes and bundles is a complex relationship of the convective heat transfer [$\partial q/\partial(\Delta T_{\text{sat}})$, $\partial q/\partial \alpha$ . . .], the hydraulic transient ($d\alpha/dt$, dP/dt, . . .), and the conduction-convection transient of the wall [$(d(\Delta T_{\text{sat}})/dt$].

A special case of the general quenching experiments on tubes and bundles exists in those experiments that are run at constant pressure and inlet mass flux. For this case,

$$\frac{dP}{dt} = \frac{dG}{dt} = 0 \, , \tag{F-191}$$

so that Eq. (F-190) reduces to

$$\frac{dq}{d(\Delta T_{\text{sat}})} = \frac{\partial q}{\partial(\Delta T_{\text{sat}})} + \frac{\frac{\partial q}{\partial \alpha}\frac{d\alpha}{dt}}{\frac{d(\Delta T_{\text{sat}})}{dt}} \, . \tag{F-192}$$

This data-reduction procedure is frequently used to obtain a minimum wall superheat, found from $dq/(d\Delta T_{sat})=0$, and a transition-boiling region, where $dq/(d\Delta T_{sat})<0$. From Eq. (F-192), it is observed that both the ΔT_{min} and transition boiling are dependent on the experimental transient. Transition boiling will thus appear to occur when, for example,

$$\frac{d\alpha}{dt} < -\left[\frac{\frac{\partial q}{\partial(\Delta T_{sat})}}{\frac{\partial q}{\partial \alpha}}\right]\frac{d(\Delta T_{sat})}{dt} \quad . \tag{F-193}$$

Equation (F-193) can now be interpreted in terms of a typical quench. Void fraction is decreasing as the conduction-convection quench front progresses toward the point being considered, and the following relationships are assumed to exist in the film-boiling regime:

$$\frac{\partial q}{\partial(\Delta T_{sat})}>0\ , \quad \frac{\partial q}{\partial \alpha}<0\ , \quad \text{and} \quad \frac{d(\Delta T_{sat})}{dt}<0\ ,$$

so that transition boiling appears to occur when $d\alpha/dt$ is decreasing at a sufficient rate. The apparent ΔT_{min} resulting from this interpretation, when Eq. (F-193) is satisfied, is greater than the homogeneous nucleation point, and, as just shown, will depend upon the experimental transient.

Another interesting result from this analysis is that the ΔT_{min} obtained from a quenching experiment, where Eq. (F-193) is satisfied, will be hydraulically controlled by the transient. When the transient does not satisfy Eq. (F-193), however—that is, does not decrease the void fraction fast enough—the resulting ΔT_{min} will be limited by the true minimum, $\partial q/\partial(\Delta T_{sat})=0$. This true minimum temperature was hypothesized by Nelson (Ref. F-41., Eq. 4, p. 51) to be approximated by the expression denoted as ΔT_{HN}. This denotes the wall superheat corresponding to a minimum temperature defined by the instantaneous interfacial-contact temperature of two semi-infinite media brought together, with the wall having a temperature corresponding to that of the homogeneous nucleation temperature in the liquid. This approximation is discussed further in Section F.2.1.9. This true minimum will be thermodynamically controlled. Similar results are obtained for the more general quenching experiment, indicated by Eq. (F-190); however, the relationships are more complex.

As discussed earlier under the boiling-surface concept, it is the improper separation of variables resulting from the apparent boiling curve–particularly void fraction, flow rates, and wall temperature–that has led to the confusion associated with ΔT_{min} and transition boiling for forced-convective heat transfer. Comparison of recent ΔT_{min} data to ΔT_{HN}, which TRAC uses, further supports this point (see Section F.2.1.9.).

Until recently, the short test session with high thermal inertia provided the only other source of ΔT_{min} data. The advantage this test section held over a long thin tube was that it

quenches, due to its shortness, with "constant" hydraulic conditions defined by the inlet conditions. Thus, the change in the hydraulic conditions over the short test section can be ignored, i.e.,

$$\frac{dP}{dt}=\frac{dG}{dt}=\frac{d\alpha}{dt}=0\ ,$$

and Eq. (F-190) reduces to

$$\frac{dq}{d(\Delta T_{sat})}=\frac{\partial q}{\partial(\Delta T_{sat})}\ . \tag{F-194}$$

The high thermal inertia prolongs the quenching period so that sufficient data can be acquired during the true transition-boiling period, $\partial q/\partial T_w<0$. Equation (F-194) indicates that the results obtained from this type of experiment will provide boiling curves that immediately separate the variables properly. The problem—if it can be termed that—created by this type of experiment has been that its results, $\Delta T_{min}\approx\Delta T_{HN}$ often disagree with tube results that are analyzed according to Eqs. (F-190) or (F-192), and confusion has arisen.

Now it should be apparent what the characteristics of the post-CHF regime must be and how quenches result. This has been heavily implied by Eq. (F-192). True minimum temperatures and true transition boiling have strict definitions relative to the boiling surface. These are denoted by

$$\frac{\partial q}{\partial(\Delta T_{sat})}=0$$

and

$$\frac{\partial q}{\partial(\Delta T_{sat})}<0\ ,$$

respectively. Similarly, film boiling can be denoted as that region where

$$\frac{\partial q}{\partial(\Delta T_{sat})}>0\ ,$$

and $T_w>T_{CHF}$. Quenches must be modeled by having the proper characteristics of the film-boiling regime with respect to void fraction and phasic flows, i.e., $\partial q/\partial\alpha$ and $\partial q/\partial G$ (mass flux is used here for simplicity). As noted earlier, strong coupling exists between the closure relations within this regime. This coupling is reflected further by the importance of these quantities.

With this understanding of how the data-reduction procedures influence the convective heat-flux correlations obtained from the quenching of tubes, bundles, or short test sections, the effect of axial conduction can be integrated into our thinking. Originally, the term $d(\Delta T_{sat})/dt$ in Eq. (F-190) was discussed in terms of 1D conduction solution. This limitation to one dimension, however, was not required by Eq. (F-190). The limitation arises because of the problem caused by multi-dimensional considerations involving the inverse-conduction solution when the heat flux must be found from the wall thermocouples. Without correct accounting of multi-dimensional conduction, erroneous convective heat fluxes are found and result in ΔT_{min} appearing higher than it really is.

This integration of multi-dimensional conduction into the situation yields a picture that better represents the real quenching process. Usually when quenching of a tube or bundle is studied, a point located immediately downstream of the quenching front is the location that provides the majority of the data with respect to transition boiling or the ΔT_{min}. Unfortunately, this is also the point where axial conduction and the rate of change of the hydraulic transient are at their maximum, making analysis of this type of experiment very difficult.

Having dissected the concepts used within the modeling of the convective heat transfer within the post-CHF regime in the code, one must note how the code models the axial conduction present in the quenching process. This is done by a renodalization of the typical coarse-mesh conduction-solution nodes into much smaller nodes capable of accurately representing the sharp temperature gradients present near the quench front. This renodalization is discussed in Section 2.2.4.4. It is important to realize that this renodalization does present a potential problem with respect to the spatial-averaging operation and the local-condition assumption that is inherent within the closure relations for the wall-to-fluid heat transfer. As noted in Appendix D, no checks are made with respect to the spatial averagers.

Spatial-Averaging Operator. Spatial averaging enters our consideration through the definitions in Eqs. (D-3) through (D-5). Nelson (Ref. F-49., pp. 1129-1132) discusses the requirements and influence of those spatial-averaging operations upon the wall-to-fluid heat transfer. An area average often enters the data-reduction procedure when steady-state experiments are analyzed. For upflow in a tube or rod bundle, thermocouples at different axial levels often define the midpoint of the area. Flowing experiments in a tube or rod bundle with a progressing quench front may contain either an area average or a line average (around the circumference of the tube/rod). Line-average data may be reported/obtained, provided the experimenter sampled the data at a sufficient rate to determine dT_w/dt accurately, that can be transformed to dT_w/dz, based on a constant quench front velocity assumption applied between thermocouples. Therefore, the reduced area-averaged data frequently include the effect of the area averaging arising from the thermocouple spacing. If analyzed in sufficient detail, the reduced line-averaged data may provide either heat flux as a function of distance from the quench front or heat flux with the accompanying dT_w/dz. It can be noted that the area-averaged data contain the same information but it is present on an average basis, i.e., it has been averaged over some axial length. When a quench front is present on either a thin tube or

rod bundle, area averaging frequently presents a problem because it will typically average over a length greater than the length of the quench front.

When the local-conditions hypothesis is used to develop correlations from the reduced data, the averaging operators also pose a potential problem if precautions are not taken. This problem is analogous to the δt_{min} problem discussed in Appendix D but arises from spatial considerations. The problem is described best by considering the example of quenching. Near the quench front, steep gradients of the wall temperature are encountered frequently. If a closure relation is developed using a history effect such as z_{CHF}, the correct amount of energy may be obtained based upon code renodalization (as described above). This assumes that the correlation is being applied to a situation similar to the data upon which it was based, i.e., dT_w/dz must have the same type of distribution. If a closure relation is developed using the local-conditions hypothesis with the wall temperature alone, additional precautions must be taken to ensure that the correct amount of energy is taken out when renodalization of the conduction solution to include axial-conduction effects occurs. These precautions must check that if the renodalization is becoming smaller than some minimum length (which must be determined from the data and its dT_w/dz), then the total heat flux over this Δz_{min} is preserved. Without this check, codes using a fine-mesh renodalization scheme will continue to increase the steepness of the quench front until axial conduction limits the process.

HTC Selection Logic. Discussion of the selection of the heat-transfer correlations to be used in the calculation of the wall-to-fluid-transfer rate will be done using the void-fraction wall-superheat plane shown in Fig. F-32. As just discussed, this plane has some advantages when considered from the heat-transfer-surface approach. This discussion will concentrate on where the different boiling regimes exist and, where necessary, the steps taken to assure continuity across boundaries where discontinuities otherwise would exist when changing from one correlation to another. The definitions of the correlations will be given in the next section because their definition is independent of the selection logic itself. Table F-6. lists the TRAC heat-transfer-regime numbers. Where appropriate, these heat-transfer-regime numbers are noted on Fig. F-32. Figure F-32. is used to discuss the selection of the HTCs (h_{wl} and h_{wg}). Note that heat-transfer surfaces could be plotted for h_{wl}, h_{wg}, $q'_{w\ell}$, q'_{wg}, and/or q_{total}.

Because Fig. F-32. considers only the effects of wall superheat and void fraction, the influence of the pressure and the phasic temperatures and velocities must be mentioned separately. The pressure enters the correlations through their physical property evaluation. No correlation switching is done based upon a pressure criterion so that the same correlations are used for all pressures. Although the physical properties may reflect a consideration of whether the pressure is greater than the critical pressure, the correlations have not been changed to reflect this effect. For the phasic temperatures, their effect generally enters the heat fluxes through the thermal potential and physical property evaluation required in the HTCs. In some cases, these sink temperatures directly enter the correlations themselves, but not frequently. No switching, to any extent, is done on phasic temperature. Finally, the phasic velocities do not give rise to

switching logic. Because, however, both natural-circulation and forced-flow conditions may exist during many of the transients considered, the natural-convection correlations are used to provide a lower boundary to the forced-convection correlations. Early versions of the code sometimes used the Grashof number or flow rate to switch between the correlations. These switches almost always produced discontinuities in the heat flux. Current versions of the code evaluate both conditions and use the maximum HTC. This can be expressed as

$$h = \max(h_{\mathrm{NC,\,lam}}, h_{\mathrm{NC,\,turb}}, h_{\mathrm{forc}}) \tag{F-195}$$

and eliminates any discontinuities with respect to flow-change logic encountered in earlier versions.

Radiation heat-transfer effects are considered in the transition-boiling and film-boiling regimes only. The radiation heat-transfer from the wall to the vapor is calculated using the Stefan-Boltzmann law of thermal radiation. The wall emissivity and geometric view factor are assumed to be unity.

The wall-to-fluid heat-transfer coefficients, h_{wl} and h_{wg}, are determined by subroutines HTCOR and HTVSSL. Subroutine HTCOR computes heat-transfer coefficients (h_{wl} and h_{wg}) based on local surface and fluid conditions for HTSTR components for which the core reflood model is not active and for 1D-component walls. For HTSTR components with the core reflood model active, wall-to-fluid heat transfer is estimated by subroutine HTVSSL. Most of correlations to model the boiling curve in these two subroutines, HTCOR and HTVSSL, are the same, except the post-CHF heat-transfer regime (film- and transition-boiling regimes). Subroutine HTVSSL considers a position-dependent post-CHF heat-transfer model for transition- and film-boiling regimes, as explained in Section F.2.2.

Figures F-33a. to F-33d. provide an overview of subroutine HTCOR, which contains the logic for the wall-to-fluid heat-transfer correlations. These four figures show the logic interconnected at the circles with letters to indicate the correct connection points. Whereas a detailed discussion of Figs. F-33a. to F-33d. relative to the regions noted in Fig. F-32. is not presented within this document, it is useful to note several points. Figure F-33a. generally denotes how those single-phase and two-phase regimes not normally considered to be part of the boiling curve (such as condensation) are selected. The "if-test" on RIDREG (corresponding to IDREG in Table F-6.) at the bottom of Fig. F-33a. decides whether we will work from right to left on the two-phase-boiling curve (Fig. F-33b.) or left to right Fig. F-33c. While this if-test adds a significant amount of Fortran coding to subroutine HTCOR, it saves a significant amount of central processing unit (CPU) time by eliminating a large number of calculations that might result if one always worked in one direction along the boiling curve. Figure F-33d. then denotes those operations performed upon the HTCs after they have been determined.

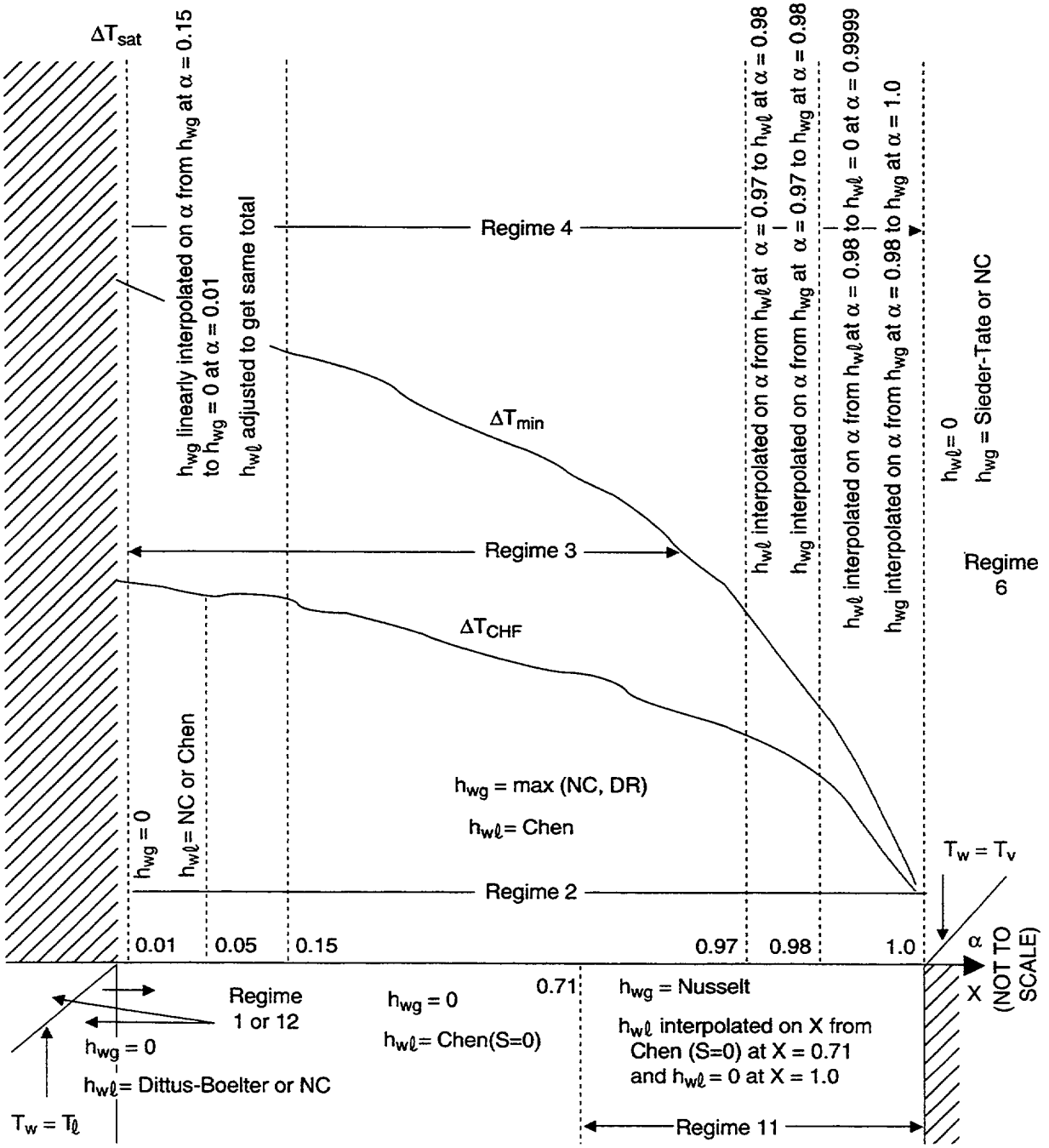

Fig. F-32. Void-fraction superheat plane.

TABLE F-6.
TRAC Heat-transfer Regimes

IDREG (IHTF)	Wall-to-Fluid Heat-Transfer Regime
1	Forced convection to single-phase liquid
2	Nucleate boiling
3	Transition boiling
4	Film boiling
6	Convection to single-phase vapor
7	Convection to two-phase mixture
11	Condensation
12	Liquid natural convection

The wall-to-fluid heat-transfer correlation selection logic used in subroutine HTVSSL for the reflood model is slightly different than that used in subroutine HTCOR. The difference is in the selection logic of transition- and film-boiling regimes (post-CHF heat-transfer regimes). Subroutines HTCOR and HTVSSL use the same HTC selection logic until points D and B shown in Figs. F-33b. and F-33c. The new HTC selection logic for the reflood model, performed after points D and B, is presented in Figs. F-33e. and F-33f.

F.2.1. Correlations Used in Subroutine HTCOR

This section discusses the HTC correlations used in subroutine HTCOR. Correlations for the wall-to-fluid heat transfer are discussed relative to the regimes denoted in Table F-6. After a discussion of each of these regimes, the critical-heat-flux and minimum wall superheat correlations are discussed.

F.2.1.1. Single-Phase Liquid (Heat-Transfer Regimes 1 and 12). Either forced convection (regime 1) or natural convection (regime 12) can occur when single-phase liquid is present. Laminar and turbulent HTCs are available. To avoid discontinuities with respect to flow-change logic encountered in earlier versions of TRAC, both laminar and turbulent conditions are evaluated and the maximum HTC is used. Because only single-phase liquid is assumed to be present, the vapor HTC, h_{wg}, is set equal to zero.

F.2.1.1.1. Forced Convection (Regime 1). Heat-transfer regime 1 is forced convection to single-phase liquid.

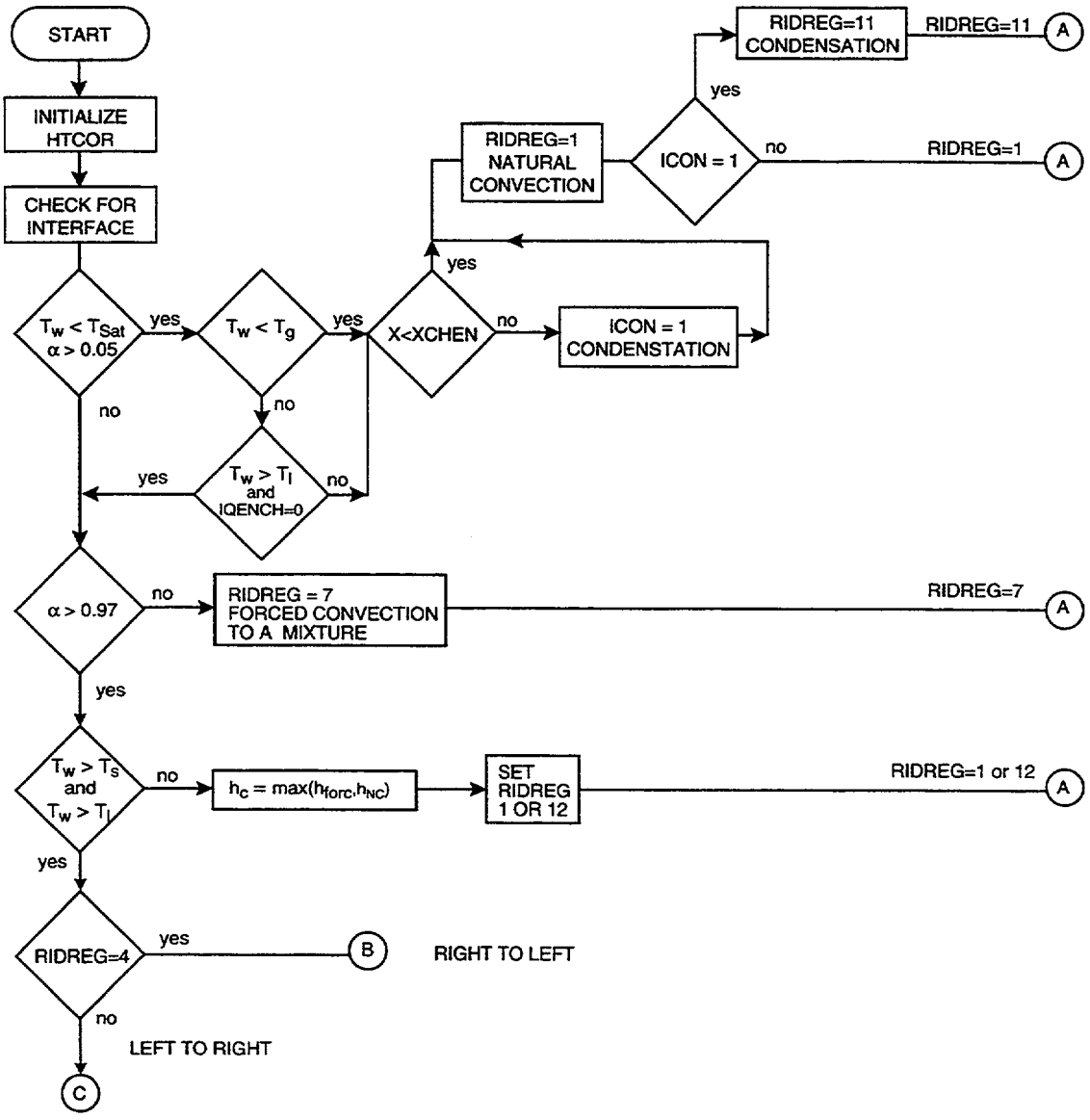

Fig. F-33a. HTC correlation selection logic.

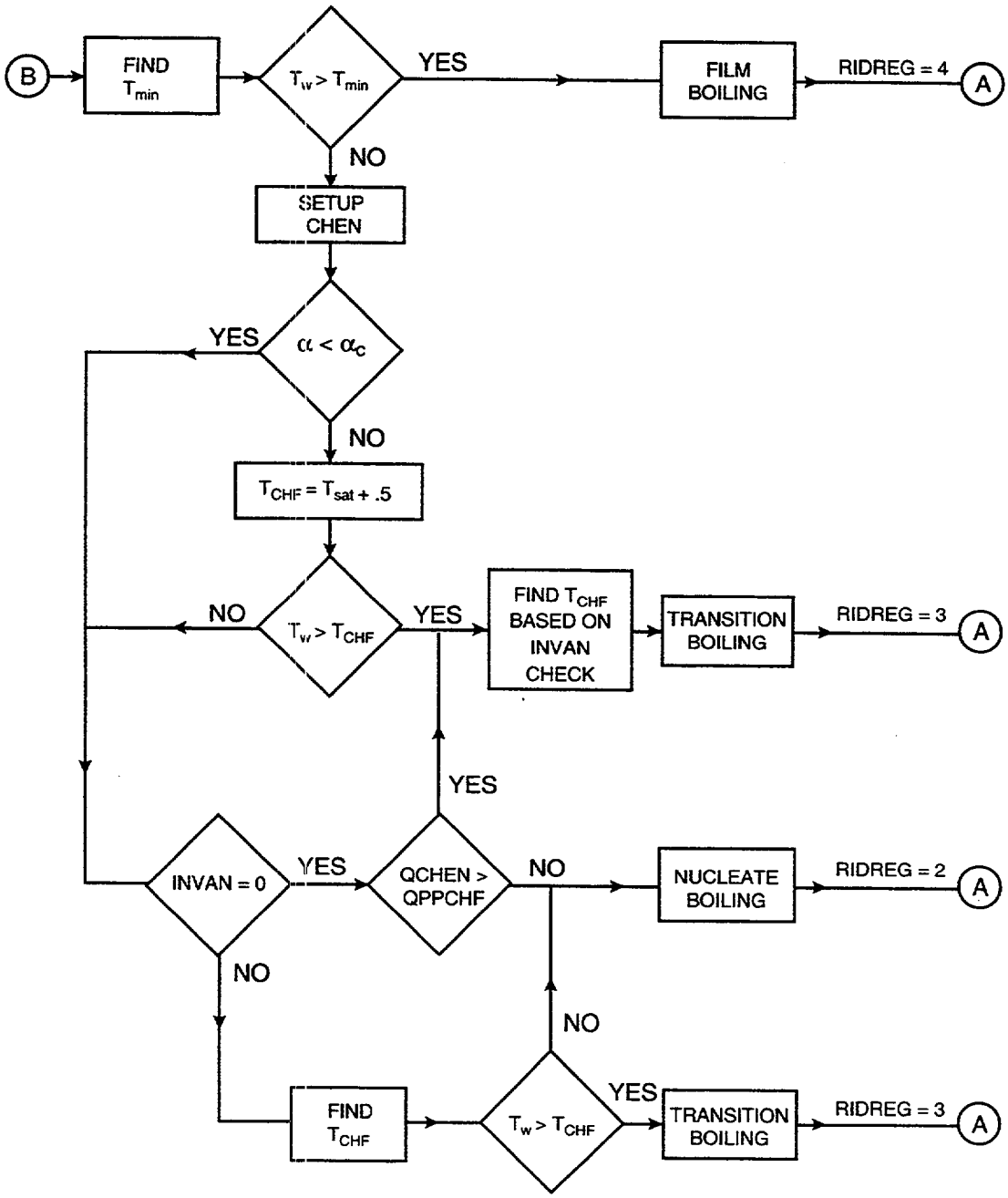

RIGHT TO LEFT ON BOILING CURVE

Fig. F-33b. HTC correlation selection logic.

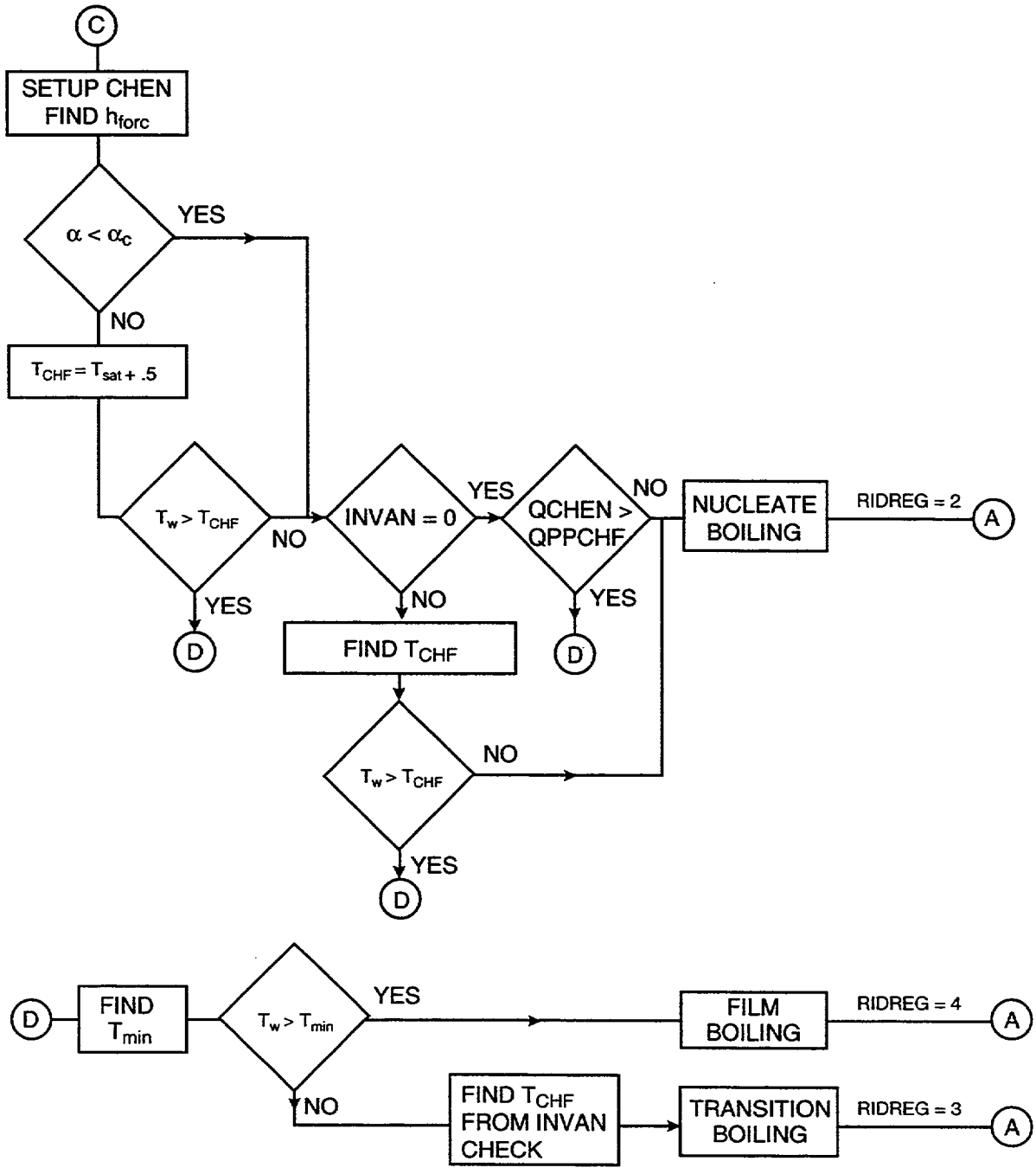

Fig. F-33c. HTC correlation selection logic.

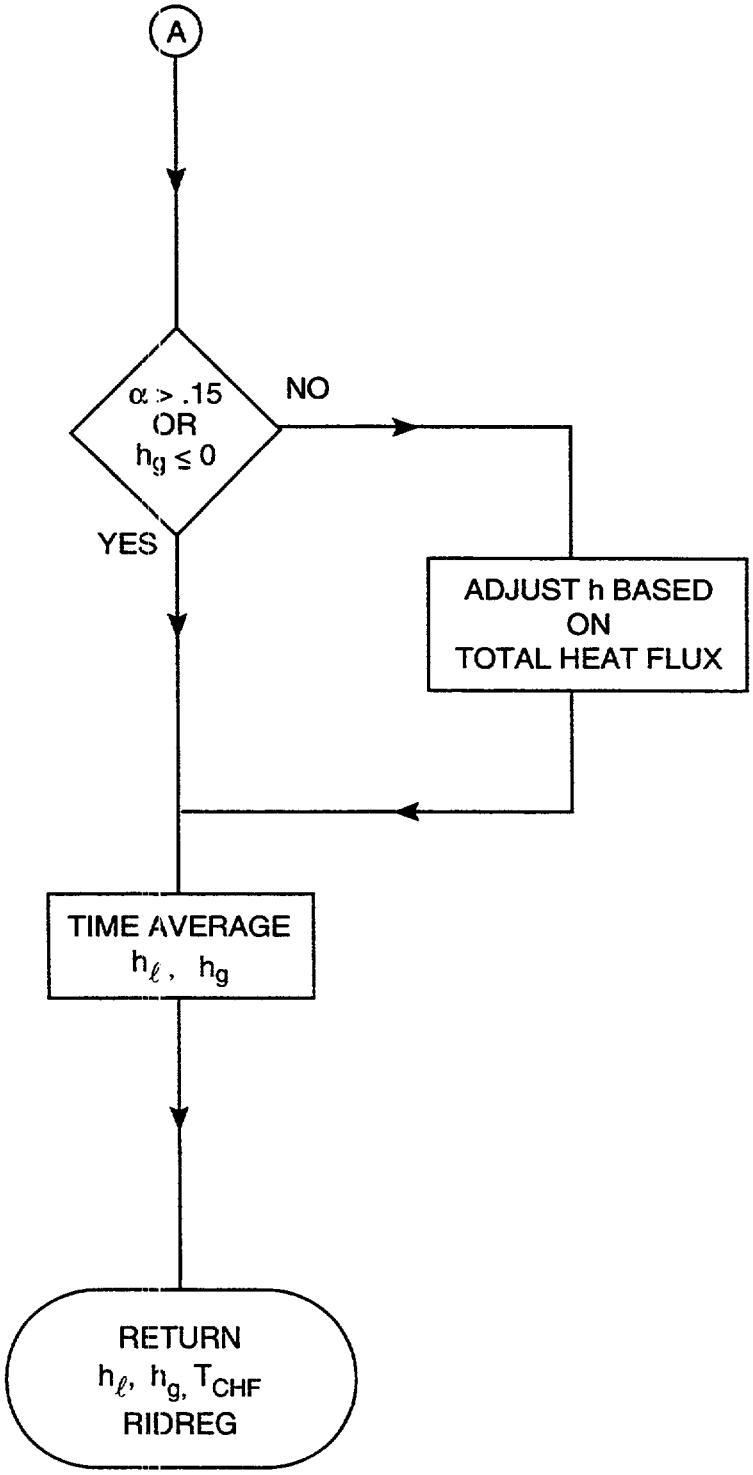

Fig. F-33d. HTC correlation section logic.

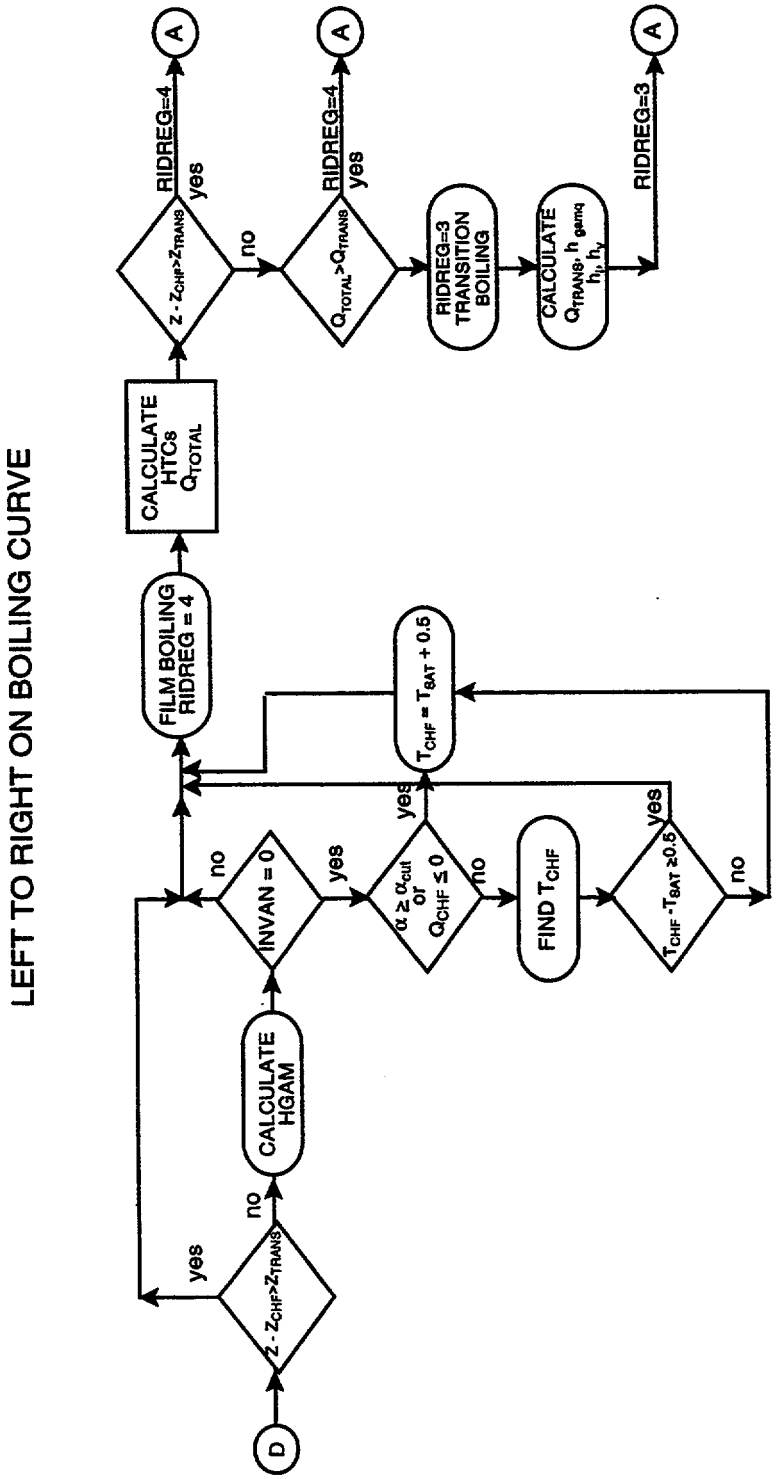

Fig. 4 – 33e.
HTC correlation selection logic for reflood model.

Fig. F-33e. HTC correlation selection logic for reflood model.

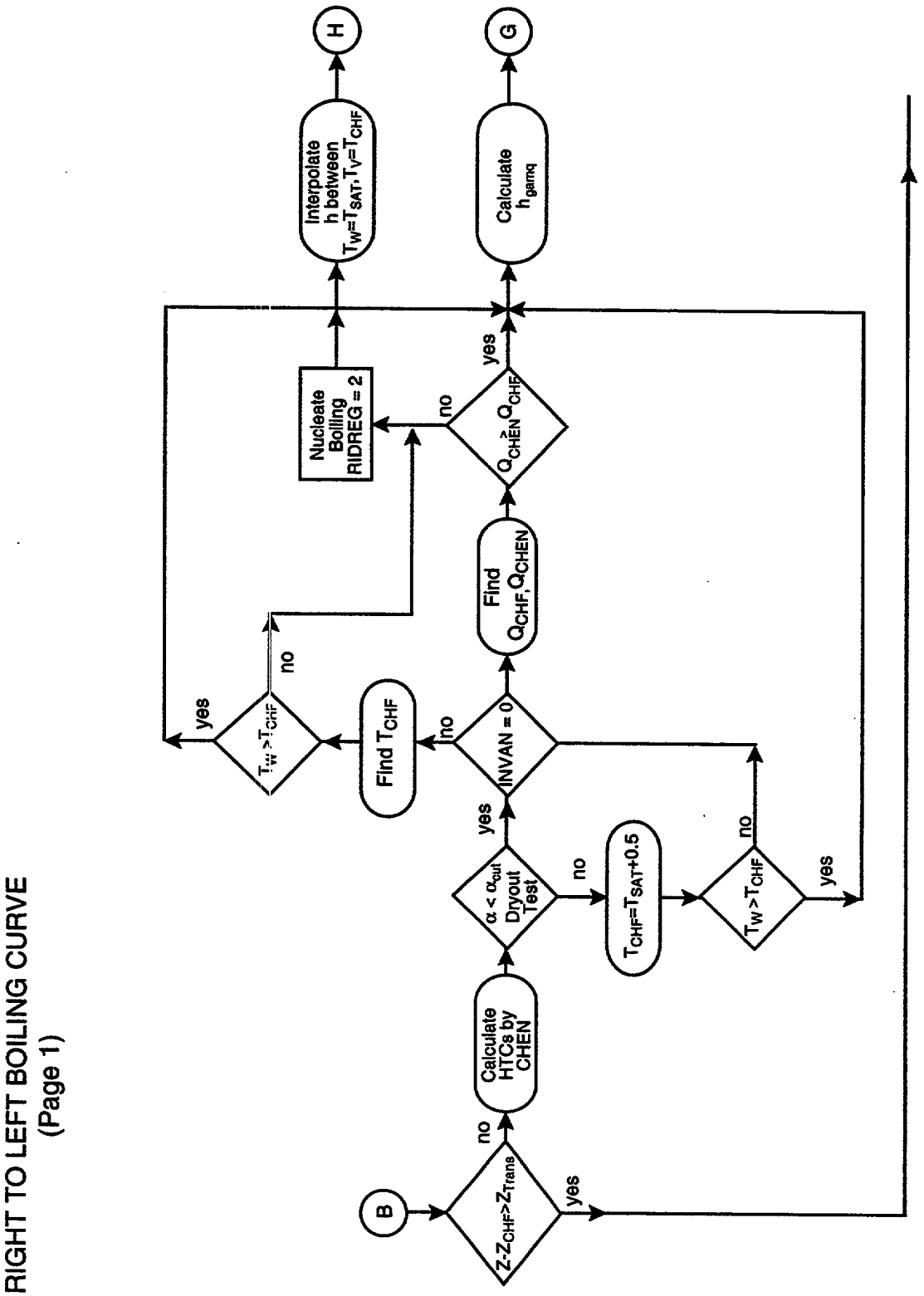

Fig. F-33f. HTC correlation selection logic for reflood model.

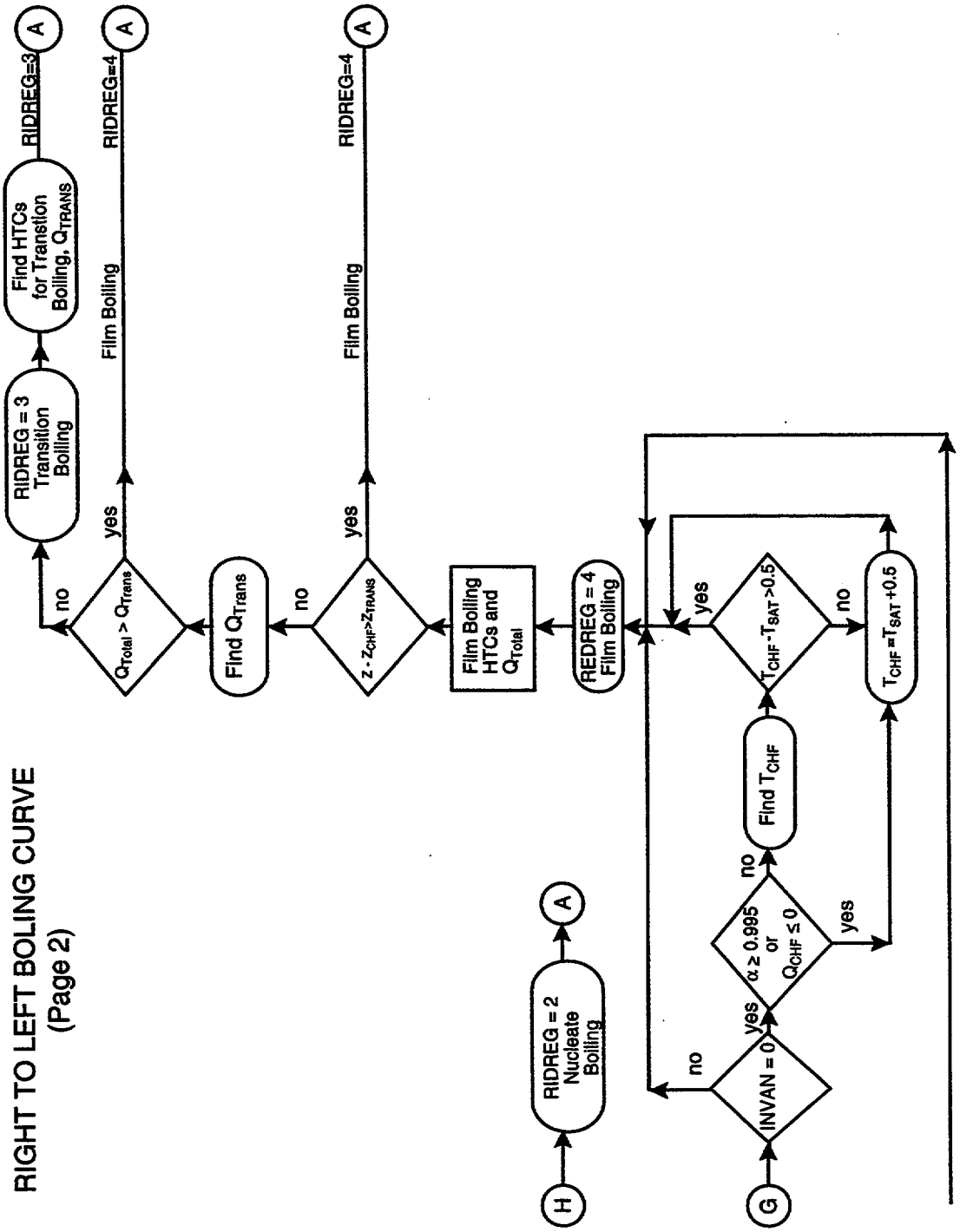

Fig. F-33f. (cont). HTC correlation selection logic for reflood model.

F.2.1.1.1.1. Basis for the Model. Wall-to-liquid heat-transfer coefficients are calculated by the Chen correlation (Ref. F-50., p. 262). The Chen correlation was developed for nucleate-boiling heat transfer and considered two separate heat-transfer mechanisms: heat transfer by nucleate boiling and heat transfer by forced convection. A Dittus-Boelter-type equation was used to represent the convective contribution. To account for the enhancement in heat transfer due to the formation of vapor bubbles, the Dittus-Boelter equation [Ref. F-51., Eq. (8-58)] was multiplied by a factor, *F*. The equation for the forced convection contribution is

$$h_{\text{forc}} = 0.023\frac{k_\ell}{D_H}Re_\ell^{0.8}Pr_\ell^{0.4}\cdot F \text{ , where} \tag{F-196}$$

$$F = 1.0 \text{ for } X_{TT}^{-1} \le 0.10 \text{ ,} \tag{F-197}$$

$$F = 2.35(X_{TT}^{-1} + 0.213)^{0.736} \text{ for } X_{TT}^{-1} > 0.01 \text{ ,} \tag{F-198}$$

$$Re_\ell = \frac{|V_\ell|\rho_\ell(1-\alpha)D_H}{\mu_\ell} \text{ , and } Pr_\ell = \left(\frac{\mu c_p}{k}\right)_\ell . \tag{F-199}$$

The convective part of the Chen correlation, Eq. (F-196), can be used for single-phase liquid heat transfer by taking *F* to be unity. In this case, the equation for h_{forc} is exactly the same as the Dittus-Boelter equation [Ref. F-51., Eq. (8-58)].

F.2.1.1.1.2. Input Quantities to the Model. The fluid properties are evaluated at the liquid temperature and pressure. The velocity used in determining the Reynolds number is the absolute value of the axial velocity of the liquid. This is the average of the velocities at the upper and lower cell edges for the VESSEL component and the average of the velocities at the left and right cell edges for 1D components. The hydraulic diameter is the hydraulic diameter of the flow passage.

F.2.1.1.1.3. Constants. None of the constants in the correlations was changed from that given in the reference cited. The dimensions used for the fluid properties, velocity, and hydraulic diameter result in HTCs with the units of $W \cdot m^{-2} \cdot K^{-1}$.

F.2.1.1.1.4. Model as Coded. The single-phase liquid HTC, h_{wl}, is calculated in subroutine CHEN (see Section F.2.1.2.). The enhancement factor, *F*, is set to unity if the inverse of the Martinelli factor, $(X_{TT})^{-1}$, is less than 0.10. The single-phase liquid HTC, h_{wl}, finally, is selected to be the maximum of those calculated by the Dittus-Boelter and the natural circulation equations [see Eq. (F-195)]. Subroutine CHEN returns the liquid HTC to subroutine HTCOR for regime 1. The final selection for the liquid HTC is the maximum of forced-convection and of laminar and turbulent natural-convection HTCs.

F.2.1.1.1.5. Assessment of the Correlations. When single-phase liquid forced convection is considered, the liquid HTC becomes the Dittus-Boelter equation in subroutine CHEN.

The Dittus-Boelter equation has been widely used for many years and has been verified by single-phase, turbulent, forced-convection data for many fluids. It is well supported by a broad database with an error of approximately 20%. Figure F-34. is a typical data correlation for forced-convection, turbulent flow in smooth tubes. The correlation is limited to forced-convection flows in which the Reynolds number, *Re*, is greater than 10^4 and with Prandtl numbers ranging from 0.7 to 160. If wide temperature differences are present in the flow such that appreciable changes in the fluid properties exist between the wall and the central flow, a correction is required to account for the property variations.

Both natural-circulation and forced-flow conditions may exist during many of the transients considered. Earlier versions of the code sometimes used the Grashof number or flow rate to switch between correlations. This method usually produced numerical instabilities and discontinuities. It was found that evaluating both the natural-convection and forced-convection correlations for laminar and turbulent flow and using the maximum HTC calculated eliminated the discontinuities caused by flow-change logic. In this heat-transfer regime, the Dittus-Boelter correlation is evaluated and maximum HTC is used; no switching between correlation is made on the basis of the Reynold's number.

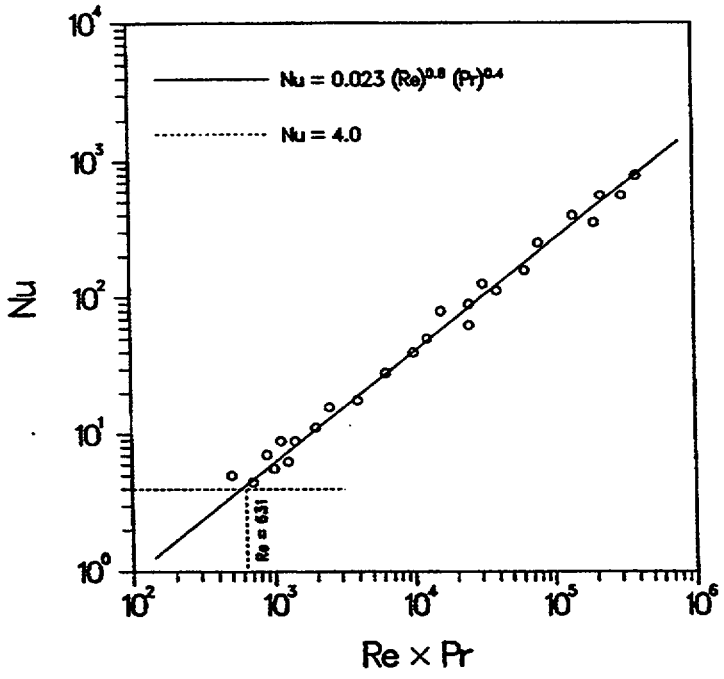

Fig. F-34. Typical data correlation for forced convection in smooth tubes, turbulent flow.

The Dittus-Boelter equation is used for external water flow parallel to tube banks. Available data indicate that the numerical coefficient varies with the pitch-to-diameter ratio. The HTCs obtained from Eq. (F-196) with $F=1$ for the pitch-to-diameter ratios of typical PWR fuel assemblies can underpredict the HTCs by 30 to 40% (Ref. F-52., Eqs. 3 and 4).

F.2.1.1.1.6. Scaling Considerations. The Dittus-Boelter correlation has been found to predict the HTC for a wide range of flow geometries and fluids at moderate temperature differences (wall-to-fluid). At high flow rates, the form of the equation should account for geometry and flow rate (Reynolds number) and fluid properties (Prandtl number). At low flows (laminar range), natural-convection flow patterns may become significant.

F.2.1.1.1.7. Summary and Conclusions. The convective contribution of the Chen correlation, with the F factor being unity, is used for single-phase liquid heat transfer. With the F factor being unity, the convective part of the Chen correlation becomes exactly the same as the Dittus-Boelter equation. If the correlations are used within their ranges of applicability, they predict HTCs within approximately 20%. The Dittus-Boelter equation has been found applicable to a wide range of geometries, flow rates, and fluids.

F.2.1.1.2. Natural Convection (Regime 12). Heat-transfer regime 12 is natural convection to a single-phase liquid.

F.2.1.1.2.1. Basis for the Model. For the laminar-flow regime, the following correlation (Ref. F-53., Table 7.1) is used:

$$h_{w\ell} = 0.59\frac{k_\ell}{L_c}(Gr \cdot Pr)^{0.25} , \tag{F-200}$$

where the Grashof number, Gr, is defined as

$$Gr = \frac{g\beta|T_w - T_\ell|\rho_f^2 L_c^3}{\mu_\ell^2} \tag{F-201}$$

and the Prandtl number, Pr, is defined as

$$Pr = \left(\frac{\mu c_p}{k}\right)_\ell . \tag{F-202}$$

To avoid extra calls to the thermodynamic properties subroutine, THERMO, all properties except β and ρ are evaluated at the liquid temperature. The properties β and ρ are approximated as

$$\rho_f = \rho_\ell + \frac{\partial \rho_\ell}{\partial T}(T_f - T_\ell) \tag{F-203}$$

and

$$\beta = -\frac{\partial \rho_\ell}{\partial T}\frac{1}{\rho_f} , \tag{F-204}$$

where

$$T_f = 0.5 \cdot (T_w + T_\ell) . \tag{F-205}$$

This correlation is valid in the range $10^4 < Gr \cdot Pr < 10^9$.

For the turbulent flow regime, the following correlation (Ref. F-53., Table 7.1) is used:

$$h_{w\ell} = 0.10\frac{k_\ell}{D_H}(Gr \cdot Pr)^{0.3333} . \tag{F-206}$$

The associated parameters are defined as in Eq. (F-200). This correlation is valid in the range $10^9 < Gr \cdot Pr < 10^{13}$.

F.2.1.1.2.2. Input Quantities to the Model. In Eqs. (F-200) and (F-206), the vertical height is normally chosen as the characteristic length in the Grashof number. To avoid nodalization dependence, the hydraulic diameter of the flow channel, D_H, is used as the characteristic length. Because the length term drops out of Eq. (F-206) and appears to the –0.25 power in Eq. (F-200), the choice of the characteristic dimension has a small effect on the value of the HTC.

All fluid properties except the density (ρ) and the coefficient of volumetric expansion (β) are evaluated at the liquid temperature T_ℓ. The properties ρ and β are approximated using Eqs. (F-203) through (F-205).

By using the maximum of the HTCs calculated from Eqs. (F-200) and (F-206), the laminar model is actually applied up to a value of $Gr \cdot Pr = 1.794 \times 10^9$; this assures continuity in the HTC.

F.2.1.1.2.3. Constants. None of the constants in the correlations was changed from that given in the reference cited. The dimensions used for the fluid properties, velocity, hydraulic diameter, temperature, and gravitational constant result in HTCs with dimensions of $W \cdot m^{-2} \cdot K^{-1}$.

F.2.1.1.2.4. Model as Coded. These correlations are evaluated in subroutine HTCOR. They are compared with the value of h_{w1} obtained from subroutine CHEN (see Section F.2.1.2.) for regime 1 and the maximum value is chosen. If the forced-convection HTC from subroutine CHEN is the largest, heat-transfer regime 1 is assigned; otherwise heat-transfer regime 12 (natural circulation to a single-phase liquid) exists.

F.2.1.1.2.5. Assessment of the Correlations. The form of Eq. (F-200) results from an analysis of a vertical surface at a uniform temperature in an extensive fluid at rest. It was assumed that the flow in the convective layer is primarily parallel to the surface. A force balance, which included the effects of buoyancy and fluid shear, resulted in an expression for the thickness of the convection layer. By considering this layer to be a thin slab across which heat is conducted, an expression for the HTC was found. For $Gr \cdot Pr < 10^4$, the boundary layer solution is no longer valid; for $Gr \cdot Pr > 10^9$, the transition to turbulent flow occurs and Eq. (F-206) should be used. As noted previously, by choosing the larger value of HTC from Eqs. (F-200) and (F-206), the transition to turbulent flow is assumed to occur when $Gr \cdot Pr = 1.794 \times 10^9$.

If the boundary layer thickness is very small compared with the diameter, D, the effect of transverse curvature is small and the results for vertical flat plates may be applied to flow over vertical cylinders. For large-diameter cylinders and Prandtl numbers near 1.0, it has been shown (Ref. F-54., Eq. 8-55) that a vertical cylinder may be treated as a vertical flat plate if

$$\frac{D}{L} \geq 35 \cdot (Gr)^{-0.25} , \qquad \text{(F-207)}$$

where D is the diameter of the cylinder, L is the vertical height, and Gr is the Grashof number based upon L. It is estimated that the flat-surface solution does not differ from the heat-transfer rate for vertical cylinders by more than 5% when Eq. (F-207) is satisfied. At small Grashof numbers, the cylinder must be short with a large diameter to satisfy Eq. (F-207).

F.2.1.1.2.6. Scaling Considerations. Both the laminar and turbulent correlations, Eqs. (F-200) and (F-206), were developed for isothermal plates in an extensive fluid at rest. The laminar-flow correlation is a weak function of geometry $L_c^{-0.25}$; in the turbulent-flow correlation, the length dependence drops out. The correlations are relatively insensitive to the choice and magnitude of the characteristic dimension.

F.2.1.1.2.7. Summary and Conclusions. If the correlations are used within their ranges of applicability, the predicted HTCs are in good agreement with data (see Fig. F-35. and Ref. F-10., Fig. 7-7). In TRAC, the correlations are applied to geometries other than those for which they were developed. Equation (F-207) provides a possible criterion to determine the applicability of the correlations to vertical cylinders.

Both correlations are evaluated and the maximum HTC is chosen; switching between correlations is not based upon the value of the parameter $Gr \cdot Pr$. This method avoids discontinuities in the HTCs and numerical instabilities. As $Gr \cdot Pr$ decreases below $\sim 1 \times 10^4$ and increases above $\sim 1 \times 10^{11}$, the correlations underestimate the experimental data.

F.2.1.2. Nucleate Boiling (Heat-Transfer Regime 2). Heat-transfer regime 2 is nucleate boiling and includes subcooled nucleate boiling.

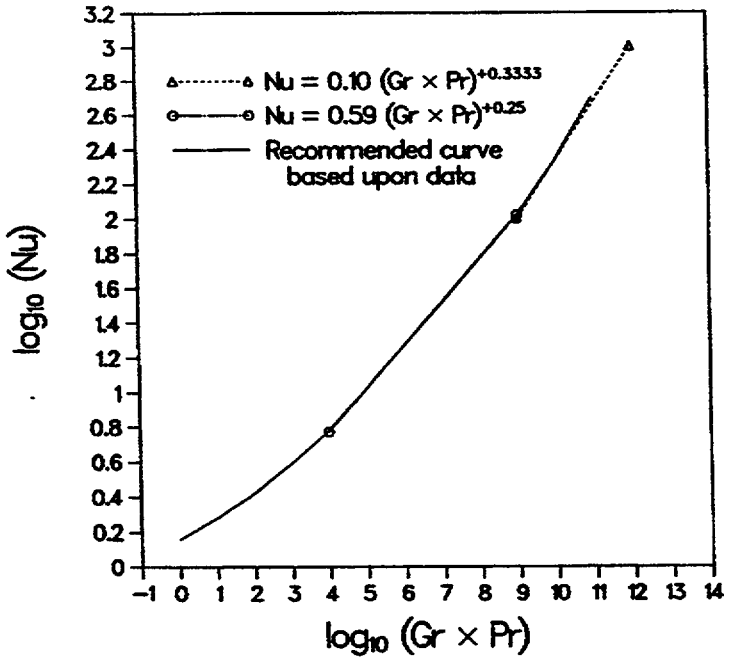

Fig. F-35. Natural convection for short vertical plates to air.

F.2.1.2.1. Basis for the Model. The Chen correlation (Ref. F-50., p. 262) is used in the nucleate-boiling heat-transfer regime. The correlation assumes that both nucleation and convective mechanisms occur and that the contributions made by the two mechanisms are additive. The convective component is assumed to be represented by a Dittus-Boelter-type equation where the thermal conductivity, Reynolds number, and Prandtl number are effective values associated with the two-phase flow. Heat is transferred to a liquid film in annular-mist and dispersed flow and it is reasonable to use the liquid conductivity. The values of the Prandtl number for liquid and vapor are normally of the same order of magnitude and it is reasonable to expect the two-phase Prandtl number to have a similar value. A parameter, $F > 1.0$, which is a function of the Reynolds number, is used to modify the convective part of the correlation, h_{forc} (called the macroterm), to account for increased agitation caused by the formation of vapor bubbles.

The basis for the nucleate-boiling component of the correlation is the analysis of Forster and Zuber (Ref. F-55.) for pool boiling. Their analysis relates a bubble Nusselt number to a bubble Reynolds number and a liquid Prandtl number. It can be shown that the product of growth rate and bubble radius is constant for a given superheat. In pool boiling and convective boiling, the superheat is not constant across the boundary layer. In pool boiling, this effect can be neglected. In forced-convective boiling, the boundary layer is thinner and temperature gradients are steeper. The difference between the wall superheat and the mean superheat to which the bubble is exposed must be considered. A suppression factor, S, modifies the nucleate-boiling part of the correlation, h_{nucb} (called the microterm), to account for this effect.

The equations for the Chen correlation are as follows:

$$q_{\text{total}} = h_{\text{forc}}(T_w - T_\ell) + h_{\text{nucb}}(T_w - T_{\text{sat}}) \,, \tag{F-208}$$

where

$$h_{\text{forc}} = 0.023 \frac{k_\ell}{D_H} \left(\frac{|V_\ell| \rho_\ell (1-\alpha) D_H}{\mu_\ell} \right)^{0.8} \left(\frac{\mu c_p}{k} \right)_\ell^{0.4} \cdot F \,, \tag{F-209}$$

$$h_{\text{nucb}} = 0.00122 \frac{k_\ell^{0.79} c_{p\ell}^{0.45} \rho_\ell^{0.49}}{\sigma^{0.5} \mu_\ell^{0.29} h_{\ell g}^{0.24} \rho_g^{0.24}} (T_w - T_s)^{0.24} (P_w - P)^{0.75} \cdot S \,, \tag{F-210}$$

$$F = 1.0 \text{ for } X_{TT}^{-1} \le 0.10 \,, \tag{F-211}$$

$$F = 2.35(X_{TT}^{-1} + 0.213)^{0.736} \text{ for } X_{TT}^{-1} > 0.01 \text{ (see also Eq. (F-217),} \tag{F-212}$$

$$X_{TT}^{-1} = (\text{Martinelli factor})^{-1} = \left(\frac{x}{1-x} \right)^{0.9} \left(\frac{\rho_\ell}{\rho_g} \right)^{0.5} \left(\frac{\mu_g}{\mu_\ell} \right)^{0.1} \,, \tag{F-213}$$

$$S = (1 + 0.12\, Re_{TP}^{1.14})^{-1} \text{ for } Re_{TP} < 32.5 \,, \tag{F-214}$$

$$S = (1 + 0.42\, Re_{TP}^{0.78})^{-1} \text{ for } 32.5 \le Re_{TP} \le 70.0 \,, \text{ and} \tag{F-215}$$

$$Re_{TP} = 10^{-4} \frac{|V_\ell| \rho_\ell (1-\alpha) D_H}{\mu_\ell} \cdot F^{1.25} \,. \tag{F-216}$$

The maximum value of X_{TT}^{-1} is limited to 100. The maximum value of Re_{TP} is limited to 70. The parameter F is defined as

$$F = \left(\frac{Re_{TP}}{Re_\ell} \right)^{0.8} = \left(\frac{Re_{TP}}{G(1-x) D_H / \mu_\ell} \right)^{0.8} \,. \tag{F-217}$$

Because this ratio is a flow parameter only, it may be expected that it could be expressed as a function of the Martinelli factor X_{TT}.

The suppression factor, S, is defined as

$$S = \left(\frac{\Delta T_e}{\Delta T_{\text{sat}}} \right)^{0.99} \,, \tag{F-218}$$

where ΔT_e is the effective superheat seen by a bubble. The functions F and S were determined from experimental data.

The vapor HTC is defined using the natural-convection and forced-convection correlations given by

$$h_{NC} = 0.13 k_g \left[\frac{\rho_g^2 g |T_w - T_g|}{\mu_g^2 T_g} \right]^{0.333} \cdot Pr_g^{0.333} \tag{F-219}$$

and

$$h_{dr} = 0.023 \, Re_{TP}^{0.8} Pr_g^{0.4} \left(\frac{k_g}{D_H} \right), \tag{F-220}$$

where

$$Re_{TP} = \frac{\left[|V_g| \alpha + |V_\ell| (1-\alpha) \right]}{\mu_g} \cdot \left(\rho_g D_H \right) \tag{F-221}$$

and

$$Pr_g = \left(\frac{c_p \mu}{k} \right)_g . \tag{F-222}$$

Equation (F-219) is a correlation for natural convection for vertical planes and cylinders in the turbulent-flow regime where $10^9 < Gr \cdot Pr < 10^{13}$ (Ref. F-10., Eq. 7-4a). It should be noted that in Eq. (F-219), the characteristic length has dropped out and β has been approximated by $1/T_g$. Equation (F-220) is the Dougall-Rohsenow correlation (Ref. F-9., Eq. F-153).

F.2.1.2.2. Input Quantities to the Model. All liquid properties are evaluated at the liquid temperature. All vapor properties are evaluated at the film temperature $T_f = 0.5(T_w + T_g)$. The velocity in the Reynolds number of Eq. (F-216) is the absolute value of the axial velocity of the liquid. The velocities in the two-phase Reynolds number [Eq. (F-221)] are the absolute values of the axial velocities of the vapor and liquid. Axial velocities are calculated as described in Section F.2.1.1.1. The characteristic length in the correlations is the hydraulic diameter of the flow passage.

F.2.1.2.3. Constants. None of the constants in the correlation was changed from that given in the references cited. The dimensions used for the fluid properties, velocity, temperature, and characteristic length result in HTCs with units of $W \cdot m^{-2} \cdot K^{-1}$. The functions F and S were determined from experimental data (see Figs. F-36. and F-37.).

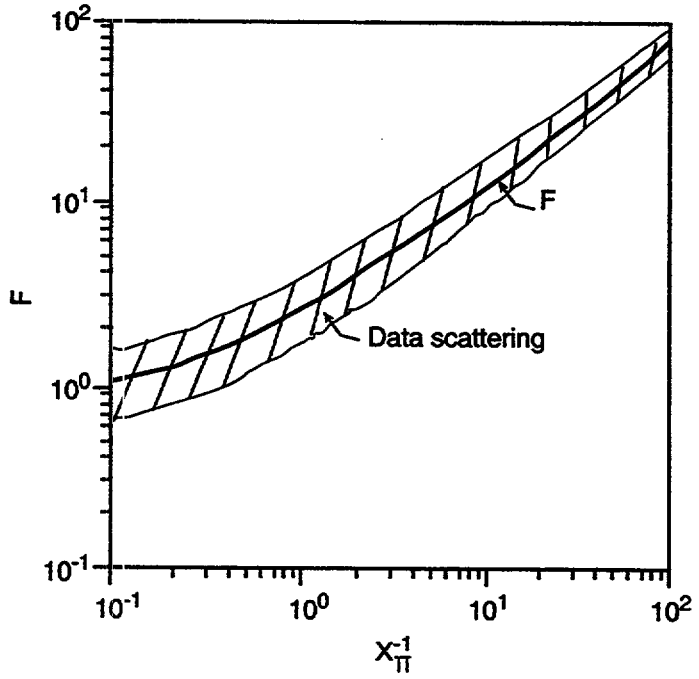

Fig. F-36. Dimensionless function *F* for forced convection in Chen's correlation.

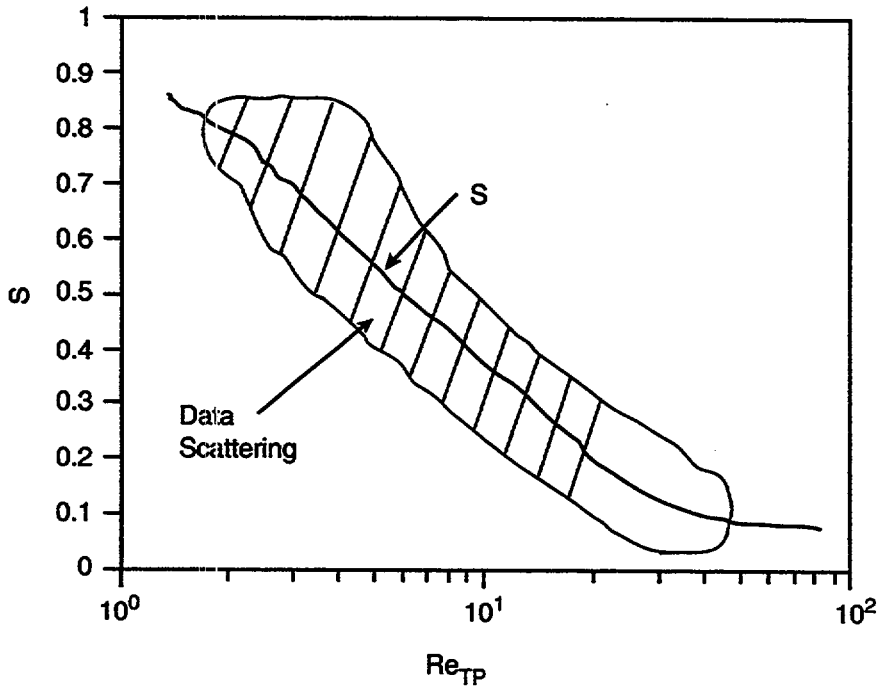

Fig. F-37. Dimensionless function *S* for nucleate boiling in Chen's correlation.

F.2.1.2.4. Model as Coded. The quantities h_{forc} and h_{nucb} are calculated in subroutine CHEN and the vapor HTC is calculated in subroutine HVNB. Because the Chen correlation was developed to represent the total heat flux and a vapor HTC is used for the phasic heat transfer, the liquid HTC is given by

$$h_{w\ell} = [h_{forc}(T_w - T_\ell) + h_{nucb}(T_w - T_{sat}) - h_{wg}(T_w - T_g)] / (T_w - T_\ell) \ . \qquad \text{(F-223)}$$

The vapor heat transfer is always limited to be 50% or less.

In subroutine HVNB, if the void fraction is ≤ 0.5, the vapor HTC, h_{wg}, is set to 0.0. If the void fraction is ≥ 0.75, h_{wg} is the maximum of the values given by Eqs. (F-219) and (F-220). Linear interpolation is done between 0.0 and max(h_{NC}, h_{dr}) for void fractions between 0.5 and 0.75.

The suppression factor, S, should approach zero as $\alpha \rightarrow 1.0$. From the definition of S, Eqs. (F-214) and (F-215), it is clear that $S \rightarrow 1.0$ as $\alpha \rightarrow 1.0$. To ensure that S approaches the correct value for $\alpha = 1.0$, the following procedure is used. When $\alpha > 0.70$, S is evaluated at $\alpha_s = 0.70$ and the current value of α; the minimum of the two values, S_{min}, is saved. Linear interpolation is then used between the two values, S_{min} and $S = 0.0$ at $\alpha_c = 0.98$. That is,

$$S = S_{min}\frac{(\alpha_c - \alpha)}{(\alpha_c - \alpha_s)} \text{ for } \alpha > \alpha_s \ (\alpha_s = 0.70) \text{, and} \qquad \text{(F-224)}$$

$$S = 0.0 \text{ for } \qquad \alpha > \alpha_c \ (\alpha_c = 0.98) \ . \qquad \text{(F-225)}$$

At high void fractions ($\alpha > \alpha_c = 0.98$), the HTCs are revised by linear interpolation between the current values of h_{wl} and h_{wg} and those for single-phase vapor ($h_{wl} = 0.0$ and $h_{wg} = h_{gsav}$) so that

$$h_{gsav} = \max(h_{gNC}, h_{gturb}) \ , \qquad \text{(F-226)}$$

where h_{gNC} and h_{gturb} are calculated as described in Section F.2.1.5.:

$$h_{gNC} = 0.13 k_g \left(\frac{\rho_g^2 g(T_w - T_g)}{\mu_g{}^2 T_g} \right)^{0.333} \cdot (Pr_g)^{0.333} \ , \qquad \text{(F-227)}$$

and

$$h_{gturb} = 0.023 \frac{k_g}{D_H} (Re_g)^{0.8} \cdot (Pr_g)^{0.4} \ . \qquad \text{(F-228)}$$

Note also in Section F.2.1.5. that Eq. (F-255) replaces Eq. (F-228) when $T_f = 0.5(T_w + T_g) \geq T_{sv}$. At high void fractions,

$$\bar{h}_{w\ell} = h_{w\ell} + (0 - h_{w\ell})\frac{(\alpha - \alpha_c)}{(\alpha_3 - \alpha_c)} \text{ for } \quad \alpha_c < \alpha < \alpha_3 , \tag{F-229}$$

$$\bar{h}_{w\ell} = 0 \text{ for } \quad \alpha \geq \alpha_3 , \tag{F-230}$$

$$\bar{h}_{wg} = h_{wg} + (h_{gsav} - h_{wg})\frac{(\alpha - \alpha_c)}{(\alpha_2 - \alpha_c)} \text{ for } \alpha_c < \alpha < \alpha_2 , \text{ and} \tag{F-231}$$

$$\bar{h}_{wg} = h_{gsav} \text{ for } \quad \alpha \geq \alpha_2 , \tag{F-232}$$

where

$$\alpha_c = 0.98 , \alpha_2 = 1.0 , \text{ and } \alpha_3 = 0.9999 .$$

F.2.1.2.5. Weighting, Limits, and Averaging. The vapor HTC is multiplied by the square of the temperature ratio $(T_w - T_{sat})/(T_{CHF} - T_{sat})$ so that h_{wg} is zero when $T_w = T_{sat}$ and goes to its transition-boiling value at $T_w = T_{CHF}$. Limits are placed on the range of values of the Chen F and S factors, the two-phase Reynolds number, and the inverse of the Martinelli factor [see Eqs. (F-211) through (F-216)]. The Chen S factor is also modified for void fractions greater than 0.70 so that it approaches its correct limit of 0.0 as the void fraction approaches 1.0. Subroutine CHEN constrains the h_{forc} term to be $\geq 4.0 \cdot (k_\ell / D_H)$.

At high void fractions, the liquid and vapor HTCs are linearly interpolated between the current values and the values for single-phase vapor to ensure that the boiling curve is smooth between heat-transfer regimes. No rate limits are used for the nucleate-boiling heat-transfer correlations.

F.2.1.2.6. Assessment of the Correlation. The Chen correlation works well for a wide variety of fluids and covers both the low- and high-quality flow regions. It approaches the Forster-Zuber pool-boiling relation at low flows. When quality is high and the flow pattern is in the form of annular-mist flow with a thin evaporating film on the wall, the correlation approaches that for forced convection of steam. The original database for the Chen correlation covered the following ranges:

Pressure:	0.09 to 3.45 MPa
Mass Flow:	54 to 4070 kg/m^2-s
Quality:	0.0 to 0.7

The pressure range has been extended to 6.9 MPa. Tables F-7. and F-8. (Ref. F-56.) show the range of conditions for data used in testing various correlations and a comparison of the correlations. The modified correlation used for subcooled boiling underpredicts the highly subcooled experimental data.

TABLE F-7.
Range of Conditions for Data Used
In testing Correlations (Ref. F-56.)

Fluid	Geometry	Flow	Pressure Bar	Liquid Inlet Velocity	Quality (wt%)	Heat Flux
Water	Tube	Up	0.55–2.76	0.06–1.45	15–71	88–630
Water	Tube	Up	2.9–34.8	0.24–4.50	3–50	205–2400
Water	Tube	Down	1.1–2.1	0.24–0.82	2–14	44–158
Water	Annulus	Up	1–2.4	0.06–0.27	1–59	100–500
Methanol	Tube	Up	1	0.3–0.76	1–4	22–54
Cyclohexane	Tube	Up	1	0.4–0.85	2–10	9.5–41
Pentane	Tube	Up	1	0.27–0.67	2–12	9.5–38
Heptane	Tube	Up	1	0.3–0.73	2–10	6.2–28
Benzene	Tube	Up	1	0.3–0.73	2–9	12.5–41

TABLE F-8.
Comparison of Correlations (Ref. F-56.)

Data	Average Percentage Deviations for Correlations				
	Dengler and Addoms	Guerrieri and Talty	Bennett et al.	Schrock and Grossman	Chen
Dengler and Addoms (water)	30.5	62.3	20.0	20.3	14.7
Schrock and Grossman (water)	89.5	16.4	24.9	20.0	15.1
Sani (water)	26.9	70.3	26.5	48.6	8.5
Bennett et al. (water)	17.9	61.8	11.9	14.6	10.8
Guerrieri and Talty (methanol)	42.5	9.5	64.8	62.5	11.3
Guerrieri and Talty (cyclohexane)	39.8	11.1	65.9	50.7	13.6
Guerrieri and Talty (benzene)	65.1	8.6	56.4	40.1	6.3
Guerrieri and Talty (heptane)	61.2	12.3	58.0	31.8	11.0
Guerrieri and Talty (pentane)	66.6	9.4	59.2	35.8	11.9
Combined average for all data	38.1	42.6	32.6	31.7	11.0

Equation (F-220) is the Dougall-Rohsenow correlation and can be recognized as a simple modification to the Dittus-Boelter correlation. The Dougall-Rohsenow correlation was developed for the film-boiling flow regime. It was postulated that the thermal resistance existed at the liquid/vapor interface and was the result of a laminar zone, a buffer zone, and a turbulent zone. As the film Reynolds number was increased, the various zones of resistance were gradually removed. None remained in dispersed flow.

Pre-CHF boiling heat transfer can occur in either a saturated two-phase mixture or in a subcooled, two-phase liquid. For the saturated two-phase mixture, the heat-transfer mechanisms are saturated nucleate boiling in the low-quality region and forced-convective evaporation (normally associated with annular-mist flow) in the high-quality, high-flow region. It is assumed that there is little difference between upflow and downflow nucleate-boiling heat transfer.

If the wall temperature exceeds the minimum temperature required for nucleation, subcooled boiling can occur. It is assumed that a simple temperature ratio correlation is sufficient to modify the nucleate-boiling part of the Chen correlation for subcooled boiling. It is assumed that both the nucleation and convection mechanisms occur and that their effects are additive.

F.2.1.2.7. **Scaling Considerations.** Most of the data from which the correlations were developed were for boiling inside vertical tubes. The accuracy of the HTCs predicted by the correlations when applied to PWR rod-bundle geometry has not been determined. The Chen correlation, although semi-empirical, does have a physical basis. It works well for a variety of fluids (including water), covers both the low- and high-quality regions, and transforms into the Forster-Zuber correlation for pool boiling at low flows.

The Dougall-Rohsenow correlation is used to make the vapor HTC continuous as a function of wall temperature. Based upon limited tube-bundle data, it seems to predict bundle data better than tube data (Ref. F-50., p. 277, and Fig. F-38.).

F.2.1.2.8. **Summary and Conclusions.** The Chen correlation has been widely used for water in the saturated, forced-convective boiling region in vertical ducts. It is valid for situations in which all surfaces are wet. Evaporation within inclined and horizontal tubes is encountered frequently (U-tubes in steam generators). Stratification of the flow results, with the majority of the fluid in the bottom of the tube, and dryout of the upper surfaces may occur. The correlation of Shah (Ref. F-57., p. 572, and Ref. F-58.) is valid for saturated, forced-convection boiling in horizontal ducts, but for water it is best suited to situations in which heating is from a fluid.

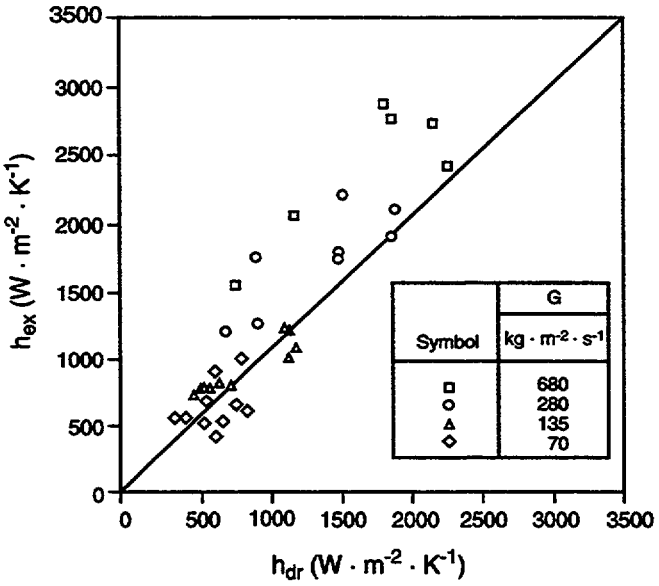

Fig. F-38. Comparison of measured HTCs during stable film boiling in rod bundles with the predictions of the Dougall-Rohsenow correlation.

Newer correlations (Refs. F-59. and F-60.) for forced-convection boiling heat-transfer data have extended the method of superposition to cover subcooled to high quality ranges. Reference F-60. uses single-phase and two-phase forced-convection equations, a pool-boiling equation, and an incipient-boiling criterion. A single, empirically determined coefficient is required. The agreement with water data is better than that provided by the Chen correlation. Reference F-60. used a large data bank (7 fluids and 28 authors) for saturated boiling in vertical and horizontal tubes, subcooled boiling, and boiling in annuli to develop a correlation giving a closer fit to the data than existing correlations. Future code development efforts should consider possible improvements to the correlations used in the nucleate boiling regime.

F.2.1.3. Transition Boiling (Heat-Transfer Regime 3). The transition-boiling regime spans the boiling surface between CHF and minimum film boiling.

F.2.1.3.1. Basis for the Model. It is assumed that transition-boiling heat transfer is composed of both nucleate-boiling (wet-wall) and film-boiling (dry-wall) heat transfer. Each component is weighted by a factor ξ, the fraction of wall area that is wet. The equations used in the transition-boiling regime are (Ref. F-61., p. 27)

$$q_{\text{trans}} = \xi q_{\text{CHF}} + (1-\xi) q_{\text{min}} \tag{F-233}$$

$$= h_{w\ell}(T_w - T_\ell) + h_{wg}(T_w - T_g)\ , \tag{F-234}$$

where

$$\xi = \left(\frac{T_w - T_{\min}}{T_{CHF} - T_{\min}} \right)^2 , \tag{F-235}$$

$$q_{\min} = h_{w\ell \min}(T_{\min} - T_\ell) + h_{wg\min}(T_{\min} - T_g) + h_{fBB}(T_{\min} - T_{sat}) , \tag{F-236}$$

$$h_{wg\min} = \max(h_{NC}, h_{dr}) \text{ at } T_{min}, \tag{F-237}$$

$$h_{NC} = 0.13 k_g \left(\frac{\rho_g^2 g_c |T_w - T_g|}{\mu_g^2 T_g} \right)^{0.3333} \cdot (Pr_g)^{0.3333} , \tag{F-238}$$

$$h_{dr} = 0.023 \, Re_{TP}^{0.8} \, Pr_g^{0.4} \frac{k_g}{D_H} , \tag{F-239}$$

$$Pr_g = \left(\frac{c_p \mu}{k} \right)_g , \tag{F-240}$$

$$Re_{TP} = \frac{\rho_g \left[|V_g| \alpha + |V_\ell| (1-\alpha) \right] D_H}{\mu_g} , \tag{F-241}$$

$$h_{w\ell \min} = h_r \cdot \frac{(T_{\min} - T_{sat})}{(T_{\min} - T_\ell)} , \tag{F-242}$$

and

$$h_r = (\alpha_3 - \alpha) \cdot \sigma_r \cdot \varepsilon \cdot \frac{(T_{\min}^4 - T_{sat}^4)}{(T_{\min} - T_{sat})} , \tag{F-243}$$

where α_3=0.9999.

The gas phasic HTC is evaluated from

$$h_{wg} = \max(h_{NC}, h_{dr}) . \tag{F-244}$$

Then, Eq. (F-234) can be used to solve for h_{wl} as follows:

$$h_{w\ell} = \frac{q_{trans} - h_{wg}(T_w - T_g)}{(T_w - T_\ell)} . \tag{F-245}$$

The critical heat flux, q_{CHF}, is calculated in subroutine CHF1 using the Biasi correlation (Section F.2.1.8.); q_{min} is the heat flux at the minimum stable film-boiling temperature. This temperature is calculated in subroutine TMSFB and is discussed in Section F.2.1.9. The Bromley HTC for film boiling, h_{fBB}, is calculated in subroutine HLFILM and discussed in Section F.2.1.4. The radiation from the wall to the liquid is included by the coefficient h_r. Equations (F-238) and (F-239) are discussed in Section F.2.1.2.

F.2.1.3.2. Input Quantities to the Model. The liquid and vapor properties are evaluated at the liquid and vapor temperatures. The velocities in the two-phase Reynolds number are the absolute values of the liquid and vapor axial velocities (see Section F.2.1.1.1.). The emissivity, ε, in the radiation HTC is assumed to be 1.0. The characteristic length is the hydraulic diameter of the flow passage.

F.2.1.3.3. Constants. The simple form of the weighting factor, ξ, defined in Eq. (F-235), was found to fit the experimental data best if an exponent of 2 was used. The constants in the correlations used in the transition-boiling regime are those given in the references cited. The dimensions used for the variables yield HTCs in units of $W \cdot m^{-2} \cdot K^{-1}$ and heat fluxes in units of $W \cdot m^{-2}$.

F.2.1.3.4. Model as Coded. Most of the calculations are carried out in subroutine HTCOR. Subroutines CHEN, CHF, CHF1, HLFILM, HVFILM, and TMSFB are called as needed to evaluate the nucleate-boiling HTC, critical heat flux (CHF), the CHF temperature T_{CHF}, the film-boiling liquid HTC, the film-boiling vapor HTC, and the minimum stable film-boiling temperature, T_{min}, respectively. A number of tests are made in subroutine HTCOR to determine if the transition-boiling regime exists. Transition boiling is assumed to exist if $T_{CHF} < T_w < T_{min}$. (See Section F.2.1.3. concerning transition boiling and Section F.2.1.9. concerning T_{min}.)

The critical heat flux, q_{CHF}, and the heat flux at T_{min}, q_{min}, are evaluated and Eq. (F-233) is used to calculate the transition-boiling heat flux, q_{trans}. If $\alpha > 0.98$, q_{trans} is reevaluated as

$$q'_{trans} = q_{trans} \frac{(\alpha_3 - \alpha)}{(\alpha_3 - \alpha_c)} + h_{gsav}(T_w - T_g) \frac{(\alpha - \alpha_c)}{(\alpha_3 - \alpha_c)}, \qquad \text{(F-246)}$$

where $\alpha_c = 0.98$ and $\alpha_3 = 0.9999$. This interpolation ensures a smooth transition to convective heat transfer to a vapor at high void fractions.

F.2.1.3.5. Weighting, Limits, and Averaging. In Eq. (F-233), a weighting factor is used to estimate the fraction of the wall area that is wet. In Eq. (F-246), interpolation is used to ensure a smooth transition to the single-phase vapor HTC at high void fractions. No rate limits are used. Limits are imposed on mass flow in the Biasi correlation for CHF and are discussed in Section F.2.1.8.

F.2.1.3.6. Assessment of the Correlation. The major assumption made in implementing the equations for the heat flux in the transition-boiling regime is that this

regime can be modeled as a combination of steady-state nucleate boiling and film boiling. As its name implies, transition boiling is a combination of unstable film boiling and unstable nucleate boiling alternately existing at any given location on a heating surface. The variation in heat-transfer rate with temperature is primarily a result of a change in the fraction of time each boiling regime exists at a given location.

The transition-boiling section of the boiling curve is bounded by the CHF and the minimum film-boiling heat flux. The CHF has been studied extensively and can be predicted by a number of correlations. The minimum heat flux has been studied less; it is known to be affected by flow, pressure, surface properties, fluid properties, and heated-surface parameters.

Data on transition boiling are relatively scarce and have a common shortcoming in that they cover only narrow ranges of conditions. The data are not considered accurate enough or plentiful enough to serve as the basis for deriving a correlation. Also, much of the data include apparent transition-boiling effects, as discussed in Section F.2., and make the amount of usable data even more limited. Some parametric trends have been deduced, however. In general, an increase in mass flux increases the transition-boiling heat flux and shifts the wall superheat at the minimum heat flux to higher temperatures. Increasing subcooling has a similar effect but the effect of quality is less obvious. Disagreement exists about whether the vapor film, which is in violent motion, will be maintained at wall superheats less than ΔT_{min} or if liquid will contact the wall.

Despite scarcity of data and disagreements on the appropriate physical model, correlations have been proposed that are of three types: those that contain boiling and convective components, those based on a physical model of heat transfer (phenomenological), and empirical correlations.

Transition boiling is inherently an unstable process and is difficult to incorporate into a code such as TRAC. In light of this fact, the choice of the simple forms of Eqs. (F-233) and (F-246) to calculate the transition heat flux was motivated by their simplicity.

F.2.1.3.7. Scaling Considerations. Application of this transition-boiling formulation to quenching problems, such as those normally encountered in a reflooding core, is not recommended. (See discussion in Section F.2. of spatial-averager problems, that is, problems where the influence of quench front progression become important.)

F.2.1.3.8. Summary and Conclusions. The major assumption of the transition-boiling model is that it can be considered a combination of steady-state nucleate boiling and film boiling. Because the data are not considered accurate or plentiful enough to provide a basis for deriving a correlation, this simple and physically based model is justified for those situations where spontaneous, convection-controlled quenches occur.

F.2.1.4. Film Boiling (Heat-Transfer Regime 4). To fully describe film boiling, the film-boiling heat-transfer regime incorporates several different correlations.

F.2.1.4.1. **Basis for the Model.** The film-boiling regime in subroutine HTCOR is assumed to occur when the wall temperature exceeds the minimum stable film-boiling temperature ($T_w > T_{min}$). The wall-to-vapor and wall-to-liquid heat transfer are treated separately. The wall-to-liquid HTC is assumed to be the sum of two components: radiation and near-wall liquid effects. The liquid HTC is given by

$$h_{w\ell} = (h_r + h_{fBB}) \cdot \left[\frac{(T_w - T_{sat})}{(T_w - T_\ell)}\right], \tag{F-247}$$

where the radiative component is

$$h_r = \alpha_1 \cdot \sigma_r \cdot \varepsilon \cdot \frac{(T_w^4 - T_{sat}^4)}{(T_w - T_{sat})} . \tag{F-248}$$

The film-boiling component is given by the modified Bromley correlation (Ref. F-50., p. 273, and Ref. F-62.) as

$$h_{fBB} = 0.62 \cdot \left(\frac{\rho_g k_g^3 (\rho_\ell - \rho_g) g h'_{\ell g}}{\mu_g (T_w - T_{sat}) \lambda}\right)^{0.25} . \tag{F-249}$$

In these correlations $\alpha_1 = (\alpha_3 - \alpha) = 0.9999 - \alpha$, σ_r is the Stefan-Boltzmann constant, ε is the wall emissivity (assumed to be 1.0), and λ is the characteristic length (Taylor wavelength) given by

$$\lambda = 2\pi \left(\frac{\sigma}{g(\rho_\ell - \rho_g)}\right)^{1/2} , \tag{F-250}$$

where $h'_{\ell g}$ is a modified latent heat to account for the superheated vapor such that

$$h'_{\ell g} = h_{\ell g} + 0.5 \cdot c_{pg} \cdot (T_g - T_{sat}) . \tag{F-251}$$

The temperature ratio in Eq. (F-247) changes the sink temperature of the HTC using T_{sat} to T_ℓ as used by the code.

The wall-to-vapor HTC used in this heat-transfer regime is the greater of the Dougall-Rohsenow (h_{dr}) or the turbulent, natural-convection (h_{NC}) correlations. That is,

$$h_{wg} = \max(h_{dr}, h_{NC}) , \tag{F-252}$$

where h_{dr} and h_{NC} are defined by Eqs. (F-238) through (F-241).

F.2.1.4.2. **Input Quantities to the Model.** The liquid and vapor properties are evaluated at the liquid and vapor temperatures. The velocities are the liquid and vapor axial velocities (see Section F.2.1.1.1.); the wall emissivity is assumed to be 1.0.

F.2.1.4.3. **Constants.** All other constants used in the correlations for the film-boiling regime are those given in the references cited. The dimensions used for the variables yield HTCs in units of $W \cdot m^{-2} K^{-1}$.

F.2.1.4.4. **Model as Coded.** The film-boiling regime, $\partial q / \partial (T_{sat}) > 0$, is assumed to occur when the wall temperature exceeds the minimum stable film-boiling temperature, that is, $T_w > T_{min}$. The wall-to-vapor HTC, evaluated in subroutine HVFILM, is the greater of the Dougall-Rohsenow or natural-convection correlations [Eqs. (F-238) and (F-239)]. The radiation HTC is evaluated in subroutine HTCOR. The Bromley correlation is evaluated in subroutine HLFILM.

If $\alpha > \alpha_c = 0.98$, the wall-to-vapor HTC is modified as follows:

$$h_{wg} = h_{wg} + (h_{gsav} - h_{wg}) \frac{\alpha - \alpha_c}{1 - \alpha_c} . \qquad \text{(F-253)}$$

This ensures that the vapor HTC approaches that for convective heat transfer to a single-phase vapor, h_{gsav}, at high void fractions.

F.2.1.4.5. **Weighting, Limits, and Averaging.** To ensure a smooth transition to convection to a single-phase vapor, h_{gsav}, at high void fractions, an interpolation is also used for the vapor HTC when $\alpha > 0.999$ in HTCOR. There are no rate limits used in the film-boiling heat-transfer regime.

F.2.1.4.6. **Assessment of the Correlation.** It was assumed that the wall heat transfer can be adequately described by the two components of radiation and pool boiling. Using a pool-boiling type of correlation, such as Bromley, to describe inverted annular-flow film boiling implicitly ignores the effect of mass flow rate on the magnitude of the HTC.

In film boiling, the liquid can be thought of as being in one of three forms. At high void fractions, the liquid is in the form of a dispersed spray of drops in a vapor and is referred to as the liquid-deficient region. At low void fractions, there is a continuous liquid core surrounded by a vapor annulus in which there may be entrained droplets; this regime is referred to as inverted annular flow (IAF). In the transition between these two regimes, the liquid is in the form of slugs and drops. It is assumed that the wall-to-liquid heat-transfer model can account for the effect of these different flow regimes by weighting factors. The Bromley correlation dominates at low void fractions.

The Bromley correlation is one of the most widely used for inverted annular-flow film boiling and was developed from data for boiling in a horizontal tube. The database for this correlation covered the following ranges:

Pressure	0.1 to 0.7 MPa
Heat Flux	30.0 to 130.0 kW · m^{-2}
Wall Superheat	278.0 to 778.0 K
Subcooling	< 77.9 K
Velocity	< 0.3 m · s^{-1}
Void	< 0.4

Recent film-boiling experiments indicate that several additional interacting factors influence heat-transfer rates during film boiling. The main ones are liquid subcooling, liquid velocity, vapor superheat, turbulence in the liquid, and instability of the vapor/liquid interface. The most important effects seem to be liquid subcooling and increased flow rate, both of which increase the heat-transfer rate. Neither of these effects is accounted for in the Bromley correlation. Figures F-39. to F-41. show some comparisons of the Bromley correlation with recent data (Ref. F-63.): in these figures T_c is the liquid subcooling and T_w is the wall superheat.

The Dougall-Rohsenow correlation was discussed in Section F.2.1.2.

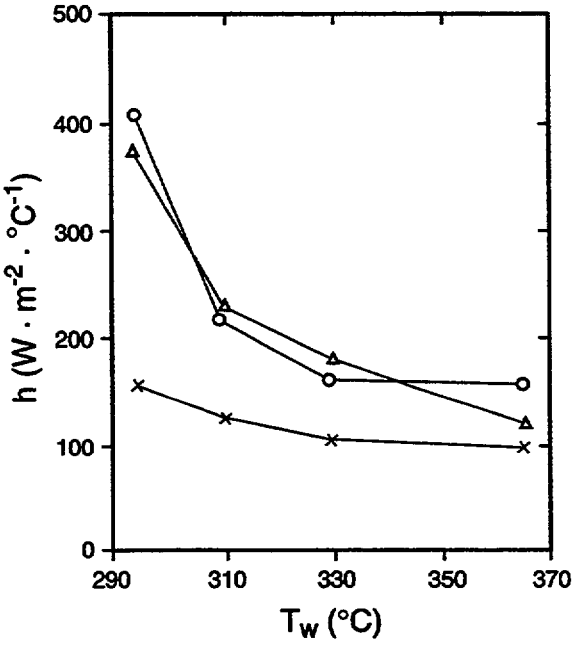

Fig. F-39. Effect of initial wall temperature. G=200 kg/m^2-s, T_c = 60°C.
o, Experimental; Δ (Ref. F-63.); ×, Bromley-type equation.

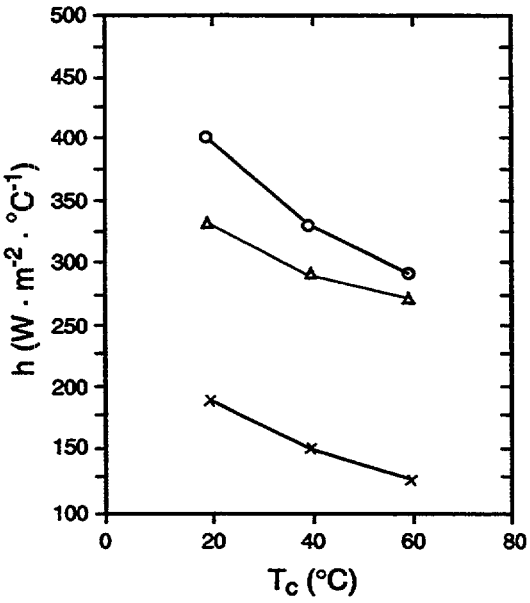

Fig. F-40. Effect of coolant inlet subcooling on the heat-transfer coefficient.
$G = 200$ kg/m^2-s, $T_w = 550$°C.
○, Experimental; Δ (Ref. F-63.); ×, Bromley-type equation.

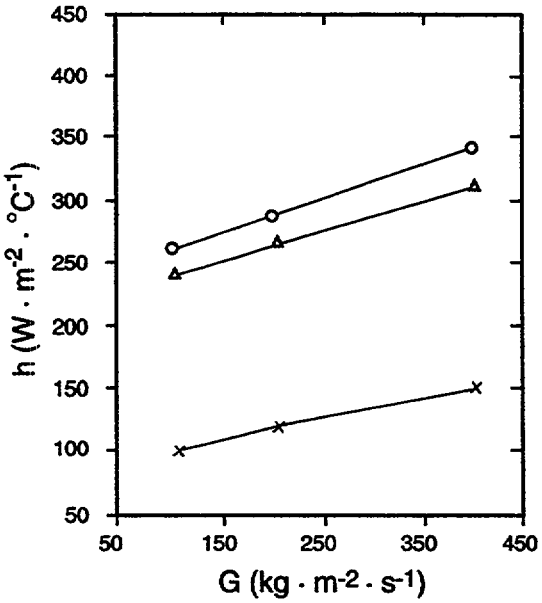

Fig. F-41. Effect of coolant inlet subcooling on the HTC. $T_w = 550$°C, $T_c = 60$°C.
○, experimental; Δ (Ref. F-63.); ×, Bromley-type equation.

A study was carried out with the TRAC-PF1/MOD1 code to calculate dispersed-flow heat transfer using different heat-transfer correlations, and the results were compared with experimental data from the heat-transfer test facility at Karlstein, FRG (Ref. F-64.). None of the film-boiling HTCs could be used with sufficient confidence over the entire post-CHF portion of the blowdown phase of a LOCA. Analysis of experimental and calculated results showed that in the post-CHF portion of the transient experiments, two significantly different HTCs could be calculated from the same thermal-hydraulic parameters. This effect of flow regime on the wall-to-liquid heat transfer cannot be reproduced by the HTCs that were developed and assessed using the data from steady-state conditions. The film-boiling model in TRAC attempts to account for the flow-regime effect by weighting the various HTCs by factors that are a function of void fraction except the Bromley correlation.

F.2.1.4.7. Scaling Considerations. Most of the experimental data on post-CHF heat transfer was obtained for tube geometry, and the validity of scaling to rod-bundle geometry has not been verified. The Bromley correlation, a pool-boiling correlation, was developed from data for a horizontal, heated cylinder. Applying it to vertical geometry in two-phase-flow film boiling is questionable.

F.2.1.4.8. Summary and Conclusions. A substantial amount of data for film-boiling heat transfer, obtained for simple geometries, is available and has been used to develop and evaluate film-boiling HTCs. Results of an evaluation of different heat-transfer correlations (Ref. F-64.) have shown that none of the correlations predicted HTCs of sufficient accuracy in the entire post-CHF region. This further emphasizes the discussion earlier in Section F.2. about how the closure relationships for Eqs. (F-185) through (F-186) should be determined.

The film-boiling model in TRAC is based upon correlations that were developed principally from post-CHF heat-transfer data for tube geometry and assuming thermodynamic equilibrium; the validity of scaling to rod-bundle geometry or thermodynamic nonequilibrium has not been verified. Significant discrepancies still exist among different correlations and between correlations and experimental data. Future code development work should examine new experimental data and correlations for possible improvements in the film-boiling model.

The discussions contained in Section F.2. concerning the minimum film-boiling temperature and Sections F.2.1.3. and F.2.1.9. should be reviewed in connection with this section.

F.2.1.5. Single-Phase Vapor (Heat-Transfer Regime 6). The case of convective heat transfer to a single-phase vapor is described by heat-transfer regime 6.

F.2.1.5.1. Basis for the Model. In this heat-transfer regime, when $T_f = 0.5\,(T_w + T_g) \geq T_{sv}$, the vapor HTC is the larger of either the turbulent natural-convection HTC, h_{gNC}, or the forced-convection HTC, h_{gturb}, obtained from the empirical correlation of Sieder and Tate (Ref. F-65., Eq. 8.59). These HTCs are expressed as

$$h_{gNC} = 0.13(k_g/D_H)Gr_g^{0.333}Pr_g^{0.333} , \quad \text{(F-254)}$$

and

$$h_{gturb} = 0.023(k_g/D_H)Re_g^{0.8}Pr_g^{0.333}(\mu_g/\mu_w)^{0.14} . \quad \text{(F-255)}$$

The viscosity ratio in Eq. (F-255) accounts for the effect of the radial viscosity gradient on the axial velocity distribution. The Sieder-Tate correlation is recommended for the following conditions:

		Reynolds number	$> 1.0\times10^4$
0.7	<	Prandtl number	< 16 700 .
		L / D	> 60

When $T_f < T_{sv}$ the Dittus-Boelter correlation

$$h_{gturb} = 0.023\ (k_g / D_H)\ Re_g^{0.8}\ Pr_g^{0.4} \quad \text{(F-256)}$$

replaces the Sieder-Tate correlation. T_{sv} is the saturation temperature of steam at its partial pressure.

F.2.1.5.2. Input Quantities to the Model. All properties are evaluated at temperature T_g in Eqs. (F-254) and (F-256) and at the film temperature, $T_f = 0.5\,(T_w + T_g)$, in Eq. (F-255), except μ_w, which is evaluated at the wall temperature, T_w. The velocity in the Reynolds number is the absolute value of the axial vapor velocity (see Section F.2.1.1.1.). The hydraulic diameter of the flow passage is used as the characteristic length. Viscosity, thermal conductivity, and specific heat are obtained from the functions VISCV, TMCV, and CPVV1. In order to avoid extra calls to the thermodynamics properties subroutine, THERMO, densities evaluated at either the film or wall temperatures are approximated by the first-order Taylor series terms as follows:

$$\rho_f = \rho_g + \frac{\partial \rho_g}{\partial T}(T_f - T_g) \quad \text{(F-257)}$$

and

$$\rho_w = \rho_g + \frac{\partial \rho_g}{\partial T}(T_w - T_g) . \quad \text{(F-258)}$$

In the correlation for the turbulent natural-convection HTC, Eq. (F-254), the coefficient of volumetric expansion, β, is approximated by $1/T_g$.

F.2.1.5.3. Constants. The correlations used in heat-transfer regime 6 are the same as in the cited references; no changes were made to any of the constants.

F.2.1.5.4. Model as Coded. The HTCs for heat-transfer regime 6 are evaluated in subroutine HTCOR. Equation (F-254) is used to calculate the turbulent, natural-convection HTC. For the turbulent, forced-convection HTC, Eq. (F-255) is evaluated if $T_f \geq T_{sv}$ and Eq. (F-256) is evaluated if $T_f < T_{sv}$. The Reynolds number is limited to minimum value of 1.0×10^{-20}.

The vapor HTC is found as follows:

$$h_{wg} = \max(h_{gNC}, h_{gturb}) \ . \tag{F-259}$$

A test is made on the void fraction. If $\alpha < 1$, two-phase liquid and vapor HTCs are calculated. For void fractions between $\alpha_c = 0.98$ and 1.0, the vapor HTC is found by interpolating between the single-phase and two-phase results and the liquid HTC is found by interpolating between a value of zero and the two-phase results. The resulting coefficients are therefore

$$\bar{h}_{w\ell} = h_{w\ell} + (0.0 - h_{w\ell}) \frac{\alpha - \alpha_c}{\alpha_3 + -\alpha_c} \tag{F-260}$$

and

$$\bar{h}_{wg} = h_{wg} + (h_{gsav} - h_{wg}) \frac{\alpha - \alpha_c}{\alpha_2 - \alpha_c} \ , \tag{F-261}$$

where h_{wl} and h_{wg} are the liquid and vapor two-phase HTCs and h_{gsav} is the HTC for single-phase vapor. If $0.97 < \alpha < 0.98$ (and $T_w \geq T_{sv}$ and $T_w \geq T_\ell$), two passes are made, first with $\alpha = 0.97$, and then with $\alpha = 0.98$. Finally, linear interpolation is done for both $h_{w\ell}$ and h_{wg} using their values computed at $\alpha = 0.97$ and $\alpha = 0.98$. The values of α_c, α_2, and α_3 are 0.98, 1.0, and 0.9999, respectively.

F.2.1.5.5. Assessment of the Correlation. When forced or natural convection to a two-phase mixture is not present and if the void fraction is $\geq \alpha_{CHF} = 0.97$, heat transfer to a single-phase fluid exists and Eqs. (F-254) to (F-256) are used together with the interpolation logic described in Section F.2.1.5.4. Equation (F-254) for the natural-convection HTC was discussed in Section F.2.1.2. Equation (F-256), the Dittus-Boelter correlation, was discussed in Section F.2.1.1. These correlations are well known and have been applied to a wide variety of fluids and geometries. If used within the recommended range of their parameters, the predicted HTCs are in good agreement with the data.

The Sieder-Tate correlation, Eq. (F-255), was developed to account for the effect of radial temperature gradients on the axial velocity distribution. For fluids with a large

temperature-dependent coefficient of viscosity or where there is a large temperature difference between the wall and the bulk fluid, a large radial gradient in the viscosity can result, which produces a velocity distribution that is considerably different from that occurring in isothermal flow. The viscosity gradient has opposite signs for heating and cooling. In channels having an axial power distribution, it is possible to have regions of $T_f \geq T_{sv}$ at the midplane yet $T_f \leq T_{sv}$ at the exit. This causes numerical problems in Eq. (F-257) in addition to the fact that high radial temperature differences have decreased so that the Dittus-Boelter equation is used for this situation.

F.2.1.5.6. **Scaling Considerations.** The Sieder-Tate correlation is a straightforward modification of the Dittus-Boelter equation. The Dittus-Boelter equation has been applied to a wide variety of fluids and geometries and is in good agreement with experimental data. The Sieder-Tate correlation should, therefore, also be applicable to the same fluids and geometries. Equation (F-256) for natural convection may be applied to flow past vertical cylinders if the criterion of Eq. (F-207) is met. In the turbulent regime, this implies $0.02 < D/L < 0.20$.

F.2.1.5.7. **Summary and Conclusions.** All of the correlations used in heat-transfer regime 6 are well known and have been applied to a wide variety of fluids and geometries. If used within the specified range of parameters, they predict HTCs that are in good agreement with experimental data.

F.2.1.6. **Condensation (Heat-Transfer Regime 11).** Heat-transfer regime 11 describes condensation of vapor on a cold wall.

F.2.1.6.1. **Basis for the Model.** The vapor HTC is determined from the following correlations:

$$h_{g\text{cond}} = 0.9428 \left[\frac{\rho_\ell^2 g k_\ell^3 h_{fg}}{\mu_\ell L (T_{sv} - T_w)} \right]^{0.25} \tag{F-262}$$

is the result of a theoretical analysis by Nusselt for the average HTC for a vapor condensing on a liquid film in laminar flow on a vertical wall (Ref. F-66., Eq. 13.6-5);

$$h_2 = 0.003 \left[\frac{\rho_\ell^2 g k_\ell^3 L (T_{sv} - T_w)}{h_{fg} \mu_\ell^3} \right]^{0.5} \tag{F-263}$$

is an empirical correlation used when the film Reynolds number is greater than 350 (Ref. F-66., Eq. 13.6-6);

$$h_{g\text{NC}} = 0.13 \frac{k_g}{D_H} Gr_g^{0.333} Pr_g^{0.333} \tag{F-264}$$

evaluates the turbulent, natural-convection vapor HTC on a vertical plate for $1.0\times10^{9}<\mathrm{Gr}\cdot\mathrm{Pr}<1.0\times10^{13}$; and

$$h_{g\mathrm{turb}} = 0.023\frac{k_g}{D_h}Re_g^{0.8}\,Pr_g^{0.3}\ . \tag{F-265}$$

The liquid HTC is evaluated from

$$h_{\mathrm{forc}} = 0.023\frac{k_\ell}{D_H}\left[\frac{\rho_\ell V(1.0-\alpha)D_H}{\mu_\ell}\right]^{0.8}(Pr_\ell)^{0.4}F\ , \tag{F-266}$$

where F is the Chen F factor defined by Eqs. (F-211) to (F-213). Equation (F-266) is the macroterm of the Chen correlation. In addition,

$$h_{w\ell} = \max(h_{\mathrm{NC1}}, h_{\mathrm{NC2}}, h_{g\mathrm{forc}})\ , \tag{F-267}$$

where

$$h_{\mathrm{NC1}} = 0.59\frac{k_\ell}{D_H}Gr_\ell^{0.25}Pr_\ell^{0.25} \tag{F-268}$$

is recommended for vertical plates and cylinders when $1.0\times10^{4}<\mathrm{Gr}\cdot\mathrm{Pr}<1.0\times10^{9}$ (Ref. F-10., Eq. 7-4b), and

$$h_{\mathrm{NC2}} = 0.10\frac{k_\ell}{D_H}Gr_\ell^{0.3333}Pr_\ell^{0.3333} \tag{F-269}$$

is recommended for vertical plates and cylinders when $1.0\times10^{9}<\mathrm{Gr}\cdot\mathrm{Pr}<1.0\times10^{13}$ (Ref. F-53., Table 7-1).

F.2.1.6.2. Input Quantities to the Model. In Eqs. (F-262) and (F-263), fluid properties are evaluated at the liquid temperature (T_ℓ), L is the cell length, and h_{fg} is the latent heat. In Eq. (F-264), vapor properties are evaluated at the vapor temperature T_g. In Eq. (F-265), if the film temperature $T_f=0.5\,(T_w+T_g)$ is less than T_{sv}, the vapor properties are evaluated at temperature T_g. If $T_f\geq T_{sv}$ the fluid properties are evaluated at temperature T_f. The characteristic length is the hydraulic diameter of the flow channel and the velocity is the absolute value of the axial vapor velocity (see Section F.2.1.1.1.).

In Eq. (F-266), the fluid properties are evaluated at the liquid temperature T_ℓ, the characteristic length is the hydraulic diameter of the flow channel, and the velocity is the absolute value of the axial liquid velocity defined previously.

In Eqs. (F-268) and (F-269), all fluid properties except density are evaluated at the liquid temperature T_ℓ. The density is evaluated at a temperature $T_f = 0.5\,(T_w + T_\ell)$ by a first-order Taylor-series approximation as

$$\rho_f = \rho_\ell + \frac{\partial \rho_\ell}{\partial T}(T_f - T_\ell) \ . \tag{F-270}$$

The coefficient of volumetric expansion is given by

$$\beta = -\frac{\partial \rho_\ell}{\partial T} / \rho_f \ . \tag{F-271}$$

F.2.1.6.3. Constants. The correlations used in heat-transfer regime 11 are the same as given in the references cited; no changes were made to the constants.

F.2.1.6.4. Model as Coded. This heat-transfer regime is assumed to exist when the following conditions are met:

a. $T_w < T_{sv}$ and $\alpha > 0.05$,

b. $T_w < T_g$ (or $T_w < T_\ell$ and IQUENCH not zero), and

c. $x \geq XCHEN = 0.71$,

where x is quality and IQUENCH is a flag indicating whether an interface exists (0 indicates no interface and 1 indicates an interface is present). When conditions *a*, *b*, and *c* are satisfied, Eqs. (F-262) to (F-265) are evaluated in subroutine HTCOR to calculate a value for the vapor HTC, h_{gcond}. For long tubes, Eq. (F-262) underestimates the HTC caused by ripples that develop on the liquid film. To account for this effect, a weighting factor WF ($0.0 \leq WF \leq 1.0$) based upon the length L is calculated. This factor is used to combine the laminar and turbulent HTCs h_{gcond} and h_2 to determine a weighted average vapor HTC. For short lengths where $WF \rightarrow 0.0$, the laminar HTC, h_{gcond}, is used; for large values of L where $WF \rightarrow 1.0$, the larger of the turbulent and laminar HTCs is used. The sink temperature for h_{gcond} is then converted from T_{sv} to T_g. These equations are as follows:

$$\bar{h}_{gcond} = h_{gcond}(1.0 - WF) + \max(h_{gcond}, h_2)WF \ , \tag{F-272}$$

$$WF = \min\left[1.0, \max\left(0.0, \frac{L - 0.2}{1.8}\right)\right] , \tag{F-273}$$

and

$$\bar{h}_{gcond} = h_{gcond}\frac{(T_{sv} - T_w)}{\max(|T_g - T_w|, 0.01)} \ . \tag{F-274}$$

The bar over h_{gcond} on the left-hand side of the equation indicates that it has been modified (as in a Fortran statement). For simplicity, the bar notation is dropped in the subsequent discussion.

The vapor HTC for single-phase vapor (called h'_{wg} here to avoid confusion with the final result) and the HTC for a condensing vapor are then found as follows:

$$h'_{wg} = \max(h_{gNC}, h_{gturb}) \tag{F-275}$$

and

$$\bar{h}_{gcond} = \max(h'_{wg}, h_{gcond}) \ . \tag{F-276}$$

For the liquid HTC, Equation (F-266) is evaluated in subroutine CHEN and the macroterm of the Chen correlation, h_{forc}, is returned to subroutine HTCOR (see Section F.2.1.2.). The microterm of the Chen correlation, h_{nucb}, is not evaluated in subroutine CHEN because in heat-transfer regime 11, $T_w < T_{sat}$. An if-test in the subroutine will cause the calculation of h_{nucb} to be bypassed when $(T_w - T_{sat}) < 0.0$. The following equation, evaluated in subroutine CHEN, determines the macroterm, h_{forc}, which is returned to subroutine HTCOR:

$$\bar{h}_{forc} = \max\left(h_{forc}, \frac{4.0k_\ell}{D_H}\right) . \tag{F-277}$$

Equation (F-268) and (F-269) are evaluated in subroutine HTCOR and the liquid HTC is determined as follows:

$$h_{w\ell} = \max(h_{NC1}, h_{NC2}, h_{forc}) \ . \tag{F-278}$$

The final values for the liquid and vapor HTCs are then determined by the following method:

If $x > 1.0$,

$$h_{w\ell} = 0.0 \quad \text{and} \tag{F-279}$$

$$h_{wg} = h_{gcond} \ . \tag{F-280}$$

If $0.71 \le x \le 1.0$,

$$\bar{h}_{w\ell} = h_{w\ell} + (0.0 - h_{w\ell}) \frac{x - XCHEN}{1.0 - XCHEN} \tag{F-281}$$

and

$$\bar{h}_{wg} = h_{gcond} \cdot \frac{x - XCHEN}{1.0 - XCHEN} \cdot \qquad \text{(F-282)}$$

F.2.1.6.5. Weighting, Limits, and Averaging. The term $L(T_{so} - T_w)$ in Eq. (F-262) is constrained to be ≥0.01. Equation (F-273) is used to weight the laminar and turbulent vapor HTCs calculated from Eqs. (F-262) and (F-263). The weighting function, *WF*, is limited to values between 0.0 and 1.0. The limits on the parameters in Eq. (F-266) are discussed in Section F.2.1.2. There are no rate limits.

F.2.1.6.6. Assessment of the Correlations. Equation (F-262) has been found to underestimate most experimental results for laminar film condensation by approximately 20%; a coefficient of 1.13 is recommended in place of 0.9428 (Ref. F-31., p. 488). Equation (F-263) is an empirical equation proposed for turbulent flow and fits the data for turbulent flow on vertical plates quite well (Ref. F-51., Fig. 13.6-2). Equations (F-264), (F-265), and (F-266) are discussed in Section F.2.1.2. and Eqs. (F-268) and (F-269) are discussed in Section F.2.1.1.

Equation (F-262) underestimates the HTC by about 20% in the laminar regime. If used at values of the Reynolds number >350, the error increases as the Reynolds number increases. Equation (F-263) will underestimate the HTC below a film Reynolds number of 350. The Dittus-Boelter correlation will underestimate the HTC below the recommended Reynolds number and L/D ratio. Equation (F-269) underestimates HTCs by approximately 10% for the range $1.0\times10^9 < Gr \cdot Pr < 1.0\times10^{13}$ as $Gr \cdot Pr$ decreases below 1.0×10^9, the correlation underestimates the HTC by an increasingly larger percentage.

F.2.1.6.7. Scaling Considerations. Although the Nusselt analysis for film-condensation heat transfer was developed for vertical flat plates, it may be applied to the internal or external surfaces of vertical tubes if the tube diameter is large compared to the film thickness (Ref. F-66., p. 527). The other correlations used in heat-transfer regime 11 are discussed in Sections F.2.1.1. and F.2.1.2.

F.2.1.6.8. Summary and Conclusions. The correlations used in heat-transfer regime 11 are all well known and, if used within the specified ranges of their parameters, predict HTCs that agree within 20% of the experimental data. Some minor adjustments of the constants [e.g., Eq. (F-262)] may improve the agreement.

The Chen correlation is based upon data for qualities, x, up to 0.71, and wall-to-fluid heat transfer. This quality limit is extrapolated in an ad hoc manner to apply to mixture-to-wall heat transfer. There is no basis for this extrapolation, however, it is assumed that when $x > 0.71$, the wall heat-transfer mechanism is convection to vapor or condensation. When $x \leq 0.71$, the wall heat-transfer mechanism is convection from a two-phase mixture.

The presence of small amounts of noncondensable gases will degrade the condensation heat transfer. This effect is not considered in the model. Future code development efforts should consider improving the wall condensation model.

F.2.1.7. Two-Phase Forced Convection (Heat-Transfer Regime 7). This heat-transfer regime is unique in that it is not part of the boiling curve discussed previously. The regime is used only when the input flag ICHF=0. The liquid and vapor HTCs, h_{wl} and h_{wg}, are calculated from regime 7 only.

F.2.1.7.1. Basis for the Model. The liquid HTC uses the Rohsenow-Choi equation (Ref. F-67.) for laminar forced convection, $h_{w\ell lam}$, and the Dittus-Boelter correlation for turbulent forced convection, $h_{w\ell turb}$, as follows:

$$h_{w\ell\,\mathrm{lam}} = \frac{4.0 k_\ell}{D_H} \tag{F-283}$$

and

$$h_{w\ell\,\mathrm{turb}} = \frac{0.023 k_\ell (Re)^{0.8} (Pr)^{0.4}}{D_H}\,, \tag{F-284}$$

where

$$Pr = \frac{c_{p\ell}\mu_\ell}{k_\ell}\,, \tag{F-285}$$

$$Re = \frac{G_m D_H}{\mu_m}\,, \tag{F-286}$$

and

$$\mu_m = \frac{1}{\frac{X_f}{\mu_g} + \frac{1-X_f}{\mu_\ell}}\,. \tag{F-287}$$

The term μ_m is the two-phase viscosity proposed by McAdams (Ref. F-68.), x_f is the flow quality, and G_m is the product of mixture velocity, V_m, and mixture density, ρ_m. Equation (F-283) is not recommended for Reynolds numbers greater than 2000. Equation (F-284) is recommended for the following conditions:

		Reynolds number	>	1.0×10^4
0.7	<	Prandtl number	<	160
		L / D	>	60

The vapor HTC is either the turbulent natural-convection HTC, h_{gNC}, or the Dittus-Boelter correlation for turbulent forced convection, h_{gturb}. These HTCs are given as

$$h_{gNC} = 0.13 k_g \left(\frac{\rho_g^2 g |T_w - T_g|}{\mu_g^2 T_g} \right)^{0.3333} \cdot (Pr)^{0.4} \tag{F-288}$$

and

$$h_{gturb} = 0.023 k_g (Re)^{0.8} (Pr)^{0.4} / D_H \, , \tag{F-289}$$

where

$$Re = \frac{\rho_g V_g D_H}{\mu_g} \tag{F-290}$$

and

$$Pr = \frac{c_{pg} \mu_g}{k_g} \, . \tag{F-291}$$

Equation (F-288) is recommended when the product of the Grashof and Prandtl numbers is in the range 1.0×10^9 to 1.0×10^{12}. Equation (F-289) is recommended for the same conditions as Eq. (F-284).

F.2.1.7.2. Input Quantities to the Model. In Eqs. (F-283) and (F-284), the liquid properties are evaluated at the liquid temperature T_ℓ. In Eq. (F-288), the vapor properties are evaluated at temperature T_g, the bulk temperature of the vapor. If the film temperature, $T_f = 0.5 (T_w + T_g)$, is greater than T_{sv}, the saturation temperature of steam at its partial pressure, the vapor properties in Eq. (F-289) are evaluated at the film temperature. If $T_f < T_{sv}$, the vapor properties in Eq. (F-289) are evaluated at the bulk temperature, T_g. The velocity in the Reynolds number in Eq. (F-290) is the axial vapor velocity (see Section F.2.1.1.1.). The hydraulic diameter of the flow channel is used as the characteristic length in Eqs. (F-286) and (F-290). Viscosity, thermal conductivity, and specific heat are obtained from the functions VISCV, THCV, and CPVV1. In order to avoid extra calls to the thermodynamic properties subroutine, THERMO, the density is approximated by a first-order Taylor-series expansion as follows:

$$\rho_f = \rho_g + \frac{\partial \rho_g}{\partial T} (T_f - T_g) \, . \tag{F-292}$$

In the correlation for turbulent natural convection, Eq. (F-288), the coefficient of volumetric expansion β has been approximated by $1/T_g$.

F.2.1.7.3. **Constants.** The correlations used in heat-transfer regime 7, Eqs. (F-283), (F-284), (F-288), and (F-289), are the same as in the references cited. No changes were made to any of the numerical constants.

F.2.1.7.4. **Model as Coded.** The HTCs for heat-transfer regime 7 are evaluated in subroutine HTCOR. If tests determine that heat-transfer regimes 1, 12, 11, and 6 (forced convection or natural convection to single-phase liquid, and condensation or forced convection to single-phase vapor) are not present and if $\alpha < \alpha_{CHF} = 0.97$ and ICHF = 0, it is assumed that heat-transfer regime 7 exists. The liquid HTC, h_{wl}, is evaluated from Eqs. (F-283) through (F-287). The liquid HTC is then determined as follows:

$$h_{w\ell} = \max(h_{w\ell\text{lam}}, h_{w\ell\text{turb}}) \ . \tag{F-293}$$

If $\alpha < \alpha_c = 0.98$, $h_{wg} = 0.0$; otherwise Eqs. (F-288) through (F-291) are used to evaluate h_{gNC} and h_{gturb}. The value of h_{wg} is determined from the equation

$$h_{wg} = \max(h_{gNC}, h_{gturb}) \ . \tag{F-294}$$

When the void fraction is greater than 0.98, the liquid and vapor HTCs are found by interpolating between the present values and the values for single-phase vapor ($h_{wl} = 0.0$ and $h_{wg} = h_{gsav}$). That is,

$$\bar{h}_{w\ell} = h_{w\ell} + (0.0 - h_{w\ell})\left(\frac{\alpha - \alpha_c}{\alpha_3 - \alpha_c}\right) \tag{F-295}$$

and

$$\bar{h}_{wg} = h_{wg} + (h_{gsav} - h_{wg})\left(\frac{\alpha - \alpha_c}{\alpha_2 - \alpha_c}\right) , \tag{F-296}$$

where

$\alpha_2 = 1.0$, $\alpha_3 = 0.9999$, and $\alpha_c = 0.98$.

F.2.1.7.5. **Weighting, Limits, and Averaging.** For void fractions between 0.98 and 1.0, Eqs. (F-295) and (F-296) are used to weight the current two-phase HTCs, h_{wl} and h_{wg}, with the single-phase vapor HTCs, h_{gsav} and $h_{wl} = 0$. The Reynolds number and temperature difference $|T_w - T_g|$ are limited to minimum values of 1.0×10^{-20}. There are no rate limits.

F.2.1.7.6. **Assessment of the Correlations.** The correlations for heat-transfer regime 7 are discussed in Sections F.2.1.1. and F.2.1.2.

F.2.1.7.7. **Scaling Considerations.** Refer to Sections F.2.1.1. and F.2.1.2.

F.2.1.7.8. Summary and Conclusions. Refer to Sections F.2.1.1. and F.2.1.2. This regime was placed in the code in its early days to minimize the execution time associated with wall heat transfer. It is recommended that the user not use the model, i.e., set ICHF = 0.

F.2.1.8. Critical Heat Flux. The code requires the CHF correlation to provide a boundary between nucleate boiling and transition boiling.

F.2.1.8.1. Basis for the Model. The CHF prediction package in TRAC consists of the Biasi correlation (Ref. F-69.) with modifications at low mass velocities and high void fractions. The Biasi correlation is chosen because it is (*i*) an empirical correlation with a wide database, (*ii*) based upon the local-condition approach, and (*iii*) valid for the high-void-fraction, dryout type of CHF. The alternatives to empirical correlations are theoretical correlations and CHF tables. Theoretical correlations have a limited applicability because of their various simplifying assumptions. Their use is difficult because, in general, they do not yield a closed-form correlation. Similarly, CHF tables are expensive to use in large, multipurpose codes such as TRAC because they require multiple interpolations or extrapolations during each iteration.

The more successful CHF correlations developed in recent years are based upon the boiling-length concept, in which the inlet quality or enthalpy explicitly appears in the correlation. During transient analysis, however, the use of boiling-length correlations is often not appropriate. (See the discussion in Section F.2.) For example, during certain reactor accidents, such as cold-leg-break LOCAs, the core experiences a flow reversal, in which case the inlet becomes ambiguous.

Consequently, the CHF-prediction package of TRAC is restricted to correlations based upon the local-condition approach. A complete CHF package should include a number of these correlations to cover the entire spectrum of thermal-hydraulic conditions. As mentioned earlier, the Biasi correlation (Ref. F-69.) is only valid for the low- and high-quality, dryout type of CHF. A very low-quality, departure-from-nucleate-boiling type of CHF correlation is not included in the TRAC package because most transients (such as LOCA) yield a high void fraction in the core before reaching the CHF.

The Biasi correlation (Ref. F-69., p. 531. Eq. 2) consists of the following two equations from which the maximum CHF value calculated by these equation is assigned:

$$q_{\mathrm{CHF}} = \frac{1.883\times10^{3}}{D^{n}G^{1/6}}\left[\frac{f_p}{G^{1/6}} - x_e\right] \qquad \text{(F-297)}$$

and

$$q_{\mathrm{CHF}} = \frac{3.78\times10^{3}}{D^{n}G^{0.6}}h_p(1-x_e)\ , \qquad \text{(F-298)}$$

where

$n = 0.4$ for $D \geq 1$ cm,

$n = 0.6$ for $D < 1$ cm,

$f_p = 0.7246 + 0.099P \exp(-0.032P)$,

$h_p = -1.159 + \frac{8.99P}{10+P^2} + 0.149P \exp(-0.019P)$,

D = diameter (cm),

G = mass flux ($g \cdot cm^{-2} \cdot s^{-1}$),

P = pressure (bar), and

x_e = equilibrium quality.

Typically, Eq. (F-297) is for low quality and Eq. (F-298) is for high quality. For a given mass flux and tube diameter, the switch-over quality between the two equations is shown as a function of pressure in Fig. F-42. As seen in this figure, the switch-over quality is not constant and varies between 0.3 and 0.68 within the pressure range of the Biasi correlation. It exhibits a peak between 2 and 3 MPa.

The Biasi correlation was originally correlated over a database containing 4551 CHF data points. The ranges of the CHF parameters within this database are as follows:

0.3 cm	$<$	D $<$	3.75 cm
20 cm	$<$	L $<$	600 cm
0.27 MPa	$<$	P $<$	14.0 MPa
10 $g \cdot cm^{-2} \cdot s^{-1}$	$<$	G $<$	600 $g \cdot cm^{-2} \cdot s^{-1}$
x_{inlet}	$<$	0	
$\frac{1}{1+\rho_\ell/\rho_g}$	$<$	x $<$	1

Figures F-43., F-44., F-45., and F-46. show the typical behavior of the Biasi correlation on the q_{CHF}–$|G|$, q_{CHF}–x_e, q_{CHF}–P, and q_{CHF}–D planes, respectively. These figures also show the parametric range of the Biasi correlation. Figure F-43. illustrates the inverse mass flux effect, where the CHF decreases with increasing mass flux. The behavior of CHF with respect to the equilibrium quality is shown in Fig. F-44. The point at which the slope is discontinuous is the intersection between Eqs. (F-297) and (F-298). As shown in Fig. F-45., CHF exhibits a maximum between 2 and 3 MPa when plotted with respect to the system pressure. Finally, Fig. F-46. shows that CHF decreases with increasing diameter. The effect for small diameters ($D \leq 1$ cm) is important, possibly because of the enhanced droplet deposition in small-diameter with increasing diameter.

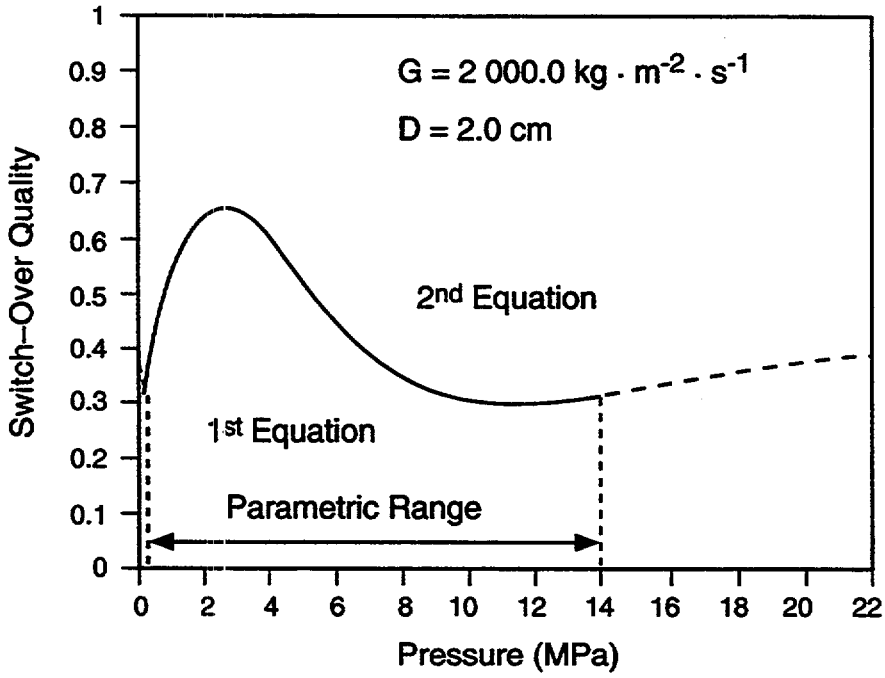

Fig. F-42. The switch-over quality between the two equations of the Biasi correlation as a function of the system pressure.

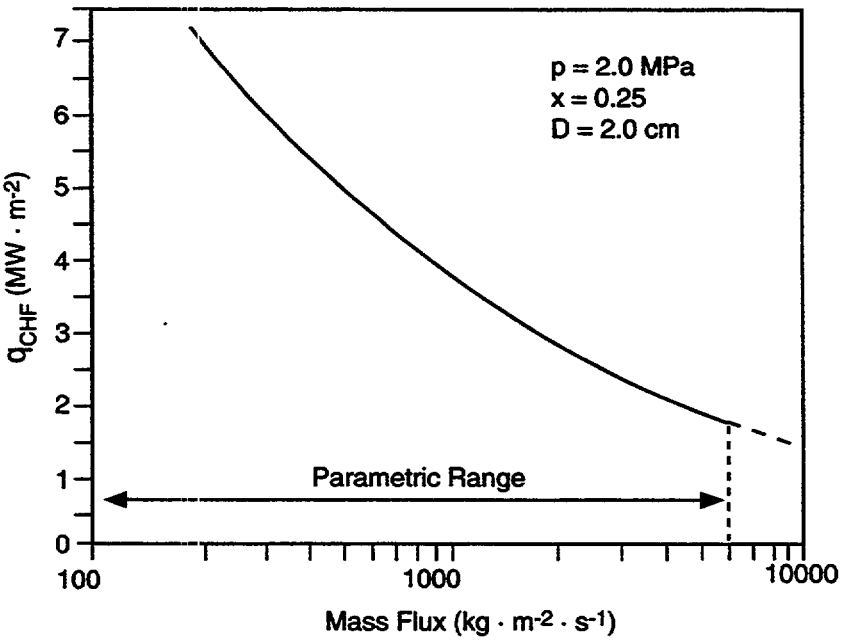

Fig. F-43. CHF vs. mass flux predicted by the Biasi correlation.

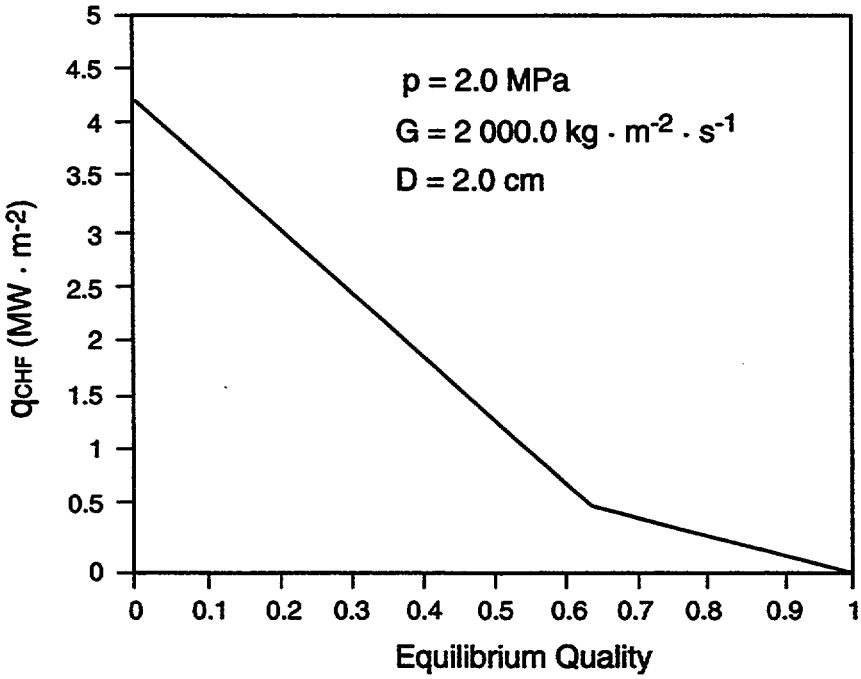

Fig. F-44. CHF vs. equilibrium quality predicted by the Biasi correlation.

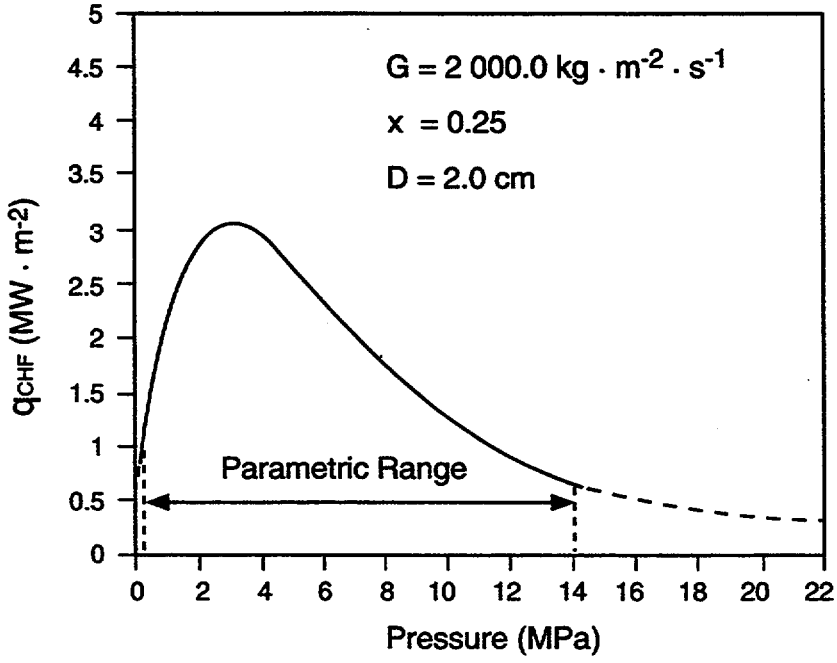

Fig. F-45. CHF vs. system pressure predicted by the Biasi correlation.

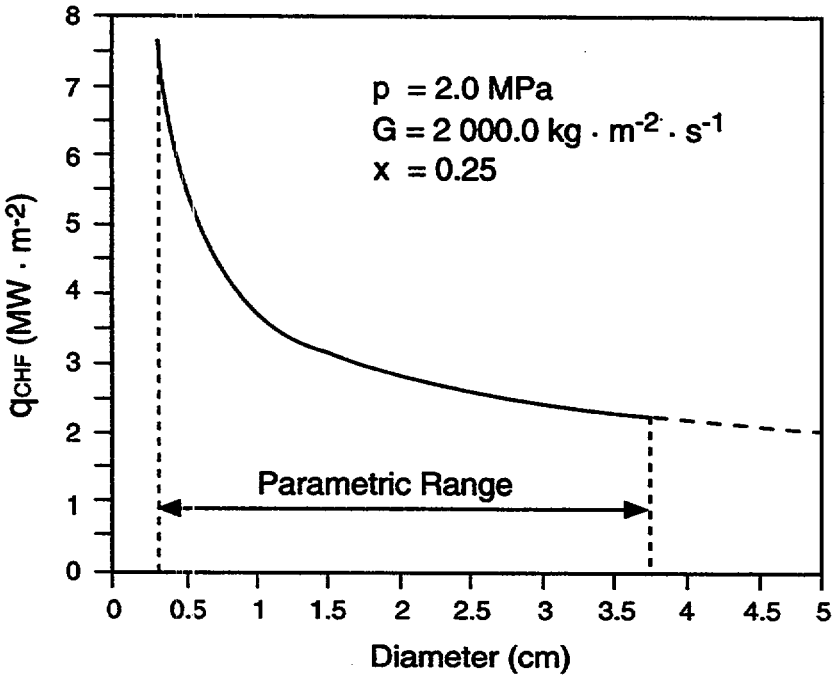

Fig. F-46. CHF vs. tube diameter predicted by the Biasi correlation.

F.2.1.8.2. Assumptions Made in Implementing the Correlations in the Code. CHF prediction in TRAC using the Biasi correlation is based upon the following assumptions:

i. CHF is only a function of the local thermal-hydraulic parameters, and the history effects are negligible.

ii. CHF is not affected by the flow direction. Using this assumption, the mass flux G in the original correlation is replaced by $|G|$ in the code.

iii. The Biasi correlation is originally written for round tubes. In the code it is assumed that the tube diameter may be replaced by the subchannel hydraulic diameter in rod-bundle geometry.

F.2.1.8.3. Constants. The Biasi correlation is written in cgs units. Thus, Eqs. (F-297) and (F-298) yield the CHF in $W \cdot cm^{-2}$. To obtain the CHF directly in $W \cdot m^{-2}$, Eqs. (F-297) and (F-298) are multiplied by 10^4 in the code. All the other constants remain unchanged.

F.2.1.8.4. Model as Coded. In TRAC, the CHF calculations are done in subroutines CHF and CHF1. The CHF temperature is needed in HTCOR to differentiate between the nucleate-boiling and transition-boiling regimes. The CHF temperature is also needed for computing the HTC in the transition-boiling regime. For this information, subroutine CHF is called from within subroutine HTCOR when the value of INVAN≠0. INVAN is a flag used to determine the wall temperature that is used in the flow regime. When

INVAN=0, T_{sat} is used as the temperature at which transition boiling begins. When INVAN≠0, T_{CHF} is used to define the start of transition boiling. In subroutine CHF, the value of the CHF calculated in subroutine CHF1 is used with the Chen nucleate-boiling heat-transfer correlation to obtain the corresponding CHF temperature. This requires an iterative solution that is done by using both the Newton-Raphson and bisection procedures as described in Ref. F-74., Chapter 2. The iteration is started by using $T_{CHF}=T_{sat}+0.5\,K$ as the initial guess. The latest calculated value of T_{CHF} is used in subsequent iterations. A maximum of 35 iterations are allowed during the solution of a single value of T_{CHF}. The magnitude of the CHF temperature is bound at the lower and upper ends as follows:

$$T_{sat}+0.5K \le T_{CHF} \le T_{sat}+100K \ .$$

The CHF prediction package of TRAC subroutine CHF1 consists of the Biasi correlation with one change in the constants, as described above. Therefore, the correlation is coded as follows:

$$q_{CHF1}=\frac{1.883\times10^{7}}{D_H^n|G|^{1/6}}\left[\frac{f_p}{|G|^{1/6}}-x_e\right], \tag{F-299}$$

$$q_{CHF2}=\frac{3.78\times10^{7}}{D_H^n|G|^{0.6}}h_p(1-x_e), \tag{F-300}$$

and

$$q_{CHF} = \max(q_{CHF1}, q_{CHF2}) \ . \tag{F-301}$$

For low mass fluxes and high void fractions, subroutine CHF1 also contains additional considerations. At mass fluxes lower than 200 kg/m^2-s, the Biasi correlation overpredicts the data due to an inverse mass-flux effect (see Fig. F-43.). Currently, for such low mass fluxes, the CHF is evaluated by using the Biasi correlation with $|G|=200$ kg/m^2-s. Figure F-47. shows this low mass flux model for a given pressure, hydraulic diameter, and equilibrium quality.

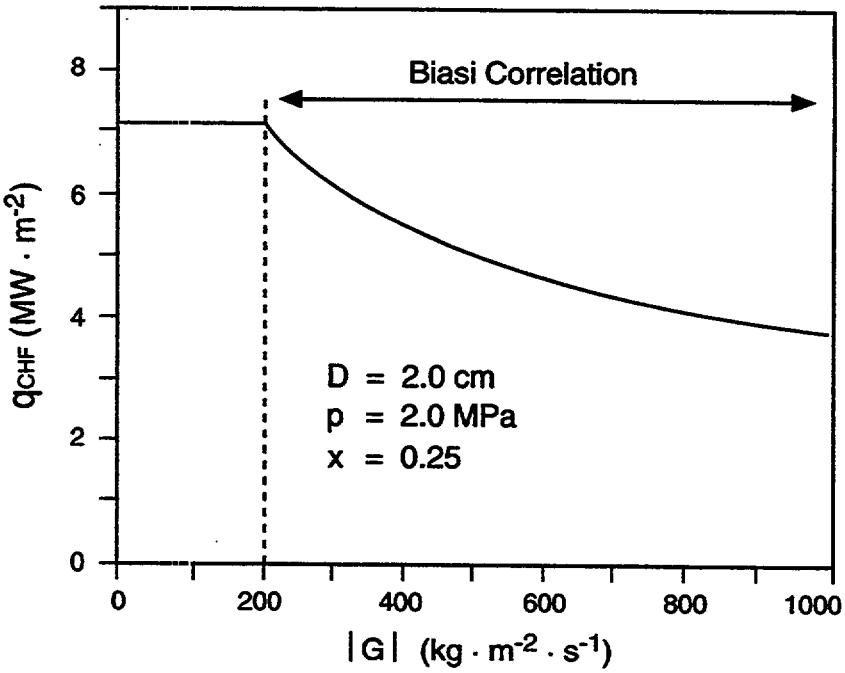

Fig. F-47. CHF model for $|G| \leq 200$ kg/m^2-s.

At high void fractions, the Biasi correlation is restricted by a limiting void fraction. In TRAC, the limiting void fraction is taken as 0.98. Above this value, CHF is assumed to be very small (1 W·m^{-2} is the value used in TRAC). Void fractions between 0.97 and 0.98 fall in the transition region where the CHF is linearly interpolated between the Biasi prediction at $\alpha = 0.97$ and 1 W·m^{-2}. Figure F-48. shows a qualitative description of this limiting-void-fraction concept. Because the Biasi correlation is written in terms of the equilibrium quality, it is hard to translate this limiting void fraction into a limiting quality. The relation between these two quantities is strongly affected by the slip ratio between the phase velocities. Figure F-49. shows the equilibrium quality corresponding to the limiting void fraction of 0.97 for a cocurrent flow, as a function of the slip ratio and system pressure. As seen in this figure, the limiting void fraction is less than or equal to 1; for some transient upflow or cocurrent downflow situations this may not be true. For this reason, slip ratios of less than 1 are shown in Fig. F-49.

F.2.1.8.5. Assessment of the Correlation. The Biasi correlation is one of the more frequently referenced correlations in the literature. The results of a major assessment of this correlation were recently reported by Groeneveld et al. (Ref. F-70., Figs. 3 and 4, Table 4), in which the Biasi correlation was compared to approximately 15000 steady-state water data points that are stored in the Chalk River Nuclear Laboratories' CHF data bank. The results of this assessment are shown in Table F-9. As shown in this table, the Biasi correlation is fairly successful in predicting the data with constant inlet subcooling, where the local equilibrium quality is calculated through an energy balance.

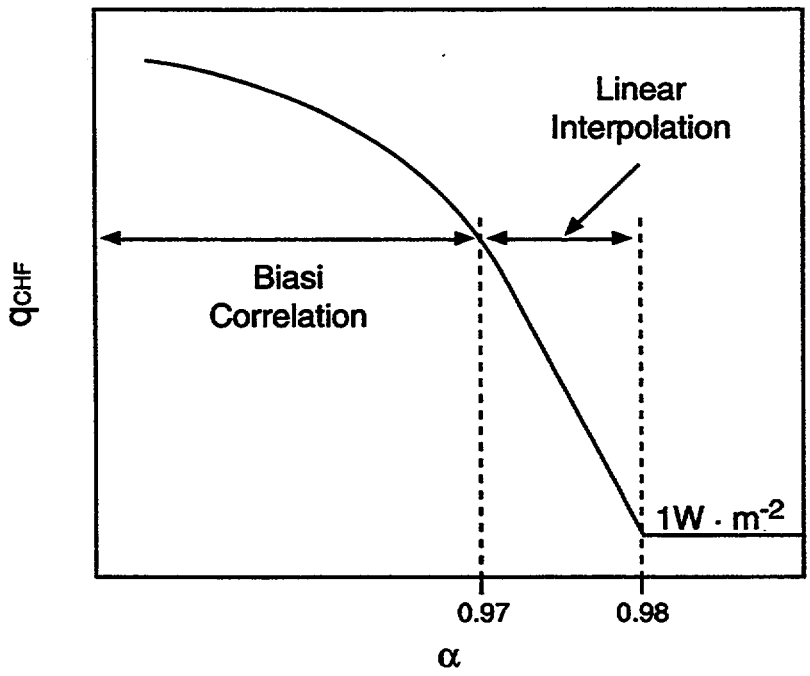

Fig. F-48. CHF model at high void fraction.

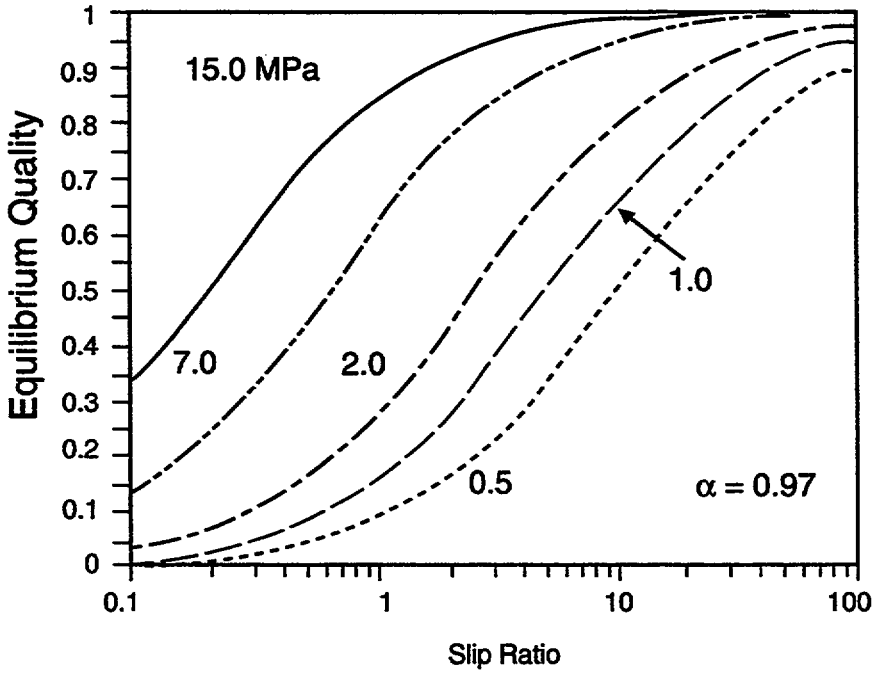

Fig. F-49. Equilibrium quality vs. slip ratio at different pressures for $\alpha = 0.97$.

TABLE F-9.
Performance of the BIASI Correlation as Compared to the Chalk River Nuclear Laboratories' CHF Data Bank (Ref. F-70., Table 4)

	DATA WITHIN THE ERROR BOUND (%)						No. of Data
	Constant Dryout Quality Data			Constant Inlet Subcooling			
	±10%	±20%	±50%	±10%	±20%	±50%	Points
All Data	19.30	36.64	67.04	71.23	92.38	99.39	14401
Range of Validity Only	21.32	41.12	73.04	77.60	96.60	99.91	9936

The Biasi correlation is also compared to transient CHF data by Leung (Ref. F-71.). Table F-10. contains the blowdown and flow transient experiments analyzed by Leung. Most of these experiments were very well-instrumented for CHF where the CHF was measured at various locations. Figure F-50. shows the results of the data comparison for the experiments with high mass fluxes. For each test, at locations at which CHF occurs more than once, only the earliest CHF is plotted in this figure. The data corresponding to low mass fluxes ($|G| < 200\ kg/m^2\text{-}s$) are not included in Figure F-50. Leung's analysis (Ref. F-71.) shows that these low-mass-flux data are best predicted by using the Griffith-Zuber correlation (Ref. F-72.). However, because of various uncertainties associated with this assessment, the Griffith-Zuber correlation is not included in TRAC. CHF modeling at low mass fluxes suffers from the following limitations:

i. As reported by Groeneveld et al. (Ref. F-70., p. 47), the number of steady-state CHF data for low mass fluxes is very limited. This makes the development of a reliable correlation very difficult.

ii. At such low magnitudes, an accurate measurement of two-phase mass fluxes is very difficult, as discussed by Leung (Ref. F-71.).

iii. At low mass fluxes, the CHF with upward flow may be considerably different from the CHF with downward flow.

iv. At low mass fluxes, the slip ratios may be very high. Therefore, a homogeneous flow analysis, as done by Leung (Ref. F-71.), may be erroneous.

v. In homogeneous flow, there is a big discontinuity between the Griffith-Zuber and Biasi correlations at their suggested boundary.

TABLE F-10.
Blowdown and Flow Transient CHF Experiments
Analyzed by Leung (Ref. F-71.)

Blowdown (high mass flux)	Blowdown (low mass flux)	Flow Transients
LOFT Columbia Loop THTF-Test 105 - Test 104 - Test 178 - Test 181 - Test 177	PBF LOC-IIC Semiscale Mod-1, S-02-1 S-06-6	Moxon-Edwards Roumy
Semiscale Mod-1-S-02-9 -S-29-2 -S-28-1		
Semiscale Mod-3-S-07-3 -S-07-9		

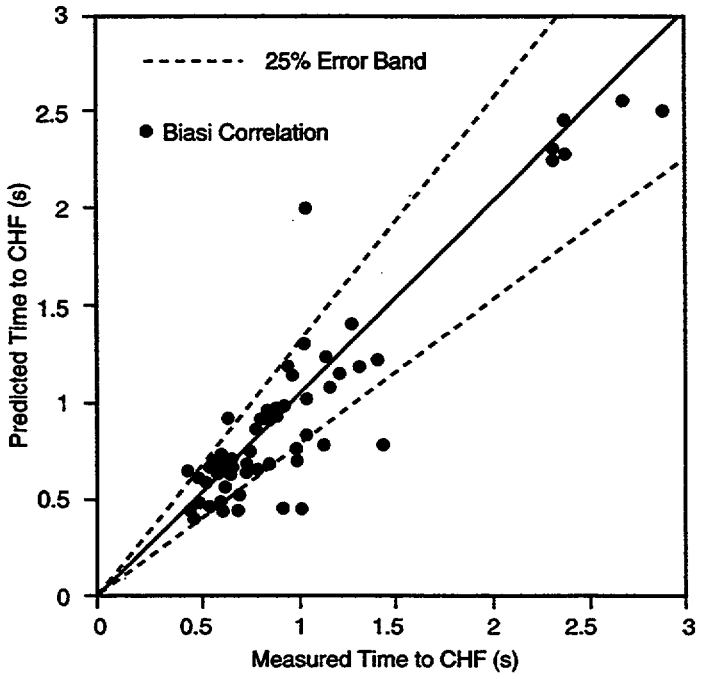

Fig. F-50. Comparison of the Biasi correlation with the blowdown CHF data.

A more detailed analysis and discussion of blowdown CHF experiments may be found within Ref. F-73., Chap. 6.

The assessment of the Biasi correlation as compared to the flow transients is shown in Fig. F-51. As shown in this figure, the earlier CHFs measured in Moxon-Edwards' tests (Ref. F-71.) are overpredicted by the Biasi correlation, whereas the later CHFs are better predicted. The only CHF measure in Roumy's experiment (Ref. F-71.) is predicted with exceptional accuracy by the Biasi correlation.

F.2.1.8.6. Scaling Considerations. The Biasi correlation is developed for round tubes; its success in predicting the blowdown data in various tests (as shown in Fig. F-50.) suggests that it can be scaled to rod-bundle geometry using a hydraulic diameter.

F.2.1.8.7. Summary and Conclusions. When compared to steady-state (Ref. F-74.) and transient (Ref. F-70.) annular-flow dryout type of CHF data, the Biasi correlation yields reasonable results, as shown in Table F-9. and Figs. F-50. and F-51. Most of the blowdown and flow transients result in an annular-flow regime prior to reaching the CHF. Consequently, the CHF package of TRAC gives reasonably accurate CHF predictions in many cases. However, the package has deficiencies in the three areas described below.

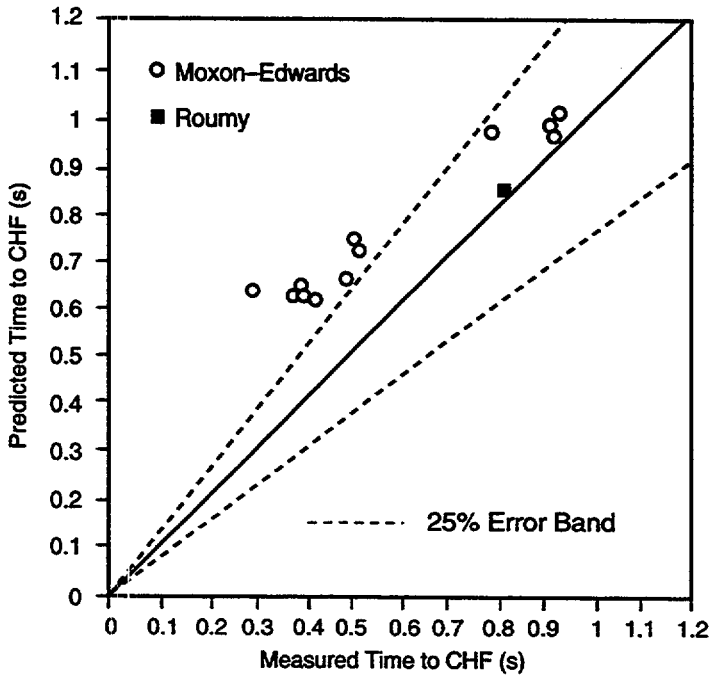

Fig. F-51. Comparison of the Biasi correlation with the flow-transient CHF data.

First, the code cannot accurately model subcooled or very low-quality departure from nucleate boiling. Future code development efforts must consider implementing a departure from the nucleate-boiling-correlation model into the code. Second, at low mass fluxes ($|G| \leq 2200\ kg/m^2\text{-}s$), one must use the code prediction with extreme caution. Very little information is available in this area, and further experimental CHF studies are required. Third, the high-void-fraction model must be further assessed even though it gives favorable results for rapid depressurization transients in which a sudden core voiding occurs.

One must also be aware of the limitations imposed by the quasi-steady approach used by TRAC. One example in which this might prove to be a problem is applying the present model to rapid transients such as quenching, where the CHF prediction is needed to calculate the return to nucleate boiling while going from right to left on a typical boiling curve. A second example would be the application of the code to reactivity-initiated accident transients.

Finally, one should be aware of the question of whether the quenching CHF is the same as the heat-up CHF. TRAC models assume this to be true, but most data show it not to be the case.

F.2.1.9. Minimum Stable Film-Boiling Temperature Correlation. The minimum stable film-boiling temperature, T_{min}, is the intersection point between the transition- and film-boiling heat-transfer regimes. It is also used in the interpolation scheme for determining the transition-boiling heat flux. It has been discussed in detail as a subtopic in Section F.2. relative to the interpretation of a true minimum temperature and an apparent minimum temperature. The quantity defined in TRAC is meant to represent the true minimum temperature.

F.2.1.9.1. Basis for the Model. The minimum stable film-boiling-temperature correlation (Ref. F-75., Eq. 7) used is

$$T_{min} = T_{NH} + (T_{NH} - T_\ell)R^{1/2} , \tag{F-302}$$

where

$$R = \frac{(k\rho c_p)_\ell}{(k\rho c_p)_w} \tag{F-303}$$

and T_{NH} is the homogenous-nucleation temperature. In Eq. (F-303), the subscript ℓ indicates liquid properties and the subscript w refers to wall properties. The homogenous-nucleation temperature, given by Fauske, is fitted by a third-order polynomial taken from the COBRA-TF code[1] and is given as

$$T_{NH} = 705.44 - (4.722 \times 10^{-2})DP + (2.3907 \times 10^{-5})DP^2 - (5.8193 \times 10^{-9})DP^3 , \tag{F-304}$$

where

$$DP = 3203.6 - P \ . \qquad \text{(F-305)}$$

The pressure is in units of pounds per square inch and the temperature is in Fahrenheit units.

F.2.1.9.2. Input Quantities to the Model. The thermal conductivity, specific heat, and density of the wall material are evaluated in subroutine MSTRCT; the corresponding fluid properties are evaluated in functions THCV, CPVV1, and subroutine THERMO. The fluid pressure is temporarily converted from Pascals to pounds per square inch in subroutine TMSFB. Equation (F-304) is evaluated and T_{NH} is converted from Fahrenheit units to Kelvin.

F.2.1.9.3. Constants. The homogeneous-nucleation temperature given by Fauske was fitted by a third-order polynomial for the pressure difference, *DP*. No changes were made to any of the numerical constants in the model.

F.2.1.9.4. Model as Coded. The minimum stable film-boiling temperature, T_{min}, is calculated in subroutine TMSFB. This subroutine is called from subroutine HTCOR when a value for T_{min} is required. All required data needed in subroutine TMSFB are in the call statement. In subroutine TMSFB, pressure is converted from units of Pascals to units of pounds per square inch and Eqs. (F-304) and (F-305) are evaluated. The homogeneous-nucleation temperature, T_{NH} is then converted from °F to K and Eq. (F-302) evaluated for T_{min}. The final value for T_{min} is determined by the following relation:

$$T_{min} = \max\,(T_{min}, T_{sat} + 0.0001\ \text{K}) \ . \qquad \text{(F-306)}$$

This value of T_{min} is returned to subroutine HTCOR.

F.2.1.9.5. Weighting, Limits, and Averaging. Equation (F-306) limits the minimum value of T_{min} to T_{sat} + 0.0001 K. There are no weighting factors or rate limits applied to the correlation.

F.2.1.9.6. Assessment of the Correlation. Cheng et al. (Ref. F-76.) have recently presented a measurement of true minimum film-boiling temperatures to which a comparison of Eq. (F-302) can be made. Cheng's experiment extends earlier work by Groeneveld and Stewart (Ref. F-77.) to separate the effects of axial conduction and hydraulic transients and is run over a short-enough test section in a steady-state manner such that these data, along with those of Groeneveld, represent the only known forced-convective true T_{min} data.

---

1. This information was provided by M. J. Thurgood and J. M. Kelly, Batelle Pacific Northwest Laboratories, December 1979.

Both Cheng and Groeneveld developed empirical correlations to represent their data. We note these correlations because they will be used in the data comparison instead of the data itself. Cheng's correlation is given by

$$T_{min} = 169.66 + 0.1050 \times 10^3 P + 0.1444G + 3.0347\Delta T_{sub} , \quad \text{(F-307)}$$

where temperature is in °C, P in MPa, G in kg/m^2-s, and ΔT_{sub} is the subcooling in °C. His database included subcoolings of 2° to 300°C, mass fluxes of 50 to 682 kg/m^2-s, and pressures of 0.101 to 1.03 MPa. Groeneveld's correlation had two parts given by

$$T_{min} = 284.7 + 44.11P - 3.72P^2 \quad \text{(F-308)}$$

for the saturated inlet flow case (quality ≥ 0), and

$$T_{min} = 284.7 + 44.11P - 3.72P^2 - \frac{x(10)^4}{2.819 + 1.22P} \quad \text{(F-309)}$$

for the subcooled case ($x < 0$), where x is the quality corresponding to the subcooling on an energy basis. His database included saturated two-phase conditions and qualities down to –0.0215 at 0.1 MPa and –0.1212 at 9.064 MPa, mass fluxes of 110 to 2750 kg/m^2-s, and pressures of 3.1 to 9.087 MPa.

Figures F-52. and F-53. plot Eq. (F-302) against Cheng's correlation, Eq. (F-307), as a function of pressure over his pressure range. Figure F-52. shows the effect of mass flux at a fixed subcooling of 10 K. Figure F-53. shows the effect of subcooling at a fixed mass flux of 200 kg/m^2-s. The TRAC correlation shows little sensitivity to the subcooling variation. It typically overpredicts the minimum temperature over the range of flows studied, but, as seen, this is a function of pressure and subcooling. For the higher pressures, higher mass fluxes, and higher subcoolings, the TRAC prediction is better. It should be noted that the range of temperatures represented by Cheng's results are much lower than those typically quoted in many reflood experiments. This is because these are true T_{min}s as opposed to apparent T_{min}s arising from transient hydraulic and axial conduction effects. Figure F-54. plots Eq. (F-302) evaluated at saturated conditions against Groeneveld's correlation, Eqs. (F-308) and (F-309). The effect of subcooling on Groeneveld's correlation is also noted. The prediction of saturated conditions is reasonable but subcooling increases the difference. Figure F-55. further investigates the subcooling effect relative to Groeneveld's correlation at 2 MPa. As observed in Figs. F-52. and F-53., Eq. (F-302) does not correctly include the effects of any significant subcoolings. It should be noted that at this pressure, Groeneveld's data had qualities of -0.0534 or greater so that the left-hand portion of his curve as plotted is an extrapolation. Nelson noted this breakdown in the model with respect to subcooling (Ref. F-41., p. 51), but these comparisons to data show the breakdown to be earlier than he indicated. (Note that there was a misprint within the reference in that the subcooling limit should be 28.7 K instead of the 287 K as shown.)

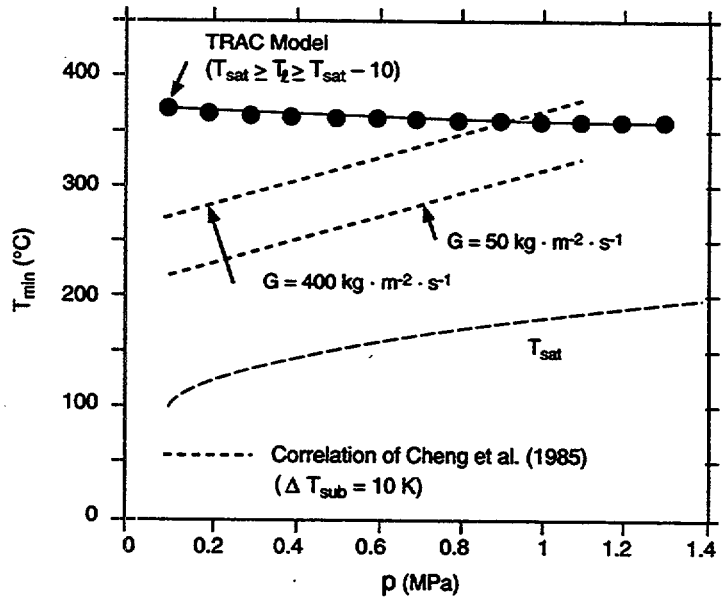

Fig. F-52. Comparison with Cheng's results of true T_{min} vs. pressure with fixed subcooling (10 K) and parametric effect of mass flux.

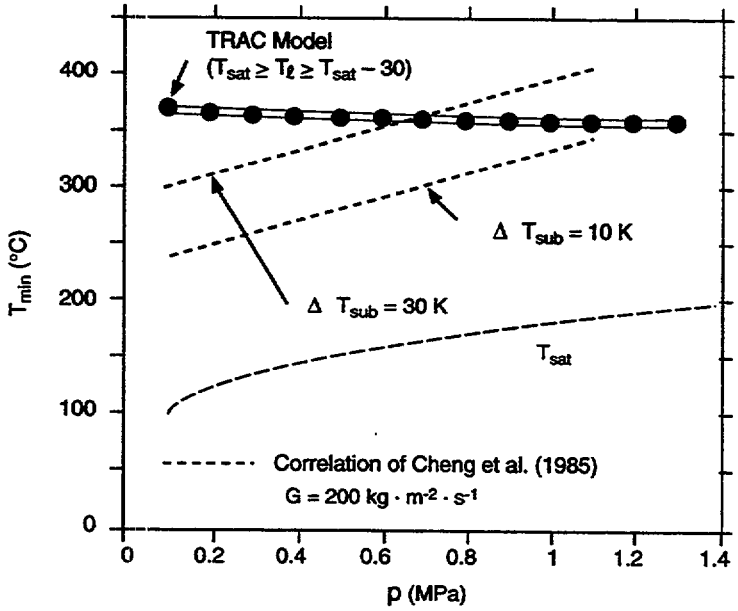

Fig. F-53. Comparison with Cheng's results of true T_{min} vs. pressure with fixed mass flux (200 kg/m^2-s) and parametric effect of subcooling.

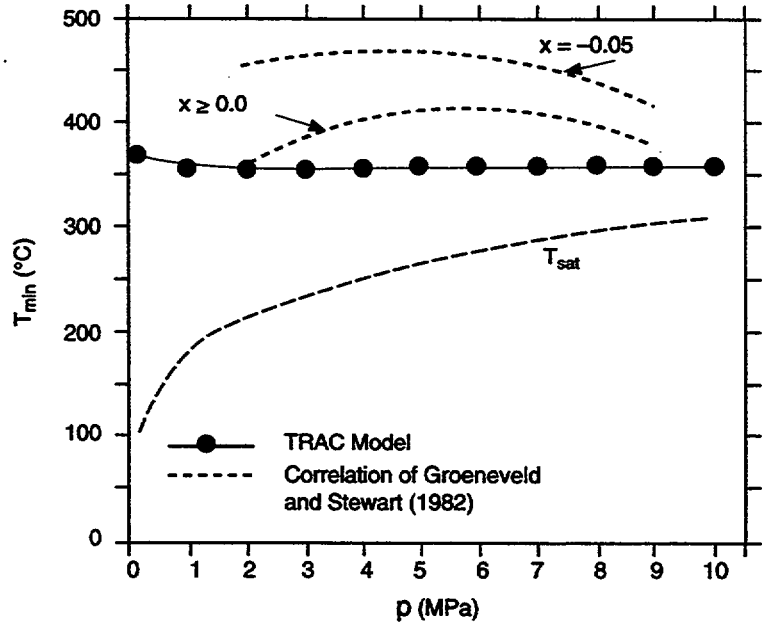

Fig. F-54. Comparison with Groeneveld's results of true T_{min} vs. pressure with parametric effect of subcooling.

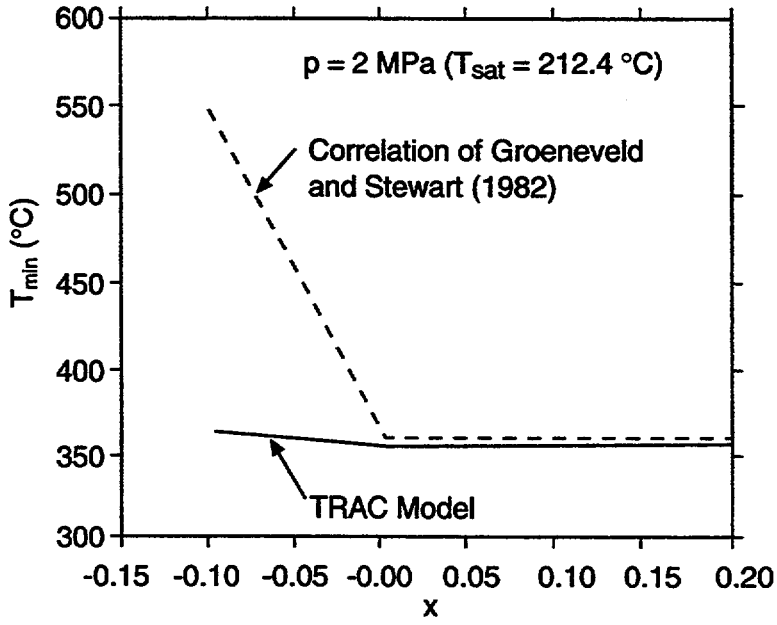

Fig. F-55. Comparison with Groeneveld's results of true T_{min} vs. subcooling at 2 MPa.

F.2.1.9.7. Scaling Considerations. There are no parameters in the correlation to account for scaling geometry or mass flux. Fluid pressure, temperature, and thermal properties and wall thermal properties are the only parameters in the correlation; no limits are specified for these parameters.

F.2.1.9.8. Summary and Conclusions. The comparison of the TRAC T_{min} model to true T_{min} data shows that the prediction is reasonable but could stand improvement in light of the more recent data. The prediction is called reasonable because the prediction is much closer to the data than are the apparent T_{min}s often developed from reflood and blowdown experiments (see the earlier discussion in Section F.2.). To predict the quenches from these experiments, the proper characteristics of the boiling surface with respect to mass flux and void fraction are required. From the comparisons presented, we can say that the current TRAC T_{min} model overpredicts the data at typical reflood conditions (0.1 to 0.4 MPa) by 100 to 150 K and underpredicts the data at typical blowdown conditions (7 MPa) by about 60 to 100 K.

F.2.2. Correlations Used in Subroutine HTVSSL (Core Reflood Model)

Subroutine HTVSSL was developed with an emphasis on the post-CHF region (transition- and film-boiling regimes). The routine, like HTCOR, is self-contained to provide HTCs for all the potential convective regimes using many of the same correlations used by HTCOR for the other boiling regimes. For completeness, all the structure of HTVSSL will be discussed in detail even though it is very similar to that of HTCOR. The correlations that are the same as those in HTCOR will be noted with the appropriate sections so that the reader may revisit them if so desired. Those correlations that are different obviously will be discussed here. We note here that the two-pass logic of HTCOR for void fractions between 0.97 and 0.98 is not in HTVSSL, and that the high-void interpolation threshold has been increased to 0.995 from 0.98.

Post-CHF heat transfer occurs in a reactor core principally during the refill and reflood phase of a LOCA. The flow regimes after CHF of quenching hot fuel rods are very important in determining the heat transfer as well as the mass and momentum transfer. If CHF occurs at low or negative (subcooling) flow qualities, the flow pattern can be expected to be an inverted annular flow where a liquid core is surrounded by an annular vapor film as shown in Fig. F-56. Further downstream, the liquid core may break up into an agitated region of slugs or large droplets and liquid filaments, and later be followed by a small droplet dispersed flow region. At moderate to high qualities, the flow pattern may be thought of as a dryout of liquid film at the wall, which creates a small droplet dispersed-flow regime downstream of the dryout.

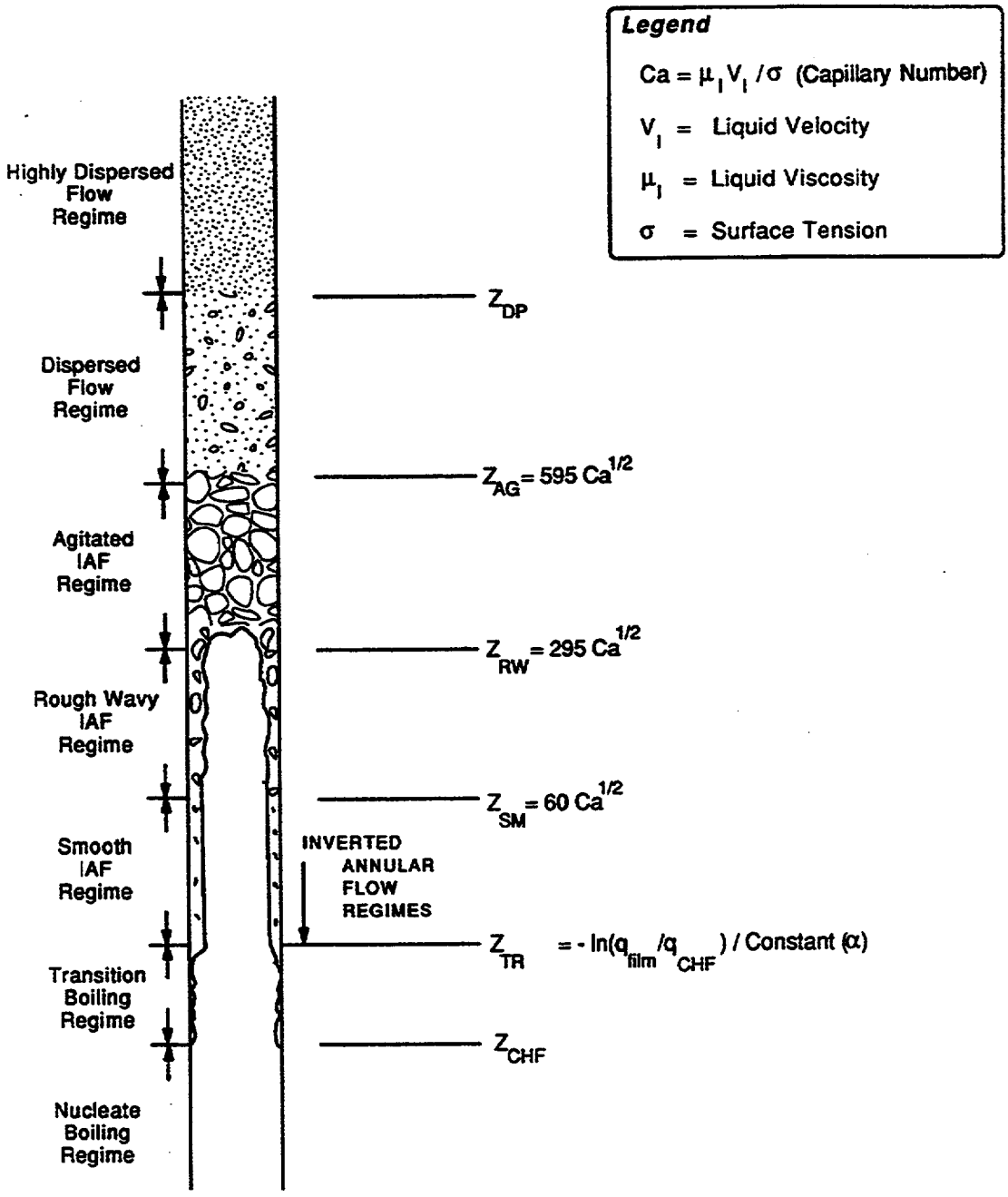

Fig. F-56. Inverted-annular-flow regimes.

Recently Ishii and his co-workers (Ref. F-31.) reported a detailed study of inverted annular flow (characterization of the post-CHF flow regimes and transitions between them). They observed that there are basically four flow regimes downstream of the transition-boiling region located next to the CHF point. It is important to note that their

test setup was constructed in such a way that the transition-boiling region could not be simulated. Inverted annular flow was simulated by two coaxial tubes with the inner tube being a thin-walled tubular nozzle. Right after the nozzle exit to as many as 20 nozzle diameters downstream, the flow was a smooth inverted annular flow with a stable liquid core. Following this smooth regime was the rough-wavy section with its dominant feature being the presence of a fairly stable, intact liquid core, along with a very rough annular gas/core-liquid interface. The agitated region was located immediately downstream of the rough-wavy region. In this regime, significant interfacial deformation was observed. The presence of a highly agitated liquid annulus in the vicinity of the heated wall and large liquid slugs in the central portion of the test section were also observed. The last flow regime observed downstream of the agitated region was a dispersed-ligaments/droplets-flow regime. A generalized transition criterion between these flow regimes was given.

The TRAC core reflood model is based upon the above-mentioned flow-regime map of inverted annular flow, as illustrated in Fig. F-56. The criterion to determine the flow-regime transitions is based upon a capillary number, except for the transition-boiling-to-smooth-inverted-annular-flow and the dispersed-flow to highly dispersed flow transitions. The highly dispersed flow is defined when the void fraction at a particular elevation is higher than 98%. The transition-boiling region is assumed to end at a location where the transition wall heat flux coincides with the heat flux typical of those encountered in the film-boiling regime. The following section describes the HTC correlations used in TRAC (subroutine HTVSSL) for wall-to-fluid heat transfer for inverted-annular-flow regimes.

F.2.2.1. Single-Phase Liquid (Heat-Transfer Regimes 1 and 12). Either forced convection (regime 1) or natural circulation (regime 12) can occur when single-phase liquid is present. Laminar and turbulent HTCs are available. Because only single-phase liquid is assumed to be present, the vapor HTC, h_{wg}, is set equal to zero. HTC correlations for forced convection and natural convection, input quantities and constants for these correlations, and the method of coding are identical to those used in subroutine HTCOR as explained in Section F.2.1.1.

F.2.2.2. Nucleate Boiling (Heat-Transfer Regime 2). Heat-transfer regime 2 is nucleate boiling and includes subcooled nucleate boiling. The Chen correlation is used in the nucleate-boiling heat-transfer regime as in subroutine HTCOR. None of the constants in the correlations was changed from that given in subroutine HTCOR. The coding for the Chen correlation, input quantities, and constants are the same as those given in Section F.2.1.2.

F.2.2.3. Transition Boiling (Heat-Transfer Regime 3). The transition-boiling regime spans the boiling surface between CHF and minimum film boiling.

F.2.2.3.1. **Basis for the Model.** Previously in subroutine HTCOR, transition boiling is represented as a combination of both nucleate-boiling (wet-wall) and film-boiling (dry-wall) heat transfer with a weighting factor applied to both parts. Transition boiling is assumed to occur if the wall temperature is between T_{CHF} and T_{min}. This modeling approach by definition does not depend upon the axial position but rather on the local wall temperature for a given control volume at a given axial distance from the CHF point. It has been observed that very different results in predicting wall-temperature history and the precursory cooling can be obtained if the axial node size is changed from small to large or vice versa. This difference arises because the only limiting factor within the code in such an analysis is that imposed by the numerics associated with axial conduction. Until the node size has been decreased to a size smaller than that required to properly model the axial-conduction effect, the axial temperature distribution will change as the node size is changed, and a sensitivity to node size will be reflected in the HTCs because they are being evaluated based upon the local wall temperatures. Nothing is present within the local wall-temperature formulation of transition boiling to prevent the "collapse in the axial direction" of convective boiling as the node size is decreased to that thermal distribution limit imposed by axial conduction. Thus, the determination of wall-to-fluid HTCs, used in the conduction solution for the transition-boiling regime, becomes axial-nodalization dependent. Whereas some flow states exist where this is the correct representation of convection, in general, this collapse of transition boiling in the axial direction to the axial-conduction limit is not correct. (See previous discussion in the spatial-averaging operator portion of Section F.2.)

As seen in many experimental studies (Refs. F-78., F-79., and F-80.), the extension of transition boiling downstream of a CHF point in forced-convective flow depends upon the thermal-hydraulic conditions at the CHF point. Thus, there is a need to develop an axial-history-dependent transition-boiling model in order to eliminate difficulties associated with the nodalization in the transition-boiling model used in subroutine HTCOR. The following paragraphs explain the axial-history-dependent transition-boiling model used in subroutine HTVSSL to determine wall-to-fluid HTCs.

The typical conditions in a post-CHF convective flow are illustrated in Figs. F-57a. and F-57b., which show Ishii's inverted annular-flow-regime maps with the postulated axial wall heat-flux profiles. The wall heat flux at the CHF point is significantly high relative to the heat flux of the film-boiling regime. The transition-boiling heat flux is limited by a maximum of q_{CHF} and a minimum of q_{film}. It is assumed in the current model that the transition-boiling heat flux exponentially decreases with the axial distance from q_{CHF} to q_{film}. The transition-boiling heat flux is given by

$$q_{TR} = q_{CHF} e^{-B(Z - Z_{CHF})}, \text{ so that at} \tag{F-310}$$

$$z = Z_{CHF}, q_{TR} = q_{CHF}, \text{ and at} \tag{F-311}$$

$$z = Z_{TR}, q_{TR} = q_{film}.$$

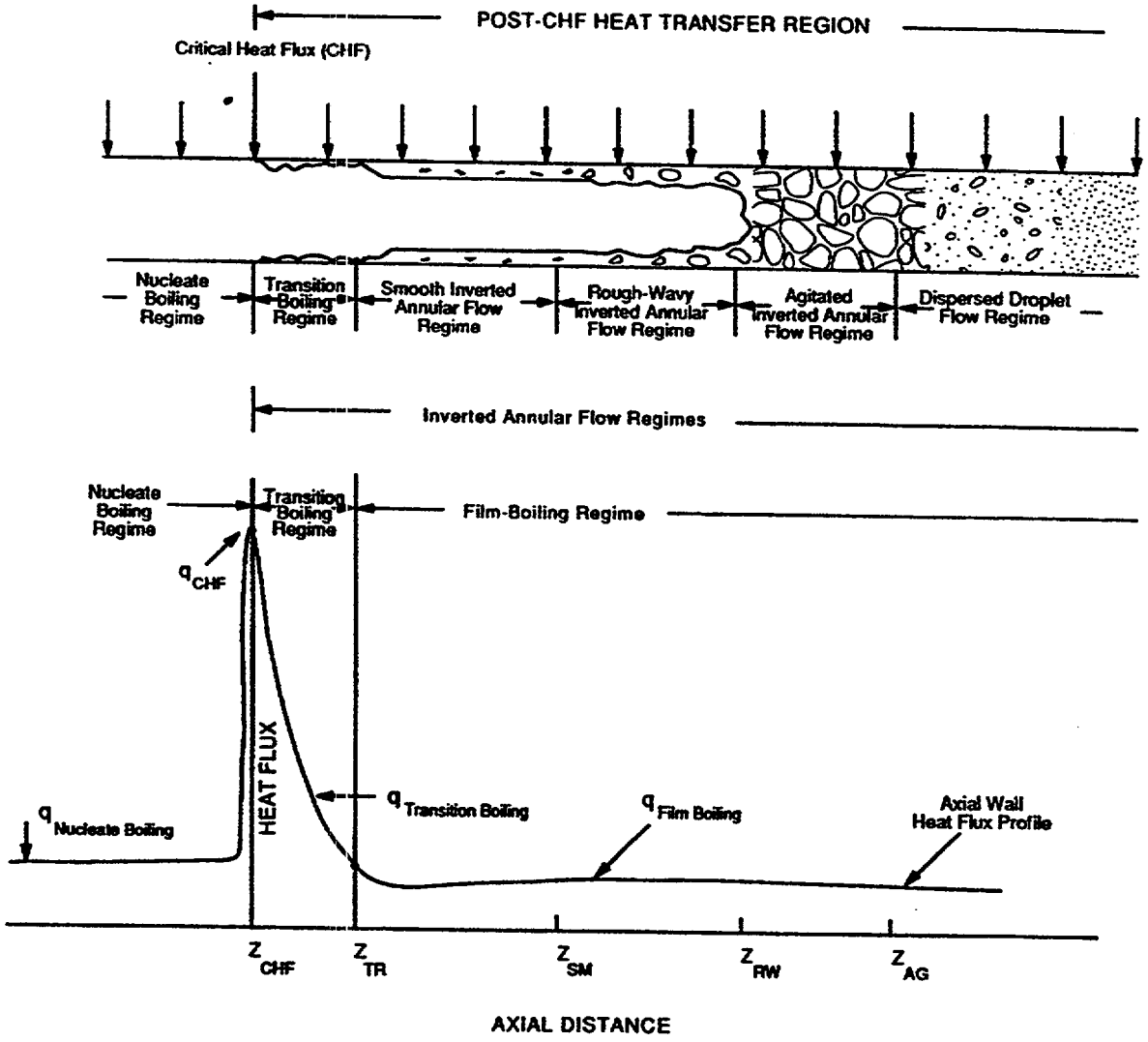

Fig. F-57a. Typical axial wall heat-flux profile for an inverted annular flow with low inlet qualities at the CHF point.

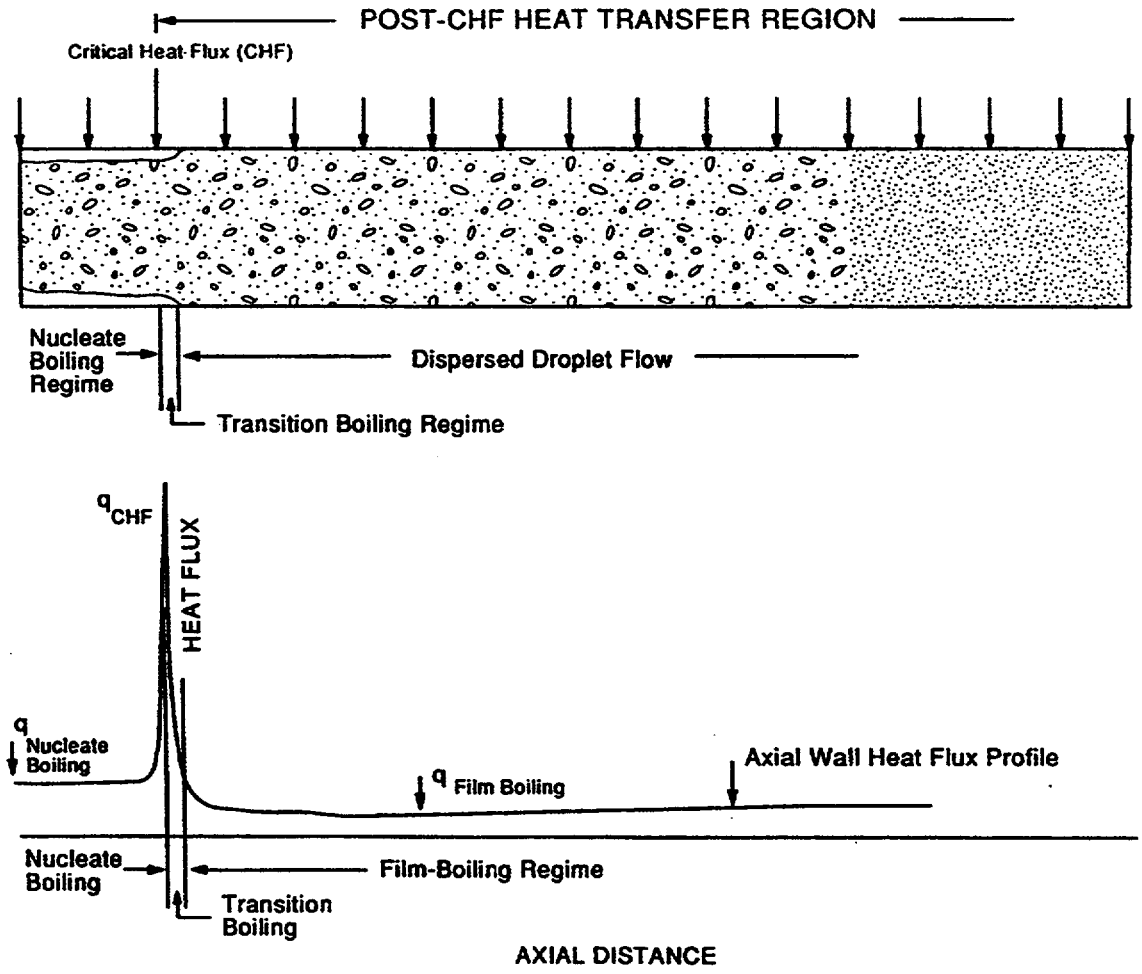

Fig. F-57b. Typical axial wall heat-flux profile for an inverted annular flow with high inlet qualities at the CHF point.

The length of the transition-boiling region then can be determined by

$$Z_{TR} - Z_{CHF} = \frac{-\ln(q_{film} / q_{CHF})}{B} \qquad \text{(F-312)}$$

if the constant B is specified. Although the ratio of the film-boiling heat flux to the peak, CHF heat flux is a function of thermal-hydraulic conditions at the quench front, the ratio is considered to be constant in the current reflood model. The CCTF Run-14 test was used to determine the constant. Determining the coefficient B is not straightforward and ideally, all possible combinations of post-CHF flow conditions, wall materials, and thicknesses that are of interest should be considered.

To partition the total transition-boiling heat flux into its phasic components, the gas-phase HTC, h_{wg}, is evaluated by the Webb-Chen correlation. This correlation and its limitations and weightings are explained in Section F.2.2.4. Once h_{wg} is evaluated, the wall-to-liquid HTC can be found by the following equation at a given axial position:

$$h_{w\ell} = (q_{TR} - h_{wg}(T_w - T_g)) / (T_w - T_\ell) \ . \tag{F-313}$$

The CHF in Eq. (F-312), q_{CHF}, is calculated in subroutine CHF1 using the Biasi correlations (see Section F.2.1.8.).

If the liquid is subcooled ($T_\ell < T_{sat}$), the heat-transfer coefficient due to the subcooled conditions is determined by

$$h_\Gamma = h_{\Gamma,CHF} e^{-B(z - Z_{CHF})} \ . \tag{F-314}$$

The final selection of h_Γ is made by

$$h_\Gamma = \min(h_{w\ell}, \max(h_\Gamma, h_{\Gamma,CHF})) \ , \tag{F-315}$$

where $h_{\Gamma,CHF}$ is the subcooled-boiling heat-transfer coefficient defined at the CHF point.

F.2.2.3.2. Input Quantities to the Model. The liquid and vapor properties are evaluated at the film temperature for h_{wg}. The velocities in the Reynolds number (Webb-Chen correlation) are the absolute values of the liquid and vapor axial velocities (see Section F.2.1.1.1.). The characteristic length is the hydraulic diameter of the unit subchannel or channel.

F.2.2.3.3. Constants. The constant B is considered to be vapor-Reynolds-number, capillary-number, and void-fraction dependent. The reasons for selecting these dimensionless numbers are discussed below.

Ishii's flow-regime map indicates that the length of each IAF regime is proportional to the square root of the capillary number defined at the CHF point. Thus, for a given pressure, the IAF regimes extend farther when the liquid velocity increases at the CHF point. We assume that the length of the transition-boiling regime should exhibit the same trend—higher liquid velocities at the CHF point should extend the transition-boiling region further downstream. Therefore, the first dimensionless parameter in determining B is the capillary number at CHF. B is assumed to be proportional to the inverse square root of the capillary number (B=Constant $\times Ca^{-1/2}$). The proportionality constant was found to vary with the vapor Reynolds number (defined at the CHF point).

For higher void fractions, the flow regimes downstream of the CHF point are expected to be annular-mist transition and dispersed flow. We believe that the transition-boiling regime should occur in a relatively short region for these high-void flow conditions and

should diminish when the void fraction goes to unity. Thus, the transition-boiling regime is forced to decrease with increasing void fraction if the void fraction at CHF is between 0.8 and 0.995.

The coefficient B is found by the following:

for $\alpha<0.8$,

$$B = \text{Cons.} Ca_\ell^{-0.5} ; \tag{F-316}$$

for $0.80<\alpha<0.995$,

$$B=e^{\left(ln(\text{Cons. } Ca_\ell^{-0.5}) + \left(\frac{\alpha-0.80}{0.995-0.8}\right)^{1.5}(7.601-ln(\text{Cons.}) Ca_\ell^{-0.5})\right)} ; \tag{F-317}$$

for $0.995<\alpha$,

$$B = 2000 ; \tag{F-318}$$

where

$$\text{Cons.}=18.75 + 1\times10^{-4}Re_v - 3\times10^{-6}Re_v^2 \qquad \text{if } Re_v<2000 ; \tag{F-319}$$

$$\text{Cons.}=10.425 - 1.93\times10^{-3}Re_v + 1.25\times10^{-7}Re_v^2 \qquad \text{if } Re_v>2000 ; \tag{F-320}$$

$$Ca_\ell = \left(\frac{V_\ell\mu_\ell}{\sigma}\right)_{\text{CHF}} ; \text{and} \tag{F-321}$$

$$Re_v = \left(\frac{\alpha\rho_v D_h V_v}{\mu_v}\right)_{\text{CHF}} . \tag{F-322}$$

To better understand this formulation, we can first note that the length of the transition-boiling region can be determined from Eq. (F-312) to be

$$Z_{\text{TR}} - Z_{\text{CHF}} = \frac{-\ln\left(\frac{q_{\text{film}}}{q_{\text{CHF}}}\right)}{\text{Constant}(Ca_\ell^{-0.5})} \tag{F-323}$$

for the case where $\alpha<0.8$. Dividing Eq. (F-313) by the diameter yields

$$\frac{Z_{\text{TR}} - Z_{\text{CHF}}}{D} = \text{Constant} Ca^{0.5} , \tag{F-324}$$

which is the same type of formulation developed by Obot and Ishii (Ref. F-84.) for their flow-regime map.

So far, we have discussed the transition-boiling region for upflow conditions. In computer code calculations, as well as in integral experiments, the vapor and/or liquid can flow downward. In such situations, the capillary and Reynolds numbers become negative. As with Ishii's flow map, the transition-boiling model discussed above is not valid under downflow conditions. Until data are available for the flow regime, as well as for other thermal hydraulic behavior in downflows, the coefficient B is assumed either to be a constant or to be void-fraction dependent.

In steady-state post-CHF tests using hot patches (Ref. F-80.), the CHF point and transition boiling are downstream of the hot patch. We believe that the transition-boiling regime for such tests should be limited to a very short region. Therefore, in calculations that include hot patches, the coefficient B is multiplied by a constant to ensure that the length of the transition region is very small.

For downward flows where the capillary number becomes negative, Cons. is assumed to be a linear function of the void fraction with a proportionality constant being 250 for void fractions less than 60%. If the void fraction is higher than 0.60, Cons. is assumed to be constant, 150. The ratio of q_{film}/q_{CHF} is taken to be 1.2×10^{-10}. These values are obtained to best fit the CCTF Run-14 data. The constants used in other correlations (Webb-Chen) are those given in the reference cited. The dimensions used for the variables yield HTCs in units of $W\cdot m^{-2}\cdot K^{-1}$ and heat fluxes in units of $W\cdot m^{-2}$.

F.2.2.3.4. Model as Coded. For the transition-boiling regime, most of the calculations are carried out in subroutine HTVSSL. Subroutines CHEN, CHF, CHF1, HLFLMR, and HVWEBB are called as needed to evaluate the nucleate-boiling HTC, CHF, the CHF temperature (T_{CHF}), the film-boiling liquid HTC, and the film-boiling vapor HTC, respectively. A number of tests are made in subroutine HTVSSL to determine if the transition-boiling regime exists. The tests involve three basic considerations: (1) occurrence of CHF, (2) axial distance, and (3) void fraction. The first consideration is relatively simple and determines that CHF has been exceeded if $T_w > T_{CHF}$ (based on temperature) or $q_{nucb} > q_{CHF}$ (based on heat flux).

The second consideration involves several steps. The first step is to use a criterion of maximum possible distance past the CHF point in an effort to save computational time. For transition boiling to be possible, this criterion requires that $z - Z_{CHF} < Z_{TR,max}$. If transition boiling is thus possible, the next step is to check whether $q_{TR} > q_{film}$. If so, transition boiling occurred at that particular z.

The third consideration involves a test on the void fraction to ensure continuity in the high-void region as the flow turns into single-phase vapor. If $\alpha > \alpha_{cut}$ (with $\alpha_{cut}=0.995$, defining single-phase vapor flow), q_{TR} is reevaluated as follows to ensure a smooth transition between flow regimes:

$$q'_{TR} = q_{TR}\frac{(\alpha_3 - \alpha)}{(\alpha_3 - \alpha_{cut})} + h_{gsav}(T_w - T_g)\frac{(\alpha - \alpha_{cut})}{(\alpha_3 - \alpha_{cut})}, \quad \text{(F-325)}$$

where $\alpha_3 = 0.9999$.

Also, if $\alpha > \alpha_3$, the wall-to-vapor HTC, h_{wg}, is interpolated to ensure a smooth transition between flow regimes using the following relationship:

$$h_{wg} = h_{wg} + (h_{gsav} - h_{wg})\frac{(\alpha - \alpha_3)}{(\alpha_2 - \alpha_3)}, \quad \text{(F-326)}$$

where

$$\alpha_2 = 1.0 .$$

This ensures that the vapor HTC approaches that for the convective heat transfer to single-phase vapor, h_{gsav}, at high void fractions.

F.2.2.3.5. Weighting, Limits, and Averaging. The maximum transition-boiling heat flux is limited by the q_{CHF} while the minimum transition-boiling length is 1×10^{-6} m. The coefficient Cons. is limited by a minimum of 50 and a maximum of 2000. Interpolation is used to ensure a smooth transition to the single-phase vapor HTC at high void fractions. No rate limits are used. Limits are imposed on mass flow in the Biasi correlation for CHF and are discussed in Section F.2.1.8.

F.2.2.3.6. Assessment of the Correlation. The major assumption made in implementing the equations for the heat flux in the transition-boiling regime is that the heat flux can be modeled as an exponentially decreasing function. The heat flux is forced to decrease over the axial elevation from q_{CHF} to q_{film}. The wall-temperature history of a quenching hot rod (Ref. F-80.) indicates that the wall temperature also increases sharply with the axial distance downstream of the quench front. If the quench-front velocities are constant when a particular small region experiences transition boiling, a temperature-time plot (at a particular elevation) can be converted to a temperature-axial distance plot by multiplying the time by the quench-front velocity (chain rule). Thus, the wall temperature increase downstream of the quench front can be represented by a function logarithmic in nature (except within a few millimeters of the quench front). The transient heat balance calculation then gives an axial-heat-flux profile indicating that it decreases sharply from q_{CHF} to q_{film}, as shown by Unal in Ref. F-80.. The comparisons of the calculated and measured axial wall heat-flux profiles obtained from a developmental assessment run for Lehigh rod-bundle data (Ref. F-82.) are shown in Fig. F-58., which shows reasonable agreement. (See also Ref. F-81. for additional discussion of the Lehigh rod-bundle work.)

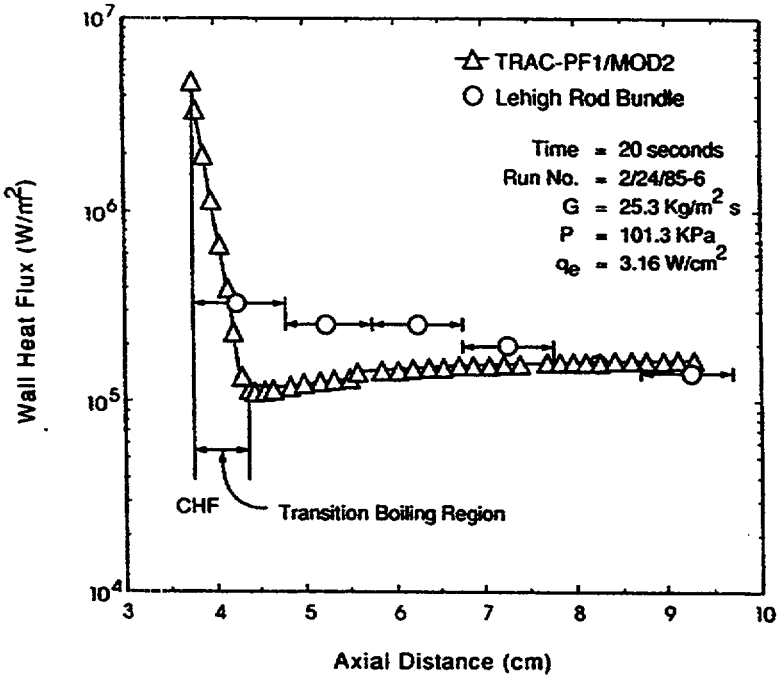

Fig. F-58. The calculated and measured axial wall heat-flux profiles for a Lehigh rod bundle test.

F.2.2.3.7. Scaling Considerations. The equation for calculating h_{wg} was based mostly on data from tubes (Ref. F-83.). The validity of using these data to calculate rod-bundle transition-boiling heat transfer has not been demonstrated. The variation of the transition-boiling heat flux with the axial distance is controlled by thermal-hydraulic conditions at the quench-front location (Ref. F-80.). Thus, coefficients defining the heat-flux profile should be functions of local thermal-hydraulic conditions at the quench front. Currently, these coefficients are assumed to be constant. In the future, code improvement efforts should consider more phenomenological modeling of the position-dependent transition boiling, for upflow and downflow conditions, and for rod bundles as well as single-tube geometries.

F.2.2.3.8. Summary and Conclusions. The major assumption used in the transition-boiling model is that the transition-boiling heat flux decreases exponentially with the axial distance downstream of the quench front. This approach eliminates problems associated with the axial nodalization. A sensitivity study on nodalization indicates that the prediction of the quench-front velocities as well as the peak wall temperatures at a particular axial elevation are not sensitive to the selection of the axial hydro and conduction cell sizes. Significant discrepancies still exist between the predicted and measured data. Future code development should emphasize more phenomenological modeling of the transition boiling, following the concepts discussed here and in

Section F.2. This would allow the prediction of transition-boiling heat transfer in all situations, such as bottom, top quenching, and reversal flows.

F.2.2.4. Film Boiling (Regime 4). The film-boiling heat-transfer regime incorporates several different correlations to describe the HTCs in the inverted annular-flow regime as observed by Ishii and his coworkers (Refs. F-31. and F-84.). The flow-regime boundaries are determined by a capillary number based upon liquid flow rate, liquid viscosity, and surface tension at the CHF point. Additional tests in determining the flow-regime boundaries are also implemented in the model. These are based upon the predetermined maximum and minimum void fractions at flow-regime transition boundaries.

F.2.2.4.1. Basis for the Model. The film-boiling regime is assumed to occur when $T_w > T_{CHF}$ and $z - Z_{CHF} > Z_{TR}$. The wall-to-liquid and wall-to-vapor HTCs are treated separately. The wall-to-liquid HTC, $h_{w\ell}$, is assumed to be the sum of two components: radiation and near-wall liquid effects. The near-wall effects are calculated by either the Denham (Ref. F-34.) or the modified Bromley correlations (Ref. F-62.) or a combination of these two, depending upon the type of flow regime at a particular location under consideration. The liquid HTC is given by

$$h_{w\ell} = (h_r + (h_{\text{Denham}} \text{ or } h_{\text{Bromley}})) \left(\frac{T_w - T_{\text{sat}}}{T_w - T_\ell} \right). \tag{F-327}$$

The radiation component, h_r, is the same as Eq. (F-248) given in Section F.2.1.4.1. The film-boiling component is calculated using either the Denham or modified Bromley correlations. The modified Bromley correlation is discussed in Section F.2.1.4.1. The heat-transfer model for the inverted annular flow proposed by Denham is summarized below.

The heat conducted across the vapor film from the wall to the vapor-water interface in an inverted annular flow is given by

$$q_{wi} = k_v \frac{(T_w - T_{\text{sat}})}{\delta_{vf}}, \tag{F-328}$$

where δ_{vf} is the vapor film thickness that is obtained from a force balance on the vapor film and given by Denham (Ref. F-34.) as

$$\delta_{vf} = \left[\frac{\xi \dot{m}_v \mu_v}{g(\rho_\ell - \rho_v)\rho_v} \right]^{1/2}. \tag{F-329}$$

The coefficient ξ depends on the velocity profile in the vapor film and is assumed to be 5. The vapor-film flow rate can be expressed in terms of vapor velocity

$$\dot{m}_v = \rho_v V_v \,. \tag{F-330}$$

Then Eq. (F-329) becomes

$$\delta_{vf} = 2.2361\left[\frac{\mu_v V_v}{g(\rho_\ell - \rho_v)}\right]^{1/2} . \tag{F-331}$$

It is assumed that the heat conducted through the vapor film, q_{wi}, goes to the liquid phase. Thus, the wall-to-liquid HTC can be obtained with the use of Denham's film thickness equation, Eq. (F-331), as

$$h_{\text{Denham}} = \frac{k_v}{\delta_{vf}} = 0.4472\left[\frac{g(\rho_\ell - \rho_v)}{\mu_v V_v}\right]^{1/2} k_v . \tag{F-332}$$

Subroutine HTVSSL calls subroutine HLFLMR to determine the near-wall liquid effects in Eq. (F-327). Subroutine HLFLMR returns either h_{Denham} or h_{Bromley} or a weighted combination of these two correlations depending upon the IAF regime. The selection logic of liquid HTC is explained below following the description of h_{wg}.

The wall-to-vapor HTC is obtained from the Webb-Chen correlation (Ref. F-83.). The Webb-Chen correlation is developed from a nonequilibrium database for single tubes. It is based upon the momentum-transfer analogy (as used by Chen-Sundaram-Ozkaynak, Ref. F-85.) and also considers the possible entrance-region effects and the effect of entrained liquid droplets. The wall-to-vapor HTC, h_{wg}, for the film-boiling component is given by

$$h_{wg} = h_{\text{mod-CSO}}(1 + F_s)\left(1 + 0.8\left(\frac{z}{D}\right)^{-1}\right) \tag{F-333}$$

and

$$h_{\text{mod}-\text{CSO}} = \frac{f}{2} c_{p,\,vf} G X_a {}^{p} r_{vf}^{-2/3} , \tag{F-334}$$

where the friction factor, f, is weighted by the ratio of wall to vapor temperatures and is given by

$$f = f_{cp}\left(\frac{T_w}{T_v}\right)^{-0.1} . \tag{F-335}$$

In Eq. (F-335), f_{cp} is the two-phase friction factor given by

$$\frac{1}{f_{cp}^{1/2}} = 3.48 - \log_{10}\left(\frac{2\varepsilon}{D_H} + \frac{9.35}{Re_v f_{cp}^{1/2}}\right), \tag{F-336}$$

where

Re_v = vapor Reynolds number = $\frac{V_v \rho_v D_H}{\mu_v}$,

ε = surface roughness, and

D_H = hydraulic diameter.

The term of $[1+0.8\,(z/D)^{-1}]$ in Eq. (F-333) represents the entrance-region effect on h_{wg}.

The sink function, which accounts for the effect of the entrained droplets, is given by

$$F_s = 250\left(\frac{P}{P_{cr}}\right)^{0.69}\left(\frac{1-x}{x}\right)^{0.49} Re_v^{-0.55}. \tag{F-337}$$

The wall-to-vapor HTC is weighted based upon the flow regime, as explained below. The HTC selection logic based upon the IAF flow regimes is illustrated in Fig. F-59. The locations of flow-regime boundaries and the void fractions at these locations are input to subroutine HTVSSL. Therefore, before calling HTVSSL, subroutine CORE1 calls subroutine ZCORE to determine the location of the quench-front and IAF-regime transition boundaries with corresponding void fractions. Subroutine ZCORE first determines the location of the quench front (CHF). Then, in the first pass, using old-time variables, it calculates elevations corresponding to each IAF-regime transition boundary, using Ishii and coworkers' flow-regime criteria based upon the capillary number (Ref. F-31.). These calculated elevations are shown in Fig. F-59. by Z_{SM}, Z_{RW}, Z_{AG}, and Z_{DP} for the smooth, rough-wavy, agitated, and dispersed IAF regimes, respectively. The void fractions at these elevations are obtained by linear interpolation using the derivative of the void fraction with respect to axial distance (determined by the hydro solution before subroutine CORE1 calls subroutine ZCORE). To assure that these calculated void fractions describing the flow-regime transitions are consistent with those expected to exist in IAF regimes, the following checks and corrections are done in the second pass. Using predefined void fractions (possible maximum and minimum void fractions defined as input to this model) at flow-regime transition boundaries, α_{SM}, α_{RW}, α_{AG}, and α_{DP}, and updated void fractions and the derivative of void fractions with respect to axial distance, subroutine ZCORE reevaluates the elevations at flow-regime transition boundaries and the corresponding void fractions at these elevations by linear interpolation. The linear interpolation using the fine-mesh nodes is applied from hydraulic cell center to cell center. At the end, subroutine ZCORE returns the elevations and void fractions at IAF regime transition boundaries to subroutine CORE1. Subroutine CORE1, then calls subroutine HTVSSL to determine HTCs at each particular axial elevation. The selection is described below.

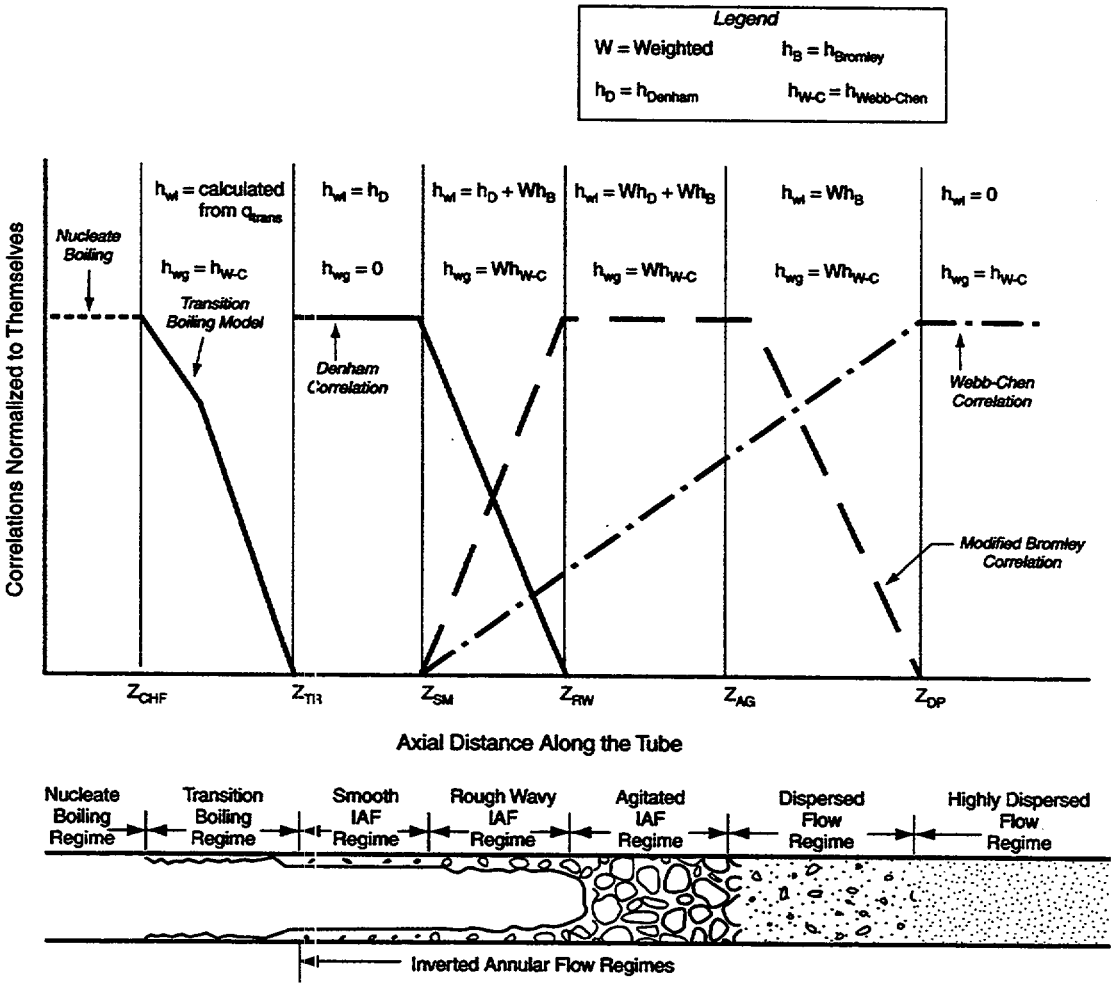

Fig. F-59. Illustration of HTCs selection logic used in the reflood model.

In the smooth IAF regime, the total heat generated by the wall is assumed to be transferred directly to the liquid interface across the vapor film surrounding the liquid core. The Denham correlation, Eq. (F-332), is used to determine the wall-to-liquid HTC. Because the total heat generated by the wall is assumed to be transferred directly to the liquid, no heat transfer to the vapor phase is assumed to occur.

In the flow regimes downstream of smooth IAF, the wall is assumed to be cooled by a combination of vapor and liquid. The Webb-Chen correlation (Ref. F-83.) is used to obtain the wall-to-vapor HTC in the remainder of the flow regimes downstream of smooth IAF.

The Webb-Chen correlation alone cannot result in the correct prediction of the heat transfer in the IAF regimes downstream of smooth IAF. Ishii (Ref. F-84.) observed the existence of a fine sheet of liquid drops/ligaments between the liquid core of the IAF

regime and the wall. From Ishii's study, it is clear that the hydrodynamic behavior in the rough-wavy and agitated IAF regimes shows a unique characteristic. Interfacial surface area is increased significantly and liquid exists near the wall, possibly in momentary contact with the wall. Hence, the heat-transfer mechanism in these flow regimes is significantly enhanced. Whereas the heat-transfer aspects of the flows were not measured by Ishii and coworkers, the existence of a post-transition-boiling region (near region) immediately downstream of the CHF point was found by Unal et al. (Ref. F-80.). The authors indicated that the evaporation of liquid is very efficient in the post-transition-boiling region, so the measured vapor temperature is close to the saturation temperature of the fluid. They hypothesized that the heat-transfer enhancement could be due to liquid/wall direct-contact heat transfer. Another mechanism that might explain this efficient process is the increase in local turbulence near the wall because of the existence of liquid droplets (Ref. F-90., F-91.).

Although either of these theories can predict heat-transfer enhancement in the IAF regimes downstream of smooth IAF, whether only one mechanism is responsible for the overall heat-transfer enhancement is not clear. Rather, it is likely that both heat-transfer mechanisms can coexist. In our model, we name this heat-transfer mechanism the "near-wall liquid" effect. We assumed that it starts at the beginning of rough-wavy IAF and gradually increases with increasing axial distance up to the agitated IAF region. In agitated flow, we postulate that the near-wall liquid effect is at a maximum due to high turbulence and some liquid-wall contact. Downstream of the agitated region, this effect gradually decreases, finally becoming negligible in highly dispersed flow (Ref. F-92.).

We consider this near-wall liquid effect through the wall-to-liquid HTC, h_{wl}. One can argue that this effect is due either to liquid/wall contact or to turbulence enhancement, where—much like Denham's model—the transport of wall energy into the vapor and then into the liquid is short-circuited because of the extremely fast and efficient transport process. Because no mechanistic model exists to predict this contribution, we selected the modified Bromley correlation (Ref. F-92.) as the "kernel" for the model. Our initial assessment attempts indicated that the magnitude of the near-wall effect for different mass and heat fluxes could not be predicted correctly by the Bromley correlation alone because this correlation depends only on the pressure and the wall temperature, a point raised several years ago by Denham. The results indicated that the near-wall effects tend to increase with increasing mass flux at a given heat flux and inlet subcooling, which is consistent with the experimental findings reported by Unal et al. (Ref. F-92., Fig. 9). They indicated that their transition region extended further downstream with an increase in vapor flux.

Therefore, for the Bromley correlation, we introduce a multiplier that depends on the vapor Reynolds number. The functional form of the multiplier was found by matching the measured wall and vapor temperatures to five of the Winfrith steady-state post-CHF tests. It was found to be a linear function of the vapor Reynolds number defined at the agitated IAF. The functional form given below gives a multiplication factor varying between 0.2 and 1.0 for a Reynolds number varying between 900 and 2300. With this

modification, low-pressure data were predicted reasonably well, whereas higher-pressure data showed an underprediction of the measured wall temperatures. This underprediction arises because the Reynolds number becomes much greater than 2300 due to the increase in vapor density with pressure. The multiplication factor always becomes 1, resulting in high wall-to-liquid HTCs at higher pressures. Therefore, a pressure-dependent exponent was introduced and applied to the Reynolds number, as summarized below. Obviously, this is an area in which phenomenological modeling is needed.

The wall-to-liquid HTC for the rough-wavy IAF regime, $Z_{SM}<z<Z_{RW}$, is given by the combination of weighted Denham and modified Bromley HTCs as

$$h_{w\ell} = h_{\text{Den}}\left(\frac{z-Z_{\text{SM}}}{Z_{\text{RW}}-Z_{\text{SM}}}\right)^{0.5} + h_{\text{Brom, Mod}}\left(\frac{z-Z_{\text{SM}}}{Z_{\text{RW}}-Z_{\text{SM}}}\right)^{0.9}, \tag{F-338}$$

where

$$h_{\text{Brom,Mod}} = F(Re_{v,\text{AG}})h_{\text{Brom}} \ . \tag{F-339}$$

The wall-to-vapor HTC was obtained from the Webb-Chen correlation (Ref. F-83.) as

$$h_{wg} = 1.2\left(\frac{\alpha-\alpha_{\text{SM}}}{\alpha_{\text{DP}}-\alpha_{\text{SM}}}\right)^{0.01} h_{\text{Webb-Chen}} \ . \tag{F-340}$$

In the agitated and post-agitated IAF regimes, $Z_{RW}<z<Z_{DP}$, the wall-to-liquid HTC is calculated by

$$h_{w\ell} = h_{\text{Brom,Mod}}\left(\frac{0.75-\alpha}{0.75-\alpha_2}\right)^{F_1(Re_{v,\text{AG}})}, \tag{F-341}$$

where

$$\alpha_2 = \min(\max(\alpha_{\text{off1}}, \alpha_{\text{AG}}), \alpha_{\text{off3}}) \tag{F-342}$$

$$F\left(Re_{v,\text{AG}}\right) = -0.51498 + 6.4895\ 10^{-4} Re_{v,\text{AG}} \ , \tag{F-343}$$

$$F_1\left(Re_{v,\text{AG}}\right) = 14.61 - 2.442\ 10^{-2} Re_{v,\text{AG}} + 1.4313\ 10^{-5} Re_{v,\text{AG}}^2 - 2.7787\ 10^{-9} Re_{v,\text{AG}}^3 \ , \tag{F-344}$$

and

$$Re_v = \left(\frac{\alpha\rho_v D_H V_v}{\mu_v}\right)_{AG}^{\left(1+(1-0.95)\left(\frac{P-2\times10^5}{10\times10^5-2\times10^5}\right)\right)} . \quad \text{(F-345)}$$

The weighting used in Eq. (F-341) allows h_{wl} to decrease gradually after the point where the void fraction equals α_2. This point could be in either the post-agitated region or at the end of the agitated region, depending upon the values of the predicted α_{AG}, and specified α_{off1} and α_{off2}. The respective α_{off1}, α_{off2}, and α_{off3} values were set to 0.45, 0.75, and 0.98. If ($\alpha_{AG}<0.45$), the turning point is extended to the point where the void fraction becomes 0.45. If $\alpha_{AG}>\alpha_{off1}$, then the turning point could be extended to a location where α equals 0.75. In the region in which ($\alpha<0.75$), h_{wl} gradually decreases according to Eq. (F-341) and becomes zero in highly dispersed flow ($\alpha>0.98$),

The wall-to-vapor HTC in the agitated, post-agitated, and highly dispersed IAF regions is calculated by Eq. (F-340).

If the liquid is subcooled in the film-boiling regime, an additional HTC, h_Γ, is calculated and used to separate the latent heat of evaporation effect from the sensible heat effect. The h_Γ is calculated in the following fashion.

As Denham (Ref. F-34.) indicated, the interface of the subcooled liquid becomes saturated due to condensation. Thus, the heat transfer from the saturated interface to the subcooled liquid core, $q_{i\ell}$, was expressed as the conduction solution of a cylinder with a change in surface temperature. The time required by Denham's expression can be calculated as the ratio of node size to liquid velocity. The $q_{i\ell}$ becomes

$$q_{i\ell} = k_\ell \sqrt{\frac{V_\ell}{\pi\alpha_\ell(z_t - Z_{TR})}} \frac{V_\ell D_H^2}{V_\ell D_H^2 + 15\alpha_\ell(z_t - Z_{TR})}(T_{sat} - T_\ell) . \quad \text{(F-346)}$$

The subcooled-boiling heat-transfer coefficient, h_Γ, is calculated by

$$h_\Gamma = \frac{h_{w\ell}(T_w - T_\ell) - q_{i\ell}}{T_w - T_\ell} . \quad \text{(F-347)}$$

This h_Γ is calculated in all IAF regimes except in highly dispersed flow. In the highly dispersed flow ($\alpha>0.98$), h_Γ is assumed as zero.

Figure F-59. shows the selection logic for HTCs h_{wl} and h_{wg}. In this figure, the trend of each correlation in each IAF regime is shown.

F.2.2.4.2. Weighting, Limits, and Averaging. Subroutine HLFLMR limits the minimum Denham and Bromley HTCs to be 1×10^{-20}. All weightings used in Eqs. (F-338), (F-339), (F-340), and (F-341) are limited with a minimum of zero and maximum of one. If $\alpha > \alpha_3$ ($\alpha_3 = 0.9999$), the wall-to-vapor HTC, h_{wg}, is reevaluated as

$$h_{wg} = h_{wg} + (h_{gsav} - h_{wg})\frac{(\alpha - \alpha_3)}{(\alpha_2 - \alpha_3)} , \tag{F-348}$$

where

$$\alpha_2 = 1.0 \quad .$$

If $\alpha > \alpha_{cut}$ ($\alpha_{cut} = 0.995$) and $h_{wl} > 0$, the wall-to-liquid HTC is reevaluated as

$$h_{w\ell} = h_{w\ell} + (0 - h_{w\ell})\frac{(\alpha - \alpha_{cut})}{(\alpha_3 - \alpha_{cut})} . \tag{F-349}$$

The above weightings are performed to ensure that the HTCs do not show discontinuities between the single-phase and two-phase results.

No limits or weighting other than those mentioned above are applied to wall-to-vapor and wall-to-liquid HTCs in the film-boiling regime. There are also no rate limits used in the film-boiling region.

F.2.2.4.3. Assessment of the Correlations. A study was carried out with the TRAC code to select the best HTC correlations to predict post-CHF heat-transfer data. The following correlations were tried before the current reflood model was finalized:

Denham (Ref. F-34.),
Analytis and Yadigaroglu (Ref. F-86.),
Forslund and Rohsenow (Ref. F-87.),
Anderson (Ref. F-88.),
Sudo (Ref. F-89.),
Bromley (Ref. F-62.), and
Webb-Chen (Ref. F-83.).

The assessment of the Webb-Chen correlation with the nonequilibrium INEEL (Ref. F-79.) and Lehigh (Ref. F-78.) single-tube post-CHF data has been discussed in Ref. F-83. The INEEL and Lehigh post-CHF data cover the following range of parameters:

Pressure	250–7000 kPa
Mass Flux	14–100 kg/m^2-s
Heat Flux	1.3–22.5 W·cm^{-2}
Quality	0–0.99

The correlation does not consider subcooled inlet conditions (qualities should be higher than zero). The calculated and measured wall-to-vapor heat-transfer coefficients are shown in Fig. F-60. (from Ref. F-83.). Although there is a considerable scatter in predicted HTCs, the overall results relative to the original modified CSO correlation were significantly improved. Applicability of the Webb-Chen correlation to rod bundles has not been verified. Future code improvement efforts should address this problem.

Denham's inverted annular-flow model is developed from the Bromley model. The thickness of the vapor film is formulated as a function of the vapor mass flow rate by a force balance as in Bromley's derivation. Assessment of this model with the experimental data obtained from the REFLEX Rig at Winfrith (Ref. F-34.) is given in Figs. F-61., F-62., and F-63. (from Ref. F-34.). Figure F-61. shows the effect of the quench-front quality on the heat-transfer coefficient. The model accounts well for the effect of subcooling, as well as positive qualities. The effect of mass flux as shown in Fig. F-62. is also well accounted for in the region approximately 40 cm downstream of the quench front. The overall assessment of the model with Winfrith data is given in Fig. F-63. Ninety-five percent of the results, for which the Weber number was less than the suggested critical value of 20 for the breakdown of the inverted annular flow, agreed to within 20 $W \cdot m^{-2} \cdot K^{-1}$ plus 5%. The parametric range of the Winfrith data is as follows:

Pressure	1–4 bar
Mass Flux	2–16 g/cm^2-s
Heat Flux	1–12 $W \cdot cm^{-2}$
Inlet Subcooling	0–80°C
Initial Temperature	600°C

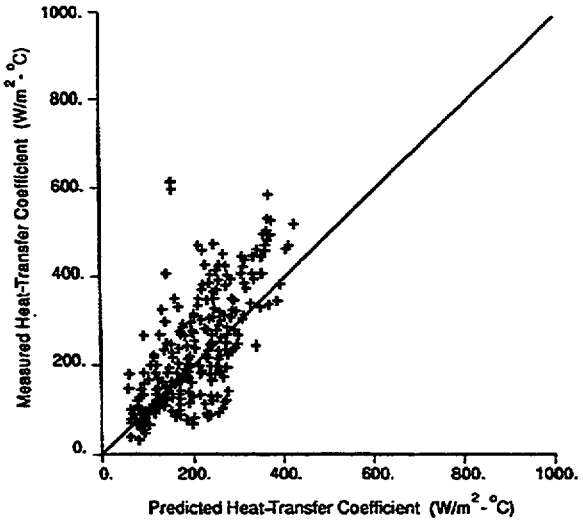

Fig. F-60. Modified heat-transfer coefficient data-model comparison for Lehigh and INEEL data (Ref. F-82.).

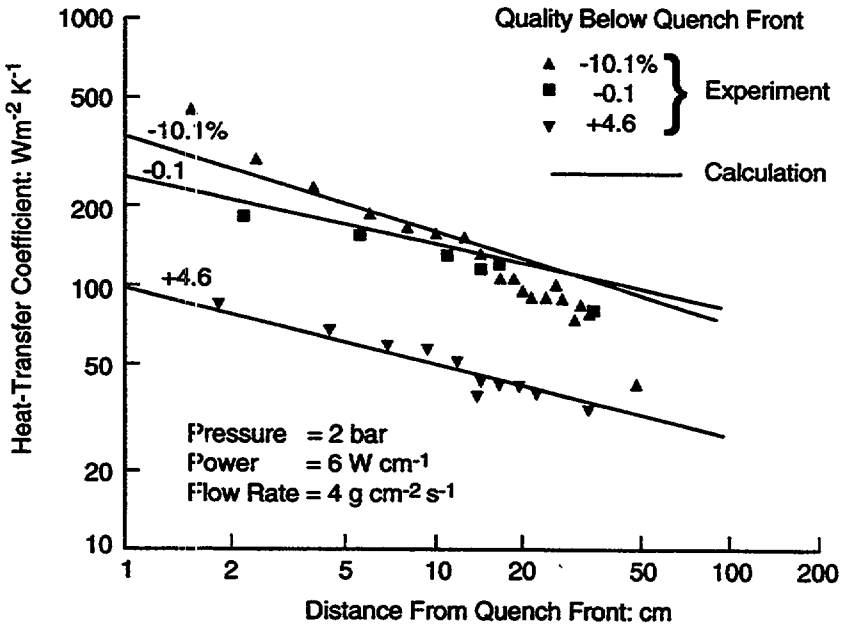

Fig. F-61. Effect of quality (Ref. F-34.).

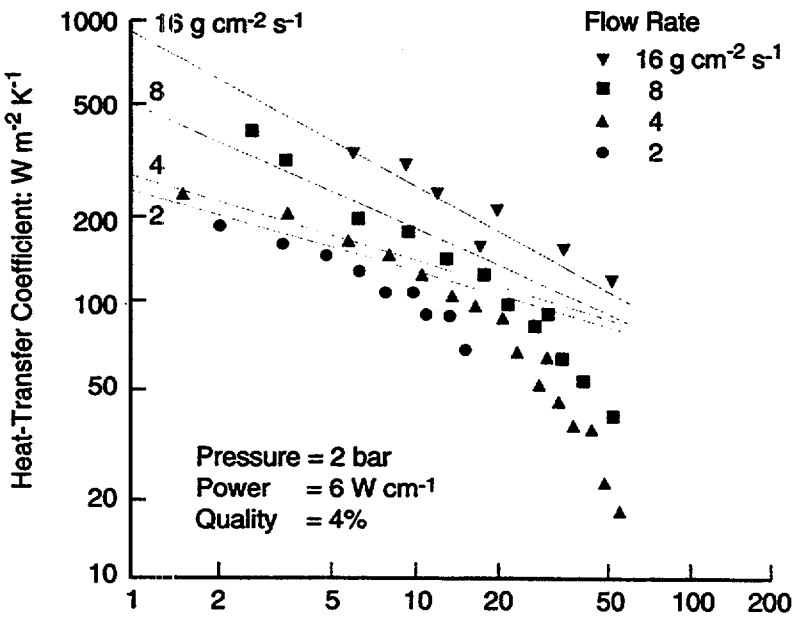

Fig. F-62. Effect of flow rate (Ref. F-34.).

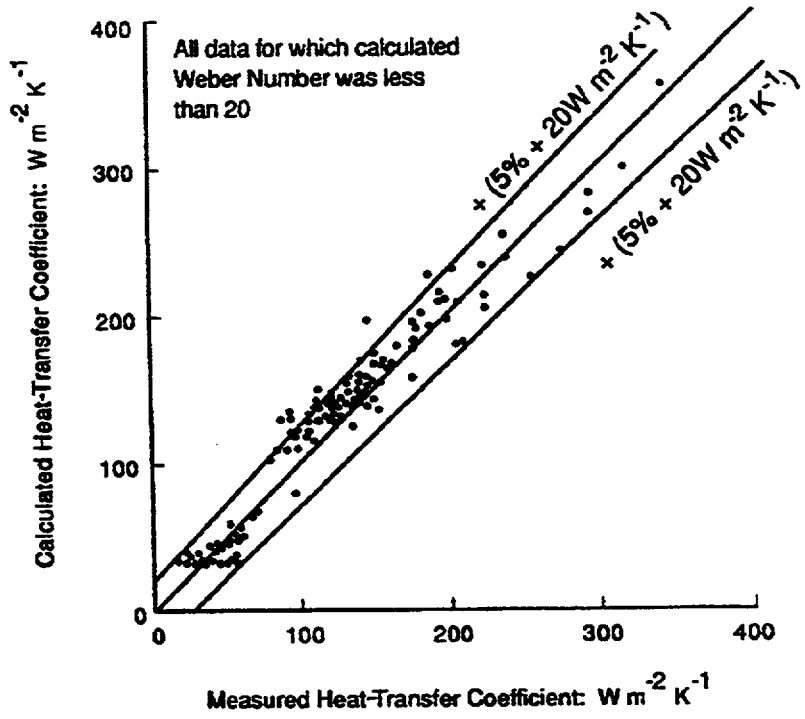

Fig. F-63. Comparison of measured and calculated heat-transfer coefficients (Ref. F-34.).

The assessment of the Denham correlation to rod-bundle data and single-tube data other than those obtained at Winfrith is not available and future code development efforts should address this problem.

F.2.2.4.4. Scaling Considerations. The Bromley correlation, a pool-boiling correlation, was developed from data for a horizontal heated cylinder. Applying it to vertical geometry in two-phase-flow film boiling is questionable, but is based upon numerous early developmental assessments. It was thought to be the best base upon which to build. The Denham correlation is developed from single-tube data, although the applicability of this correlation to rod bundles needs to be justified. The Webb-Chen correlation is developed from a nonequilibrium database for tube geometry. The validity of scaling to rod-bundle geometry has not yet been verified.

F.2.2.4.5. Summary and Conclusions. A substantial amount of data for film-boiling heat transfer, obtained mainly for simple geometries except for a few for rod bundles, is available and has been used to develop and evaluate film-boiling HTCs. Results of an evaluation of different heat-transfer correlations (Refs. F-33. and F-64.) have shown that none of the correlations predicted HTCs with sufficient accuracy over the entire post-CHF region. This further emphasizes the earlier discussion in Section F.2. concerning how the closure relationships for film-boiling equations should be determined.

The film-boiling model in TRAC was based upon correlations developed primarily from post-CHF heat-transfer data for tube geometry and assumed thermodynamic equilibrium (except the Webb-Chen correlation). The validity of scaling to rod-bundle geometry or thermodynamic nonequilibrium has not been verified. The Webb-Chen correlation for the wall-to-vapor HTC is developed from a nonequilibrium post-CHF database for single tubes. The validity of scaling to rod-bundle geometry has not been verified. Significant discrepancies still exist among different correlations and between correlations and experimental data. Future code development work should examine new experimental data and correlations for possible improvements in the film-boiling model.

The discussions contained in Section F.2. concerning the minimum film-boiling temperature and in Sections F.2.1.3. and F.2.1.9. should be reviewed in connection with this section.

F.2.2.5. Single-Phase Vapor (Heat-Transfer Regime 6). The case of convective heat transfer to a single-phase vapor is described by heat-transfer regime 6. Correlations, constants, weighting, and coding used in subroutine HTVSSL are exactly the same as those used in subroutine HTCOR and given in Section F.2.1.5. Subroutine HTVSSL will evaluate this regime when the void fraction is ≥0.995.

F.2.2.6. Condensation (Heat-Transfer Regime 11). All correlations used in heat-transfer regime 11 are well known and have been applied to a wide variety of fluids and geometries. Correlations, constants, weighting, and coding in subroutine HTVSSL are exactly the same as those used in subroutine HTCOR and given in Section F.2.1.6.

F.2.2.7. Two-Phase Forced Convection (Heat-Transfer Regime 7). This heat-transfer regime is unique in that it is not part of the boiling curve discussed. The regime is used only when the input flag ICHF=0. The liquid and vapor HTCs, h_{wl} and h_{wg}, are calculated from regime 7 only. Correlations, constants, weighting, and coding are exactly the same as those used in subroutine HTCOR and given in Section F.2.1.7.

F.2.2.8. Critical Heat Flux. The CHF is required to define the boundary between nucleate and transition boiling. Subroutine HTVSSL calls the same subroutines that are called by subroutine HTCOR to determine CHF, as explained in Section F.2.1.8.

F.2.3. TRAC-Data Comparisons

In the total- and phasic-wall-heat-flux portion of Section F.2., we indicated that comparison calculations are used with numerous experiments (including some of the older separate-effects experiments where data were reduced using the equilibrium assumption) to ensure that the correct amount of energy was being extracted from the wall. This is done because many modifications have been made to what were basically equilibrium mixture heat-transfer correlations to use them in a two-phase two-fluid model. The phasic heat fluxes and their relationship to the total heat flux were given by Eqs. (F-185) through (F-187). Many of these comparisons (typically called assessments) have been made to large-scale systems, such as LOFT (Loss-of-Fluid Test), SCTF

(Slab Core Test Facility), CCTF (Cylindrical-Core Test Facility), and UPTF (Upper-Plenum Test Facility). Whereas these comparisons give an assessment of the code's overall ability, it is frequently difficult, if not impossible, to separate the coupling that exists among all the closure relations. Even the nonequilibrium, separate-effects experiments performed to date do not provide the detailed information necessary. Thus, whereas we know how well a given wall temperature (and, therefore, heat flux) may be predicted, we do not know the corresponding hydraulic conditions well enough to ensure that this prediction is being obtained from the right conditions. Therefore, whereas this assessment is useful, it does not provide direct evidence as to the capability of the wall heat-transfer models discussed in Section F.2.

Whereas the nonequilibrium separate-effects experiments noted above do have the problem indicated, they can be used to provide an assessment of the models because of the greater confidence in the boundary conditions being applied to the test apparatus. This section will not look at any flow regimes other than the post-CHF regime because it is the only one that has had experimental work done to investigate the thermal nonequilibrium effects. Thermal nonequilibrium effects are very significant in terms of correct modeling of the heat transported by convection into the fluid. Two other regimes where thermal nonequilibrium is of importance are condensation and subcooled boiling. These regimes are investigated in Section F.1. in terms of the interfacial heat transfer. Mechanical nonequilibrium has not been studied in terms of its relationship to wall heat transfer, and whereas parametric studies can be done, no direct comparisons can be made.

TRAC calculations have been compared to the results of four post-CHF experiments. One of the databases was generated at the Idaho National Engineering and Environmental Laboratory (INEEL) and three other databases were generated at Lehigh University (LU). These data were chosen because they represent the only thermal nonequilibrium data available having a high degree of confidence in the measured superheated vapor temperature. The four databases represent a total of 1719 data points. A brief description of each of the four experiments follows.

F.2.3.1. LU: Evans, Webb, and Chen. Forced-convection, nonequilibrium post-CHF experiments were conducted at LU for water flowing upwards within a vertical Inconel tube of 15.4-mm i.d. with a heated length of 135.0 cm. The tests utilized a slow reflood process during which wall temperature and nonequilibrium vapor temperature were obtained as functions of distance from the quench front. In all the runs, the quench-front velocity was sufficiently slow to satisfy the criterion for quasi-steady-state thermal conditions downstream of the quench front. The test pressure varied from 0.24 to 0.57 MPa, mass flux ranged from 13.0 to 85.0 kg/m^2-s, inlet vapor quality varied from 0% to 70%, and the range of wall heat fluxes was 18.0 to 58.0 $kW \cdot m^{-2}$. The tests are described in Ref. F-78.

F.2.3.2. INEEL. Forced-convection, nonequilibrium, post-CHF heat-transfer experiments were conducted at INEEL for water flowing upwards within a vertical tube. Steady-state (fixed-quench-front) tests similar to those run at LU were conducted at

pressures of 0.2 to 0.7 MPa, mass fluxes of 12.0 to 24.0 kg/m^2-s, test section inlet qualities of 38% to 64%, and heat fluxes of 7.7 to 27.5 kW·m^{-2}. Quasi-steady-state (slow-moving quench front) experiments also were run with test section inlet qualities of 7% to 47% and heat fluxes of 8.0 to 225.0 kW·m^{-2}. Eighty-three steady-state and 683 quasi-steady-state heat-transfer data points were reported. The test section was an Inconel-625 seamless tube (19.14-mm o.d., 15.70-mm i.d.) with a heated length of 213.4 cm. High-pressure test results are given in Ref. F-79.

F.2.3.3. **LU: Rod Bundle.** Forced-convection, nonequilibrium, post-CHF experiments were conducted at LU for water flowing upwards within a rod bundle consisting of a square array of nine Inconel-600 rods of 9.5-mm o.d. surrounded by a square shroud. The pitch of the rods was 12.6 mm, which provided a rod-to-rod gap of 3.1 mm. The distance between the shroud surface and the nearest row of rods was chosen to obtain thermal-hydraulic conditions similar to those of a PWR. The heated section was 122.0-cm long.

Two separate databases were generated from these LU rod-bundle experiments. Moving-quench-front (276 data points) and fixed-quench-front (98 data points) experiments were run and reported as two sets of data. For the advancing-quench-front data, the pressure range was 0.1 to 0.12 MPa, the mass flow range was 7.08 to 26.15 kg·m^{-2}·s^{-1}, wall heat fluxes ranged from 11.47 to 45.15 kW·m^{-2}, and equilibrium inlet qualities varied from –1.6% to 69%. For the fixed-quench-front data the pressure range was 0.1 to 0.127 MPa, mass flows varied from 8.44 to 29.51 kg/m^2-s, heat fluxes varied from 14.45 to 43.31 kW·m^{-2}, and equilibrium inlet qualities varied from 0.6% to 40%. Detailed descriptions of both the fixed and advancing quench-front experiments for the rod bundles are given in Ref. F-80.

F.2.3.4. **Method of Comparison.** In making a code comparison to data such as these four data sets, we have the following three choices:

1. We can model the test section and apply the proper hydraulic boundary conditions (inlet flow conditions and pressure) and the power to the test rod(s). For the bundle, the test rods must be modeled separately. The measured wall temperatures would be compared to the predicted ones.

2. Here we can do the same as (1) but specify the wall temperature history for the measured levels. (This requires internal modification to the code.) The measured heat fluxes would be compared to the predicted ones. This eliminates the conduction solution in the code and removes the problem caused by slight energy imbalances. These energy imbalances may cause the quench of some steady-state experiments when only an insignificant but excess amount of energy is being calculated as being convected into the fluid. When this happens, a quench will result at some time in the calculation and a problem that is not really serious will appear to be serious.

3. Local-conditions-type calculations can be made (see Section F.2.). These calculations remove the coupling between the different closure relations that will still be part of choices (1) and (2). This, however, requires either the definition of a slip relationship or a parametric study of the effects of slip between the phases.

Because we wish to study only the wall heat-transfer closure relations themselves, we have chosen the third method.

TRAC-calculated results and the data were compared in the following manner. The experimental data provided the thermal-hydraulic conditions at the location of the vapor probe. These conditions were supplied to TRAC subroutine HTCOR, which determined values for the vapor and liquid HTCs. It should be emphasized that the experimental apparatus was not modeled with the TRAC code to simulate the conditions in the test section, i.e., neither method (1) nor method (2) was used. Only local test conditions were supplied to subroutine HTCOR. The call statement to subroutine HTCOR requires that a number of thermodynamic parameters be supplied in addition to the data available from the database. It was necessary to write a driver program to read the thermal-hydraulic information from the databases and to calculate the additional information required by subroutine HTCOR. A number of other subroutines and functions from TRAC were also incorporated into the driver program to compute the additional input required by HTCOR.

To calculate the void fraction from the known experimental quality, it is necessary to know the slip ratio. Because this parameter is not known, a set of parametric calculations was made for slip ratios of 1.0, 5.0, 10.0, and 20.0. Subroutine HTCOR returns values for the liquid HTC, h_{wl}, and the vapor HTC, h_{wg}. The heat transfer from the wall to the liquid, $q'_{w\ell}$, and the heat transfer from the wall to the vapor, q'_{wg}, are then calculated from the following equations:

$$q'_{w\ell} = h_{w\ell}\,(T_w - T_{\text{sat}}) \tag{F-350}$$

and

$$q'_{wg} = h_{wg}\,(T_w - T_g)\ . \tag{F-351}$$

The total TRAC HTC, which is compared to the experimental HTC, is then calculated as

$$h_{\text{total}} = (q'_{w\ell} + q'_{wg})\,/\,(T_w - T_g)\ . \tag{F-352}$$

F.2.3.5. Results of Comparisons. Figures F-64. to F-78. show the TRAC data-comparison plots for the four databases. Figures F-64. to F-66. are plots of the experimental HTC and the calculated HTC for each of the databases for a slip ratio of 1.0. For the INEEL database (Fig. F-64.), it can be seen that several calculated HTCs are much greater than the experimental values. These points generally represent data points

where the fractions were lowest. The databases for the Evans-Webb experiment and the rod-bundle experiment with the advancing quench front (Figs. F-65., F-66.) cover a relatively narrow void-fraction range ($\alpha > 0.99$) and the comparisons with the TRAC predictions are much better than for the INEEL data. The comparison with the rod-bundle data with a fixed quench front indicates that TRAC underpredicts the HTC for a slip ratio of 1.0 (Fig. F-67.). For a slip ratio of 5.0, the comparison is much better (Fig. F-68.). Results from the Evans-Webb experiment indicate that there is a zone near the quench front where the vapor generation is quite high (Ref. F-78.). When the vapor probe location is close to the quench front, the high vapor-generation rate can result in slip ratios larger than unity. In this case, the TRAC results would correlate better with the data if a larger slip ratio were assumed.

Figures F-69. to F-71. are plots of the ratio of the TRAC HTC to the experimental HTC as a function of void fraction at the vapor-probe location assuming a slip ratio of 1.0. It can be seen that at high void fractions, the HTC ratio is approximately unity and the points are grouped quite closely. For the INEEL data (Fig. F-69.), the scatter becomes greater as the void fraction decreases; TRAC overpredicts the experimental HTC by as much as a factor of 10 for void fractions less than 0.95. For the other databases, the range of the experimental parameters is much smaller and most of the void fractions are greater than 0.99. TRAC predictions in these cases are close to the experimental values. At the lower void fractions, the contribution from the wall to the liquid heat transfer dominates, and the HTC is overpredicted.

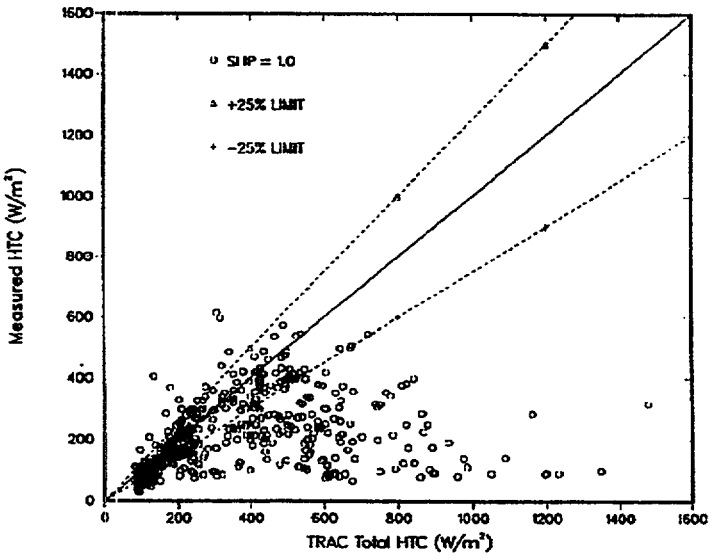

Fig. F-64. INEEL data comparison: experimental HTC vs. TRAC total HTC, slip ratio = 1.0.

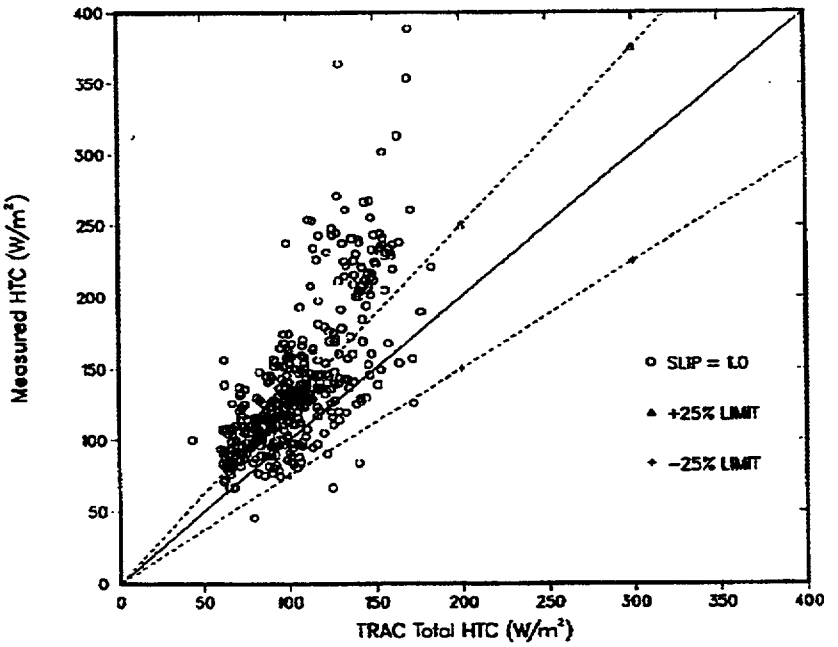

Fig. F-65. Evans-Webb data comparison: experimental HTC vs. TRAC vs. total HTC, slip ratio = 1.0.

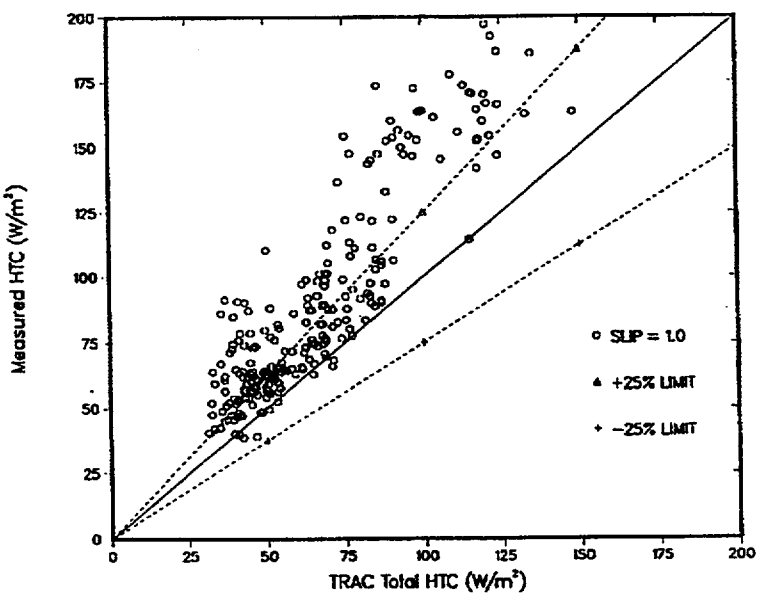

Fig. F-66. LU rod-bundle data comparison: experimental HTC vs. TRAC total HTC, advancing quench front, slip ratio = 1.0.

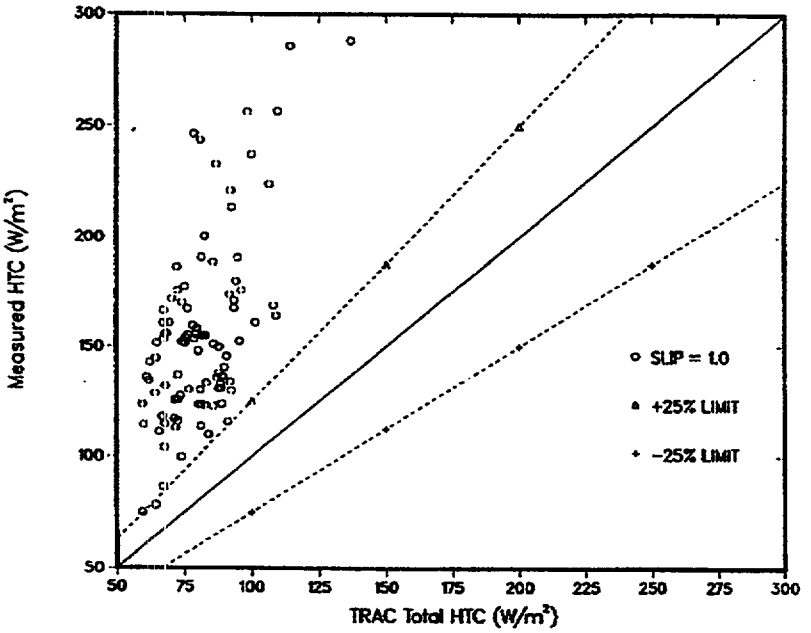

Fig. F-67. LU rod-bundle data comparison: experimental HTC vs. TRAC total HTC, fixed quench front, slip ratio = 1.0.

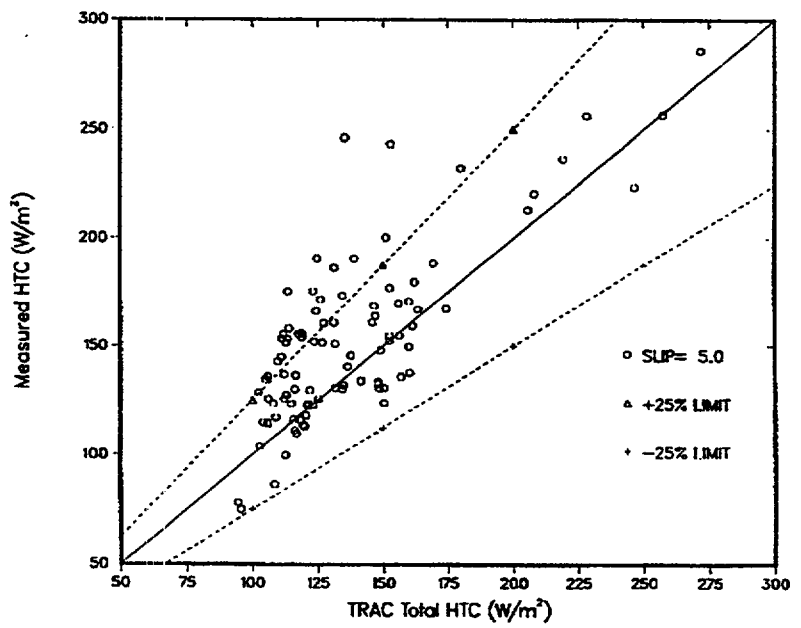

Fig. F-68. LU rod-bundle data comparison: experimental HTC vs. TRAC total HTC, fixed quench front, slip ratio = 5.0.

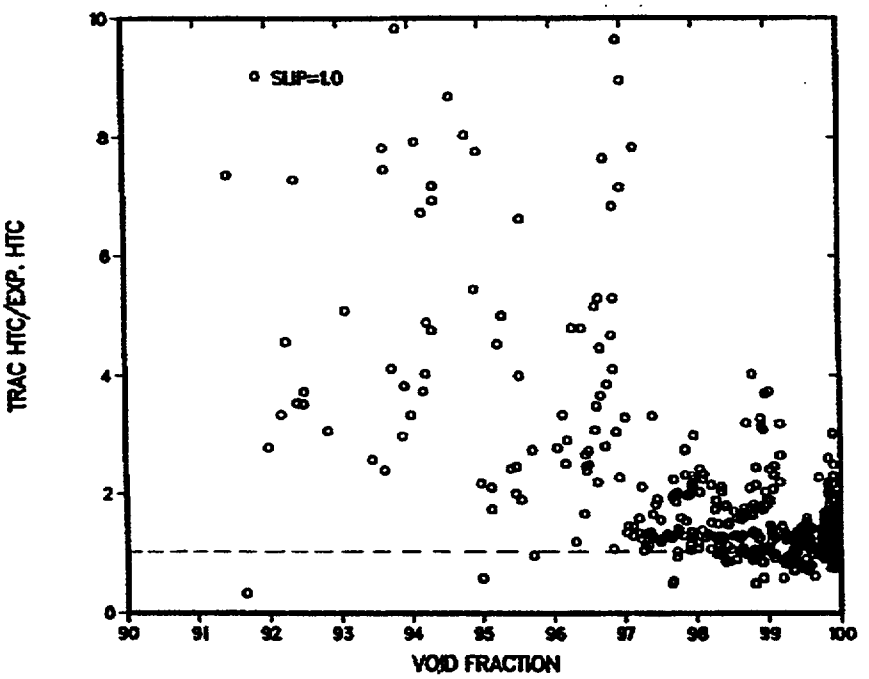

Fig. F-69. INEEL data comparison: ratio of TRAC total HTC to experimental HTC vs. void fraction, slip ratio = 1.0.

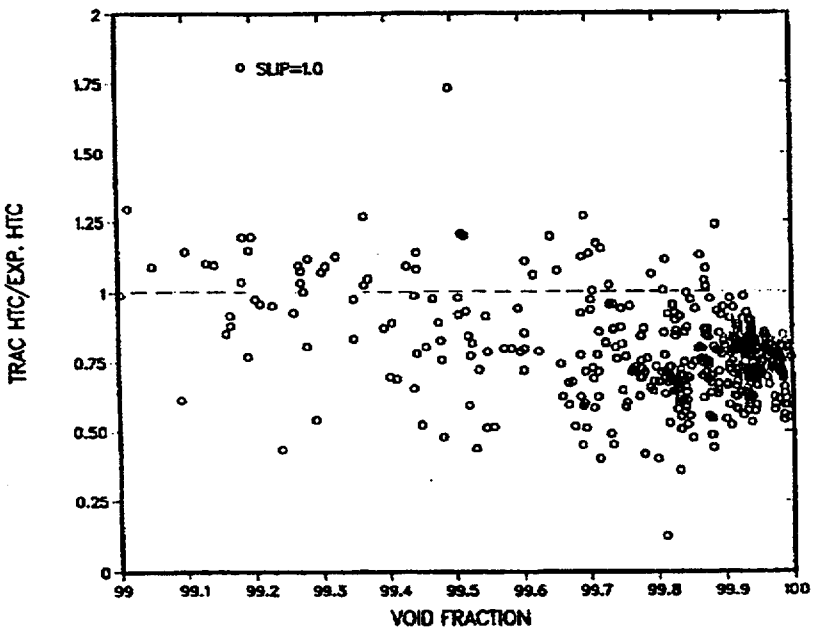

Fig. F-70. Evans-Webb data comparison: ratio of TRAC total HTC to experimental HTC vs. void fraction, slip ratio = 1.0.

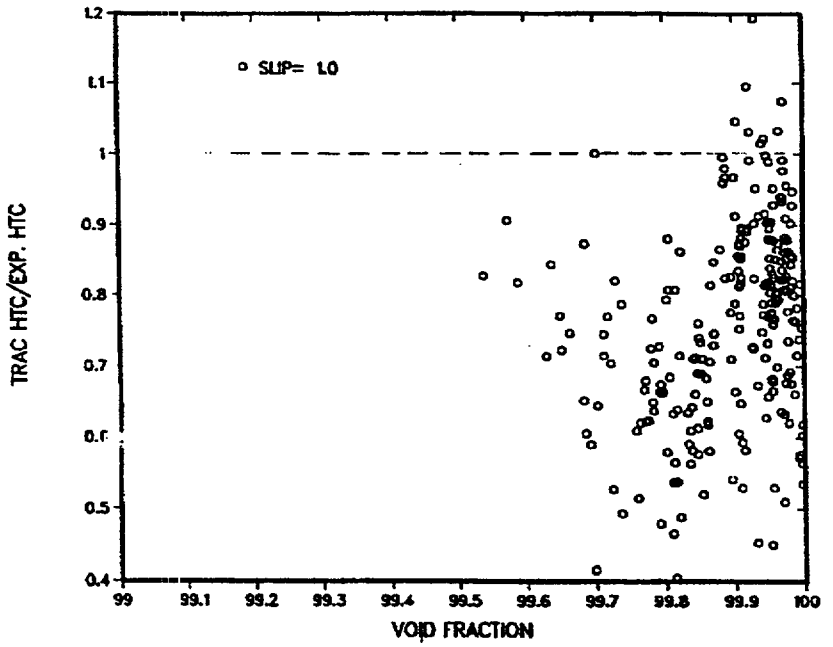

Fig. F-71. LU rod-bundle data comparison: ratio of TRAC total HTC to experimental HTC vs. void fraction, advancing quench front, slip ratio = 1.0.

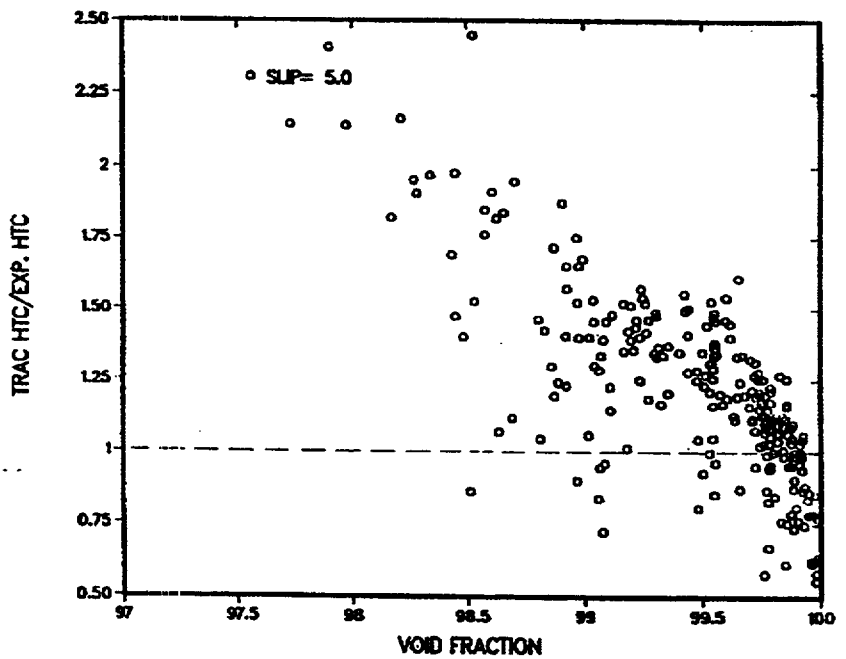

Fig. F-72. LU rod-bundle data comparison: ratio of TRAC total HTC to experimental HTC vs. void fraction, advancing quench front, slip ratio = 5.0.

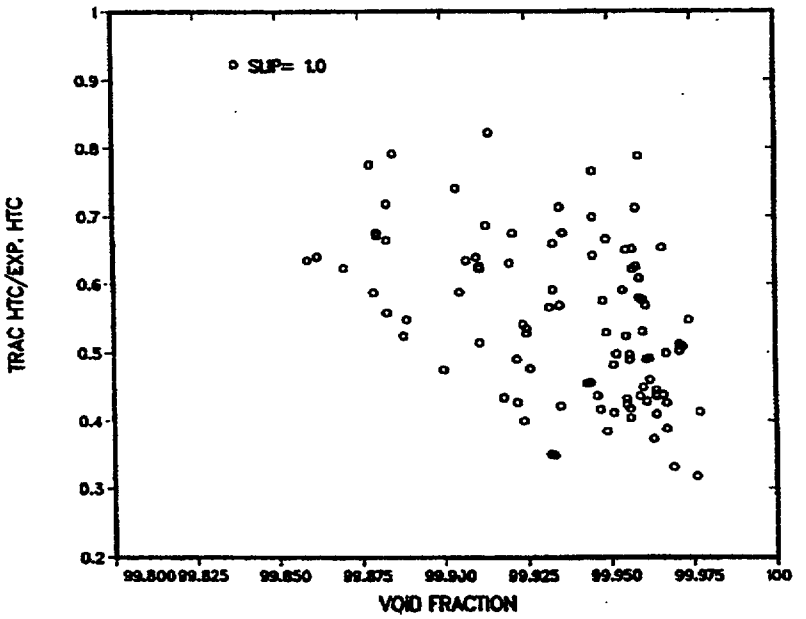

Fig. F-73. LU rod-bundle data comparison: ratio of TRAC total HTC to experimental HTC vs. void fraction, fixed quench front, slip ratio = 1.0.

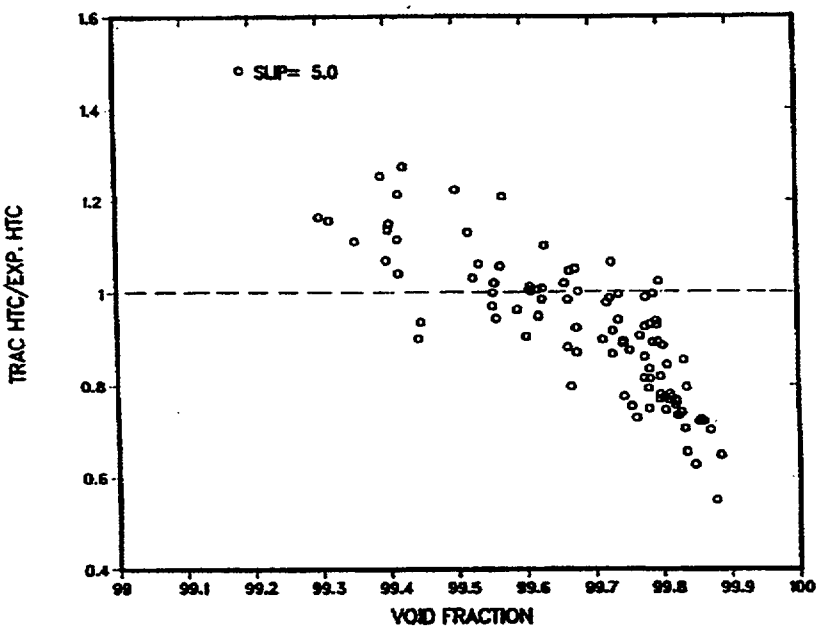

Fig. F-74. LU rod-bundle data comparison: ratio of TRAC total HTC to experimental HTC vs. void fraction, fixed quench front, slip ratio = 5.0.

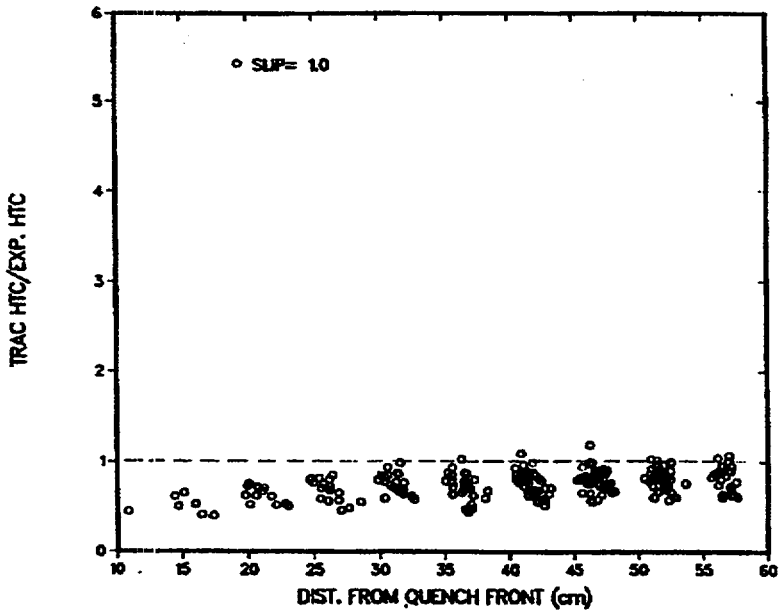

Fig. F-75. LU rod-bundle data comparison: ratio of TRAC total HTC to experimental HTC vs. distance from quench front, advancing quench front, slip ratio = 1.0.

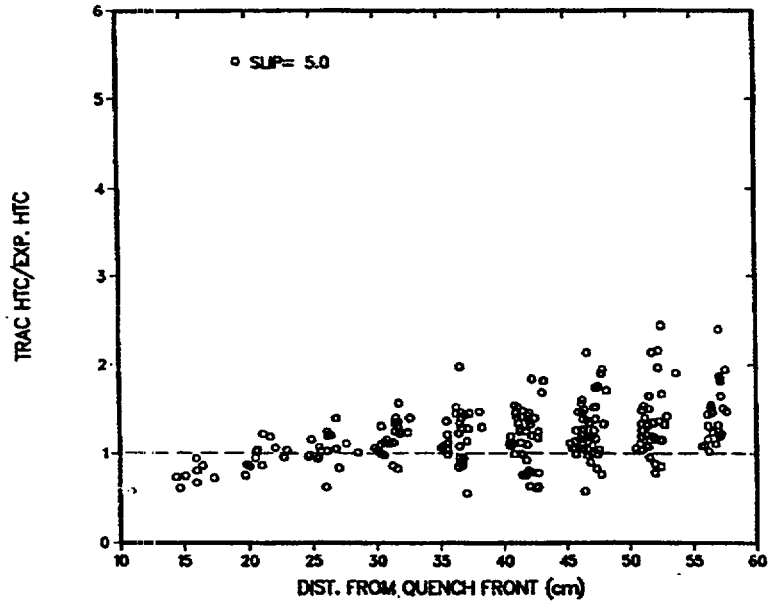

Fig. F-76. LU rod-bundle data comparison: ratio of TRAC total HTC to experimental HTC vs. distance from quench front, advancing quench front, slip ratio = 5.0.

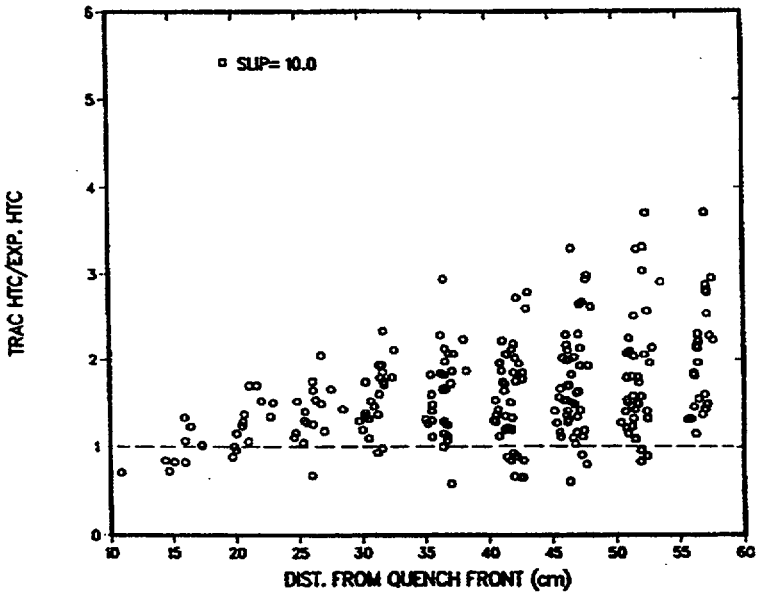

Fig. F-77. LU rod-bundle data comparison: ratio of TRAC total HTC to experimental HTC vs. distance from quench front, advancing quench front, slip ratio = 10.0.

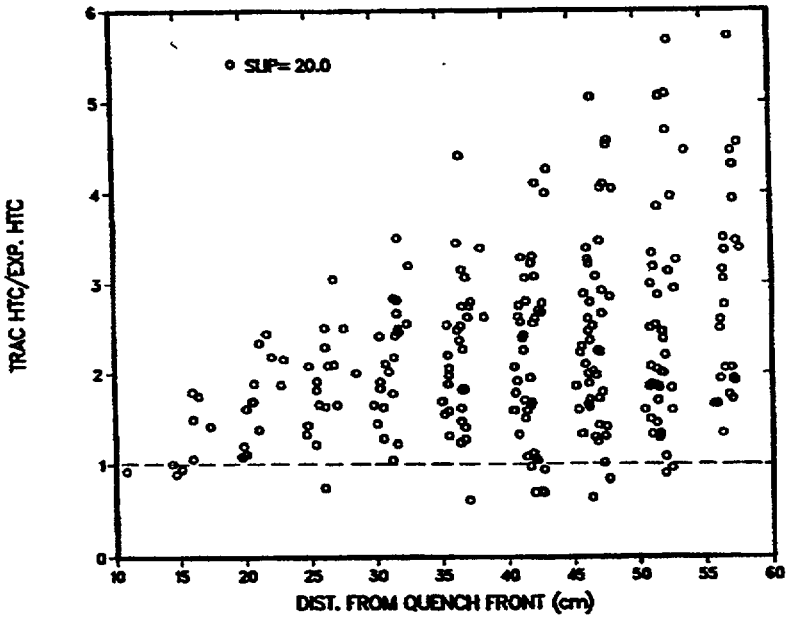

Fig. F-78. LU rod-bundle data comparison: ratio of TRAC total HTC to experimental HTC vs. distance from quench front, advancing quench front, slip ratio = 20.0.

Figures F-72. to F-74. show the sensitivity of the TRAC HTC to the void fraction. It can be seen that for a slip ratio of 1.0, the TRAC HTC is less than the experimental HTC for almost all of the LU rod-bundle data points. When the slip ratio is assumed to be 5.0 (void fraction decreases), the TRAC HTC is greater than the experimental HTC for most data points for the advancing quench front and for approximately one-third of the data points for the fixed quench front.

Figures F-75. to F-78. show the ratio of the TRAC HTC to the experimental HTC as a function of the distance between the vapor probe and the quench front for the LU rod-bundle data with an advancing quench front. The slip ratios are 1.0, 5.0, 10.0, and 20.0. Close to the quench front, the comparison between the calculations and the experimental data improves as the slip ratio increases, which is a consequence of the high vapor-generation rate close to the quench front resulting in a slip ratio greater than 1.0. For a slip ratio of 1.0, the TRAC predictions are grouped quite closely and are in reasonable agreement with the data when the vapor probe is far from the quench front. As the slip ratio increases, the HTCs predicted by TRAC become very scattered and reach values that are as much as six times as large as the experimental values. However, as the slip is increased, the data groups near the quench front are shifted from below 1.0 up through 1.0, indicating again an apparent increasing slip closer to the quench front. Similar trends can be seen in the other data sets. There is nothing in the TRAC correlations to correlate this distance effect and the trend is to overpredict the HTCs. *The distance effect must* be represented by the correct slip being allowed by the interfacial-drag correlation, as discussed in Appendix H. Again, this reflects the tight coupling that can exist between the different closure relationships.

Most experimental data points reported in the four databases examined were taken at very high void fractions–higher than are present during the reflood portion of large-break LOCAs. The CCTF and SCTF tests analyzed using TRAC indicated that even though the void fractions predicted in the upper half of the core were too high, the predicted cladding temperatures were reasonably good. This implies that the heat transfer predicted by the TRAC code exhibits too much sensitivity to void fraction.

F.2.4. TRAC-Data Comparison of the Reflood Model

The TRAC-data comparison of the reflood model coded in subroutine HTVSSL is discussed in Refs. F-93., F-94., and F-95. It uses method 1 as discussed in Section F.2.3.4. The independent data comparison available in these references considered steady-state Winfrith (Ref. F-96.) tests as well as transient Berkeley reflood tests (Ref. F-97.). The results presented were obtained with the earlier version of 5.3.

The results presented in Refs. F-93., F-94., and F-95. indicated that the thermal-hydraulic model gave reasonable predictions of Winfrith post-CHF void fractions (Ref. F-96.) and their variation with axial distance. The relative error between predicted and measured void fractions was 10% at locations far downstream of the post-agitated IAF for a pressure range of 2–10 bar and a heat flux range of 3.6–8.03 $W \cdot cm^{-2}$. Just downstream of the post-agitated IAF, the predictions deviated by about 40% from the measured values. The predictions improved for lower pressures and higher heat fluxes. The effects of

pressure and power on the void fraction and its variation with axial distance were predicted correctly. The effect of pressure is more apparent than the effect of heat flux.

The effects of pressure and test section power on axial wall temperature for Winfrith post-CHF data are predicted reasonably well for steady-state data. A comparison of the predicted and measured wall temperatures at the beginning, middle, and end of the test tube for 20 Winfrith steady-state post-CHF tests (Ref. F-96.) indicated that the maximum average deviation in the predictions was 15.15%.

The vapor temperature for Winfrith steady-state data (Ref. F-96.) was underpredicted and the average deviation was 37.63% for 14 data points. The predicted wall temperature histories show very reasonable agreement for all the Berkeley transient reflood tests (Ref. F-97.) used in this work, indicating reasonable prediction of overall wall and interfacial heat transfer. The agreement was very good for relatively low heat fluxes. At high heat fluxes, the wall temperature trace showed some oscillations that were not seen in the experiments. Further improvements are needed for high-heat-flux conditions in which the vapor generation rate could be high or the interfacial drag model could not consider the correct void fraction effect so that the void fraction could change drastically causing large frequency oscillations in calculations.

The predicted rewetting velocity and its variation along the test tube was in reasonable agreement with measured data for all Berkeley runs (Ref. F-97.). The overall comparison of predicted and measured data indicated an average deviation of 26% and a standard deviation of 40%. These values are considered reasonable.

It was concluded that the thermal-hydraulic reflood model used in TRAC gives very reasonable results in predicting void fraction, wall temperature, and their variations with tube axial distance for Winfrith steady-state, post-CHF databases (Ref. F-96.). It is expected that assessment results will also be very reasonable for any other steady-state, post-CHF database or any other Winfrith steady-state, post-CHF test. The model also gave very satisfactory results in predicting the Berkeley reflood test data (Ref. F-97.), except for the conditions included in high heat fluxes where some disagreement between predicted and measured data existed.

REFERENCES

F-1. M. Ishii and K. Mishima, "Study of Two-Fluid Model and Interfacial Area," Argonne National Laboratory report ANL-80-111 (NUREG/CR-1873) (1980).

F-2. D. Barnea and L. Shemer, "Void Fraction Measurements in Vertical Slug Flow: Applications to Slug Characteristics and Transition," *Int. J. Multiphase Flow* **15**, 495-504 (1989).

F-3. J. F. Lime, "Memorandum on Interfacial Drag from M. Ishii to R. Nelson, July 28, 1987," Los Alamos National Laboratory document LA-UR-01-1591 (March 2001).

F-4. I. Kataoka and M. Ishii, "Drift Flux Model for Large Diameter Pipe and New Correlation for Pool Void Fraction," *Int. J. Heat Mass Transfer* **30**, 1927-1939 (1987).

F-5. J. R. Grace, T. Wairegi, and J. Brophy, "Breakup of Drops and Bubbles in Stagnant Media," *Can. J. Chem. Eng.* **56**, 3-8 (1978).

F-6. J. Kitscha and G. Kocamustafaogullari, "Breakup Criteria for Fluid Particles," *Int. J. Multiphase Flow* **15**, 573-588 (1989).

F-7. Y. M. Chen and F. Mayinger, "Measurement of Heat Transfer at the Phase Interface of Condensing Bubbles," in *ANS Proc. 1989 National Heat Transfer Conf.* (Philadelphia, Pennsylvania, August 6-9, 1989) HTC-Vol. 4, pp. 147-152.

F-8. S. Whittaker, "Forced Convection Heat Transfer Correlations for Flows in Pipes, Past Flat Plates, Single Cylinder, Single Sphere, and Flows in Packed Bids and Tube Bundles," *AIChE J.* **18**, 361-372 (1972).

F-9. R. T. Lahey, Jr. and F. J. Moody, *The Thermal-Hydraulics of a Boiling Water Nuclear Reactor*, ANS monograph (1977).

F-10. W. M. McAdams, *Heat Transmission*, 3rd Ed. (McGraw-Hill Book Co., Inc., New York, 1954).

F-11. G. C. Vliet and G. Leppert, "Forced Convection Heat Transfer from an Isothermal Sphere to Water," *Trans. ASME, J. Heat Transfer* **83**, 163-171 (1961).

F-12. G. G. Brucker and E. M. Sparrow, "Direct Contact Condensation of Steam Bubbles in Water at High Pressure," *Int. J. Heat Mass Transfer* **20**, 371-381 (1977).

F-13. R. Clift, J. R. Grace, and M. E. Weber, *Bubbles, Drops, and Particles*, (Academic Press, New York, 1978).

F-14. B. B. Mikic, W. M. Rohsenow, and P. Griffith, "On Bubble Growth Rates," *Int. J. Heat Mass Transfer* **13**, 657-665 (1970).

F-15. I. Kataoka and M. Ishii, "Mechanism and Correlation of Droplet Entrainment and Deposition in Annular Two-Phase Flow," Argonne National Laboratory report ANL-82-44 (NUREG/CR-2885) (1982).

F-16. I. Kataoka, M. Ishii, and K. Mishima, "Generation and Size Distribution of Droplet in Annular Two-Phase Flow," *Trans. ASME, J. Fluid Engineering* **105**, pp. 230-238 (1983).

F-17. M. Ishii and K. Mishima, "Correlation for Liquid Entrainment in Annular Two-Phase Flow of Low-Viscous Fluid," Argonne National Laboratory report ANL/RAS/LWR 81-2 (1981).

F-18. M. Ishii and K. Mishima, "Droplet Entrainment Correlation in Annular Two-Phase Flow," *Int. J. Heat Mass Transfer* **32**, 1835-1846 (1989).

F-19. K. O. Pasamehmetoglu and R. A. Nelson, "Transient Direct-Contact Condensation on Liquid Droplets," *Nonequilibrium Transport Phenomena*, ASME: New York, HTD-Vol. 77, pp. 47-56 (1987).

F-20. J. D. Ford and A. Lekic, "Rate of Growth of Drops During Condensation," *Int. J. Heat Mass Transfer* **16**, 61-64 (1973).

F-21. J. Iciek, U. Cyvinska, and R. Blaszcyck, "Hydrodynamics of Free Liquid Jets and Their Influence on Heat Transfer," in *Handbook of Heat and Mass Transfer*, "Vol. 1: Heat Transfer Operations," N. P. Cheremisinoff, editor (Gulf Publishing Co., Houston, Texas, 1986) pp. 151-181.

F-22. M. Ishii, "One Dimensional Drift-Flux Model and Constitutive Equations for Relative Motion Between Phases in Various Two-Phase Flow Regimes," Argonne National Laboratory report ANL-77-47 (1977).

F-23. G. Ryskin, "Heat and Mass Transfer from a Moving Drop–Some Approximate Relations for the Nusselt Number," *Int. Comm. Heat Mass Transfer* **14**, pp. 741-749 (1987).

F-24. S. G. Bankoff, "Some Condensation Studies Pertinent to Light Water Safety," *Int. J. Multiphase Flow* **6**, 51-67 (1980).

F-25. J. C. B. Lopes and A. E. Dukler, "Droplet Size, Dynamics and Deposition in Vertical Annular Flow," (NUREG/CR-4424) (1985).

F-26. S. Aoki, A. Inoue, Y. Kozawa, and H. Akimoto, "Direct-Contact Condensation of Flowing Steam onto Injected Water," *Proc. 6th Int. Heat Transfer Conf.* (Toronto, Canada, 1982) Vol. 6, pp. 107-112.

F-27. H. Akimoto, Y. Kozawa, A. Inoue, and S. Aoki, "Analysis of Direct-Contact Condensation of Flowing Steam onto Injected Water with Multifluid Model of Two-Phase Flow," *J. Nucl. Sci. Tech.* **20**, 1006-1022 (1983).

F-28. J. H. Linehan, M. Petrick, and M. M. El-Wakil, "The Condensation of Saturated Vapor on a Subcooled Film During Stratified Flow," *Chem. Eng. Symp. Series* **66** (102), 11-20 (1972).

F-29. H. J. Kim, "Local Properties of Countercurrent Stratified Steam-Water Flow," US Nuclear Regulatory Commission contractor report (NUREG/CR-4417) (1985).

F-30. H. Akimoto, Y. Tanaka, Y. Kozawa, A. Inoue, and S. Aoki, "Oscillatory Flows Induced by Direct-Contact Condensation of Flowing Steam with Injected Water," *J. Nucl. Sci. Tech.* **22**, 269-283 (1985).

F-31. G. DeJarlais and M. Ishii, "Inverted Annular Flow Experimental Study," Argonne National Laboratory report ANL-85-31 (NUREG/CR-4277) (1985).

F-32. C. Unal, K. Tuzla, C. A. Tuzla, and J. C. Chen, "Vapor Generation Model for Dispersed Drop Flow," in *ANS Proc. 1989 National Heat Transfer Conf.* (August 1989), HTC-Vol. 4.

F-33. Y. Y. Hsu and R. W. Graham, *"Transport Processes in Boiling and Two-Phase Systems* (Hemisphere Publishing Corporation, Washington, 1976).

F-34. M. K. Denham, "Inverted Annular Film Boiling and the Bromley Model," AEEW-R 1590, Winfrith, Rochester (January 1983).

F-35. A. H. P. Skelland, *Diffusional Mass Transfer* (Robert E. Kreiger Publishing Co, Malabar, Florida, 1985).

F-36. G. G. Sklover and M. D. Rodivilin, "Condensation on Water Jets with a Cross Flow of Steam," *Teploenergetika* **23**, 48-51 (1976).

F-37. R. V. Shilimkan and J. B. Stepanek, "Interfacial Area in Cocurrent Gas-Liquid Upflow in Tubes of Various Sizes," *Chem. Eng. Sci.* **32**, 149-154 (1977).

F-38. G. Kasturi and J. B. Stepanek, "Two-Phase Flow-III. Interfacial Area in Co-Current Gas-Liquid Flow," *Chem. Eng. Sci.* **29**, 713-719 (1974).

F-39. J. M. DeJesus and M. Kawaji, "Measurement of Interfacial Area and Void Fraction in Upward, Cocurrent Gas-Liquid Flow," *ANS Proc. 1989 National Heat Transfer Conf.* (Philadelphia, Pennsylvania, August 6-9, 1989) HTC-Vol. 4, pp. 137-145.

F-40. G. F. Hewitt, "Liquid-Gas Systems," Chapter 2 in *Handbook of Multiphase Flow,* G. Hestroni, editor (Hemisphere Publishing Corporation, Washington, 1981).

F-41. R. A. Nelson, "Forced Convective Post-CHF Heat Transfer and Quenching," *J. Heat Trans.* **104**, 48-54 (1982).

F-42. Safety Code Development Group, "TRAC-PF1/MOD1: An Advanced Best-Estimate Computer Program for Pressurized Water Reactor Thermal-Hydraulic Analysis," Los Alamos National Laboratory report LA-10157-MS (NUREG/CR-3858) (July 1986).

F-43. "RELAP4/MOD6–A Computer Program for Transient Thermal-Hydraulic Analysis of Nuclear Reactors and Related Systems, User's Manual," Idaho National Engineering Laboratory report CDAP-TR-003 (January 1978).

F-44. I. Nukiyama, "Maximum and Minimum Values of Heat Transmitted from a Metal to Boiling Water Under Atmospheric Pressure," *J. Soc. Mech. Eng. Japan* **37** (1934).

F-45. S. C Yao and R. E. Henry, "An Investigation of the Minimum Film Boiling Temperature on Horizontal Surfaces," *J. Heat Trans.*, **100**, 260-267 (1987).

F-46. L. Y. Lee, J. C. Chen, and R. A. Nelson, "Liquid-Solid Contact Measurement Using a Surface Thermocouple Temperature Probe in Atmospheric Pool Boiling Water," *Int. J. Heat Mass Transf.*, **28**, 1415-1423 (1985).

F-47. M. T. Farmer, B. G. Jones, and R. W. Spencer, "Analysis of Transient Contacting in the Low Temperature Film Boiling Regime. Part I: Modeling of the Process," *Nonequilibrium Transport Phenomena*, ASME HTD-Vol. 77, pp. 23-29 (1987).

F-48. M. T. Farmer, B. G. Jones, and R. W. Spencer, "Analysis of Transient Contacting in the Low Temperature Film Boiling Regime. Part II: Comparison With Experiment," *Nonequilibrium Transport Phenomena*, ASME HTD-Vol. 77, pp. 39-45 (1987).

F-49. R. A. Nelson, "Mechanisms of Quenching Surfaces," in *Handbook of Heat and Mass Transfer*, "Vol. 1: Heat Transfer Operations," N. P. Cheremisinoff, editor (Gulf Publishing Company, Houston, Texas 1986), pp. 1103-1153.

F-50. J. M. Delhaye, M. Giot, and M. L. Riethmuller, *Thermohydraulics of Two-Phase Systems for Industrial Design and Nuclear Engineering* (Hemisphere Publishing Corporation, New York, 1981).

F-51. F. E. Incropera and D. P. DeWitt, *Fundamentals of Heat Transfer* (John Wiley & Sons, Inc., New York, 1981).

F-52. J. Weisman, "Heat Transfer to Water Flowing Parallel to Tubes, " *Nucl. Sci. Eng.* **6**, 79 (1959).

F-53. J. P. Holman, *Heat Transfer*, 5th ed. (McGraw-Hill Book Co., Inc., New York, 1981).

F-54. B. Gebhart, *Heat Transfer*, 2nd ed. (McGraw-Hill Book Co., Inc., New York, 1971).

F-55. H. K. Forster and N. Zuber, "Bubble Dynamics and Boiling Heat Transfer," *AIChE J.* **1**, 532-535 (1955).

F-56. J. G. Collier, *Convective Boiling and Condensation*, 2nd ed. (McGraw-Hill Book Co., Inc., New York, 1981).

F-57. A. E. Bergles, J. G. Collier, J. M. Delhaye, G. F. Hewitt, and F. Mayinger, *Two-Phase Flow and Heat Transfer in the Power and Process Industries* (Hemisphere Publishing Corporation, New York, 1981).

F-58. M. Shah, "A New Correlation for Heat Transfer During Boiling Flow Through Tubes," *ASHRAE Trans.* **82** (2), 66-86 (1976).

F-59. R. W. Bjorge, G. R. Hall, and W. M. Rohsenow, "Correlation of Forced Convection Boiling Heat Transfer Data," *Int. J. Heat Mass Transfer* **25** (6), 753-757 (1982).

F-60. K. E. Gungor and R. H. S. Winterton, "A General Correlation for Flow Boiling in Tubes and Annuli," *Int. J. Heat Mass Transfer* **29** (3), 351-358 (1986).

F-61. O. C. Jones, Jr. and S. G. Bankoff, editors, *Thermal and Hydraulic Aspects of Nuclear Reactor Safety, Volume 1: Light Water Reactors* (ASME, New York, 1977).

F-62. L. A. Bromley, "Heat Transfer in Stable Film Boiling," *Chem. Eng. Prog.* **46** (5), 221-227 (May 1950).

F-63. Y. Lee and K. H. Kim, "Inverted Annular Flow Boiling," *Int. J. Multiphase Flow* **13** (3), 345-355 (1987).

F-64. I. Vojtek, "Investigation of Dispersed Flow Heat Transfer Using Different Computer Codes and Heat Transfer Correlations," The First International Workshop on Fundamental Aspects of Post-Dryout Heat Transfer, report (NUREG/CP-0060) (April 2-4, 1984).

F-65. R. B. Bird, W. E. Stewart, and E. N. Lightfoot, *Transport Phenomena* (John Wiley & Sons, Inc., New York, 1960).

F-66. F. Kreith, *Principles of Heat Transfer*, 3rd ed. (Harper and Row, Inc., New York, 1973).

F-67. W. M. Rohsenow and H. Choi, *Heat, Mass, and Momentum Transfer* (Prentice-Hall, Englewood Cliffs, New Jersey, 1961).

F-68. W. H. McAdams, "Vaporization Inside Horizontal Tubes-II-Benzene-Oil Mixtures," *Trans. ASME* **64**, 193 (1942).

F-69. L. Biasi, G. C. Clerici, S. Garribba, R. Sala, and A. Tozzi, "Studies on Burnout, Part 3: A New Correlation for Round Ducts and Uniform Heating and Its Comparison with World Data," *Energia Nucleare* **14**, 530-536 (1967).

F-70. D. C. Groeneveld, S. C. Cheng, and T. Doan, "1986 AECL-UO Critical Heat Flux Lookup Table," *Heat Transfer Engineering* **7**, 46-62 (1986).

F-71. J. C. M. Leung, "Transient Critical Heat Flux and Blowdown Heat Transfer Studies," Ph.D. dissertation, Northwestern University (June 1980).

F-72. P. Griffith, J. F. Pearson, and R. J. Lepkowski, "Critical Heat Flux During a Loss-of-Coolant Accident," *Nuclear Safety* **18**, 298-309 (1977).

F-73. K. O. Pasamehmetoglu, "Transient Critical Heat Flux," Ph.D. dissertation, University of Central Florida (also EIES report 86-87-1) (August 1986).

F-74. M. L. James, G. M. Smith, and J. C. Wolford, *Applied Numerical Methods for Digital Computation with FORTRAN and CSMP*, 2nd ed. (Harper and Row, Inc., New York, 1977).

F-75. R. E. Henry, "A Correlation for the Minimum Film Boiling Temperature," *AIChE Symposium Series* **138**, 81-90 (1974).

F-76. S. C. Cheng, P. W. K. Law, and K. T. Poon, "Measurements of True Quench Temperature of Subcooled Water Under Forced Convection Conditions," *Int. J. Heat Mass Transfer*, **20** (1), 235-243 (1985).

F-77. D. C. Groeneveld and J. C. Stewart, "The Minimum Film Boiling Temperature for Water During Film Boiling Collapse," in *Proc. 7th Int. Heat Transfer Conf.* (Munich, FRG, 1982), Vol. 4, pp. 393-398.

F-78. D. G. Evans, S. W. Webb, and J. C. Chen, "Measurement of Axially Varying Non-equilibrium in Post-Critical-Heat-Flux Boiling in a Vertical Tube," Lehigh University report (NUREG/CR-3363) (June 1983).

F-79. R. C. Gottula, R. G. Condie, R. K. Sundaram, S. Neti, J. C. Chen, and R. A. Nelson, "Forced Convective, Nonequilibrium, Post-CHF Heat Transfer Experiment Data and Correlation Comparison Report," Idaho National Engineering Laboratory report EGG-2245 (NUREG/CR-3193) (March 1985).

F-80. C. Unal, "An Experimental Study of Thermal Nonequilibrium Convective Boiling in Post-Critical-Heat-Flux Region in Rod Bundles," Ph.D. dissertation, Lehigh University (1985).

F-81. C. Unal, K. Tuzla, O. Badr, S. Neti, and J. C. Chen, "Convective Film Boiling in a Rod Bundle: Transverse Variation of Vapor Superheat Temperature Under Stabilized Post-CHF Conditions," *Heat Mass Transfer* **34** (7), 1695-1706 (1991).

F-82. K. Tuzla, C. Unal, O. Badr, S. Neti, and J. C. Chen, "Thermodynamic Nonequilibrium in Post-Critical-Heat-Flux Boiling in a Rod Bundle," US Nuclear Regulatory Comission report (NUREG/CR-5095, Volumes I-IV) (July 1987).

F-83. S. Webb and J. C. Chen, "A Two-Region Vapor Generation Rate Model for Convective Film Boiling," Int. Workshop of Fundamental Aspects of Post-Dryout Heat Transfer, Salt Lake City, Utah, April 1-4, 1984.

F-84. N. T. Obot and M. Ishii, "Two-Phase Flow Regime Transition Criteria in Post-Dryout Region Based on Flow Visualization Experiments," Argonne National Laboratory report ANL-87-27 (NUREG/CR-4972) (June 1987).

F-85. J. C. Chen, F. T. Ozkaynak, and R. K. Sundaram, "Vapor Heat Transfer in Post-CHF Region Including the Effect of Thermodynamic Non-Equilibrium," *Nuclear Eng. and Design* **51**, 143-155 (1979).

F-86. Th. Analytis and G. Yadigaroglu, "Analytical Modeling of Inverted Annular Film Boiling," *Nuclear Eng. and Design* **99** (1987).

F-87. R. P. Forslund and W. M. Rohsenow, "Dispersed Flow Film Boiling," *J. Heat Trans.* **90** (6), 399-407 (1968).

F-88. G. M. Anderson, "Low Flow Film Boiling Heat Transfer on Vertical Surfaces; Part 1: Theoretical Model," *AIChE Symposium Series* **73** (164), 2-6 (1977).

F-89. Y. Sudo, "Film Boiling Heat Transfer During Reflood Phase in Postulated PWR Loss-of-Coolant Accident," *J. Nuclear Science and Tech.* **17** (7), 516-530 (July 1980).

F-90. A. F. Varone, Jr. and W. M. Rohsenow, "Post-dryout Heat-Transfer Predictions," *Nuclear Eng. and Design* **95**, 315-327 (1986).

F-91. K. Kiangah and D. K. Dhir, "An Experimental and Analytical Study of Disposed Flow Heat Transfer," *Int. J. Thermal and Fluid Science*, **2**, 410-424 (1989).

F-92. R. A. Nelson and C. Unal, "A Phenomenological model of the Thermal hydraulics of convective boiling during the quenching of hot rod bundles. Part I: Thermal hydraulic model," Nuclear *Eng. and Design* **136**, 277-298 (1992).

F-93. R. A. Nelson and C. Unal, "A Phenomenological Model of the Thermal-Hydraulics of Convective Boiling During the Quenching of Hot Rod Bundles Part I: Thermal Hydraulic Model," *Nuclear Engineering and Design*, Vol. 136 pp. 277-298, 1992.

F-94. C. Unal and R. A. Nelson, "A Phenomenological Model of the Thermal-Hydraulics of Convective Boiling During the Quenching of Hot Rod Bundles Part II: Assessment of the Model with Steady-State and Transient Post-CHF Data," *Nuclear Engineering and Design*, Vol. 136, pp. 298-319, 1992.

F-95. C. Unal, E. Haytcher, and R. A. Nelson, "Thermal-Hydraulics of Convective Boiling During the Quenching of Hot Rod Bundles Part III: Model Assessment Using Winfrith Steady-State Post-CHF Void Fraction and Heat Transfer Measurements and Berkeley Transient Reflood Test Data," *Nuclear Engineering and Design*, Vol. 19, 1993.

F-96. D. Swinnerton, R. A. Savage, and K. G. Pearson, "Heat Transfer Measurements in Steady-State Post-Dryout at Low Quality and Medium Pressure," AEA Thermal Reactor Services, Physics and Thermal Hydraulic Division report AEA-TRS-1045, Winfrith United Kingdom Atomic Energy report AEEW-R 2503 (April 1990).

F-97. R. Seban., et al., "UC-B Reflood Program: Experimental Data Report," NP-743, Research Project 248-1, April 1978.

F-98. Safety Code Development Group, "TRAC-PF1/MOD1 Correlations and Models," Los Alamos National Laboratory report LA-11208-MS (NUREG/CR-5069) (December 1988).

F-99. B. E. Boyack, J. F. Lime, D. A. Pimental, J. W. Spore, and J. L. Steiner, "TRAC-M/F77, Version 5.5, Developmental Assessment Manual, Volume I: Assessment Sections not Including 2D/3D Tests," Los Alamos National Laboratory document LA-UR-99-6480 (December 1999).

F-100. B. E. Boyack, J. F. Lime, D. A. Pimental, J. W. Spore, and J. L. Steiner, "TRAC-M/F77, Version 5.5, Developmental Assessment Manual, Volume II: Assessment Sections for 2D/3D Tests," Los Alamos National Laboratory document LA-CP-99-345 (December 1999).

F-101. R. A. Nelson, Jr., D. A. Pimentel, S. J. Jolly-Woodruff, and J. W. Spore, "Reflood Completion Report, Volume I: A Phenomenological Thermal-Hydraulic Model of Hot Rod Bundles Experiencing Simultaneous Bottom and Top Quenching and an Optimization Methodology for Closure Development," Los Alamos National Laboratory report LA-UR-98-3043 (April, 1998).

F-102. B. E. Boyack, J. F. Lime, D. A. Pimentel, J. W. Spore, and T. D. Knight, "Reflood Completion Report, Volume II: Developmental Assessment of a New Reflood Model for the TRAC-M/F77 Code," Los Alamos National Laboratory report LA-UR-98-3043 (April, 1998).